Aus dem National Center for Radiation Research in Oncology – OncoRay
Direktorin: Prof. Dr. Mechthild Krause

Dual-Energy Computed Tomography for Accurate Stopping-Power Prediction in Proton Treatment Planning

D i s s e r t a t i o n s s c h r i f t

zur Erlangung des akademischen Grades
Doktor der Medizintechnologie
Doctor rerum medicinalium (Dr. rer. medic.)

vorgelegt

der Medizinischen Fakultät Carl Gustav Carus
der Technischen Universität Dresden

von

M.Sc. Patrick Wohlfahrt
aus Ebersdorf / Thüringen

Dresden 2018

1. Gutachter: Prof. Dr. Wolfgang Enghardt

2. Gutachter: Prof. Dr. Antony J. Lomax

Tag der mündlichen Prüfung: 2. August 2018

Prof. Dr. Esther G. C. Troost
Vorsitzende der Promotionskommission

Abstract

Range uncertainty in proton therapy currently hampers the full exploitation of its physical advantages. A substantial amount of this uncertainty arises from proton range prediction based on X-ray computed tomography (CT). Dual-energy CT (DECT) has often been suggested as a promising imaging modality to reduce this CT-related range uncertainty. Within this thesis, the translation of DECT into application in proton therapy was evaluated. First, a CT scan protocol was optimised for radiotherapy considering the image quality and CT number stability for various body regions and sizes. The patient-specific DECT-based range prediction was then calibrated and its accuracy validated in two ground-truth experiments using an anthropomorphic phantom and homogeneous biological tissues. Subsequently, the clinical relevance of DECT was demonstrated in a retrospective cohort analysis of cerebral, pelvic and thoracic tumour patients. The systematic range deviations between the DECT and state-of-the-art approach were then reduced by adapting the standard method utilizing additional patient information obtained from DECT. Hence, DECT was clinically applied for the first time to refine proton range calculation. As a further step, the use of patient-specific DECT-based range prediction also considers intra- and inter-patient tissue variabilities as quantified in brain-tumour patients. A future implementation will be an important cornerstone to improve proton range calculation and might open up the possibility to reduce clinical safety margins accounting for the CT-related range uncertainty.

Kurzfassung

Derzeitige Reichweiteunsicherheiten in der Protonentherapie verhindern das vollständige Ausschöpfen ihrer physikalischen Vorteile. Ein wesentlicher Anteil ist dabei auf die Vorhersage der Reichweite mittels Röntgen-Computertomographie (CT) zurückzuführen. Um die CT-bezogene Unsicherheit zu verringern, wird die Zwei-Spektren-Computertomographie (DECT) als vielversprechend angesehen. Innerhalb dieser Arbeit wurde die Anwendbarkeit von DECT in der Protonentherapie untersucht. Zunächst wurde ein CT-Scanprotokoll für die Strahlentherapie hinsichtlich Bildqualität und Konstanz der CT-Zahlen für verschiedene Körperregionen und -größen optimiert. Anschließend wurde die patientenindividuelle DECT-basierte Reichweitevorhersage kalibriert und ihre Genauigkeit in zwei Experimenten mit bekannter Referenz unter Verwendung eines anthropomorphen Phantoms und von homogenen biologischen Geweben verifiziert. Die klinische Relevanz von DECT wurde in einer retrospektiven Analyse von Krebspatienten mit Tumoren im Kopf, Becken oder Thorax nachgewiesen. Die systematischen Reichweiteunterschiede zwischen DECT und dem klinischen Standardverfahren konnten durch die Optimierung der Standardmethode basierend auf zusätzlichen mit DECT erworbenen Patienteninformationen reduziert werden. Somit wurde DECT erstmalig klinisch genutzt, um die Reichweiteberechnung zu verbessern. Die patientenindividuelle DECT-basierte Reichweitevorhersage kann zusätzlich Gewebevariabilitäten innerhalb eines und zwischen Patienten berücksichtigen, wie für Kopftumorpatienten gezeigt wurde. Dies legt den Grundstein für eine genauere Reichweiteberechnung und eröffnet neue Möglichkeiten für die Reduktion klinischer Sicherheitssäume, in denen die CT-bezogenen Unsicherheiten berücksichtigt sind.

Contents

List of Figures

List of Tables

List of Symbols and Acronyms

1D	one-dimensional
2D	two-dimensional
3D	three-dimensional
4D	four-dimensional
4D-DECT	time-resolved dual-energy CT
4D-SECT	time-resolved single-energy CT
ADMIRE	Advanced Modelled Iterative Reconstruction
ALARA	as low as reasonably achievable (radiation protection principle)
β	velocity related to the vacuum speed of light
BEV	beam's eye view
BHC	beam hardening correction
BHR	beam-hardening ratio
CT	computed tomography
CTDIvol	computed tomography dose index
CTV	clinical target volume
DECT	dual-energy computed tomography
DICOM	Digital Imaging and Communications in Medicine
DIR	deformable image registration
DirectSPR	direct stopping-power prediction from dual-energy CT
DVH	dose-volume histogram
EAN	effective atomic number, Z_{eff}

ED	electron density, ϱ_e
FBP	filtered back projection
FOV	field of view
FWHM	full width at half maximum
GTV	gross tumour volume
H	CT number
HLUT	Hounsfield look-up table
HU	Hounsfield unit
iGTV	internal gross tumour volume
iMAR	Iterative Metal Artefact Reduction
INR	image-noise ratio
I-value	mean excitation energy, I
L	stopping number
LET	linear energy transfer
MAI	metal-artefact index
MD	mass density, ϱ
MLIC	multi-layer ionisation chamber
MonoCT	pseudo-monoenergetic CT
MSE	mean square error
μ	attenuation coefficient of photon interaction
NCC	normalised cross correlation
NIST	National Institute of Standards and Technology, USA
NSCLC	non-small-cell lung cancer
OAR	organ at risk

PTV	planning target volume
RBE	relative biological effectiveness
RCS	photon attenuation cross section relative to water, $\hat{\sigma}$
RED	electron density relative to water, $\hat{\varrho}_\mathrm{e}$
RhoSigma	stopping-power prediction using electron density and photon attenuation cross section derived from dual-energy CT
RhoZ	stopping-power prediction using electron density and effective atomic number derived from dual-energy CT
RMSE	root mean square error
ROI	region of interest
RSN	stopping number relative to water, $\hat{L}$
SAFIRE	Sinogram Affirmed Iterative Reconstruction
SECT	single-energy computed tomography
σ_e	photon attenuation cross section per electron
SOBP	spread-out Bragg peak
S	stopping power
SPR	stopping-power ratio, $\hat{S}$
syngo.Mono	syngo.CT Monoenergetic imaging
syngo.MonoPlus	syngo.CT DE Monoenergetic Plus
syngo.RhoZ	syngo.CT DE Rho/Z
TPS	treatment planning system
voxel	volume element
WET	water-equivalent thickness
Z	atomic number

1 Introduction

An efficient diagnosis and treatment of cancer is a worldwide demanding task to overcome the increasing number of cancer incidents and cancer-related mortality of millions of people (Stewart and Wild, 2014). One important cornerstone is the individual prevention of cancer disease by following evidence-based instructions and recommendations provided by the World Health Organisation as a "world code against cancer" (Espina et al., 2018). An additional pillar of cancer control is the development of techniques for both an early tumour detection and high-precision treatment strategies. To account for the complexity of the cancer genome and individual differences in carcinogenesis, the field of oncology aims at targeted therapies to tailor the treatment to the individual requirements of each patient (Moscow et al., 2017; Karczewski and Snyder, 2018). The individually targeted therapy of more than 50% of all cancer patients would benefit from a contribution of radiotherapy as determined by the European Society for Radiotherapy and Oncology (Lievens and Grau, 2012; Borras et al., 2015). Especially in this field, the synergy of technological improvements in treatment conformity and accuracy as well as novel biological concepts tackling differences in tumour radiation resistance and sensitivity allow for an increase of the therapeutic window (Baumann et al., 2016).

In radiation oncology, the clinical application of particle therapy using protons or heavier ions such as carbons is promising to be the treatment of choice for most patients with static and localised tumours due to the defined particle range in tissue (Bortfeld and Loeffler, 2017). To fully exploit the physical advantages of particle therapy, medical imaging plays a vital role for the delineation of the targeted tumour region and especially for precise and accurate dose calculation. However, uncertainties in treatment planning, specifically in the predicted particle range, currently results in the irradiation of a margin encompassing healthy tissue around the tumour. This margin corresponds approximately to 3.5% of the target depth in beam direction, i.e. 7 mm for a tumour situated at 20 cm depth within the patient (Goitein, 1985; Paganetti, 2012b). A substantial amount of this uncertainty arises from the dose calculation based on X-ray computed tomography (CT). Since the stopping power

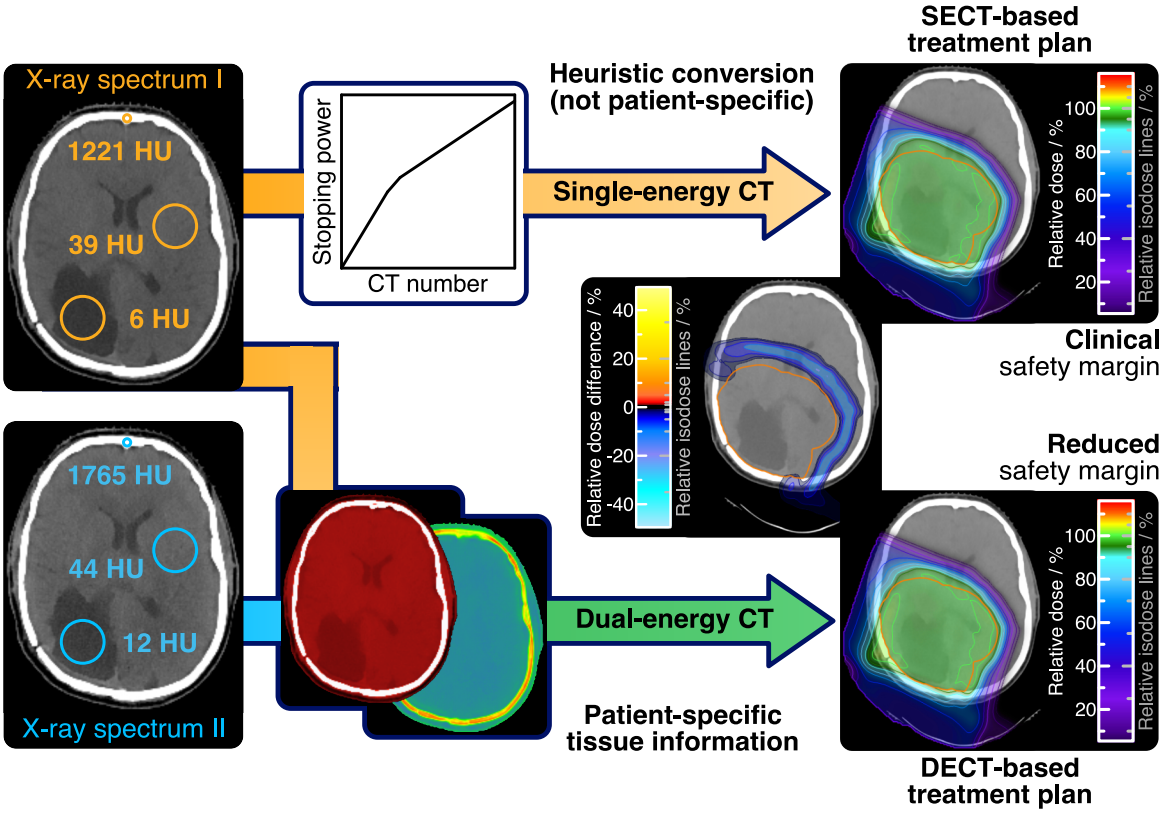

Figure 1.1: Schematic representation of proton range prediction using single-energy CT (SECT) and dual-energy CT (DECT). A more accurate patient-specific range prediction using DECT might allow for a reduction of clinical safety margins. This leads to a better sparing of healthy tissue as illustrated in the dose difference between the DECT- and SECT-based treatment plan.

of protons, describing the mean energy loss of protons in tissue, cannot be fully derived from X-ray attenuation, a heuristic conversion of CT numbers to proton stopping power is clinically applied (Fig. 1.1). This method is not patient-specific and allows only for a limited differentiation of the respective stopping power in soft tissues. For an improved material differentiation and incorporation of patient-specific tissue variations, the acquisition of two CT scans with different X-ray spectra, referred to as dual-energy computed tomography (DECT), was suggested for proton therapy (Goitein, 1977). Based on the additional information gathered by DECT, the proton stopping power can be obtained with only a small empirical component, which might allow for an improved range prediction and thus smaller clinical safety margins (Fig. 1.1). After DECT was proposed in the 1970s (Hounsfield, 1973), its routine clinical application has been introduced to diagnostic radiology about 30 years later (Flohr et al., 2006). In radiotherapy, however, no clinical application of DECT has been reported until 2015 despite its potential advantages (van Elmpt et al., 2016).

The aim of this thesis, carried out in the framework of a joint project between OncoRay (Dresden, Germany) and the German Cancer Research Centre (Heidelberg, Germany) within the National Centre for Radiation Research in Oncology in Germany, was the evaluation and quantification of the benefits of DECT for range prediction in proton therapy and its translation into clinical application. For a detailed assessment of its clinical applicability and potential for proton treatment planning, a comprehensive characterisation of a DECT scanner was performed at first to optimise a CT scan protocol for radiotherapy and calibrate the different CT-based stopping-power prediction methods (section 5). Afterwards, the clinical feasibility of DECT was investigated in a stepwise procedure starting with a DECT-derived pseudo-monoenergetic CT (MonoCT) dataset ensuring the compatibility with the treatment planning system and preserving the precision of proton range prediction compared with single-energy computed tomography (SECT). Subsequently, the accuracy of different approaches for CT-based stopping-power prediction were validated in a ground-truth anthropomorphic head phantom, simulating the geometrical complexity of patients, and homogeneous biological tissues, representing the tissue composition of humans (section 6). Finally, the clinical relevance of DECT-based stopping-power prediction was evaluated in several cohorts including brain-tumour, prostate-cancer and lung-cancer patients (section 7). Based on the experimental and clinical evidence, patient information gathered by DECT were used for the first time to clinically adapt the range prediction in patients. Prior to these investigations, the physical principles of CT imaging (section 2), proton therapy (section 3) and CT-based stopping-power prediction (section 4) are summarised.

2 Physical Principles of Computed Tomography

Computed tomography is a medical imaging technique gathering three-dimensional (3D) anatomical information using X-rays from various directions. This method was initially proposed and technically implemented by Hounsfield (1973). For each projection angle φ, the X-ray attenuation profile after traversing an object is determined by measuring the remaining intensity $I_{\varphi}(\tau)$ of the polychromatic X-ray spectrum $\Omega(E)$ with an initial intensity I_0 integrated over energy E.

$$I_{\varphi}(\tau) = I_0 \cdot \int_E \Omega(E) \cdot e^{-\int \mu\left[E, \mathbf{r}_{\varphi}(\tau)\right] \mathrm{d}\mathbf{r}} \, \mathrm{d}E \tag{2.1}$$

Angle-specific projections contain the total attenuation along trajectories $\mathbf{r}_{\varphi}(\tau)$ with a perpendicular distance τ from the rotational axis at the isocentric plane. Based on this information, dedicated image reconstruction algorithms provide the individual attenuation coefficient μ of each volume element (voxel) within the field of view (FOV).
The attenuation coefficient μ varies with the mass density and stoichiometric composition of the scanned material as well as the energy of the interacting photon. In general, μ can be described as product of electron density ϱ_{e} and photon attenuation cross section per electron σ_{e}.

$$\mu(E, Z) = \varrho_{\mathrm{e}} \cdot \sigma_{\mathrm{e}}(E, Z) = \varrho_{\mathrm{e}} \cdot \left[\sigma_{\mathrm{e}}^{\mathrm{ph}}(E, Z) + \sigma_{\mathrm{e}}^{\mathrm{coh}}(E, Z) + \sigma_{\mathrm{e}}^{\mathrm{inc}}(E)\right] \tag{2.2}$$

For the energy range typically used in diagnostic radiology ($E < 200\,\mathrm{keV}$), cross sections of human tissues depend on three photon interaction processes (Rutherford et al., 1976; Jackson and Hawkes, 1981):

- photoelectric effect with $\sigma_{\mathrm{e}}^{\mathrm{ph}} \propto Z^{3.62}/E^{3.3}$,
- coherent scattering with $\sigma_{\mathrm{e}}^{\mathrm{coh}} \propto Z^{1.86}/E^{2}$,
- incoherent scattering with $\sigma_{\mathrm{e}}^{\mathrm{inc}}$ described by the Klein-Nishina formula (Heitler, 1954).

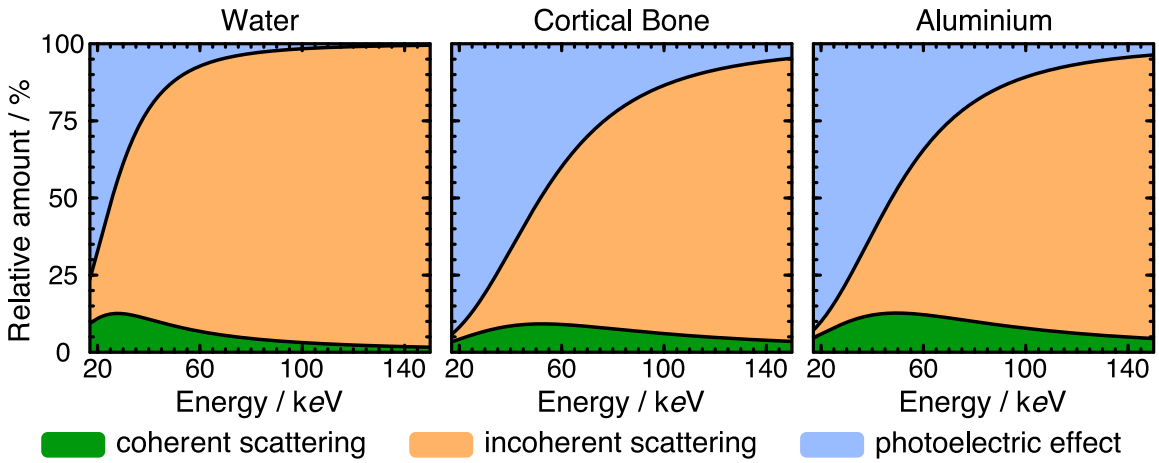

Figure 2.1: Energy-dependent relative fraction of photoelectric effect, coherent and incoherent scattering contributing to the attenuation coefficient of water, cortical bone (Woodard and White, 1986) and aluminium. Data is provided by Berger et al. (1990) in the XCom Photon Cross Section Database of the National Institute of Standards and Technology, USA (NIST). Adapted from Wohlfahrt (2014).

Further interactions with matter, such as pair productions and photonuclear reactions, only arise for $E > 1\,\mathrm{MeV}$. Due to the different physical dependencies, the probability of each interaction process varies with energy and atomic number Z (Fig. 2.1). For tissues, liquids and other materials occurring in humans, the photoelectric effect dominates for $E < 30\,\mathrm{keV}$, whereas incoherent scattering is the most frequent interaction for $E > 30\,\mathrm{keV}$.

Within the presented work, three different CT scanner models manufactured by Siemens Healthineers (Forchheim, Germany) were used:

- two single-source CT scanners SOMATOM Definition AS,
  Department of Radiotherapy and Radiation Oncology, University Hospital Carl Gustav Carus, Dresden, Germany
- a dual-source CT scanner SOMATOM Definition Flash,
  German Cancer Research Centre, Heidelberg, Germany
- a dual-source CT scanner SOMATOM Force.
  Department of Diagnostic Radiology, University Hospital Carl Gustav Carus, Dresden, Germany

In the following, technical features and the functionality of CT scanners will be described exemplarily based on the models available in the participating institutions in Dresden and Heidelberg, Germany.

2.1 Image Acquisition

A single-source CT scanner consists of a rotating X-ray tube with an opposing detector system. To improve the temporal resolution of cardiac CT imaging, a dual-source CT scanner was developed, containing two X-ray tubes and detector systems with an angular offset of approximately 95° (Flohr et al., 2006).

2.1.1 X-Ray Tube

X-ray spectra originate from a continuous energy spectrum induced by Bremsstrahlung and a superimposed spectrum of characteristic X-ray emissions caused by photoelectric effect. For the variety of clinical applications requiring an optimal tissue differentiation, X-ray tubes should be highly efficient and allow for an individual adjustment of tube voltage and current to define the maximal energy and number of emitted X-rays, respectively. To generate X-ray spectra appropriate for diagnostic purposes, a rotating envelope tube was designed (e.g. Straton® X-ray tube used in CT scanners Definition AS and Flash), which includes a tungsten cathode for electron emission, electromagnetic coils for electron beam deflection and focusing as well as an anode disk with a focal-spot track made of tungsten and rhenium (Schardt et al., 2004). This concept allows for a sufficient cooling of X-ray tubes due to the direct contact of the anode surface with the cooling fluid. Low-energy photons are completely ($E < 20\,\mathrm{k}e\mathrm{V}$) or partly absorbed by the tube exit window consisting of beryllium or titanium, a wedge and bowtie filter as well as additional pre-filtering materials (e.g. aluminium, tin, gold) leading to typical clinical X-ray spectra (Fig. 2.2).
Pre-patient collimators limit the longitudinal beam extension (Kachelrieß et al., 2006a). The spatial resolution in each direction is improved by a periodic motion of the focal spot on the anode in longitudinal direction (z-flying focal spot), which doubles the amount of projections (Flohr et al., 2004; Flohr et al., 2005). Furthermore, aliasing artefacts in terms of hyper- and hypodense "windmill" structures at high-density gradients (e.g. bone edges) in heterogeneous regions are suppressed by an increased sampling (Kachelrieß et al., 2006a).
With current state-of-the-art X-ray tubes (e.g. Vectron™ used in the CT scanner Force), a high tube power (120 kW) with currents up to 1300 mA and voltages from 70 kV to 150 kV in 10 kV steps can be clinically applied while maintaining the size of the focal spot (Meinel et al., 2014; Meyer et al., 2014).

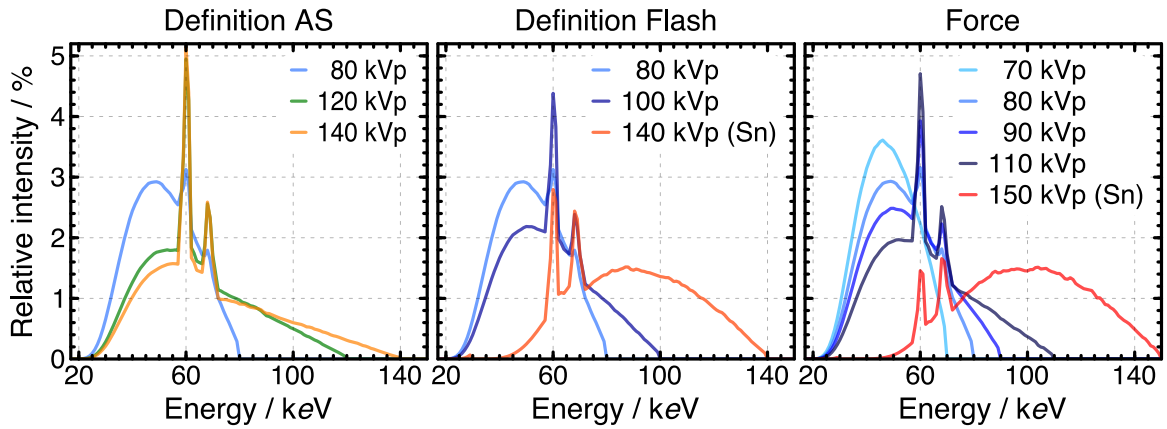

Figure 2.2: X-ray spectra of three commercial CT scanners normalised to the total number of photons. A tube voltage of 120 kV (green) is commonly used in single-energy mode and different combinations of low (light to dark blue) and high voltages (orange to red) can be applied in dual-energy mode depending on the capability of the CT scanner. Tin (Sn) as additional pre-filtering material is used to further harden the X-ray spectrum. Data provided by Siemens Healthineers.

2.1.2 Detector System

At the beginning of CT imaging, gas-filled (e.g. Xenon) multi-channel ionisation chambers were used to convert X-ray spectra into electric charge. To improve the overall detector efficiency and spatial resolution, solid-state detectors consisting of ceramic scintillators (e.g. gadolinium oxysulfide as basis for Ultra Fast Ceramics, UFC^{TM}, used in the CT scanner Definition AS) with a high X-ray absorption, short decay time and low afterglow were introduced (Fuchs et al., 2000). The visible light generated by scintillators is converted into electric current by a photodiode array and then digitised by analog-to-digital converters. The electronic noise, resulting from this multi-step conversion on separate electronic boards, could be reduced by combining all components in one (e.g. Stellar detector in CT scanners Definition Flash and Force). In combination with collimation grids aligned to the detector elements (1.2 mm pixel size), which effectively suppress photon scattering, high-resolution CT scans with a slice thickness of 0.5 mm can be generated (Ulzheimer and Freund, 2011).

The next detector generation will be composed of semiconductors such as cadmium telluride, which directly convert X-rays into electric charge dependent on the respective energy (Ulzheimer and Kappler, 2017). These photon-counting detectors allow for discriminating X-ray spectra in several energy bins and thus provide energy-resolved attenuation information for material characterisation. The image quality and quantitative accuracy is currently assessed with a close-to-clinical prototype scanner (Yu et al., 2016; Leng et al., 2017).

2.1.3 Acquisition Mode

CT acquisition for diagnostic purposes in radiotherapy can be performed by selecting one of three different frequently used scan modes: sequential, spiral or time-resolved respiratory four-dimensional (4D) acquisition.

Sequential Acquisition

A sequential CT scan is a collimation-wise acquisition mode without couch movement during rotation of the imaging system. After X-ray acquisition, the couch is automatically moved to the next slice position. This stepwise procedure is repeated until the whole scanning region is covered.

Spiral Acquisition

The spiral mode comprises a continuous X-ray acquisition with simultaneous couch movement gathering volumetric attenuation information along a spiral-shaped track. The automatic couch feed per full rotation and axial distance covered by the detector (pitch) can be set individually, mostly between 0.5 and 1.0.

Time-Resolved Respiratory 4D Acquisition

In addition to a spiral CT scan with a small pitch of approximately 0.1, an external motion surrogate signal is recorded. For examinations within the thoracic region, breathing patterns of patients can be detected by spirometry, a pressure belt or infrared tracking systems (e.g. positioned onto the patient's abdomen). Such a surrogate signal representing the respiration during CT acquisition allows for a retrospective time-resolved CT image reconstruction including only X-ray projections of a specific respiratory phase obtained from a relative local amplitude-based binning per motion cycle.

2.2 Image Reconstruction

Based on the X-ray attenuation measured for a variety of projection angles covering at least 180° in parallel-beam geometry, a spatially precise 3D image dataset of the scan object can be reconstructed. The respective attenuation coefficient μ of each CT voxel represents its

material composition and is expressed as CT number H in Hounsfield unit (HU) to assure the comparability and reproducibility between CT scanners.

$$H = \frac{\mu - \mu_{\text{water}}}{\mu_{\text{water}} - \mu_{\text{air}}} \cdot 1000 \approx \left(\frac{\mu}{\mu_{\text{water}}} - 1 \right) \cdot 1000 \quad \text{with} \quad \mu_{\text{air}} \ll \mu_{\text{water}} \tag{2.3}$$

A Hounsfield scale ranging from -1024 HU to 3071 HU (12 bit encoding) is commonly used in clinical applications of radiology and radiotherapy. This is sufficient to differentiate human tissue, but often not enough for materials with a high effective atomic number (e.g. metals and tooth implants). In such cases, a 16 bit encoding can be applied to increase the maximal feasible CT number.

Algorithms for analytical image reconstruction, which have been applied since the advent of clinical CT imaging, are based on filtered back projection (FBP) in parallel-beam geometry (Ramachandran and Lakshminarayanan, 1971). The continuous development of CT systems to satisfy the clinical demands regarding temporal and spatial resolution led to refinements in FBP algorithms, which are compelled to consider the gradual transition from sequential fan-beam to spiral fan-beam to finally cone-beam CT acquisition in multi-slice CT scanners (Kachelrieß et al., 2004). To further improve image quality with respect to image artefacts and noise, iterative reconstruction algorithms were clinically introduced (Hsieh et al., 2013).

2.2.1 Filtered Back Projection

Current CT scanners in radiology and radiotherapy are typically equipped with a detector array covering a circular arc and thus gather projections in fan-beam geometry. Since parallel projections in the axial plane are convenient for CT image reconstruction, the projections measured in fan-beam geometry are transaxially rebinned and transferred to parallel rays. This three-step conversion comprises an azimuthal, longitudinal and radial rebinning (Kachelrieß et al., 2004). The resulting parallel X-ray projections $\psi_{||}(\tilde{\varphi}, \tilde{\tau})$ correspond to the Radon transform $\mathcal{R}$ (Radon, 1917) of $\mu(\tilde{\mathbf{r}})$:

$$\psi_{||}(\tilde{\varphi}, \tilde{\tau}) = \ln \frac{I_{||}(\tilde{\varphi}, \tilde{\tau})}{I_0} = \mathcal{R}\left[\mu(\tilde{\mathbf{r}})\right]. \tag{2.4}$$

To derive the distribution of attenuation coefficients $\mu(\tilde{\mathbf{r}})$, the projections are convolved with a convolution or reconstruction kernel $k(\tilde{\tau})$ followed by a weighted FBP, which is a

close approximation of the inverse Radon transform $\mathcal{R}^{-1}$. The weighting function $w(\tilde{\varphi})$ normalises the contributions to 180°.

$$\mu(\tilde{\mathbf{r}}) = \int_0^{\pi} \left[\psi_{||}(\tilde{\varphi}, \tilde{\tau}) * k(\tilde{\tau})\right] w(\tilde{\varphi}) \, \mathrm{d}\tilde{\varphi} \tag{2.5}$$

In theory, k is the inverse Fourier transform of the ramp filter $\mathcal{F}^{-1}K(\nu) = \mathcal{F}^{-1}|\nu|$, a high-pass filter suppressing low frequencies to consider each frequency ν with respect to its intrinsic relative fraction. However, the projections are only measured at discrete positions, which requires a limitation of the frequency band by an additional filter, e.g. a Shepp-Logan filter (Shepp and Logan, 1974). Furthermore, the spatial resolution and image noise can be adjusted with such a filter.
FBP needs less computational effort compared to an iterative reconstruction, but has to make a compromise between spatial resolution and image noise. It is also prone to image artefacts (e.g. streak artefacts) induced by deviations from the cone-beam geometry or the equal weighting of projections without considering the respective number of photons detected for each projection.

2.2.2 Iterative Reconstruction

The limitations of FBP can be addressed by iterative reconstruction including a model of all components integrated in a CT scanner (e.g. X-ray tube and detector system). An iterative reconstruction starts typically with a CT dataset previously reconstructed using FBP and continues with minimising a cost function until a high conformity between projections derived from the reconstructed image and measured projections is reached. Within each iteration, the intermediate CT images are forward projected to create projections simulating X-ray attenuations based on the computational modelling of the CT system. Subsequently, the difference between calculated and measured projections is computed, reconstructed by FBP (correction image) and finally added to the current intermediate CT dataset. These steps are repeated until the cost function converges, which results in a reduction of image noise and geometrical artefacts induced by spiral acquisition (Hsieh et al., 2013).
A statistical iterative reconstruction method, referred to as Sinogram Affirmed Iterative Reconstruction (SAFIRE), was developed (applicable in CT scanners Definition AS and Flash) containing a CT system modelling in forward projection, projection-based correction and

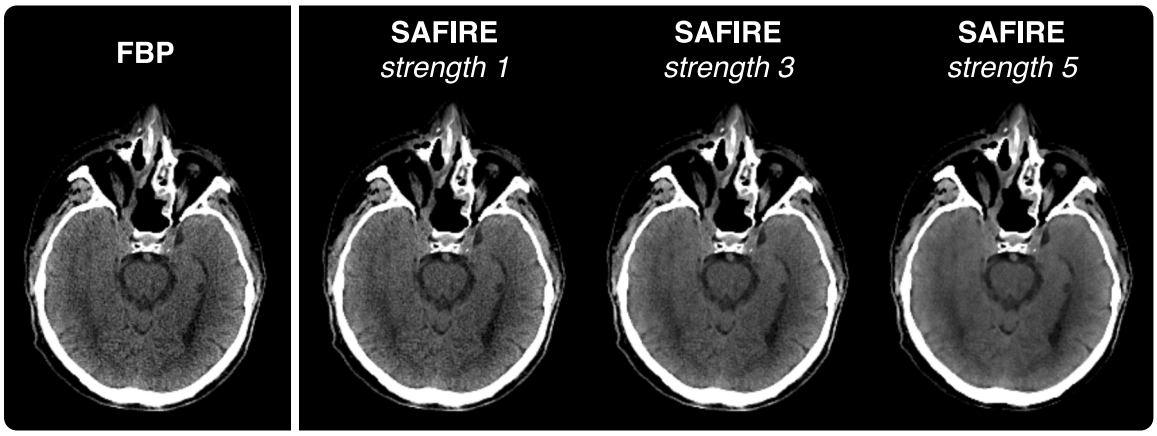

Figure 2.3: DECT-derived 50 keV MonoCT dataset of a brain-tumour patient reconstructed using FBP and SAFIRE with different strength settings. The reconstruction kernels of similar type D34 and Q34 were applied for FBP and SAFIRE, respectively. The application syngo.CT DE Monoenergetic Plus of the Siemens image post-processing software syngo.via was used for MonoCT generation.

statistical modelling in the image domain for noise reduction (Grant and Raupach, 2012). Different SAFIRE strength settings from 1 to 5 can be applied to select the desired noise level (Fig. 2.3). This method was extended by statistical weighting of projections with respect to their statistical quality (Ramirez-Giraldo et al., 2016) and introduced as Advanced Modelled Iterative Reconstruction (ADMIRE) for the CT scanner Force.

2.2.3 Image Correction Algorithms

The use of prior knowledge about several physical processes and the well-known performance of the CT system, which is already incorporated in image correction algorithms, clearly improves the geometrical accuracy and robustness of CT imaging (Hsieh, 2015).

Beam Hardening Correction

When traversing an object, the initial X-ray intensity reduces and low-energy photons of the spectrum are preferably absorbed. This non-linear effect, referred to as beam hardening, leads to an increased mean energy and eventually reduced attenuation coefficient with increasing penetration depth. Accordingly, the CT number decreases within a homogeneous object from edge to centre and so-called cupping artefacts occur in CT images. To consider this effect, a water-based beam hardening correction (BHC), assuming a scan object solely consisting of water, is commonly integrated in CT reconstruction kernels (Herman,

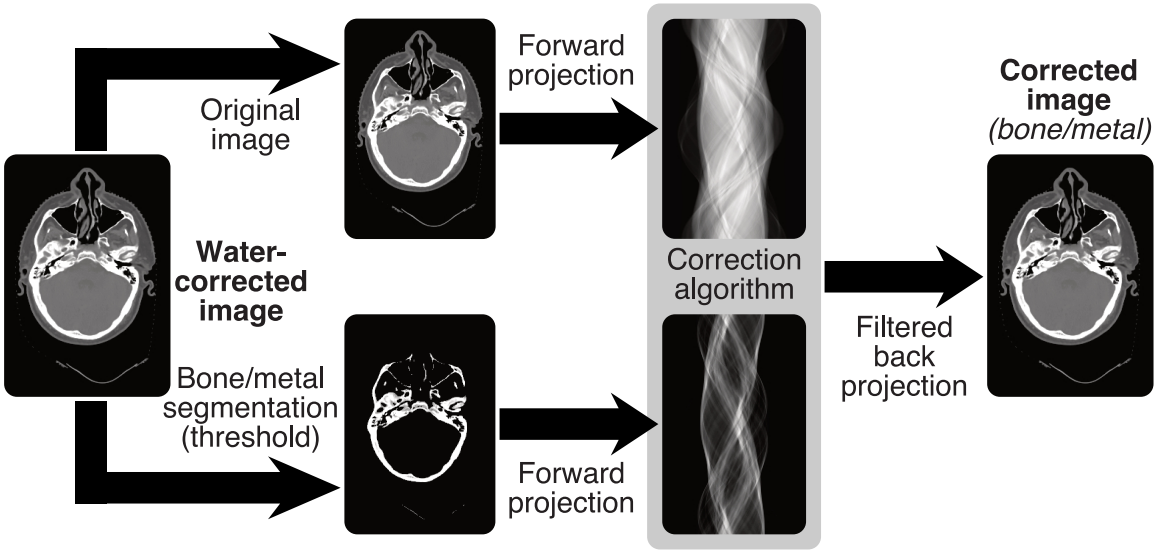

Figure 2.4: Image-based algorithm for beam hardening correction (BHC) concerning bone included in the reconstruction kernels D34 and Q34. A segmentation of metal and a metal-based BHC is applied in algorithms for metal artefact reduction.

1979; Kachelrieß et al., 2006b). Nevertheless, beam hardening depends on the X-ray spectrum and elemental composition of the materials traversed. Since photoelectric absorption is strongly increased in materials with higher effective atomic number (EAN) than water, the influence of beam hardening can be only partly corrected by standard BHC. To further reduce beam hardening effects, specific reconstruction kernels (e.g. D34 and Q34) contain an additional BHC concerning bones (Kyriakou et al., 2010).

The BHC algorithm integrated in D34/Q34 performs a stepwise correction. After water precorrection, bones are separated in the image domain with a predefined threshold value depending on the X-ray spectrum. To quantify the contribution of bones to the X-ray attenuation of each projection, the water-corrected non-segmented and bone-only CT images are forward projected to derive artificial projections for the full and bone-induced attenuation, respectively. Subsequently, a two-material decomposition (water and bone) is applied to correct each projection with respect to the relative fraction of water and bone. Finally, the water- and bone-corrected CT dataset is reconstructed (Fig. 2.4).

Metal Artefact Correction

Metal artefacts originate from a combination of effects like beam hardening, photon scattering and starvation as well as data undersampling at sharp high-density gradients. First

algorithms for metal artefact reduction were clinically applied in the early stages of CT (Hinderling et al., 1979; Kalender et al., 1987). Extensive research within the last decades led to further developments of clinical applications, which pursue different strategies comprising improved CT acquisition, physics-based correction, projection completion, iterative reconstruction and incorporation of prior knowledge (Gjesteby et al., 2016).

In the following, the principal functionality of the Iterative Metal Artefact Reduction (iMAR) algorithm is explained (Kachelrieß and Krauss, 2015), which is available on CT scanners Definition AS, Flash and Force. First, the metal is detected by thresholding in the image domain and then a BHC for metal is applied (Fig. 2.4). The iterative process starts with the forward projection of a prior image, where all voxels of soft tissue and metal are overridden with 0 HU. The measured projections are divided by the calculated projections derived from the prior image for normalisation and linear interpolation of high-attenuation regions to remove unreliable projections affected by metals. Subsequently, these linearly modified projections are denormalised to substitute metal regions within the measured projections after BHC. The mixed projections are reconstructed, low-pass filtered and combined with the high-pass filtered original image to renew potentially missing textures. These steps are repeated up to 6 times to obtain the finally corrected CT dataset (Fig. 2.5).

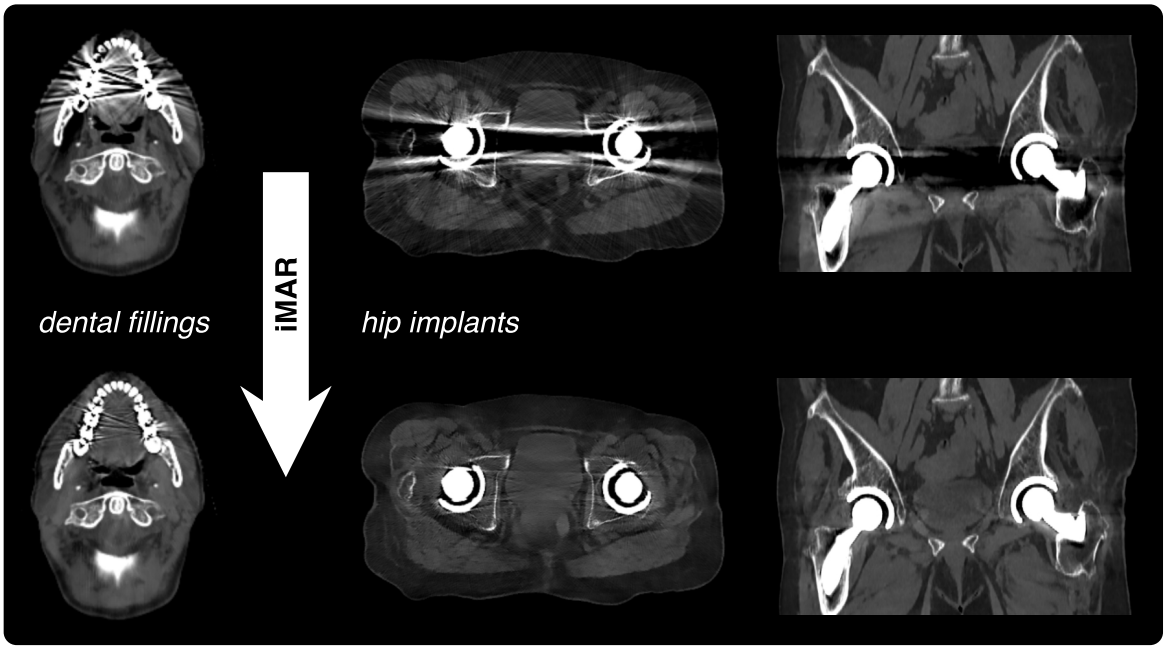

Figure 2.5: DECT-derived 170 k*e*V MonoCT dataset of a patient with dental fillings or hip implants reconstructed using SAFIRE (Q34/5) only (top) or in combination with iMAR (bottom). The application syngo.CT DE Monoenergetic Plus of syngo.via was used for MonoCT generation.

Scatter Correction

Despite collimation grids attached to the detector array, coherently and incoherently scattered photons can increase the intensity measured by a detector element. This effect increases with object size and slice thickness leading to cupping artefacts in large homogeneous scan objects or low-attenuated regions close to high-attenuation materials. To consider the influence of X-ray scattering on the detector signal, the scatter contribution has to be determined and subtracted from the measured intensity. The scatter distribution for the specific geometry of a CT scanner can be obtained from measurements or simulations of pencil beams using tabulated cross sections of photon scattering (Ohnesorge et al., 1999).

2.3 Dual-Energy Computed Tomography

Conventional CT imaging with one X-ray spectrum (SECT) was optimised over the last decades regarding dose deposition, geometrical accuracy, quantitative imaging, tissue contrast and image noise. However, the large variation in tissue composition within one patient and between patients (Woodard and White, 1986) cannot be sufficiently resolved and quantified. Due to the energy-dependent contribution of photon interactions, additional information about human tissues can be gathered by two CT scans of different X-ray spectra, allowing for a better material differentiation (Hounsfield, 1973). With the advent of clinical DECT scanners (Flohr et al., 2006), this technique has been frequently used for various applications in diagnostic radiology (Kaup et al., 2016; Lestra et al., 2016). While benefits of DECT for treatment planning with photons, protons or heavier ions are also widely expected and DECT is part of intensive radiotherapy research, applications in clinical routine are currently limited (van Elmpt et al., 2016).

Nowadays, several technical implementations for DECT imaging are provided by CT vendors. Both CT scans can be acquired simultaneously with a dedicated dual-source DECT scanner (Flohr et al., 2006). Since such DECT scanners with a gantry opening of approximately 80 cm are limited in radial space for two rotating detector systems providing the full FOV of 50 cm, the DECT information is only available within a FOV of 30-35 cm. For applications in radiotherapy, a FOV of 50 cm is typically required to cover the patient with immobilisation devices in anatomical regions such as thorax, abdomen or pelvis. Hence, a single-source CT scanner can be used to acquire both CT scans

- consecutively (dual-spiral), i.e. two separate CT scans directly one after the other (Hounsfield, 1973; Wohlfahrt et al., 2017b),
- almost simultaneously by continuous fast voltage switching (Kalender et al., 1986),
- simultaneously by a dual-layer detector (Heismann et al., 2004), or
- simultaneously by a split-beam filter (Almeida et al., 2017).

Dual-spiral DECT acquisition is practically feasible with commonly applied CT scanners in radiotherapy and profits from an independent tube current modulation and appropriate selection of X-ray spectra to increase the energy separation between both single DECT scans. However, this approach is prone to uncertainties induced by patient motion during image acquisition (e.g. breathing, swallowing, heartbeat, gastro-intestinal peristalsis), because motion-related changes in patient anatomy hamper the image post-processing of dual-spiral DECT scans.

2.3.1 Monoenergetic CT Imaging

To satisfy the demands for each individual clinical use case, pseudo-monoenergetic CT (MonoCT) datasets of various energies E_{mono} ranging from 40 k*e*V to 190 k*e*V can be derived from DECT scans to select the desired tissue contrast (Fig. 2.6).

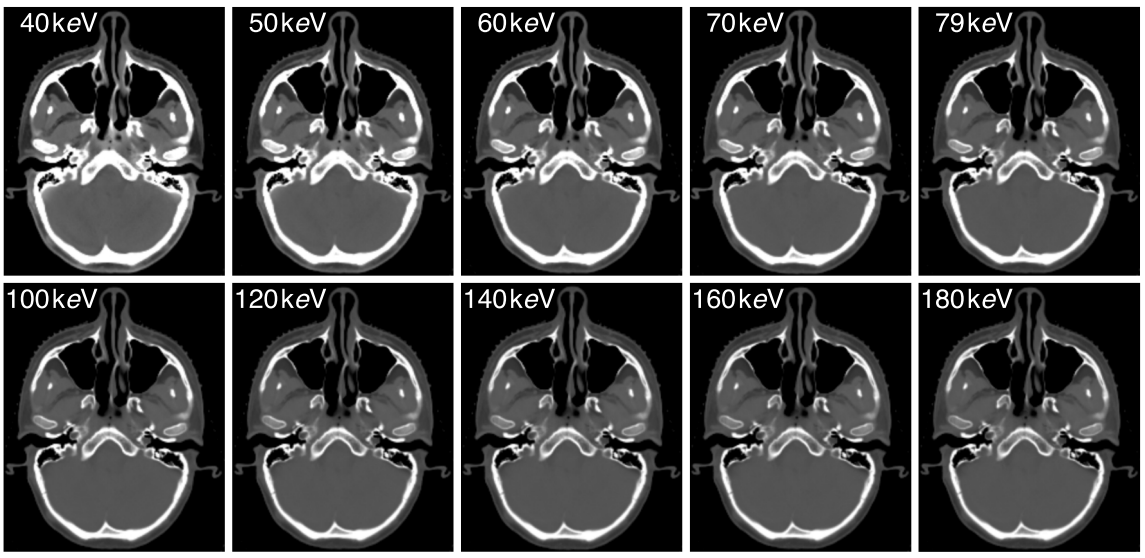

Figure 2.6: DECT-based MonoCT datasets of different X-ray energy calculated with the application syngo.CT DE Monoenergetic Plus of syngo.via. Images were reconstructed using Q34 and SAFIRE of maximal strength.

An energy-dependent weighted sum of the low- (H_{low}) and high-energy (H_{high}) DECT scan yields a MonoCT dataset (Kuchenbecker et al., 2015).

$$H\left(E_{\text{mono}}\right) = \alpha\left(E_{\text{mono}}\right)\, H_{\text{low}} \,+\, \left[1 - \alpha\left(E_{\text{mono}}\right)\right]\, H_{\text{high}} \tag{2.6}$$

The weighting factor $\alpha\left(E_{\text{mono}}\right)$ depends on the tube voltage combination, detector design and beam hardening correction included in reconstruction kernels. A scanner-specific calibration is thus inevitable. For MonoCT generation, the two applications syngo.CT Monoenergetic imaging (syngo.Mono) and syngo.CT DE Monoenergetic Plus (syngo.MonoPlus) are provided in the Siemens image post-processing software syngo.via. Syngo.MonoPlus is a further development of syngo.Mono, including a noise-suppression algorithm based on multi-band filtering (Grant et al., 2014; Schabel et al., 2014; Albrecht et al., 2015). To ensure voxelwise computations for dual-spiral DECT scans, a deformable image registration (DIR) is integrated in both applications by default.

2.3.2 Determination of Electron Density and Effective Atomic Number

DECT can also be used to predict material parameters, such as electron density relative to water (RED or $\hat{\varrho}_{\text{e}}$) and effective atomic number (EAN or Z_{eff}), which mainly influence X-ray attenuation. Many algorithms are proposed for DECT-based RED/EAN determination (Brooks, 1977; Heismann et al., 2003; Saito, 2012; Landry et al., 2013; Hünemohr et al., 2014; Saito and Sagara, 2017a). As recently demonstrated by Möhler et al. (2018b), all stated approaches are mathematically equivalent and can be transferred to the equations of Brooks (1977) by simple arithmetic conversions. The methods differ only in the number of calibration parameters, which do not seem to have a major effect on the prediction accuracy. However, the practical calibration procedure (CT scan parameter, measurement setup, materials used) can have a substantial impact on the performance and robustness (Möhler et al., 2017).

The application syngo.CT DE Rho/Z (syngo.RhoZ) included in syngo.via (Hünemohr et al., 2014) calculates RED based on a linear superposition of both DECT scans according to eq. 2.6 with the appropriate weighting factor α_{ϱ}.

$$\left(\hat{\varrho}_{\text{e}} - 1\right) \,\cdot\, 1000\,\text{HU} = \alpha_{\varrho}\, H_{\text{low}} \,+\, \left(1 - \alpha_{\varrho}\right)\, H_{\text{high}} \tag{2.7}$$

For arbitrary mixtures of human tissues (excluding high-Z elements, e.g. iodine in thyroid), an accurate and robust RED determination is achievable with a maximum methodological uncertainty below 0.2% (Möhler et al., 2017).
EAN follows from

$$Z_{\text{eff}}^{n} = \frac{1}{\hat{\varrho}_{\text{e}}} \cdot \left[\alpha_Z \left(\frac{H_{\text{low}}}{1000\,\text{HU}} + 1 \right) + \left(Z_{\text{eff, water}}^{n} - \alpha_Z \right) \left(\frac{H_{\text{high}}}{1000\,\text{HU}} + 1 \right) \right] \tag{2.8}$$

with α_Z as an additional calibration parameter and $n = 3.1$ as Mayneord's exponent (Mayneord, 1937) derived from photon absorption simulations.

3 Physical Principles of Proton Therapy

Particle irradiation using protons or heavier ions benefits from the inverse depth-dose profile compared to conventional radiotherapy with photons. It is characterised by a narrow dose peak (Bragg peak) with a steep distal fall-off close to the finite penetration depth (Fig. 3.1 A). As exemplarily illustrated in Fig. 3.1 C, the physical behaviour of protons or heavier ions can contribute to high tumour coverage while sparing organs at risk more effectively than photons (van de Water et al., 2011; Nichols et al., 2012; Jakobi et al., 2015).

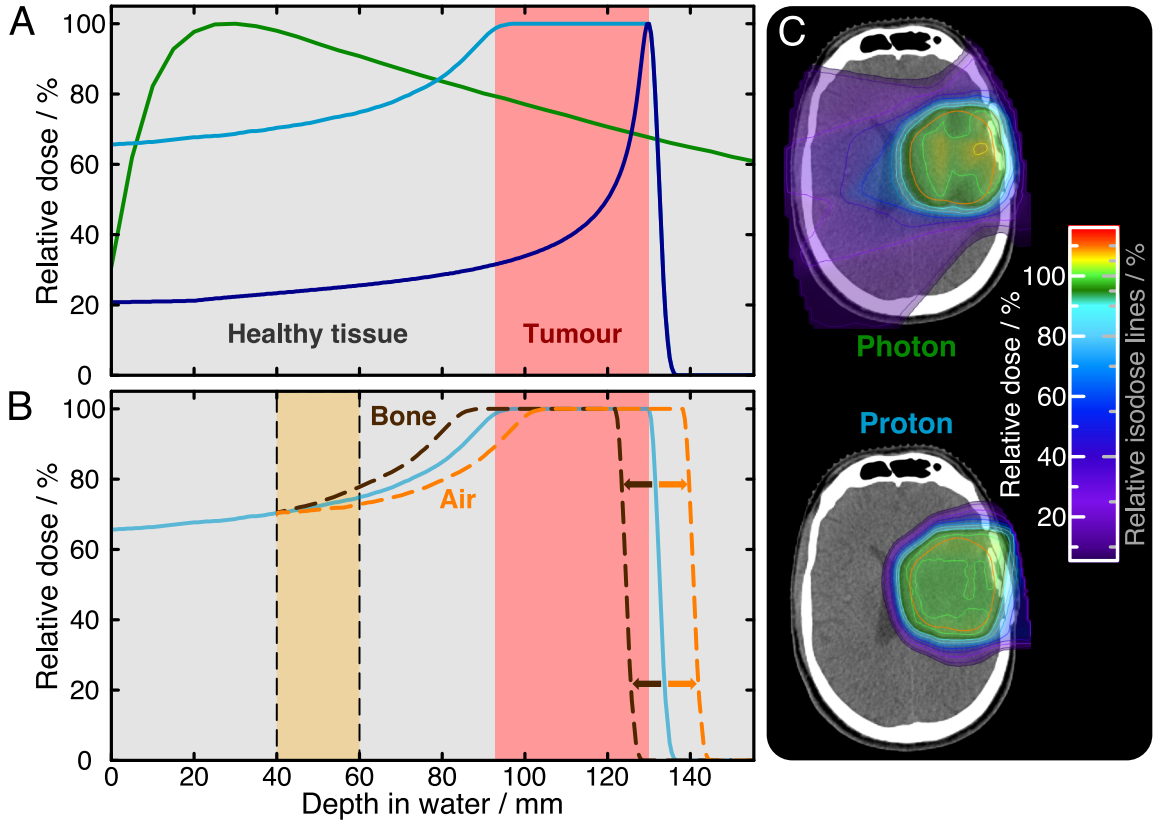

Figure 3.1: (A) Depth-dose distribution of 15 MV photons (green), 135 M*e*V protons (dark blue) and multi-energy protons (light blue) forming a SOBP to cover the tumour (red). (B) Tissue variations in beam direction (yellow) decrease (higher density, e.g. bone) or increase (lower density, e.g. air) the proton range, leading to reduced (raised) dose within the tumour (healthy tissue). (C) Dose distribution of a photon (top) and proton (bottom) treatment plan.

In the continuous slowing down approximation, the range R of protons is defined by its initial energy E_0 and the material-specific energy-dependent stopping power S.

$$R = \int_{E_0}^{0} \frac{1}{S\,(E)}\,\mathrm{d}E \;=\; \int_{0}^{E_0} \frac{1}{\mathrm{d}E(x)/\mathrm{d}x}\,\mathrm{d}E \tag{3.1}$$

The stopping power in matter describes the mean energy loss of protons per unit path length, $S = -\left(\mathrm{d}E/\mathrm{d}x\right)$. Since the energy loss of protons is a statistical process, a single proton can deviate from the average range (energy straggling). To cover the entire tumour region in depth, a spread-out Bragg peak (SOBP) is formed by a well-conceived combination of protons with various energies. For clinically relevant proton energies up to approximately 300 M*e*V, the stopping power is dominated by inelastic collisions with electrons, whose contribution is at least 3 orders of magnitude larger than the respective amount of radiative stopping and nuclear interactions (Das and Paganetti, 2015). Hence, the stopping power can be expressed by the approximated Bethe formula (Bethe, 1930; ICRU, 1993):

$$S = k_0 \frac{z^2}{\beta^2}\,\varrho_\mathrm{e}\,L\,(\beta, I) \;\approx\; k_0 \frac{z^2}{\beta^2}\,\varrho_\mathrm{e}\,\left[\ln\left(2m_\mathrm{e}c^2\frac{\beta^2}{1-\beta^2}\right) - \beta^2 - \ln I\right] \tag{3.2}$$

with the constant $k_0 = 5.1 \cdot 10^{-25}\,\mathrm{MeV\,cm^2}$, the projectile charge z and relativistic velocity β, the stopping number L, the rest energy of electrons $m_\mathrm{e}c^2$ and the mean excitation energy I, also referred to as I-value. Range prediction in a treatment planning system (TPS) relies on voxelwise computation of stopping-power ratio (SPR, $\hat{S}$), which only depends on relative electron density $\hat{\varrho}_\mathrm{e}$ and stopping number (RSN, $\hat{L}$).

$$\hat{S} = \frac{S}{S_\mathrm{water}} = \hat{\varrho}_\mathrm{e}\,\hat{L}\,(\beta, I) = \hat{\varrho}_\mathrm{e}\,\frac{\ln\left(2m_\mathrm{e}c^2\frac{\beta^2}{1-\beta^2}\right) - \beta^2 - \ln I}{\ln\left(2m_\mathrm{e}c^2\frac{\beta^2}{1-\beta^2}\right) - \beta^2 - \ln I_\mathrm{water}} \tag{3.3}$$

An accurate SPR determination is essential, because the SPR of protons is sensitive to tissue properties and anatomical variations in beam direction, which may lead to a reduced tumour coverage and/or increased dose within the surrounding healthy tissue (Fig. 3.1 B). Several treatment techniques and strategies to handle uncertainties in proton therapy are described in the following. For information beyond the scope of this thesis, readers are referred to Paganetti (2012a), Das and Paganetti (2015), and Newhauser and Zhang (2015).

3.1 Treatment Techniques

Clinical accelerators are required to provide protons of therapeutic energy reaching a penetration depth in water of up to 30 cm (approximately 220 M*e*V). Current proton and ion therapy facilities are equipped with a synchrotron, isochronous cyclotron or synchrocyclotron. In synchrotrons, proton bunches are circularly accelerated to the desired energy by varying the magnetic field of the deflection magnets and the radio frequency within the acceleration cavity according to the increasing proton energy. Clinical isochronous cyclotrons are configured to accelerate protons up to a fixed energy of approximately 230-250 M*e*V. To account for relativistic effects during acceleration, the orbital frequency can be maintained with a radially increasing magnetic field in spiral-shaped magnets for axial focusing. Alternatively, the radio frequency can be decreased with radius as realised in synchrocyclotrons, which results in a pulsed proton beam. Since the energy of cyclotron-accelerated protons is fixed, an energy selection system is necessary after beam extraction to decelerate protons to their desired energy. It consists of a wedge degrader composed of graphite or lucite followed by a magnetic bending system with divergence slits for energy restriction.
Finally, the proton beam is transported to the treatment room using an evacuated pipe with continuous focusing by magnets. Further beam preparation takes place within the treatment room to shape the treatment field in lateral and longitudinal direction for optimal tumour coverage. Two dose delivery techniques are currently applied in proton therapy – passive scattering and pencil beam scanning (Das and Paganetti, 2015).

3.1.1 Passive Scattering

To treat the entire target volume at once, the lateral spread of the narrow proton beam with a full width at half maximum (FWHM) of about 1 cm can be increased by additional scatter materials in beam direction before entering the patient. Inserting a foil of a high-density material, e.g. lead or tungsten, results in an almost Gaussian-shaped lateral proton distribution with a FWHM of several cm. The centre of the distribution is cut by a brass collimator with small aperture and used for small-field therapeutic irradiations (e.g. ocular melanoma). The beam intensity of this so-called single scattering technique is thus reduced and only a small fraction (few per cent) reach the patient. For larger tumour regions, the double scattering technique can be applied. A second scatterer is inserted consisting of a roughly

Gaussian-shaped high-density material (e.g. lead or tungsten) and a material of lower density (e.g. lucite) with an almost inverted shape, causing the same energy reduction as the high-density material. This leads to a flat lateral intensity profile (10-30% of initial intensity). The longitudinal target extension is considered by energy modulation using e.g. a rotating wheel with steps of variable thickness. Since the width of the resulting SOBP corresponds to the maximal target extension in beam direction, healthy tissue in front of a thinner target area still receives high dose. A patient-specific collimator with an aperture composed of brass conforms the proton beam to the individual tumour shape in lateral direction. The distal field shaping is realised by a lucite compensator of varying thickness with respect to the water-equivalent thickness (WET) in beam direction (Das and Paganetti, 2015).
Analytical dose calculation algorithms are applied in current TPS for passively scattered proton beams. For an initial dose estimation, a fast broad beam algorithm is often used by default. Based on ray tracing in beam direction (Siddon, 1985), the WET of beam paths within the patient is determined. Depth-dose profiles measured in a water phantom with the range corresponding to the obtained WET are selected and combined to a 3D dose distribution. Since such models cannot adequately consider the influence of multiple Coulomb scattering in heterogeneous regions and field-shaping devices, pencil beam algorithms were introduced for proton dose calculations. These methods distinguish between a central-axis and off-axis contribution. The central-axis expression equals the broad beam algorithm with a quadratic correction term including the distance from the patient surface. The off-axis contribution is estimated by a Gaussian distribution with respect to multiple Coulomb scattering originating from each field-shaping device and the patient (Hong et al., 1996). All passively scattered proton dose distributions investigated in this thesis are calculated with this pencil beam algorithm implemented in the TPS XiO (Elekta AB, Stockholm, Sweden).

3.1.2 Pencil Beam Scanning

For pencil beam scanning, the narrow proton beam is deflected by two magnets in a plane perpendicular to the beam direction to scan the target region (Lomax, 1999). In contrast to passive scattering, the initial beam intensity is almost completely used for dose delivery in patients. Proton pencil beams of equal energy are collected in a single energy layer. Each layer is then irradiated sequentially, starting with the highest energy until the target region is completely covered in lateral and longitudinal direction. Since the beam transport of pro-

tons with energies smaller than 70-100 M*e*V cannot be efficiently processed, an additional range shifter (usually of lucite) is inserted in front of the patient to enable treatments of superficial targets (e.g. localised in the head-and-neck region).
Dose distributions for pencil beam scanning are optimised by a cost function according to predefined objectives for the target region and organs at risk (OARs). After the manual definition of beam angles, an optimisation algorithm calculates the pencil-beam spot positions and its respective number of protons. Treatment fields can be optimised individually (single-field optimisation), resulting in a homogeneous dose distribution for each field, or collectively (multi-field optimisation), leading to inhomogeneous dose distributions for single fields, which are homogeneous in combination (Lomax et al., 2001). Consequently, a highly conformal tumour coverage can be achieved. However, these techniques are associated with an increased sensitivity to uncertainties induced by intra- and inter-fractional variations in patient anatomy and positioning as well as deviations in dose calculation and delivery (Lomax et al., 2004; Unkelbach et al., 2007; Lomax, 2008a; Lomax, 2008b).
In current commercial TPS, analytical dose calculation algorithms are mostly applied for pencil beam scanning, e.g. Soukup et al. (2005) in XiO. Since the accuracy of such algorithms is limited in heterogeneous anatomical regions, the application of Monte Carlo algorithms can contribute to reduce deviations caused by multiple Coulomb scattering (Urie et al., 1986; Fippel and Soukup, 2004). Recently, a simplified and fast Monte Carlo dose calculation engine was developed and introduced in the TPS RayStation 6.0 (RaySearch Laboratories, Stockholm, Sweden) for clinical use (Saini et al., 2017).

3.2 Uncertainties in Proton Therapy

Due to the physical characteristics of charged particles, dose deposition in proton therapy is highly sensitive to uncertainties. For each step in the radiotherapy chain, several strategies have been developed to incorporate and reduce their influence on the treatment outcome.

3.2.1 Sources of Uncertainty

To assure reliable proton treatments of appropriate accuracy and precision, uncertainties originating from numerous sources during treatment preparation or within the course of treatment are thoroughly assessed (Urie et al., 1991; van Herk, 2004; Baumann et al.,

2016). In addition to the uncertainty arising from assumptions in analytical dose calculation (section 3.1), various sources of uncertainty are summarised in the following and their impact on the intended proton dose distribution and treatment response is discussed.

Range Prediction

Treatment planning commonly relies on SECT scans owing to its high geometrical fidelity, quantitative reliability and fast acquisition time. For dose calculation, the anatomical information of patients derived from CT require a conversion into proton stopping power to consider the different interaction processes of X-rays and protons (Chen et al., 1979), as described in section 4.1. The typically applied heuristic CT-number-to-SPR conversion, referred to as Hounsfield look-up table (HLUT), can be optimised to fit human tissue, but non-tissue materials like polymers, contrast agents or metals often widely deviate from the HLUT (Jäkel et al., 2001). Furthermore, human tissues reveal large variations in elemental composition within one patient and between patients (Woodard and White, 1986; White et al., 1991), which cannot adequately be covered by any generic HLUT. In current clinical practice, the impact of CT-related uncertainties on proton range are assessed with 1-4% (Schaffner and Pedroni, 1998; Moyers et al., 2001; Yang et al., 2010; Paganetti, 2012b).

Target Delineation

Different imaging modalities, comprising CT, positron emission tomography and magnetic resonance imaging, are commonly used to identify, localise and delineate the gross tumour volume (GTV) and its associated clinical target volume (CTV), including micro- and macroscopic tumour extensions, as well as surrounding OARs (Troost et al., 2015). An accurate target definition provides the basis for treatment planning, but often lacks patient-specific CTV margins (Apolle et al., 2017) and is prone to intra- and inter-observer variability (Sharp et al., 2014). The delineation uncertainty directly transfers into an under- and over-dosage of tumour and healthy tissue, respectively.

Intra- and Inter-Fractional Variation

Dose deposition in patients can be affected by daily variations in machine delivery and patient positioning (Lowe et al., 2016), anatomical changes within a single treatment fraction,

e.g. induced by gastro-intestinal peristalsis, swallowing, oesophageal or respiratory motion (Bert and Durante, 2011), or during the overall course of treatment, e.g. tumour shrinkage, swelling of healthy tissue and patient weight loss (Stützer et al., 2017a). Consequently, the proton dose distribution delivered for weeks in numerous single fractions very likely differ from the desired one planned before start of treatment.

Biological Effect

The physical energy deposition of proton irradiation is associated with biological effects on cellular level, causing damages to cellular structures such as double-strand breaks in deoxyribonucleic acid. This radiation-induced biological effect depends on the spatial distribution of interactions leading to an energy deposition. Since protons have a larger linear energy transfer (LET) than photons, i.e. protons transfer on average more energy per unit path length to the traversed medium, the cellular damage caused by protons is more severe (Goodhead et al., 1993; Holley and Chatterjee, 1996; Rydberg, 1996). To specify the influence of different radiation types on biological damages, the relative biological effectiveness (RBE) was introduced and thoroughly investigated (Paganetti et al., 2002; Lühr et al., 2017b). In current proton treatment planning, a constant RBE of 1.1 is assumed. Hence, the physical dose of protons is reduced by 10% to achieve the same biological effect as photons. Based on such dose response relations, the tumour control probability and normal tissue complication probability can be assessed to estimate the potential benefit for each patient using proton instead of photon therapy (Langendijk et al., 2013; Jakobi et al., 2015; Lühr et al., 2017a). However, several studies have shown that the RBE of protons increases with depth in a SOBP from approximately 1.1 in the entrance region up to 1.35 and 1.7 at the distal edge and fall-off, respectively (Paganetti, 2014). This may be considered in future RBE-optimised proton treatment planning.

3.2.2 Management and Minimisation

Uncertainties in proton therapy are currently tackled by different approaches from treatment planning to online dose tracking. In this context, imaging during the course of treatment gains importance for patient positioning and early plan adaptation. Furthermore, range verification methods were developed to monitor the dose delivery of each fraction and to detect potential proton range shifts caused by anatomical variations.

Patient Positioning

A reproducible and precise patient positioning in each fraction is inevitable for a reliable delivery of the planned dose distribution. Depending on the treatment site, several immobilisation devices attached to the patient surface, e.g. a patient-individually shaped vacuum cushion and thermoplastic mask, as well as inserted in cavities, such as a water-filled rectum balloon, are used to prevent misalignment and organ motion, respectively. Current patient positioning in proton therapy is still mostly based on orthogonal X-ray imaging. If clinically indicated, fiducial markers are implanted in the target region (e.g. prostate) for its better visibility. However, to meet the requirements of a highly conformal proton therapy with an efficient adaptive clinical workflow, further imaging techniques, such as cone-beam CT and diagnostic in-room CT-on-rails, are available in new proton facilities, allowing for continuous tracking of anatomical changes and regular adaptive replanning if required.

Treatment Margins and Robust Optimisation

Remaining uncertainties are considered as safety margins in proton treatment planning. The generation of a planning target volume (PTV), assigning an isotropic margin to the CTV, is often not appropriate, because the range uncertainty in beam direction induced by CT-number-to-SPR conversion or anatomical changes outweighs the uncertainty for lateral beam shaping. Therefore, beam-specific proximal and distal safety margins are commonly applied in passive scattering (Moyers et al., 2001; Paganetti, 2012b; Schuemann et al., 2014). However, the PTV concept has been used standardly for pencil beam scanning, because an individual consideration of uncertainties for each spot could not be performed within a TPS.

To replace clinically applied PTV margins in pencil beam scanning, robust optimisation techniques were developed and validated (Fredriksson et al., 2011; Li et al., 2015; Van Der Voort et al., 2016; Stützer et al., 2017b). These approaches incorporate the patient setup uncertainty still remaining after image-based adjustment of the patient position as well as the uncertainty of CT-based range prediction in proton treatment planning. Different treatment scenarios are simulated by varying combinations of setup and range uncertainty and used in an optimisation algorithm to calculate a treatment plan still fulfilling the clinical treatment goals under these certain conditions.

Range Verification

Range verification with a clinically appropriate accuracy of 1-2 mm is highly challenging, since protons stop within the patient and a direct measurement is currently not feasible during treatment. Hence, several techniques have been developed and evaluated under clinical conditions, measuring secondary particles emitted during proton irradiation. One approach uses the spatial distribution of positron-emitting nuclei for *in vivo* range verification (Enghardt et al., 1992; Enghardt et al., 1999; Nischwitz et al., 2015). Three further techniques are based on detecting prompt-gamma rays emitted during proton treatment: prompt-gamma imaging (Smeets et al., 2012; Richter et al., 2016), spectroscopy (Verburg and Seco, 2014; Verburg et al., 2015) and timing (Golnik et al., 2014; Pausch et al., 2016). At baseline, additional proton transmission measurements can be performed for positioning and validating CT-based range prediction (Schneider and Pedroni, 1995; Farace et al., 2016; Müller et al., 2017). Biological changes induced by irradiation can be visualised by magnetic resonance imaging (Gensheimer et al., 2010; Yuan et al., 2013). All approaches can potentially contribute to increase the accuracy of patient treatments.

4 Principles of Stopping-Power Prediction from Computed Tomography

For proton range calculation, a 3D image dataset is required, which contains anatomical information as tissue-specific proton stopping power in each voxel. The use of protons for image acquisition, e.g. proton CT (Penfold et al., 2009; Poludniowski et al., 2015; Prall et al., 2016), would allow for direct *in vivo* SPR determination. However, this technique is still under development and thus no clinical system with appropriate properties is currently available (Johnson et al., 2016). Moreover, current proton therapy facilities equipped with a cyclotron mostly cannot deliver proton energies sufficient for traversing all body regions.
Instead, proton treatment planning is generally based on patient information derived from X-ray CT scans, mostly acquired with 120 kVp. Even though X-rays and protons interact differently with matter, both share a linear dependence on electron density and correlation in elemental composition for human tissues. Hence, a scanner-specific heuristic translation from measured CT number to SPR is currently applied. As discussed in section 3.2, this conversion is however associated with a large uncertainty leading to additional safety margins. Minimising the CT-related range uncertainty might allow for a reduction of safety margins and thereby better sparing of healthy tissue surrounding the tumour region.
In the following, different approaches for CT-number-to-SPR conversion based on single-energy (SECT) and dual-energy CT (DECT) are explained.

4.1 Single-Energy Computed Tomography

Proton treatment planning is currently performed on SECT scans of patients. The information on X-ray attenuation gathered by a single CT number in each voxel is translated into SPR using a piece-wise linear function, referred to as Hounsfield look-up table (HLUT). A distinction is made between empirical (Chen et al., 1979; Jäkel et al., 2001) and stoichiometric prediction (Schneider et al., 1996; Schneider et al., 2000) of material-specific CT

numbers and SPRs. To determine a calibration curve for the respective CT scanner and scan protocol, each CT scanner needs to be calibrated accordingly.

4.1.1 Empirical Prediction

CT number and SPR of several tissue surrogates – polymers simulating X-ray attenuation and proton stopping power of human tissues – are obtained from CT acquisition with clinical scan settings and proton transmission measurement or calculation using the Bethe formula (eq. 3.3), respectively. Subsequently, the values determined for each material are described by a step-wise linear function covering the entire Hounsfield scale from typically -1024 HU to 3071 HU. This calibration curve can be established by connecting adjacent tissues or by combining separate linear fit functions for specific tissue types, e.g. low-density, soft and bone tissue (Chen et al., 1979).

4.1.2 Stoichiometric Prediction

X-ray attenuation can be calculated according to eq. 2.2 using the cross-section parametrisation proposed by Jackson and Hawkes (1981):

$$\sigma_{\mathsf{e}}\left(E, Z\right) = A\left(E\right) + B\left(E\right) C\left(Z\right) \quad \text{with} \quad C\left(Z\right) = Z^{n}, \tag{4.1}$$

which separates the dependence on energy (coefficients A and B) and atomic number (coefficient C) and results in (Rutherford et al., 1976; Schneider et al., 1996)

$$\mu = \varrho_{\mathsf{e}} \cdot \left[A\left(E\right) + B_{\mathsf{ph}}\left(E\right) Z^{3.62} + B_{\mathsf{coh}}\left(E\right) Z^{1.86}\right] \tag{4.2}$$

with $A\left(E\right) = A_{\mathsf{ph}}\left(E\right) + A_{\mathsf{coh}}\left(E\right) + A_{\mathsf{inc}}\left(E\right)$. Based on the attenuation sum rule $\mu = \sum_i \mu_i$, eq. 4.2 can be adapted to compounds and mixtures using an effective atomic number

$$Z_{\mathsf{eff}} = \left(\sum_i \nu_i Z_i^n\right)^{1/n} \tag{4.3}$$

derived from the electron density fraction ν_i and atomic number Z_i of each constituent i:

$$\mu = \varrho_{\mathsf{e}} \cdot \sigma_{\mathsf{e}}\left(E, Z_{\mathsf{eff}}\right) = \varrho_{\mathsf{e}} \cdot \left[A\left(E\right) + B_{\mathsf{ph}}\left(E\right) Z_{\mathsf{ph}}^{3.62} + B_{\mathsf{coh}}\left(E\right) Z_{\mathsf{coh}}^{1.86}\right] \tag{4.4}$$

with $Z_{\text{ph}}^{3.62} = \sum_i \nu_i Z_i^{3.62}$ and $Z_{\text{coh}}^{1.86} = \sum_i \nu_i Z_i^{1.86}$. For the calculation of CT numbers, i.e. X-ray attenuation relative to water (index w), the three coefficients are condensed to $c_{\text{ph}} = B_{\text{ph}}/A$ and $c_{\text{coh}} = B_{\text{coh}}/A$.

$$\frac{H}{1000\,\text{HU}} + 1 = \hat{\varrho}_{\text{e}} \, \frac{1 + c_{\text{ph}}\,(E)\, Z_{\text{ph}}^{3.62} + c_{\text{coh}}\,(E)\, Z_{\text{coh}}^{1.86}}{1 + c_{\text{ph}}\,(E)\, Z_{\text{ph,w}}^{3.62} + c_{\text{coh}}\,(E)\, Z_{\text{coh,w}}^{1.86}} \tag{4.5}$$

Based on CT scans of tissue surrogates with known elemental composition, the scanner-specific coefficients c_{ph} and c_{coh} are obtained for each scan protocol and setup using a multiple regression analysis to eq. 4.5. After calibration, CT numbers of tabulated human tissues (Woodard and White, 1986; White et al., 1987) are calculated and in combination with SPRs derived from eq. 3.3 an HLUT is defined analogously to the empirical prediction (section 4.1.1).

4.2 Dual-Energy Computed Tomography

In recent years, numerous algorithms for direct stopping-power prediction from dual-energy CT (DirectSPR) were proposed (Hünemohr et al., 2013; Bourque et al., 2014; Hünemohr et al., 2014; Han et al., 2016; Möhler et al., 2016; Taasti et al., 2016b; Saito and Sagara, 2017b) and the respective accuracy was assessed using homogeneous tissue surrogates (Hansen et al., 2015; Hudobivnik et al., 2016; Bär et al., 2017; Li et al., 2017) and polymers (Taasti et al., 2016a; Zhu and Penfold, 2016). These studies indicate that DECT can potentially lead to more precise proton range prediction.
Within this thesis, three different DECT-based SPR prediction approaches were thoroughly investigated, which are described in the following. SPRs can be obtained from DECT-derived MonoCT datasets still using an HLUT as CT-number-to-SPR conversion (section 4.2.1) or directly from DECT-derived material parameters inserted into the Bethe formula (sections 4.2.2 and 4.2.3).

4.2.1 Monoenergetic Approach

As described in section 2.3.1, MonoCT datasets of different energies can be calculated from DECT scans by linear superposition (eq. 2.6). The optimal MonoCT energy for treatment planning can be determined in phantoms composed of tissue surrogates with respect

to image quality and CT number constancy. For the resulting MonoCT dataset, an HLUT is defined empirically with homogeneous tissue surrogates or based on the elemental composition of tabulated human tissues and their respective monoenergetic photon attenuation cross section.

4.2.2 RhoZ Approach

According to the Bethe formula (eq. 3.3), the stopping power of protons depends on two material-specific parameters, namely electron density and I-value. The electron density can be directly derived from DECT scans in an accurate and robust manner (section 2.3.2). The I-value can be obtained from the DECT-derived effective atomic number (section 2.3.2) using a linear parametrisation for the logarithmic I-value as proposed by Yang et al. (2010). This I-value parametrisation is specified based on tabulated human soft and bone tissues, but lacks continuity for effective atomic numbers between approximately 8 to 10 (Fig. 4.1). Hence, the accuracy of I-value determination is reduced by mixtures of soft and bone tissue falling into this undefined region. Such tissue mixtures occur at material transitions within heterogeneous regions of patients and their influence on proton range prediction cannot be neglected.

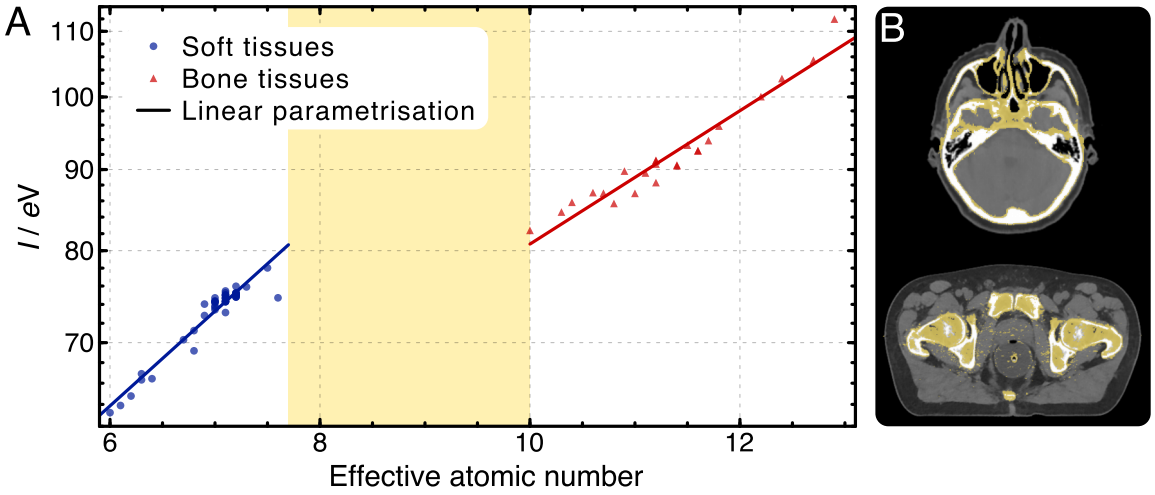

Figure 4.1: (A) Correlation of I-value and effective atomic number (EAN) for tabulated human soft and bone tissues (Woodard and White, 1986; White et al., 1987). The EAN of each tissue was obtained from syngo.RhoZ using an 80/140 kVp DECT scan of the CT scanner Definition AS (reconstructed with D34). (B) Axial slices of a 79 k*e*V MonoCT dataset derived from syngo.MonoPlus for a brain- and prostate-cancer patient. Voxels with EAN between 8 and 10 are coloured.

4.2.3 RhoSigma Approach

Möhler et al. (2016) proposed to describe the SPR as a product of relative electron density (RED) and relative stopping number (RSN) according to the Bethe formula (eq. 3.3). RED is the dominating physical quantity and ranges approximately from 0 to 2 for human tissues. RSN depends logarithmically on the I-value, whose variation is limited within human tissues from adipose ($I = 63$ *e*V) to cortical bone ($I = 112$ *e*V), and are thus restricted to values of approximately 0.95-1.02 for a proton energy of 200 M*e*V (Fig. 4.2).
RED can be directly derived from DECT (section 2.3.2) and thus only an empirical approximation for RSN is required. Hence, the impact of the empirical component on the accuracy of SPR prediction is clearly mitigated compared to HLUT-based approaches using a SECT scan (section 4.1) or MonoCT dataset (section 4.2.1). The RSN can be empirically obtained from the relative photon attenuation cross section (RCS or $\hat{\sigma}_\mathrm{e}$). Owing to the X-ray attenuation sum rule $\mu = \sum_i \mu_i$ and Bragg's additivity rule for proton stopping power $S = \sum_i S_i$ (Bragg and Kleeman, 1905), both quantities share a convenient mixing behaviour:

$$\left(\hat{\sigma}_\mathrm{e}, \hat{L}\right) = \sum_i \nu_i \left(\hat{\sigma}_\mathrm{e}, \hat{L}\right)_i \tag{4.6}$$

with $0 < \nu_i < 1 \; \forall i$ and $\sum_i \nu_i = 1$. Within this variable space (Fig. 4.3), mixtures are a linear combination of a set of base materials forming a convex hull (Möhler et al., 2016).

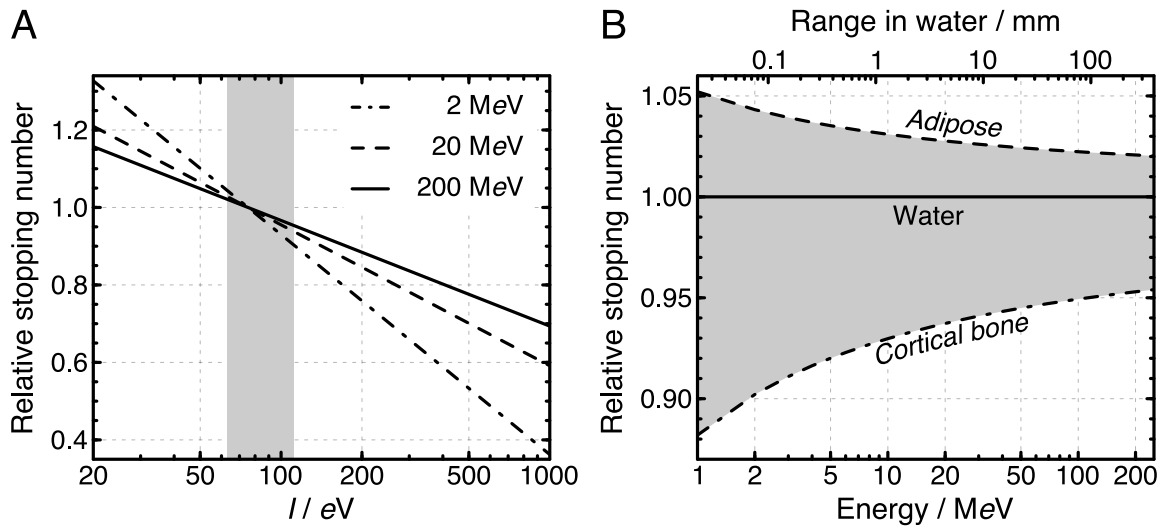

Figure 4.2: Relative stopping number (RSN) depending on material-specific I-value (A) and proton energy or range (B). The grey-shaded region covers tabulated human tissues (Woodard and White, 1986; White et al., 1987). Adapted from Möhler et al. (2016).

According to eq. 2.2, the energy-dependent RCS of a material results from its DECT-derived RED and CT number determined for a specific X-ray spectrum or MonoCT energy.

$$\hat{\sigma}_{\mathrm{e}} = \frac{1}{\hat{\varrho}_{\mathrm{e}}} \left(\frac{H}{1000\,\mathrm{HU}} + 1 \right) \tag{4.7}$$

As shown in eqs. 4.1 and 4.4, RCS comprises similar information as an effective atomic number used for I-value parametrisation, but requires less assumptions (Möhler et al., 2017) and allows for proper consideration of tissue mixtures and unambiguous quantification of uncertainties (Möhler et al., 2016). For DECT-based SPR prediction, an empirical conversion from RCS to RSN is established based on tabulated human tissues.

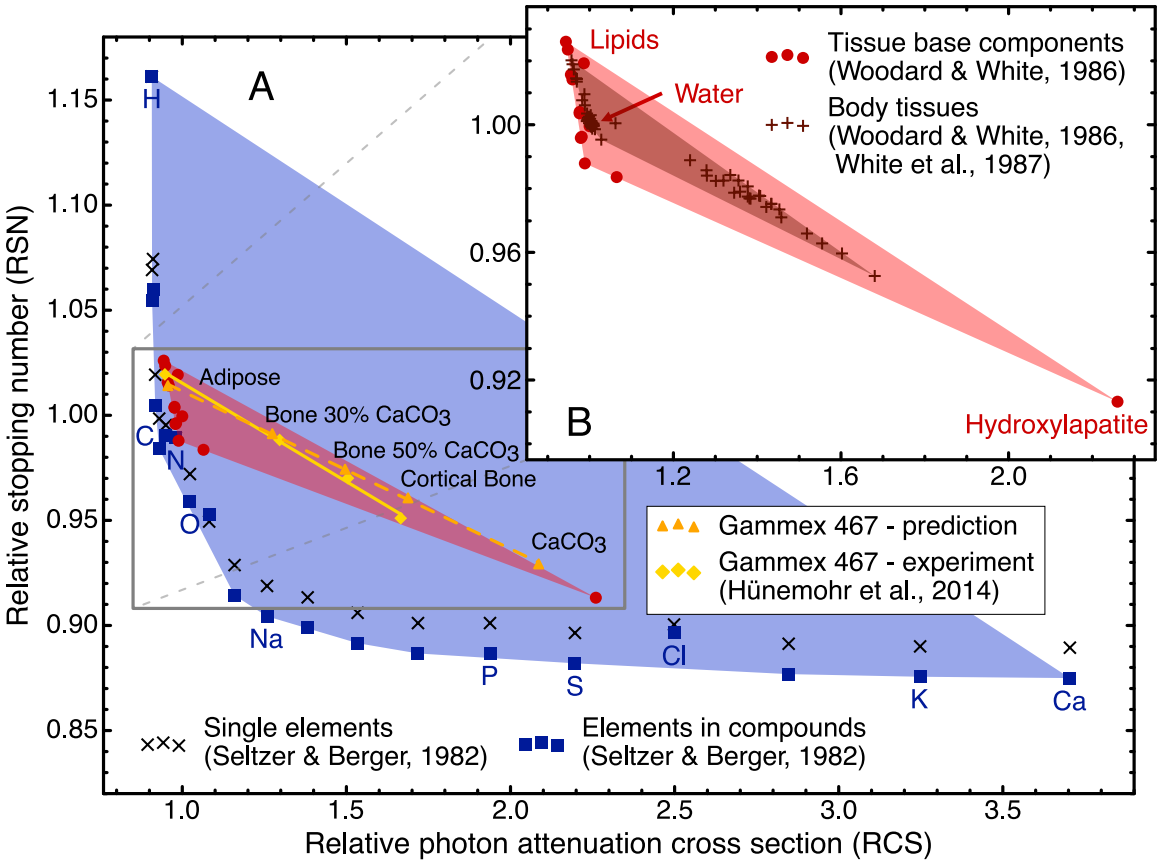

Figure 4.3: Correlation of relative photon attenuation cross section (RCS) and stopping number (RSN) for elements up to $Z = 20$ (A) as well as tissue base components and body tissues (B). The shaded areas illustrate the convex hull of each set of base materials. The linear mixing behaviour (straight line for two base materials) is demonstrated for exemplary tissue surrogates. The RCS is determined according to eq. 4.1 with $A = 0.907 \pm 0.012$, $B = (8.5 \pm 3.5) \cdot 10^{-5}$ and $n = 3.47 \pm 0.13$ for an 80 kVp CT scan acquired at the CT scanner Definition Flash and reconstructed with D30. The RSN is calculated for 200 MeV protons. Adapted from Möhler et al. (2016).

5 Experimental Calibration of Stopping-Power Prediction

Within this thesis, a comprehensive characterisation and experimental calibration of the single-source dual-spiral DECT scanner Definition AS was performed to define optimal CT scan settings for proton treatment planning. The calibration procedure performed exemplarily for this specific CT scanner can be transferred to other CT scanner models.

5.1 Scan Protocol Optimisation in Computed Tomography

Proton treatment planning requires high overall CT image quality with regard to an X-ray dose fulfilling the "As-Low-As-Reasonably-Achievable" (ALARA) principle. Whereas CT acquisition in diagnostic radiology mainly focuses on improving image contrast for a better case-specific tissue differentiation, radiotherapy additionally aims at quantitative CT imaging for accurate material assignment in each voxel. However, depending on scan location (e.g. head vs. pelvis) as well as patient size and geometry, different CT numbers are obtained for the same tissue. This uncertainty, arising from beam hardening of the X-ray spectrum (section 2.2.3), needs to be considered thoroughly in image reconstruction. Consequently, a CT scan protocol with sophisticated beam hardening correction would be ideal to assign the same CT number to all voxels of the same material independently from size, geometry and surrounding tissue. Furthermore, a universal CT scan protocol applicable to all treatment regions would reduce the clinical effort in quality assurance and susceptibility to errors.

To define an optimal CT scan protocol satisfying the requirements of proton treatment planning, the effect of adjustable CT scan parameters on CT number stability and image noise was experimentally quantified. The following scan parameters were investigated in detail: tube voltage and current, slice thickness and collimation, pitch and FOV, reconstruction algorithm and kernel.

5.1.1 Investigated Material Samples and Phantoms

Since different hard- and software components of a CT scanner and their manufacturer-approved calibration can lead to variations in CT numbers, a user-originated characterisation of each individual CT scanner is recommended to guarantee the high demands on CT number accuracy and constancy in radiotherapy. Accordingly, different material samples, representing the X-ray attenuation of human tissues and covering the clinically required CT number scale, as well as phantoms simulating various human body regions are used to assess the influence of CT scan settings.

Tissue Surrogates and Non-Tissue Materials

In this thesis, 19 tissue surrogates – 10 produced by Gammex, Inc. (Middleton, WI, USA) and 9 manufactured by CIRS, Inc. (Norfolk, VA, USA) – as well as 6 polymers and aluminium were investigated. To avoid edge artefacts within a CT scan, each material sample has a cylindrical shape with three different diameters (10 mm, 25 mm, 50 mm) and a length of 10 mm or 20 mm (according to material availability). For CT measurements, the materials were aligned in series along the central scanner axis. The material-specific CT number and its standard deviation were determined in a circular region of interest (ROI) inside each material on axial CT slices unaffected by material transitions. Material edges in axial CT images were excluded by selecting a ROI diameter equal to 70% of the material diameter. Reference properties of all materials were provided by the manufacturers.

Tabulated Human Tissues

An encompassing compilation of overall 71 human tissues obtained from adults is currently often applied in radiotherapy, e.g. for stoichiometric conversion of CT number into SPR (Schneider et al., 2000). The elemental composition of these tissues, which were thoroughly compiled by Woodard and White (1986) and White et al. (1987), are also used within this thesis.

Phantoms of Simplified Geometry

To simulate different beam hardening conditions occuring in clinical CT scans of the head, thoracic or pelvic region, all material samples were measured in three CT scan setups

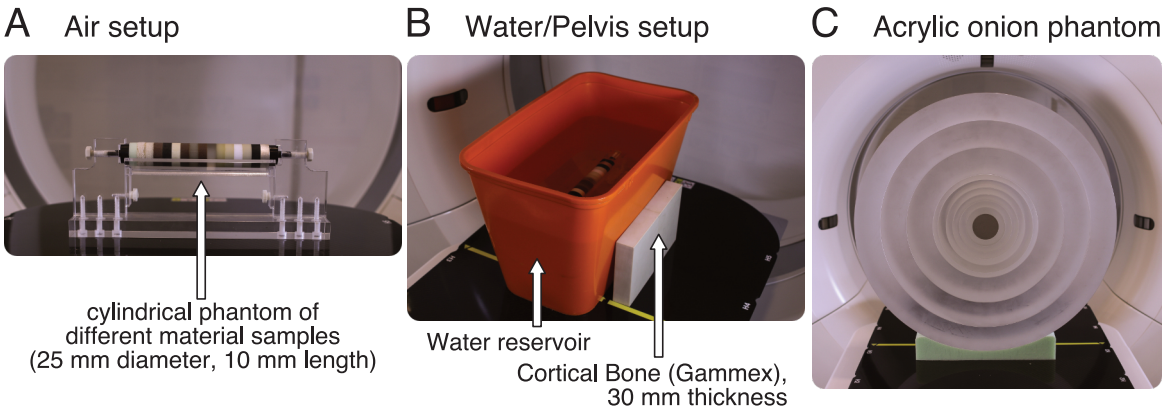

Figure 5.1: Different CT scan setups to simulate various beam hardening conditions. (A) Cylindrical material stack composed of 16 different samples without surrounding phantom (air setup). (B) Material stack within a water tank only (water setup) or with additional lateral bone surrogates (pelvis setup). (C) Pluggable acrylic onion phantom with material samples positioned centrally for systematic evaluation of beam hardening effects. Adapted from Wohlfahrt et al. (2017b).

(Fig. 5.1, A and B): without an additional phantom (referred to as air), in a water reservoir with a dimension of $(300 \times 200 \times 250)\,\mathrm{mm}^3$ (water) and in the water reservoir with additional lateral cortical bone surrogates with a total thickness of 60 mm (pelvis). The water setup was defined as clinical default setting.

Furthermore, the influence of beam hardening on CT number stability was systematically assessed using a cylindrical phantom composed of pluggable acrylic hollow cylinders with varying outer diameter from 25 mm up to 500 mm and a length of 100 mm (Fig. 5.1 C). This so-called "onion phantom" allows for a diameter-dependent quantification of variations in material-specific CT numbers, resulting in an estimation of the clinically relevant uncertainty induced by beam hardening.

Anthropomorphic Phantoms

To evaluate the influence of CT scan parameters on image quality in a realistic close-to-clinical patient scenario, two anthropomorphic head phantoms were investigated: the head of the Whole Body Phantom PBU-60 (Kyoto Kagaku, Kyoto, Japan) and the Proton Therapy Dosimetry Head 731-HN (CIRS, Inc., Norfolk, USA). The first head phantom is composed of synthetic bones based on epoxy resin and different soft tissues based on urethane resin. The latter (Fig. 5.2) consists of 9 tissue substitutes, which were optimized to mimic tabulated human tissues in their X-ray attenuation and proton interaction properties. Addi-

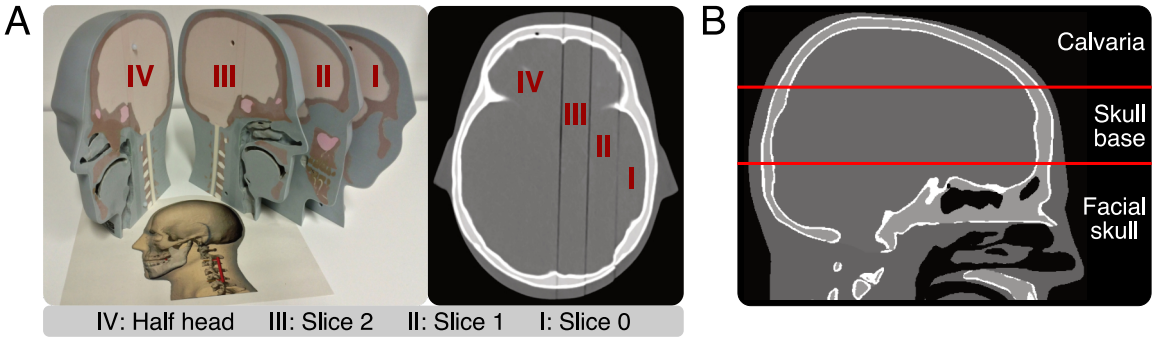

Figure 5.2: Illustration of the anthropomorphic Proton Therapy Dosimetry Head 731-HN. (A) The head phantom is cut in half and one side is additionally divided in three parts with two plane-parallel edges and a nominal thickness of 20 mm each. (B) Sagittal image of the reference 3D SPR map illustrating three head areas (facial skull, skull base, calvaria) evaluated within this thesis. Adapted from Wohlfahrt et al. (2018a).

tionally, the phantom contains a replaceable tungsten-filled and a tissue-equivalent molar tooth as well as a non-removable titanium prosthesis fixated by two screws in the vertebrae. These (partly removable) metal implants allow for validating metal artefact reduction algorithms.

5.1.2 Quantitative Parameters for Image Quality Assessment

The influence of different CT scan and image reconstruction settings on image noise, beam hardening and artefacts caused by metal implants was assessed by quantitative image parameters.

Quantification of Image Noise

The standard deviation σ of CT numbers within an ROI covering a homogeneous material sample i in a scan setup s serves as measure for image noise. Compared with a reference CT scan setting (index r), changing a parameter of interest Υ can result in a change of the noise level. The image-noise ratio (INR) quantifies the effect relative to the reference setting.

$$\mathrm{INR_r}\left(\Upsilon\right) = \sqrt{\frac{1}{N}\sum_{i=1}^{N}\frac{\sum\limits_{s\in\mathcal{S}}\sigma_{s,i}^2\left(\Upsilon_\mathrm{r}\right)}{\sum\limits_{s\in\mathcal{S}}\sigma_{s,i}^2\left(\Upsilon\right)}} \tag{5.1}$$

A set $\mathcal{S}$ of various CT scan setups and N different material samples can be considered for INR assessment. An INR > 1 corresponds to noise reduction.

Quantification of Beam Hardening

The beam-hardening ratio (BHR) describes the difference between maximal and minimal CT number of a material obtained in several CT scan setups relative to the reference setting. A BHR > 1 means that the influence of beam hardening on CT number constancy is reduced. A high BHR corresponds to a small influence of beam hardening.

$$\mathrm{BHR}_{\mathrm{r}}\left(\Upsilon\right) = \frac{\sum\limits_{i=1}^{N}\left[\max\limits_{s\in\mathcal{S}}\left\{H_{s,i}\left(\Upsilon_{\mathrm{r}}\right)\right\} - \min\limits_{s\in\mathcal{S}}\left\{H_{s,i}\left(\Upsilon_{\mathrm{r}}\right)\right\}\right]}{\sum\limits_{i=1}^{N}\left[\max\limits_{s\in\mathcal{S}}\left\{H_{s,i}(\Upsilon)\right\} - \min\limits_{s\in\mathcal{S}}\left\{H_{s,i}(\Upsilon)\right\}\right]} \tag{5.2}$$

Quantification of Metal Artefacts

According to Lin et al. (2011), the severity of metal artefacts can be assessed by the metal-artefact index (MAI), measuring CT number variations in an ROI for two cases: with and without presence of a metal implant. Identical noise levels lead to MAI $= 0$.

$$\mathrm{MAI} = \begin{cases} \sqrt{\left|\sigma^2_{\mathrm{metal}} - \sigma^2_{\mathrm{none}}\right|} & \text{for } \sigma^2_{\mathrm{metal}} \geq \sigma^2_{\mathrm{none}} \\ -\sqrt{\left|\sigma^2_{\mathrm{metal}} - \sigma^2_{\mathrm{none}}\right|} & \text{for } \sigma^2_{\mathrm{metal}} < \sigma^2_{\mathrm{none}} \end{cases} \tag{5.3}$$

5.1.3 Influence of Scan Protocol Settings

For an appropriate selection of CT scan settings in radiotherapy, the influence of each individual parameter on image noise and material-specific CT number needs to be assessed. Based on CT scans of Gammex tissue surrogates acquired in three scan setups (air, water and pelvis) representing different beam hardening conditions (Fig. 5.1), Wohlfahrt (2014) demonstrated that the FOV, pitch and scan acquisition modus (sequential or spiral) do not influence absolute CT numbers and image noise. A variation of tube current, reconstructed slice thickness or sharpness function of reconstruction kernels (high spatial resolution or reduced noise level) affect the overall image noise and can be adjusted accordingly. For a constant computed tomography dose index (CTDIvol), the selection of tube voltage (different X-ray spectra), reconstruction kernel (especially the integrated BHC algorithm) and

slice collimation (X-ray scattering and applied scatter correction) causes only slight variations in image noise, but large differences in absolute CT numbers. Consequently, scan parameters only affecting the image quality in terms of image noise can be selected individually for each patient. However, the tube voltage, slice collimation and reconstruction kernel should be predefined in a clinical CT scan protocol to guarantee a constant accuracy and precision in proton treatment planning.

Image Reconstruction Algorithm

To assess the influence of the iterative reconstruction algorithm SAFIRE on CT numbers in comparison with FBP, CT scans of 10 Gammex tissue surrogates positioned within three different scan setups (Fig. 5.1, A and B) were acquired with a constant $CTDIvol_{32\,cm}$ of 28.5 mGy. Considering four X-ray spectra ranging from 80 kVp to 140 kVp in steps of 20 kVp and two BHC algorithms included in reconstruction kernels (D30/Q30 and D34/Q34), the material-specific CT numbers show a negligible maximal difference of 3 HU and mean deviation of below 1 HU between FBP and SAFIRE. Consequently, both reconstruction algorithms yield similar CT numbers and can be interchangeably used for treatment planning without additional adjustments.

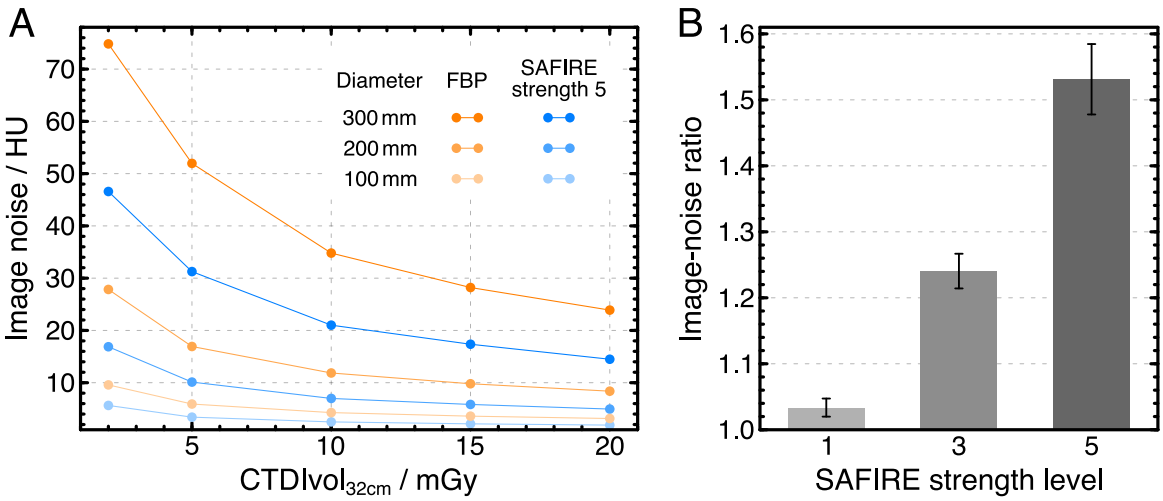

Figure 5.3: (A) Image noise of a 120 kVp CT scan (slice collimation of 1.2 mm) representative for soft tissues depending on $CTDIvol_{32\,cm}$ and object diameter. CT scans of the material sample soft tissue grey (CIRS) with a diameter of 50 mm, centrally positioned within the onion phantom, were acquired and reconstructed with FBP (D34) and SAFIRE of maximal strength (Q34/5). (B) Mean image-noise ratio INR_{FBP} with standard deviation for different SAFIRE strengths considering four X-ray spectra, two slice collimations and five CT dose levels.

The reduction of image noise achievable with iterative image reconstruction relative to FBP was quantified for four cylindrical CIRS tissue surrogates (sinus cavity, soft tissue grey, trabecular bone and cortical bone) with a diameter of 50 mm, covering the typical CT number scale of human tissues. All material samples were centrally positioned inside the onion phantom with an outer diameter of 100 mm, 200 mm or 300 mm (Fig. 5.1 C). Depending on the $\mathrm{CTDIvol}_{32\,\mathrm{cm}}$ selected for CT acquisition (2 mGy, 5 mGy, 10 mGy, 15 mGy or 20 mGy), the respective image noise within soft tissues is shown exemplarily for a 120 kVp CT scan in Fig. 5.3 A. Compared with FBP, the application of SAFIRE clearly reduces image noise independent from object size and dose. Considering all CT scans of the four materials, which differ in X-ray spectrum (80 kVp to 140 kVp in steps of 20 kVp), slice collimation (0.6 mm or 1.2 mm) and $\mathrm{CTDIvol}_{32\,\mathrm{cm}}$, a mean $\mathrm{INR}_{\mathrm{FBP}} \pm$ standard deviation of up to 1.53 ± 0.05 can be obtained by SAFIRE of maximal strength (Fig. 5.3 B). The strengths 1 and 3 result in a smaller mean $\mathrm{INR}_{\mathrm{FBP}}$ of 1.03 ± 0.01 and 1.24 ± 0.03, respectively.
As an alternative, a lower dose can be applied for CT acquisition to obtain a noise level similar to FBP. For SAFIRE of maximal strength, the CT dose can be reduced by at least 60% (Fig. 5.3 A) – e.g. from a $\mathrm{CTDIvol}_{32\,\mathrm{cm}}$ of 20 mGy, currently used for treatment planning of brain-tumour patients at OncoRay, to below 8 mGy.

Beam Hardening Correction

To quantify the variation of CT numbers under clinically realistic beam hardening conditions, 11 material samples (10 Gammex tissue surrogates and styrodur) were measured in three scan setups (Fig. 5.1, A and B) using different X-ray spectra. Two BHC algorithms were applied during image reconstruction, which perform either a correction based on water only (Q30) or water and bone consecutively (Q34). As shown in Fig. 5.4 A, both algorithms reveal comparable results for low-density and soft tissues ($H < 100$ HU), but differ considerably for bone surrogates. The additional correction concerning bone results in an improved overall CT number stability. Consequently, CT scans reconstructed using a BHC for bone (as included in Q34) are more robust against different beam hardening conditions. Compared with image reconstruction using Q30, the kernel Q34 clearly reduces the effect of beam hardening on CT numbers of bones for each X-ray spectrum. With an additional bone BHC, CT number variations induced by beam hardening are at least 3 times smaller. Furthermore, beam hardening effects decrease with increasing tube voltage (Fig. 5.4 B).

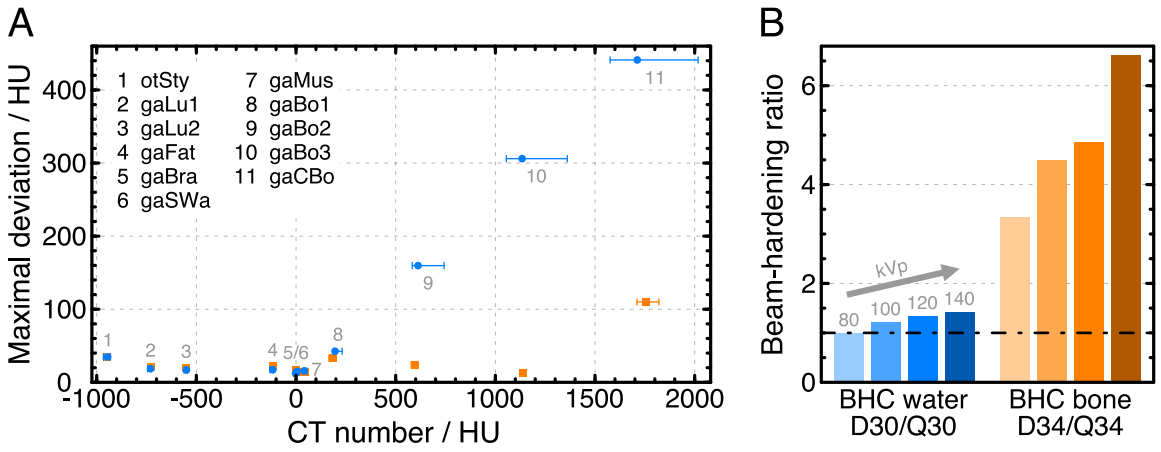

Figure 5.4: (A) Maximal CT number difference between three scan setups (air, water, pelvis) as exemplarily shown for an 80 kVp CT scan of 11 material samples with a diameter of 25 mm. Two different BHC algorithms are applied during image reconstruction considering only water (Q30, blue) or additionally bone (Q34, orange). The error bar illustrates the minimal and maximal CT number. (B) Beam-hardening ratio (BHR) depending on X-ray spectrum and applied BHC algorithm including all 11 material samples. The 80 kVp CT scan reconstructed with Q30 reveals the largest influence of beam hardening and was set as BHR reference.

For a systematic assessment of the size-dependent influence of beam hardening on bones, CT scans of a low-density (trabecular bone) and high-density (cortical bone) CIRS bone surrogate positioned within the onion phantom were evaluated. These surrogates can be assumed as lower and upper limit of X-ray attenuation for various bone tissues occurring in humans and thus serve as reliable estimator of beam hardening effects in clinical CT scans. With increasing phantom diameter, the CT numbers of both bone substitutes decrease continuously for CT images reconstructed using Q30 (Fig. 5.5). Between the largest (400 mm) and smallest (50 mm) phantom diameter, the CT numbers of cortical bone and trabecular bone vary by more than 300 HU and roughly 100 HU, respectively.

Size-dependent CT numbers derived from images reconstructed with Q34 show a completely different behaviour. CT numbers slightly increase for phantom diameters smaller than 200 mm. This is caused by an overcompensation of beam hardening, because the integrated BHC is calibrated under certain conditions assuming a minimal WET of the object. For diameters up to 300 mm, the maximal CT number difference is mostly within 40 HU. Consequently, the bone BHC clearly reduces beam hardening effects, but still there is a remaining variation, which would be removed by an optimal correction.

The severe decrease of CT numbers for a phantom diameter of 400 mm, especially in 80 kVp CT scans, is only partly induced by beam hardening. Photon scattering, which is

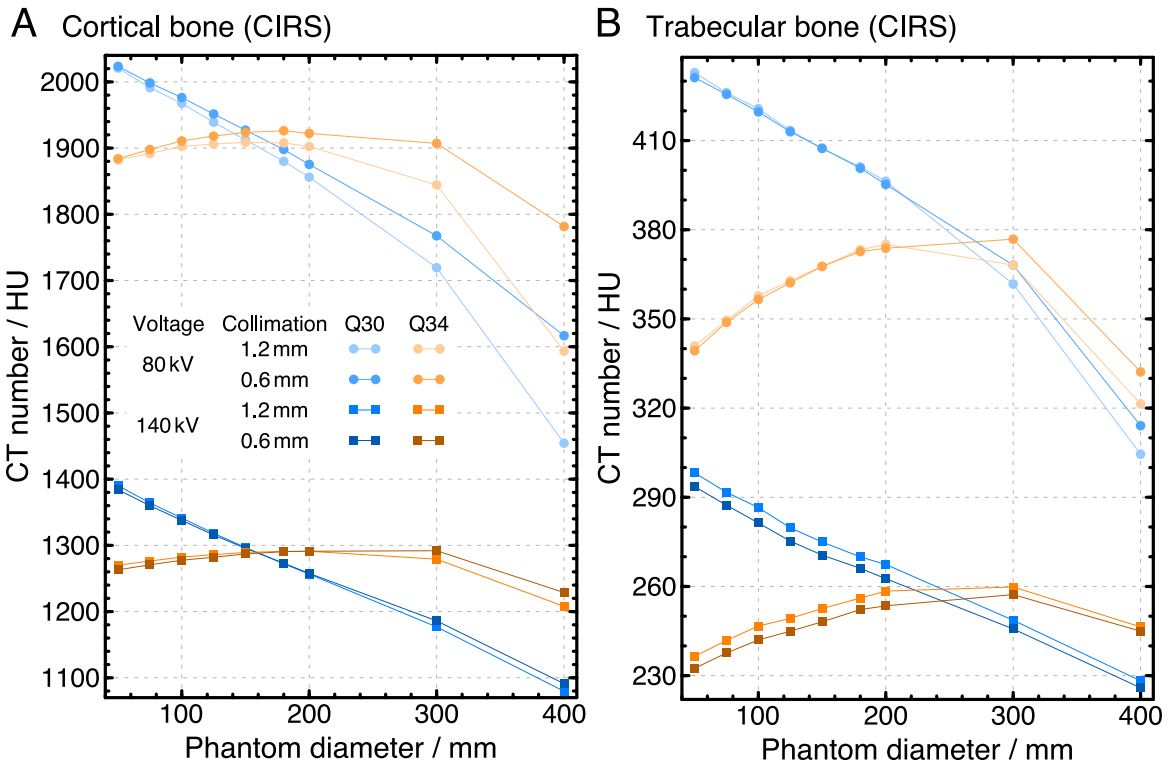

Figure 5.5: CT number of a cylindrical high-density (A) and low-density bone substitute with a diameter of 25 mm (B) for an 80 kVp and 140 kVp CT scan depending on the outer diameter of the acrylic onion phantom, selected BHC algorithm included in the investigated reconstruction kernels and slice collimation.

more pronounced in low-energy CT scans and increases with phantom size, can affect CT numbers in a similar manner. If both effects are of comparable magnitude (e.g. in large scan objects), the BHC algorithm cannot perform properly. This influence can be reduced using a smaller slice collimation, e.g. 0.6 mm instead of 1.2 mm (Fig. 5.5), but it still hampers the performance and finally the accuracy of the BHC algorithm.

Metal Artefact Reduction

Patients with severe artefacts caused by metal implants are currently not treated with protons, because an appropriate dose calculation cannot be ensured. The application of commercial algorithms for metal artefact reduction can clearly increase the visibility of anatomical structures (Fig. 2.5), leading to an overall better visual impression as confirmed by experienced clinicians and medical physicists (Negwer, 2016). However, treatment planning also requires reliable quantitative CT numbers close to metallic implants, especially in

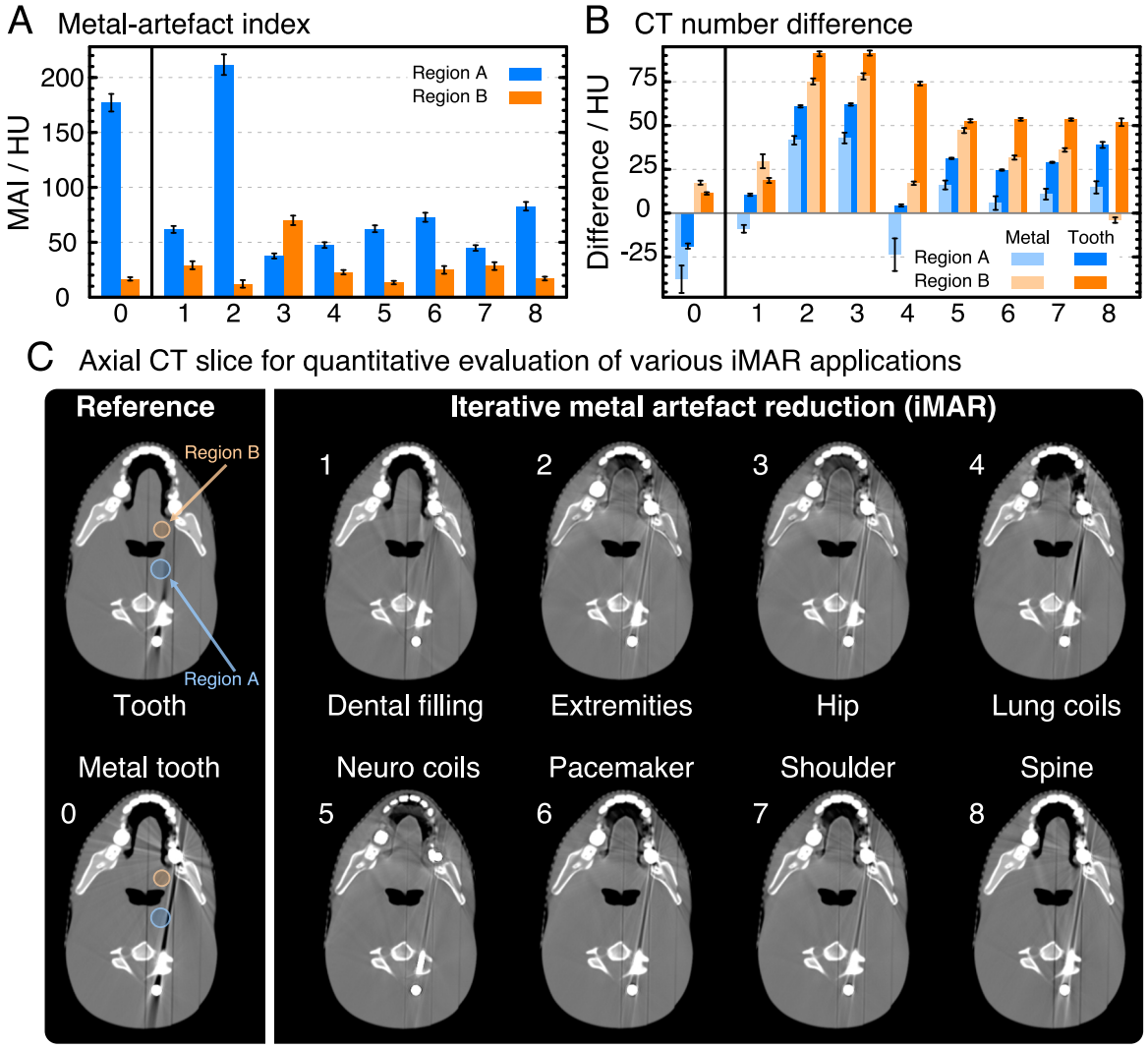

Figure 5.6: Influence of metal artefacts on CT image quality. Quantitative evaluation of 120 kVp CT datasets of an anthropomorphic head phantom reconstructed without (0) and with various iMAR applications (1-8) as illustrated in alphabetical order. A CT scan with a tissue-equivalent molar tooth instead of a tungsten-filled one was used as reference setting. The metal-artefact index (A) and CT number difference (B) were quantified for two regions (C) of an axial CT slice consisting of soft tissue grey. The reference CT number of 30 HU was determined in another axial CT slice not affected by metal artefacts.

proton therapy. To assess the accuracy of CT numbers in a typical scenario, e.g. a head-and-neck tumour patient with tooth implant, CT scans of an anthropomorphic head phantom (Fig. 5.2) with a replaceable tungsten-filled or a tissue-equivalent tooth were analysed. Depending on the evaluated region and applied iMAR algorithm, metal artefacts can be reduced or even further increased (Fig. 5.6). The iMAR application optimised for dental fillings improves the image quality in general, but also introduces new artefacts in region B.

Other algorithms clearly overestimate CT numbers in the oral cavity or remove parts of the tongue, even in the CT dataset without tooth implant. The application of iMAR does also not implicitly result in more reliable CT numbers within both evaluated regions. Consequently, case-specific improvements in visual impression and accuracy of CT numbers can be achieved using iMAR, but additional artefacts or even distortions in anatomy are introduced. A routine clinical application of iMAR might be beneficial for delineating the tumour region and healthy tissues, because an additional dataset with better visual impression can be provided. However, its geometrical reliability should always be confirmed by experienced clinicians or medical physicists. From the author's perspective, the application for proton treatment planning is currently not recommended.

5.1.4 Conclusion on Scan Protocol Optimisation for Radiotherapy

Based on various experimental studies performed within this thesis, clinical CT scan settings appropriate for proton therapy and applicable to all treatment sites can be defined. This requires an all-encompassing CT number stability, which can be achieved by predefining an X-ray spectrum, slice collimation and reconstruction kernel with integrated BHC for water and bone (e.g. D34/Q34) in the CT scan protocol. If CT scanners do not support such reconstruction kernels, the influence of beam hardening on CT numbers has to be considered by selecting several CT scan protocols for different body regions and adapting the calibration of the respective CT-number-to-SPR conversion used (HLUT or DECT-based DirectSPR approach). However, this manual selection will not reduce the uncertainty in body regions with severe size variability (e.g. in head-and-neck tumour patients), because beam hardening conditions can substantially differ within a single CT acquisition (e.g. the small size of the patient head vs. the large extent of a shoulder).
Since the accuracy of dose calculation can be affected by image noise, an iterative reconstruction (e.g. SAFIRE) with maximal noise suppression is recommended for treatment planning. Moreover, this allows for a reduction in CT dose (about 60%) without hampering image quality compared with FBP.
Commercially available algorithms for metal artefact reduction (e.g. iMAR) can be used to generate additional CT datasets with improved visual impression for delineation purposes. However, these CT datasets are currently not sufficient for the high demands of proton treatment planning.

5.2 Characterisation of Pseudo-Monoenergetic CT Calculation

As an alternative to treatment planning on SECT scans, dose calculation can be performed on DECT-derived MonoCT datasets. Its optimal energy E_{mono} with regard to image quality and beam hardening was assessed for two applications syngo.Mono and syngo.MonoPlus (section 2.3.1) as described in the following and published by Wohlfahrt et al. (2017b).

5.2.1 Data Acquisition

CT scans of 17 cylindrical materials (10 Gammex tissue surrogates, 6 polymers and aluminium) with a diameter of 25 mm positioned in three scan setups (Fig. 5.1, A and B) were acquired in single- and dual-energy mode with identical CT dose and scan settings optimised for radiotherapy (Table 5.1). In addition to the experimentally determined CT number H_i and corresponding standard deviation σ_i of each material sample i, CT numbers of 71 human tissues (section 5.1.1) were calculated with an in-house optimised scanner-specific stoichiometric CT number prediction (Supplement B), which was calibrated using the elemental composition and measured CT numbers of the tissue substitutes.

5.2.2 Evaluation of Image Quality

For all MonoCT energies, the DECT image post-processing software syngo.Mono shows an $\text{INR}_{\text{SECT}} < 1$ with a maximum at 70 k*e*V (Fig. 5.7). Consequently, syngo.Mono leads to an overall increased image noise independent from the respective energy in comparison with 120 kVp SECT scans of identical CT dose. Owing to the additional multi-band filtering

Table 5.1: Single-energy and dual-energy CT scan protocol with clinical parameters optimised for radiotherapeutic application.

CT scan modus	CT scan parameter				
	Tube voltage	Current-time product	$\text{CTDIvol}_{32\,\text{cm}}$	Slice collimation	Reconstruction kernel
	kV	mAs	mGy	mm	
SECT	120	258	20.8	1.2	D34
DECT	80	400	9.6		
	140	95	11.1		

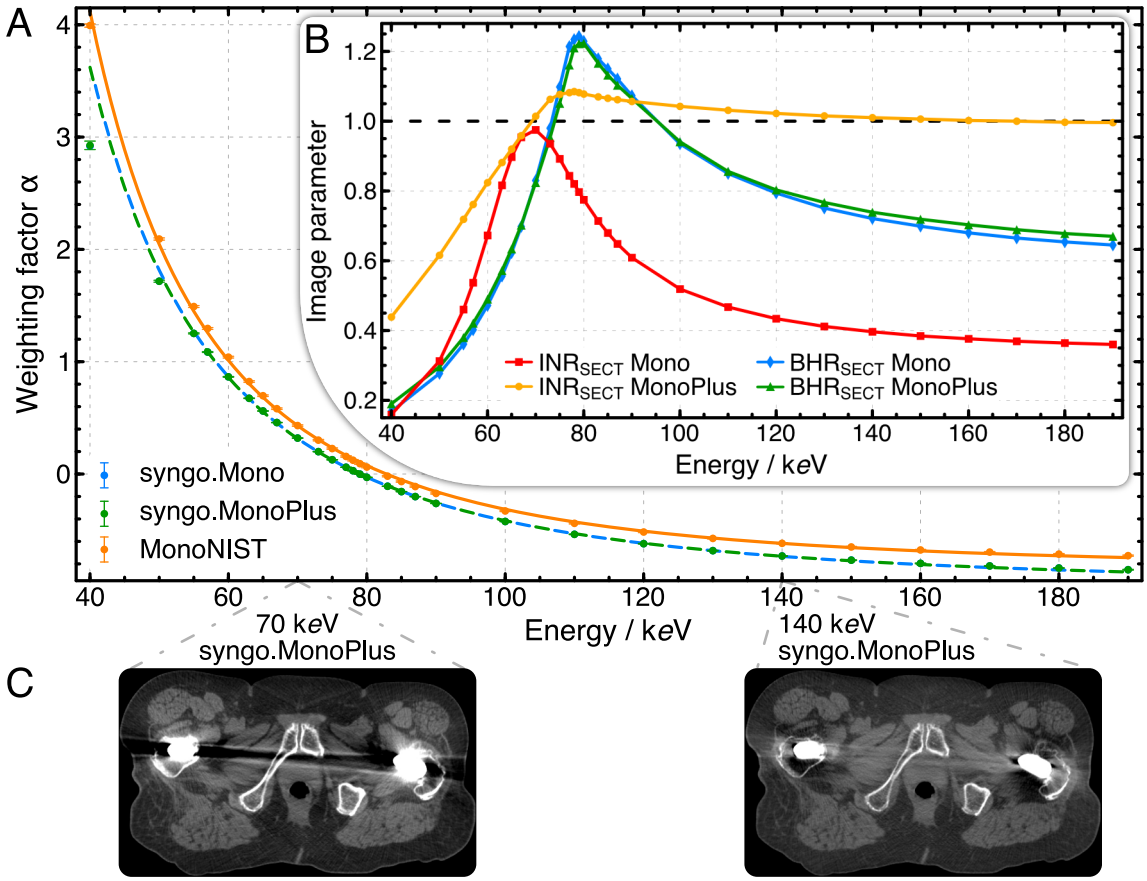

Figure 5.7: (A) Energy-dependent weighting factor α for MonoCT calculation using syngo.Mono, syngo.MonoPlus and the XCom Database of NIST (Berger et al., 1990) referred to as MonoNIST. The respective standard deviation is illustrated as error bar. (B) Image-noise ratio (INR_{SECT}) and beam-hardening ratio (BHR_{SECT}) as well as (C) metal artefact reduction for a patient with hip implants depending on MonoCT energy. DECT scans of 80/140 kVp were acquired at the CT scanner Definition AS and reconstructed with D34. Adapted from Wohlfahrt et al. (2017b).

in syngo.MonoPlus, image noise can be clearly reduced in comparison with syngo.Mono (Fig 5.7). Especially for low and high energies, syngo.MonoPlus leads to a raised INR_{SECT} in comparison with syngo.Mono by up to 25% and 60%, respectively. For energies above 70 keV, syngo.MonoPlus provides MonoCT datasets with an image noise comparable to that of 120 kVp SECT scans. In the energy region from 75 keV to 80 keV, the INR_{SECT} can even be increased by 10%.

The use of an iterative reconstruction algorithm (e.g. SAFIRE) instead of a FBP also leads to an energy-dependent noise reduction in MonoCT datasets (Fig. 5.8). The image noise (except for 40 keV) decreases with increasing SAFIRE strength and reaches an INR_{FBP} of almost 2 at roughly 70 keV. Hence, image noise can be halved at best relative to FBP.

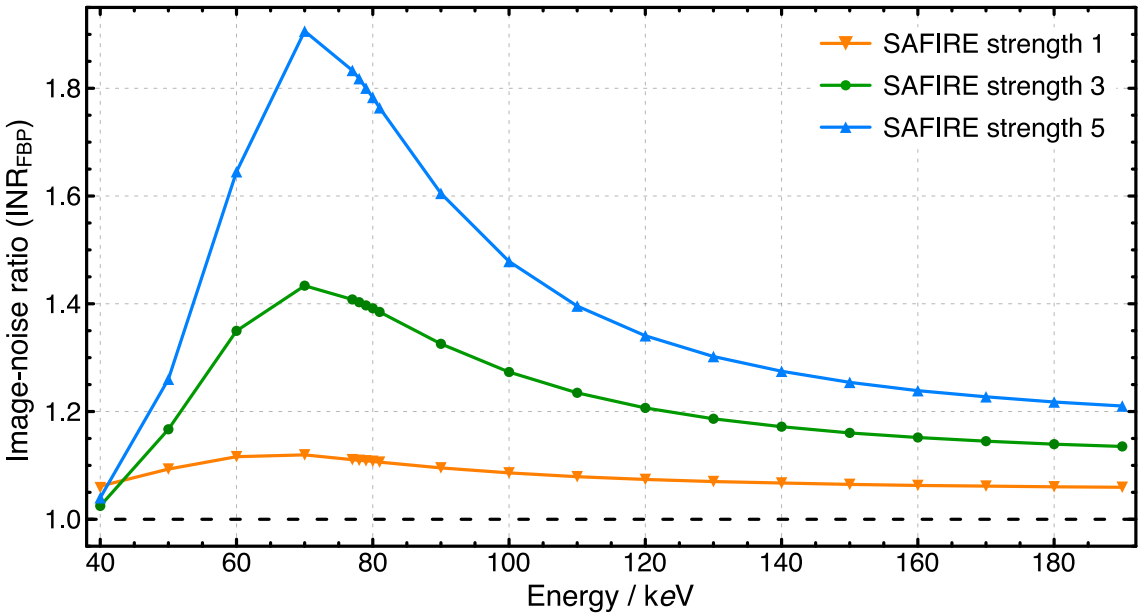

Figure 5.8: Energy-dependent INR_{FBP} for MonoCT datasets using SAFIRE of different strengths instead of the FBP (as reference) for image reconstruction. MonoCT calculation was performed using syngo.MonoPlus. The 80/140 kVp DECT scans of the water setup were acquired with a $CTDIvol_{32\,cm}$ of 28 mGy and reconstructed with D34 and Q34, respectively. Adapted from Negwer (2016).

Both image post-processing applications syngo.Mono and syngo.MonoPlus reveal a similar energy-dependent BHR_{SECT} (Fig. 5.7). For MonoCT energies between 75 k*e*V and 95 k*e*V, an improved CT number stability concerning three different beam hardening conditions is achieved in comparison with 120 kVp SECT. The maximal BHR_{SECT} is reached at 79 k*e*V. Compared to SECT, this leads to a reduced influence of beam hardening on CT numbers by 23% on average including all investigated tissue surrogates and up to 69% for bone substitutes only. Hence, an increased CT number stability corresponds to a reduction of proton range variations. Considering CT numbers of all tabulated human tissues (excluding lung) in the three scan setups and the respective HLUT (Fig. 5.4.1) to convert each CT number in SPR, range deviations induced by beam hardening can be decreased on average from 1.0 mm to 0.8 mm and maximal from 2.7 mm to 2.2 mm for 150 mm tissue penetration.

5.2.3 Determination of the Weighting Factor

Pseudo-monoenergetic CT datasets can be obtained by a linear superposition of DECT scans according to eq. 2.6. For this purpose, the XCom Photon Cross Section Database of NIST (Berger et al., 1990) serves as reference for monoenergetic X-ray attenuation. To

calibrate the CT scanner Definition AS for DECT-based calculation of MonoCT datasets, the energy-dependent weighting factor $\alpha\left(E_{\text{mono}}\right)$ was computed by minimising the mean square error (MSE):

$$\text{MSE} = \sum_{s\in\mathcal{S}}\sum_{i=1}^{88}\left\{H_{\text{r},s,i}(E_{\text{mono}}) - \left[\alpha\left(E_{\text{mono}}\right)H_{80,s,i} + \left[1-\alpha\left(E_{\text{mono}}\right)\right]H_{140,s,i}\right]\right\}^2 \tag{5.4}$$

including all 17 scanned material samples and 71 tabulated human tissues. For each scan setup, the monoenergetic CT number, $H_{\text{r},s,i}(E_{\text{mono}})$, as well as the corresponding 80 kVp, $H_{80,s,i}$, and 140 kVp CT numbers, $H_{140,s,i}$, were determined for each material as illustrated in Fig. C.1 of Supplement C.

The energy dependence of the weighting factor $\alpha\left(E_{\text{mono}}\right)$ for syngo.Mono, syngo.MonoPlus and CT numbers derived from the XCom Photon Cross Section Database of NIST (Berger et al., 1990) can be described with a power-law function (Fig. 5.7, Table C.1 of Supplement C). Both clinically available image post-processing applications syngo.Mono and syngo.MonoPlus use the same energy-dependent weighting factor. Given that the weighting factor is nearly 0 for MonoCT datasets of 79 k*e*V, these datasets are comparable with those of 140 kVp SECT in image noise and beam hardening. Hence, the maximal INR_{SECT} and BHR_{SECT} reached for 79 k*e*V MonoCT datasets can also be obtained by an increase in tube voltage from 120 kVp to 140 kVp using SECT.

Pseudo-monoenergetic CT numbers calculated by syngo.Mono and syngo.MonoPlus differ from monoenergetic CT numbers derived from NIST (MonoNIST), which may be caused by the vendor-specific calibration of syngo.Mono and syngo.MonoPlus. For example, 120 k*e*V pseudo-monoenergetic CT numbers correspond to 140 k*e*V monoenergetic CT numbers, because $\alpha =$ -0.62 is used for MonoCT calculations in syngo.Mono and syngo.MonoPlus instead of $\alpha =$ -0.52 for MonoNIST. A 79 k*e*V MonoCT dataset derived from syngo.Mono and syngo.MonoPlus is equivalent to monoenergetic X-rays of approximately 82 k*e*V.

The evaluation of all investigated materials and scan setups reveals negligible error bars of $\alpha\left(E_{\text{mono}}\right)$ as shown in Fig. 5.7. This indicates a sufficiently precise calculation of monoenergetic CT numbers. Even MonoCT datasets below the mean energy of the 80 kVp CT scan ($\alpha > 1$) and beyond the mean energy of the 140 kVp CT scan ($\alpha < 0$) can be accurately determined by compensating the different impact of X-ray interactions (incoherent scattering vs. photoelectric effect) as also discussed by Möhler et al. (2018b).

5.2.4 Conclusion on Monoenergetic Imaging

After optimising SECT and DECT for radiotherapy applications concerning image noise and beam hardening it was demonstrated that DECT-based MonoCT datasets can contribute to improve image quality (i.e. increased INR and BHR) in comparison with 120 kVp SECT. A 79 k*e*V MonoCT dataset is particularly suitable for treatment planning because beam hardening is less pronounced (BHR maximum) and image noise is most reduced for syngo.MonoPlus (INR maximum). Owing to an efficient noise reduction included within the syngo.MonoPlus application, the image quality of MonoCT datasets is considerably enhanced compared with syngo.Mono. Consequently, clinical calculations of MonoCT datasets should be performed with syngo.MonoPlus.
Various MonoCT datasets of different energy can be derived from a patient's DECT scan, offering clinicians more possibilities for delineating – e.g. a low-energy MonoCT dataset for better contrast-to-noise ratio and a high-energy MonoCT dataset for metal artefact reduction (Mangold et al., 2014; Kuchenbecker et al., 2015), as exemplarily shown in Fig. 5.7 C. Whether these additional options can lead to a reduction of delineation uncertainties still has to be shown in clinical studies. So far, studies have mostly focused only on improving image contrast and noise (Grant et al., 2014; Wichmann et al., 2014; Forghani et al., 2015; Husarik et al., 2015; Kaup et al., 2016).

5.3 Determination of Proton Stopping Power

The stopping power of a material depends on its elemental composition and can be calculated or determined by relative range measurements. The different methods applied within this thesis are described in the following.

5.3.1 Stopping-Power Calculation

The material-specific SPR can be calculated based on the elemental composition according to the Bethe formula (eq. 3.3). The required electron density ϱ_e follows from

$$\varrho_\mathrm{e} = \varrho \sum_i \omega_i \frac{Z_i}{A_i} \tag{5.5}$$

with the mass density of the compound ϱ as well as the element-specific mass fraction ω_i, atomic number Z_i and mass number A_i. The mean excitation energy I of the respective compound was calculated using element-specific mean excitation energies I_i (Seltzer and Berger, 1982) and Bragg's additivity rule (Bragg and Kleeman, 1905).

$$\ln I = \frac{\sum\limits_i \omega_i \frac{Z_i}{A_i} \ln I_i}{\sum\limits_i \omega_i \frac{Z_i}{A_i}} \tag{5.6}$$

The calculated SPRs of all investigated tissue substitutes are summarised in Table A.1 of Supplement A.

5.3.2 Relative Proton Range Measurements

Relative range measurements in water provide information about the material-specific stopping power. Inserting a plane-parallel material slab of well-defined thickness within the proton beam shifts the depth-dose distribution to smaller penetration depths. This range shift divided by the slab thickness results in the material-specific SPR (Jäkel et al., 2001). To increase the SPR accuracy and ensure an independent verification, the SPR of each investigated material was measured by different methods, which are briefly described in the following. All determined SPRs are collected in Table A.1 of Supplement A.

Water Phantom

The depth-dose distribution of proton pencil beams with an initial energy of 125 M*e*V and 160 M*e*V was detected by a movable Bragg-peak ionisation chamber (TM34070-2,5, PTW, Freiburg, Germany) in a water-filled phantom (Blue Phantom, IBA Dosimetry, Schwarzenbruck, Germany). These range measurements were performed in the clinical treatment room of OncoRay using the proton therapy system Proteus 235 (Ion Beam Applications, Louvain-la-Neuve, Belgium) equipped with a cyclotron providing proton beams with an energy up to 226.7 M*e*V, a universal nozzle and a rotating gantry covering an angle of 360°.

Water Absorber of Variable Thickness

A water absorber of variable thickness (PEAKFINDER Water Column, PTW) can also be used to record depth-dose curves. It consists of a dual-channel electrometer (TANDEM,

PTW) and two Bragg-peak ionisation chambers in a closed water column for beam monitoring and field measurements, respectively. Relative range measurements with an accuracy of < 0.1 mm were performed at the Heidelberg Ion-Beam Therapy Centre (HIT, Heidelberg, Germany) using a horizontal proton pencil beam with an initial energy of 150 M*e*V.

Multi-Layer Ionisation Chamber

Proton depth-dose curves can also be acquired by a multi-layer ionisation chamber (MLIC) consisting of a stack of ionisation chambers. Within this thesis, a Giraffe MLIC (IBA Dosimetry) was used, which is composed of 180 Stingray ionisation chambers with a diameter of 120 mm and nominal distance of 2 mm.
Since the proton beam is not directly measured in water, the WET of the built-in ionisation chambers needs to be determined. The MLIC calibration was performed in the clinical treatment room of OncoRay as described by Wohlfahrt et al. (2018a) using depth-dose distributions of isocentric proton pencil beams with nominal energies ranging from 100 M*e*V to 225 M*e*V in steps of 5 M*e*V, which were measured by the MLIC and a movable Bragg-peak ionisation chamber in a water-filled phantom as reference. All depth-dose curves recorded for MLIC calibration were fitted with the analytical Bortfeld equation (Bortfeld, 1997). For each nominal energy and both measurement devices, the distal range of 80% of maximum dose R_{80} was determined and linearly correlated.

$$R_{80,\,\text{reference}}\,(E) = a_{\text{MLIC}} \cdot R_{80,\,\text{MLIC}}\,(E) + b_{\text{MLIC}}\,(E) \tag{5.7}$$

The slope a_{MLIC} corresponds to the WET of an ionisation chamber within the MLIC and the intercept b_{MLIC} describes an absolute range shift caused by interactions in air owing to an off-centre positioning of the MLIC. For the WET calibration, the MLIC was aligned 20 cm behind the isocentre, which leads to

$$a_{\text{MLIC}} = \left(1.867 \pm 1 \cdot 10^{-5}\right) \text{ mm / chamber} \quad \text{and} \quad b_{\text{MLIC}} = (-0.22 \pm 0.11) \text{ mm}. \tag{5.8}$$

Considering all measurement uncertainties caused by MLIC calibration, positioning and dose acquisition, an overall absolute range uncertainty of 0.25 mm can be achieved for an MLIC measurement. However, the overall uncertainty for relative range measurements (WET determination) is even smaller (< 0.1 mm).

The material-specific SPRs were determined in the experimental room of OncoRay using a horizontal proton pencil beam with an initial energy of 150 M*e*V and 200 M*e*V. The MLIC was aligned 47 cm behind the beam exit window.

5.4 Calibration of Stopping-Power Prediction Methods

After defining clinical CT scan protocols in single-energy and dual-energy mode with respect to image noise and beam hardening (Table 5.1), CT-based SPR prediction methods are calibrated for these scan settings optimised for radiotherapy. The current-time product and application of iterative reconstruction algorithms may differ for various body regions or different purposes of CT scans (treatment planning vs. anatomical control during the course of treatment), but these changes do not affect the calibration presented in the following.

5.4.1 Heuristic CT-Number-to-SPR Conversion

For HLUT specification as described by Wohlfahrt et al. (2017b), the Hounsfield scale was divided into three parts representing different tissue types: low-density ($H <$ -150 HU), soft (-150 HU $\leq H \leq$ 150 HU) and bone tissues ($H >$ 150 HU). Each CT number segment was described by a linear function using only Gammex tissue substitutes. To avoid steps between adjacent linear functions, the intersection was set as transition point.
The HLUTs defined for 120 kVp SECT (mean energy of 64 k*e*V) and 79 k*e*V MonoCT datasets are shown in Fig. 5.9. Both HLUTs are quite similar for low-density materials and soft tissues ($H <$ 50 HU) owing to their major dependence on electron density. HLUT differences in the bone region ($H >$ 200 HU) are induced by the strong energy dependence of X-ray attenuation for materials with a higher effective atomic number than water. This implies a steeper slope with increasing X-ray energy, which is associated with a more sensitive response on CT number changes. For 79 k*e*V MonoCT datasets, SPR deviations of tabulated human tissues from the HLUT are slightly reduced from a root mean square error (RMSE) of 1.5% to 1.2% compared with 120 kVp SECT scans, suggesting slightly fewer differences between tissue substitutes (used for calibration) and the tabulated human tissues. Materials differing from tissue compositions, such as polymers or metals, can significantly deviate from the calibration curve and are therefore in general not appropriately covered by any heuristic CT-number-to-SPR conversion.

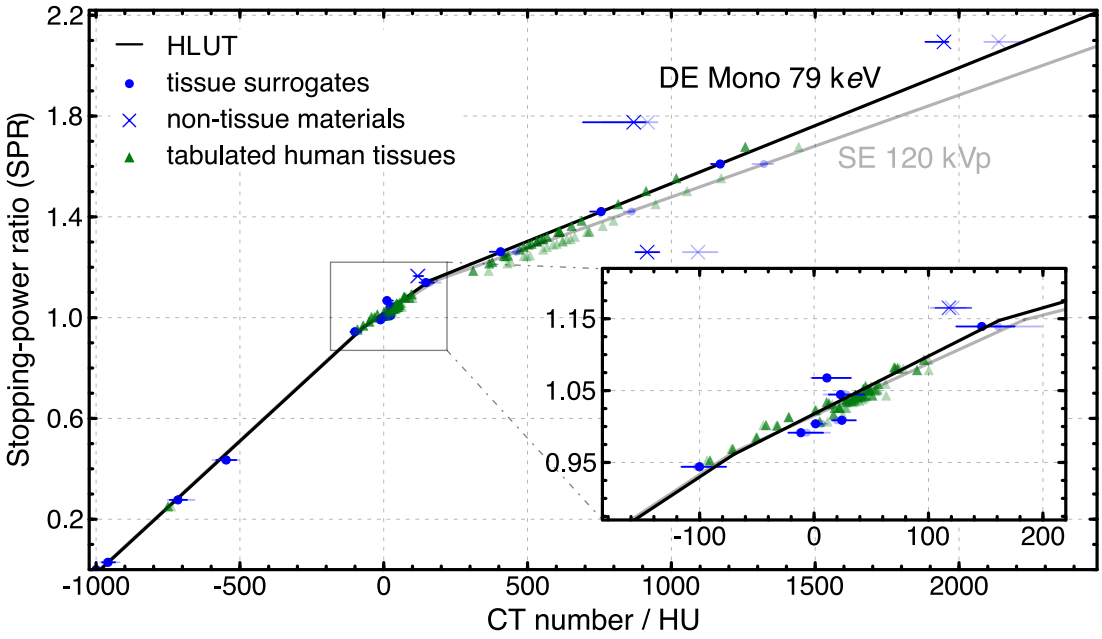

Figure 5.9: Heuristic CT-number-to-SPR conversion (HLUT) for proton treatment planning based on a 79 k*e*V MonoCT dataset derived from syngo.MonoPlus using 80/140 kVp DECT scans (non-transparent) and 120 kVp SECT scan with a mean energy of 64 k*e*V (semi-transparent). CT scans were acquired at the CT scanner Definition AS and reconstructed with the D34 kernel. CT numbers were obtained for cylindrical material samples with a diameter of 10 mm positioned within the water setup. The error bars illustrate the CT numbers derived from the air and pelvis setup. The material-specific SPRs were determined for 125 M*e*V protons. Adapted from Wohlfahrt et al. (2017b).

5.4.2 Direct Stopping-Power Prediction

Within this thesis, two approaches for direct stopping-power prediction from dual-energy CT (DirectSPR) were thoroughly investigated (sections 4.2.2 and 4.2.3). Both SPR prediction methods rely on an image-based extraction of tissue-specific material parameters for each CT voxel.

The electron density as dominating physical quantity is directly derived from DECT using a linear superposition of both single DECT scans. The second material parameter for solving the Bethe equation (eq. 3.3), e.g. the I-value or stopping number, is approximated based on the effective atomic number or X-ray attenuation cross section. These DirectSPR methods still contain an empirical component, but the influence on CT-based SPR prediction is clearly reduced compared with HLUT approaches (Wohlfahrt et al., 2017b; Möhler et al., 2018a). The following sections describe the results of the calibrations performed for the respective approach as published by Wohlfahrt et al. (2018a).

Electron Density

For voxelwise RED computation using 80/140 kVp DECT with scan parameters optimised for radiotherapy, an appropriate weighting factor α_ϱ as introduced in eq. 2.7 needs to be determined. The calibration was performed as described in section 5.2.3. Reference electron densities were calculated based on the elemental composition of the investigated materials according to eq. 5.5.
This evaluation yields an optimal weighting factor α_ϱ of -0.819 $\pm$ 0.003, which equals the weighting factor of 170 k*e*V MonoCT datasets derived from syngo.MonoPlus (Fig. 5.7). To benefit from the sophisticated noise suppression algorithm applied in syngo.MonoPlus, the 170 k*e*V MonoCT dataset has been selected for DECT-based RED determination instead of simply calculating the weighted sum of the two single DECT scans.

Effective Atomic Number for RhoZ Approach

The material-specific effective atomic number (EAN) in each CT voxel was obtained from syngo.RhoZ using an 80/140 kVp DECT scan. To predict the I-value based on EAN, a calibration curve was specified for soft tissues and bones, respectively (Fig. 5.10). For each CT voxel with RED $>$ 0.5 (minimal selectable value in syngo.RhoZ), the Bethe equation (eq. 3.3) is solved for a specific proton energy by inserting the obtained RED and I-value. To prevent instabilities in EAN determination for RED $\leq$ 0.5 (division by small RED), the RED of the respective CT voxel is directly used as SPR. This assumption is justified in this case, because lung tissue is almost water-equivalent and differs particularly in density.

X-Ray Cross Section for RhoSigma Approach

The material-specific relative photon attenuation cross section (RCS) was computed for X-rays of 82 k*e*V. Since the 79 k*e*V MonoCT dataset derived from 80/140 kVp DECT using syngo.MonoPlus corresponds to an X-ray energy of 82 k*e*V, this dataset was divided by the RED dataset to obtain the RCS dataset. Based on the RCS of each CT voxel, the relative stopping number (RSN) is determined by a calibration curve consisting of multiple line segments (Fig. 5.10). Finally, the RED and RSN datasets are multiplied for SPR prediction according to eq. 3.3. To guarantee robustness and stability of the RhoSigma approach (similar reason as for RhoZ), RSN is set to 1 for each CT voxel with RED $<$ 0.3.

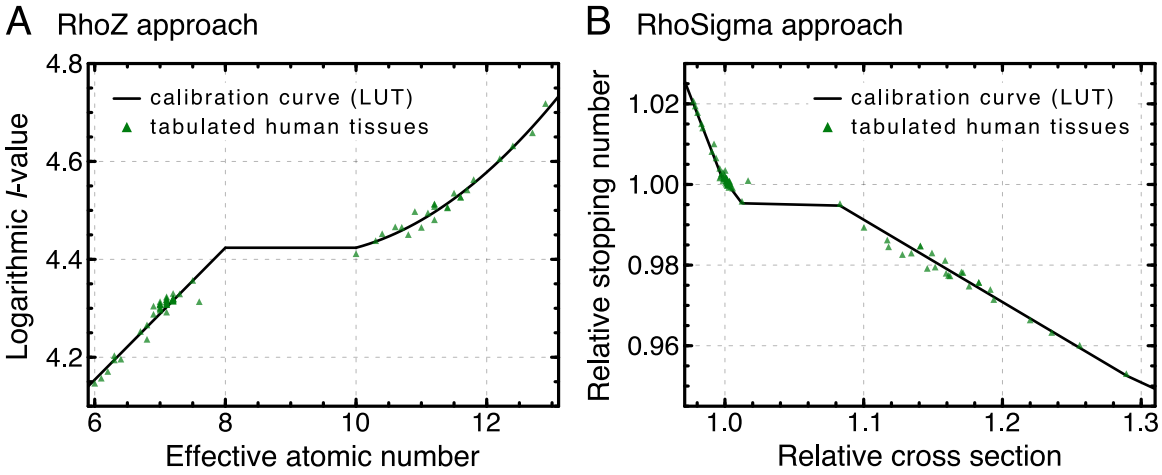

Figure 5.10: (A) Conversion from effective atomic number to logarithmic I-value used in the RhoZ approach. The calibration curve is composed of a linear (quadratic) fit to the human soft (bone) tissues respectively, joined by a straight line between the intermediate effective atomic numbers 8 and 10. (B) Conversion from relative monoenergetic cross section for 82 k*e*V X-rays to relative stopping number for 200 M*e*V protons used in the RhoSigma approach. The cross sections were calculated based on elemental composition and elemental cross sections from the NIST database. The calibration curve is designed analogously to a HLUT consisting of multiple line segments representing different tissue types such as adipose, soft and bone tissue (here: from left to right). Adapted from Wohlfahrt et al. (2018a).

6 Experimental Verification of Stopping-Power Prediction

After a comprehensive evaluation of CT scan and reconstruction parameters resulting in a CT scan protocol optimised for radiotherapy and the calibration of the respective SPR prediction approach, the accuracy and precision of each method needs to be quantified. Since range verification in patients with a clinically appropriate accuracy of 1 mm to 2 mm is currently highly challenging, a direct verification of the accuracy of CT-based SPR prediction in patients is not feasible. Hence, a stepwise indirect verification scheme (Fig. 6.1)

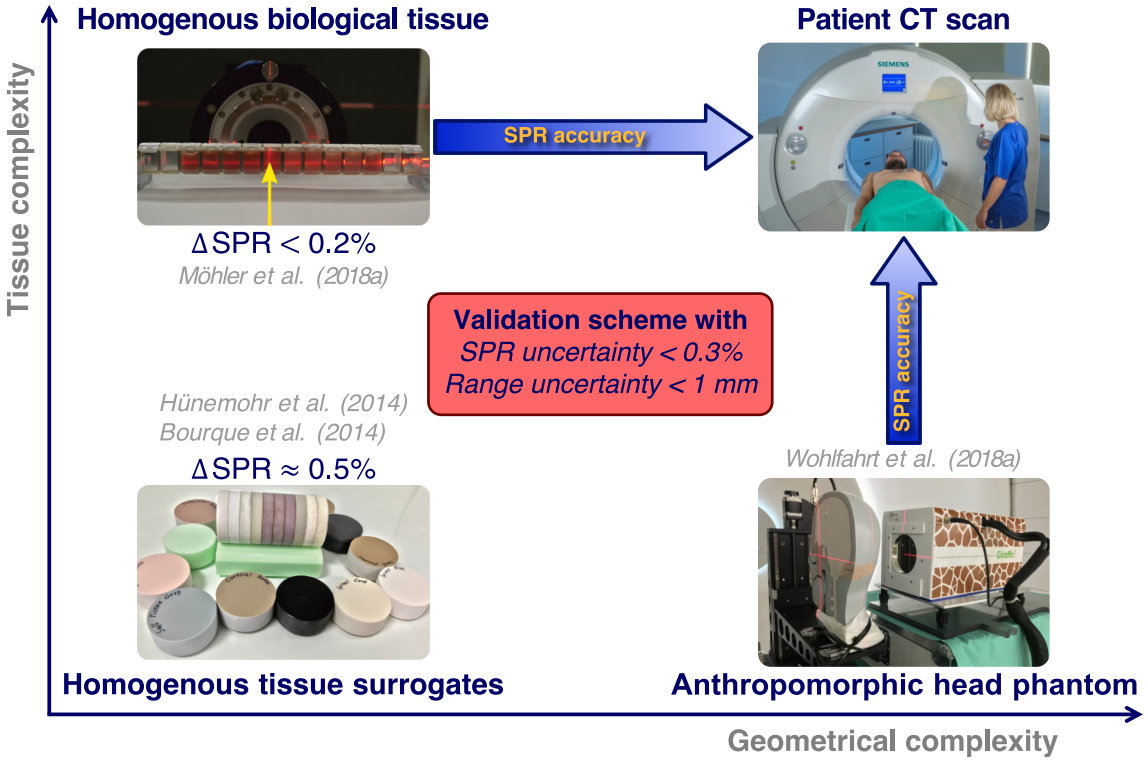

Figure 6.1: Experimental validation scheme to assess the accuracy of different CT-based SPR prediction approaches by separating the two complexity levels arising in humans, i.e. tissue composition and geometrical inhomogeneities. The red box states the achieved measurement uncertainty.

is proposed within this thesis separating the two complexity levels arising in humans: tissue composition and geometrical inhomogeneities. The validation results obtained in a ground-truth anthropomorphic head phantom (section 6.1) and homogeneous biological tissue samples (Möhler et al., 2018a) can then be translated to patient CT scans. Although a minor uncertainty still remains in this chain of evidence, an accuracy of 1 mm or even less could be achieved for the respective validation method in each single study.

6.1 Anthropomorphic Head Phantom

To assess the accuracy of four different SPR prediction approaches (section 5.4) based on SECT (clinical HLUT) and DECT (79 k*e*V MonoCT dataset with clinical HLUT, RhoSigma and RhoZ) in a realistic clinical scenario, an anthropomorphic head phantom with known SPR in each voxel was investigated (Fig. 5.2). The results of this evaluation were published in Wohlfahrt et al. (2018a) and are presented in the following.

6.1.1 Reference Stopping-Power Map

A geometrically appropriate reference SPR dataset of the head phantom is required for evaluating the accuracy of CT-based SPR prediction approaches. The elemental composition of each built-in tissue surrogate is provided by the vendor. However, a 3D reference SPR map still needs to be defined using measured material-specific SPRs and independently validated to ensure a ground truth of high spatial and quantitative precision.

Generation of Reference Dataset

For each tissue surrogate within the head phantom, relative range measurements were performed to determine the material-specific SPR using separate homogeneous slabs with a nominal thickness of 20 mm (section 5.3.2). The maximal measurement uncertainty was dominated by the uncertainty of the slab thickness and experimentally determined as 0.3% related to the SPR of water, combining the results of two individual measurements using different devices (Peakfinder Water Column, Giraffe MLIC).

To produce the 3D reference SPR map, a high-resolution sequential CT scan (0.5 mm isotropic spacing, X-ray spectrum of 150 kVp with additional tin filter, reconstruction kernel Hr69h using ADMIRE of maximal strength, $\mathrm{CTDIvol}_{16\,\mathrm{cm}}$ of 37.8 mGy) of the head phantom

was acquired using a dual-source CT scanner Force. A median CT dataset of five subsequent CT scans was created to preserve material transitions and decrease image noise resulting from less-smoothing but highly spatially resolved image reconstruction. Each material was then manually delineated on axial CT slices with a remaining uncertainty of up to 2 voxels using the TPS RayStation 5.0. Finally, the segmented volumes of the different phantom materials were overridden with the experimentally determined SPRs (Fig. 5.2 B).

Validation Strategy of Reference Dataset

The geometrical accuracy of the reference SPR map is dominated by the delineation uncertainty, whereas the SPR uncertainty of each correctly assigned CT voxel is affected by the accuracy of the measured material-specific SPRs and their transferability to the head phantom. For validation, the cumulative effect on traversing pencil beams was independently evaluated by MLIC measurements for five distinct areas of the head phantom (Fig. 6.2). Since one side of this phantom is divided into three parts with a nominal thickness of 20 mm, range measurements could be performed in areas of different geometrical complexity using plane-parallel head phantom slabs or the other half of the phantom, referred to as “half-head” (Fig. 5.2 A). Depth-dose curves were acquired with the MLIC for 245 spot positions within fields of $(66\,\mathrm{mm})^2$, covering a regular grid with 3 mm spacing in the inner $(30\,\mathrm{mm})^2$ and 6 mm spacing outside.

The distal depth at 80% maximum dose was then compared with results of Monte Carlo transport simulations based on the SPR reference map. To this end, the segmented CT dataset for material assignment was used with the FLUKA multi-particle transport code, version 2011.2c.5 (PRECISIon defaults). In the Monte Carlo simulation, material properties for water were left unchanged from standard settings (especially $I = 75\,\mathrm{eV}$), whereas initial kinetic energy and momentum spread of the proton beam were adjusted to match measured depth-dose profiles in water with nominal energy of 150 M*e*V at OncoRay. The density and elemental composition of each phantom material was used in FLUKA as provided by the manufacturer (CIRS, Inc., Norfolk, USA). The corresponding I-values were adapted to match the material-specific SPRs experimentally determined in the homogeneous slabs. This was done in dedicated runs with simple slab geometry prior to the actual simulation of the MLIC experiments. Relative statistical fluctuation on range (distal depth at 80% maximum dose) was kept below one standard deviation of 0.1‰ in all cases, yielding

a maximum standard error of 0.02 mm on range differences derived from Monte Carlo simulations, well below all experimental uncertainties. Details on the Monte Carlo simulation are shown in Table D.1 of Supplement D.

Verification of Reference Dataset

For three fields (S1A, S1B, and S2A; Fig. 6.2) measured on plane-parallel head phantom slices (slice 1 and 2 / II and III; Fig. 5.2 A) without sinus cavity, the range differences between MLIC depth-dose measurements and Monte Carlo simulated depth-dose curves of all beam spots agree within a CT voxel size of $\pm$ 0.5 mm. This confirms the transferability of material-specific SPR to the head phantom and the accuracy of the ground-truth SPR map in general. For more-complex fields (S2B, containing sinus cavity and air; and HA, with a considerably larger thickness and curved surface) the distribution of range differences broadens. This is caused by the larger methodological uncertainty in the validation procedure itself (e.g. influence of range mixing) and a potentially higher delineation uncertainty

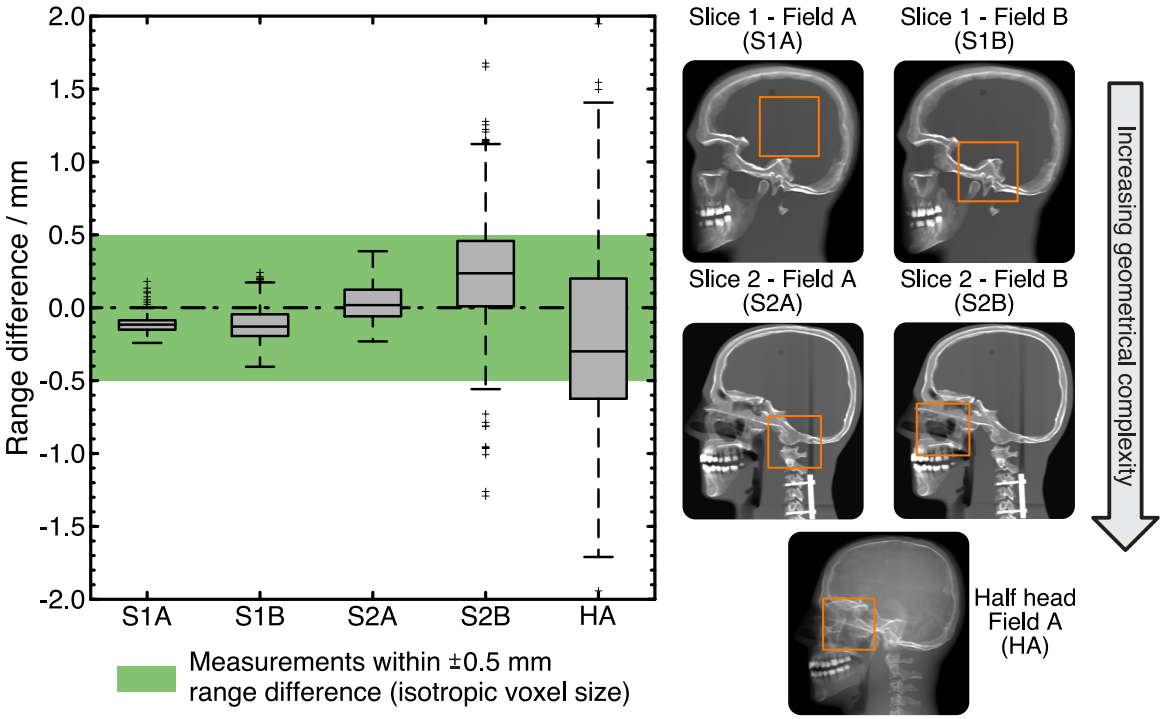

Figure 6.2: Independent validation of the reference SPR map using distal range differences at 80% of maximal dose between depth-dose measurements with a MLIC and Monte Carlo simulated depth-dose curves for five distinct areas illustrated in two-dimensional (2D) radiographs. Box plots are defined as illustrated in Fig. 6.3. Adapted from Wohlfahrt et al. (2018a).

at transitions toward sinus cavity and air. Still, the median range difference is smaller than ± 0.3 mm, and in the most complex scenario (HA), the range difference of 91% of the spots was within ± 1 mm, corresponding to the estimated maximum delineation uncertainty.
The reference map was thus validated for usage in the verification of SPR and proton range predictions with a conservative upper limit of 0.3% and 1 mm uncertainty, respectively, even in the most complex inhomogeneous case.

6.1.2 Assessment of Stopping-Power and Range Accuracy

For SPR prediction, 120 kVp SECT and 80/140 kVp DECT scans were acquired with clinical settings ($1 \times 1 \times 2\,\text{mm}^3$ spacing, reconstruction kernel Q34 using SAFIRE of maximal strength, $\text{CTDIvol}_{32\,\text{cm}}$ of 20.8 mGy) at a single-source CT scanner Definition AS.

Evaluation Procedure

The clinical SPR maps were first compared with the reference SPR map on a voxel level, evaluating each segmented material in the non-sliced side of the head phantom separately. To consider the delineation uncertainty, a 2D γ analysis (Low et al., 1998) with passing criteria of 1% or 2% SPR difference ($\Delta\hat{S}_{\text{crit}}$) and 1 mm distance to agreement (Δd_{crit}) in each case were performed for all axial CT slices of the full head as well as for each phantom material separately. Hence, the SPR at each voxel position within the reference dataset ($\mathbf{r}_{\text{r}}$) is compared with the SPR at the same and adjacent positions ($\mathbf{r}_{\text{comp}}$) in the SPR dataset derived from CT scans. The γ value at a specific position follows from

$$\gamma\left(\mathbf{r}_{\text{r}}\right) = \min\left\{\Gamma\left(\mathbf{r}_{\text{r}}, \mathbf{r}_{\text{comp}}\right)\right\} \forall \left\{\mathbf{r}_{\text{comp}}\right\} \tag{6.1}$$

with

$$\Gamma\left(\mathbf{r}_{\text{r}}, \mathbf{r}_{\text{comp}}\right) = \sqrt{\frac{\left[\mathbf{r}_{\text{r}} - \mathbf{r}_{\text{comp}}\right]^2}{\Delta d_{\text{crit}}^2} + \frac{\left[\hat{S}_{\text{r}}\left(\mathbf{r}_{\text{r}}\right) - \hat{S}_{\text{comp}}\left(\mathbf{r}_{\text{comp}}\right)\right]^2}{\Delta \hat{S}_{\text{crit}}^2}}. \tag{6.2}$$

If $\gamma \leq 1$, the CT voxel passes the criteria and otherwise it fails. The number of passed CT voxels divided by the total number of voxel within the investigated region yields the γ passing rate, which is a quantitative measure of accuracy.

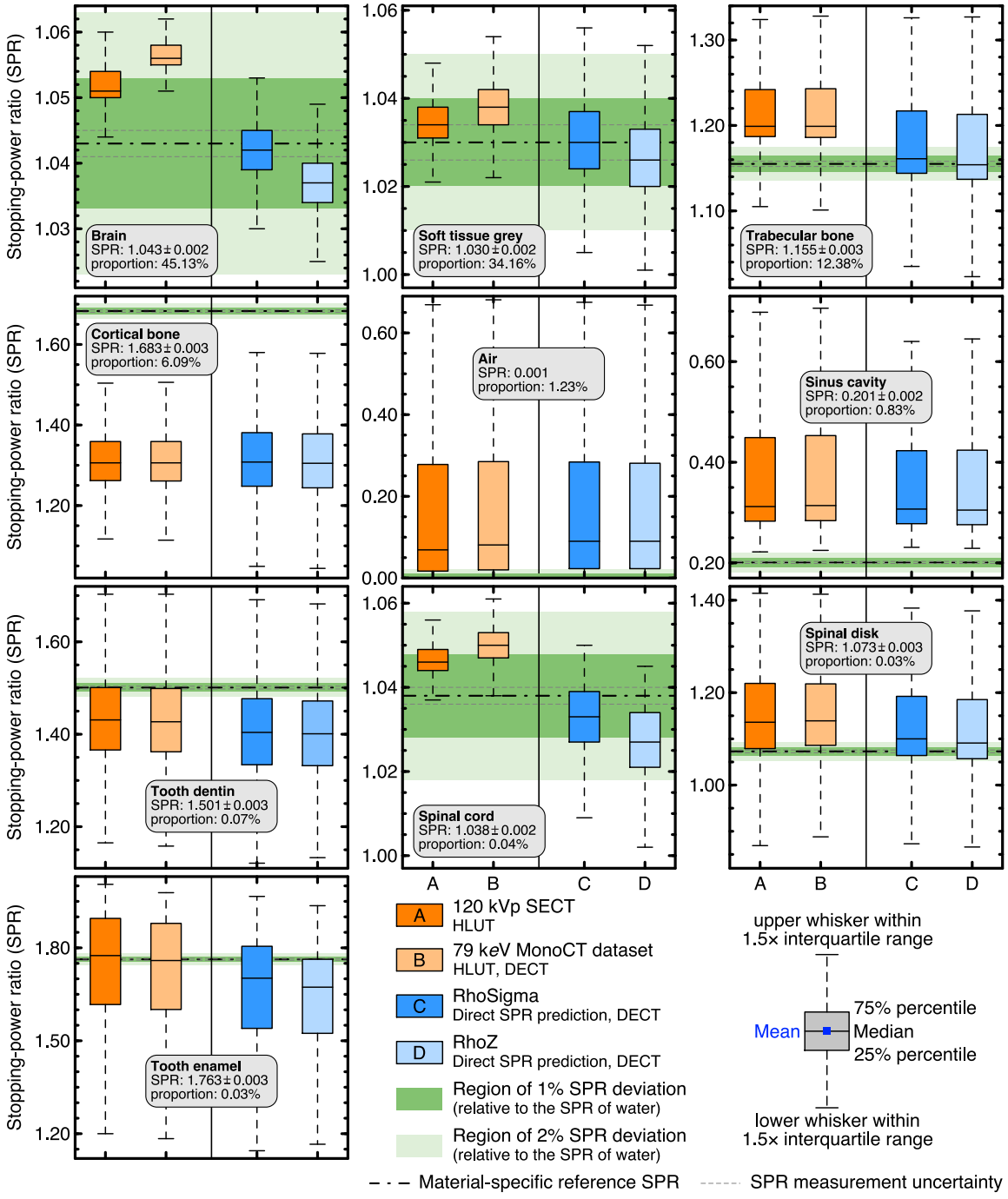

Figure 6.3: SPR distribution of each segmented material within the anthropomorphic head phantom for all investigated CT-based SPR prediction approaches. Adapted from Wohlfahrt et al. (2018a).

The phantom was divided into three regions in caudo-cranial direction (facial skull, skull base, and calvaria; Fig. 5.2) to evaluate heterogeneity-related effects on SPR accuracy. The facial skull is the most heterogeneous and the skull base the most homogeneous area.

To exemplarily quantify the accuracy of SPR prediction approaches on the level of proton range, a passively scattered proton treatment plan with two beams from 210° and 305° was computed with the TPS XiO using a $(1 \times 1 \times 1)\,\mathrm{mm}^3$ dose grid. The treatment plan was optimized on the reference SPR dataset and recalculated on each clinical SPR dataset. More than 400 line-dose profiles in beam direction were extracted using RayStation 5.0 and the distal range at 80% of prescribed dose was analysed to calculate range shifts.

Accuracy of SPR Prediction

As shown in Fig. 6.3, all investigated CT-based methods predict the SPR of the two most abundant materials, brain and soft tissue grey, with a median deviation to the reference below 1% (except for brain in the 79 k*e*V MonoCT dataset). The two DirectSPR approaches reveal smaller SPR deviations compared with both HLUT methods, and in general RhoSigma performs best. However, the DirectSPR approaches are more affected by image noise ($\approx$ 4 HU standard deviation), which is reflected in larger interquartile ranges.
For the third most frequent material, trabecular bone, a similar SPR accuracy is obtained for RhoSigma and RhoZ (median deviation $<$ 1%), in contrast to the HLUT approaches (median deviation $>$ 5%). Since trabecular bone is almost entirely surrounded by a thin layer of the high-density material cortical bone, all predicted SPR distributions are positively skewed owing to image smoothing at material transitions. This smoothing affects all SPR methods in a similar manner and is particularly pronounced in small-volume materials close to high-density gradients, resulting in either a systematic SPR underestimation for high-density materials, such as cortical bone, or overestimation for low-density materials, such as air and sinus cavity. The SPR distribution in these materials is not only skewed as in trabecular bone, where smoothing affects only the outer part of the volume, but the entire distribution is shifted.
In the tooth surrogates, the SPR underestimation due to the smoothing effect is partly compensated by an SPR overestimation, which is an inherent property of the investigated SPR prediction methods for materials containing an element with high atomic number (Möhler et al., 2017). The SPR predictions for spinal cord and spinal disk show similar results as for soft tissue grey and trabecular bone, respectively.
The DirectSPR approaches reveal considerably higher γ passing rates compared with the HLUT methods (Fig. 6.4, Table 6.1). For example, both DirectSPR methods, unlike the

HLUT approaches, can accurately predict SPR within 1% for most of trabecular bone (γ passing rates of approximately 60% vs. <10%; Table 6.1). In all regions, RhoSigma achieves the highest γ passing rates for the severest criterion $\gamma(1\,\text{mm}, 1\%)$. Applying the less-restrictive γ criterion of 2% SPR difference, RhoSigma and RhoZ show similar results, and both perform still considerably better than the HLUT approaches. The small γ passing rates of the 79 k*e*V MonoCT approach for the $\gamma(1\,\text{mm}, 1\%)$ criterion are mainly caused by

Table 6.1: Evaluation results of 2D γ analysis for each segmented material within the anthropomorphic head phantom and all investigated CT-based SPR prediction approaches. Adapted from Wohlfahrt et al. (2018a).

Material	Proportion full head %	(γ passing rate $\pm$ standard deviation) / % for $\gamma(1\,\text{mm}, 1\%)$ and $\gamma(1\,\text{mm}, 2\%)$			
		120 kVp SECT	79 k*e*V MonoCT	RhoSigma	RhoZ
Brain	43.44	73.4 ± 0.8 93.3 ± 0.6	14.4 ± 0.2 91.9 ± 0.6	93.4 ± 0.5 95.3 ± 0.4	85.6 ± 0.6 95.2 ± 0.4
Soft tissue grey	34.84	82.3 ± 0.7 87.6 ± 0.7	69.3 ± 0.6 86.1 ± 0.7	79.5 ± 0.8 86.7 ± 0.7	78.2 ± 0.7 86.8 ± 0.7
Trabecular bone	13.58	8.1 ± 0.3 9.1 ± 0.3	8.2 ± 0.3 9.4 ± 0.3	65.6 ± 0.9 74.6 ± 1.0	59.2 ± 0.7 72.1 ± 0.8
Cortical bone	6.00	0.0 ± 0.0 0.0 ± 0.0	0.0 ± 0.0 0.0 ± 0.0	0.2 ± 0.0 0.2 ± 0.0	0.1 ± 0.0 0.2 ± 0.0
Air	1.19	26.2 ± 1.6 38.1 ± 1.5	20.5 ± 1.4 31.8 ± 1.6	20.8 ± 1.3 28.7 ± 1.5	20.8 ± 1.3 28.7 ± 1.5
Sinus cavity	0.77	0.0 ± 0.0 0.1 ± 0.0	0.0 ± 0.0 0.1 ± 0.0	0.1 ± 0.0 0.2 ± 0.0	0.1 ± 0.0 0.2 ± 0.0
Tooth dentin	0.07	45.2 ± 1.8 47.9 ± 1.8	43.8 ± 1.8 46.5 ± 1.9	31.2 ± 2.2 35.1 ± 2.4	27.6 ± 2.1 31.7 ± 2.3
Spinal cord	0.05	84.7 ± 1.5 99.0 ± 0.1	68.9 ± 1.0 99.2 ± 0.1	79.8 ± 1.5 88.0 ± 0.7	61.5 ± 2.8 82.7 ± 1.0
Spinal disk	0.03	43.2 ± 4.2 49.9 ± 4.5	32.3 ± 5.0 44.4 ± 4.7	51.2 ± 3.5 55.8 ± 4.0	51.9 ± 3.2 57.0 ± 3.7
Tooth enamel	0.03	65.9 ± 2.3 67.3 ± 2.2	64.5 ± 2.2 65.9 ± 2.3	62.2 ± 2.7 63.8 ± 2.7	55.2 ± 2.4 56.9 ± 2.4
Global		62.4 ± 0.7 73.1 ± 0.7	32.4 ± 0.9 71.9 ± 0.7	77.7 ± 0.7 82.4 ± 0.6	73.0 ± 0.6 82.0 ± 0.6

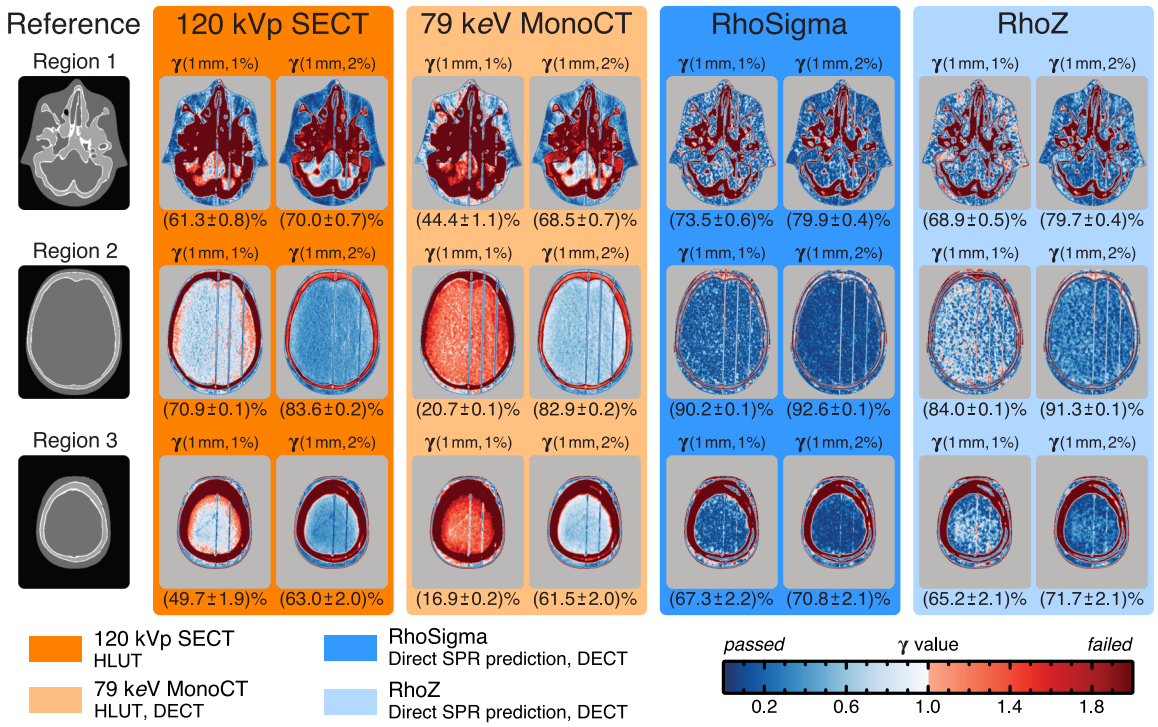

Figure 6.4: Representative γ-value maps for three head regions and all investigated CT-based SPR prediction methods. The mean γ passing rates and standard deviations for the respective head regions are specified below the γ-value maps. Adapted from Wohlfahrt et al. (2018a).

the SPR prediction of brain, simply because most CT voxels are out of the range of 1% SPR deviation (Fig. 6.3).

The highest γ passing rates were achieved in the head region 2, which is characterised by large homogeneous areas of a single material and fewer material transitions. The increasing heterogeneity (region 1) and relative amount of bone tissue surrogates (region 3) leads to considerably smaller γ passing rates. This reflects the approach-independent influence of smoothing on voxelwise SPR prediction.

Accuracy of Range Prediction

In the chosen exemplary treatment plan, the obtained mean range deviations to the reference plan are reasonably small for all methods, with a maximum of 1.4 mm for beam 2 in the RhoZ method. However, the HLUT approaches reveal smaller range deviations compared with the DirectSPR methods (Fig. 6.5). The HLUT systematically overestimates the SPRs of the three most frequent materials, which is compensated in beam direction by the sys-

tematic SPR underestimation of cortical bone owing to image smoothing. For beam 1, the methodological overestimation (especially brain and trabecular bone) is fully compensated by the smoothing-induced SPR underestimation of cortical bone. Since beam 2 traverses a higher amount of brain and trabecular bone, the compensation due to cortical bone is not sufficient. In contrast, the range error of RhoSigma is constant for both beam directions, because it is mainly caused by image smoothing. RhoZ reveals an increased range error for beam 2 arising from a raised amount of brain in beam direction as compared with beam 1.

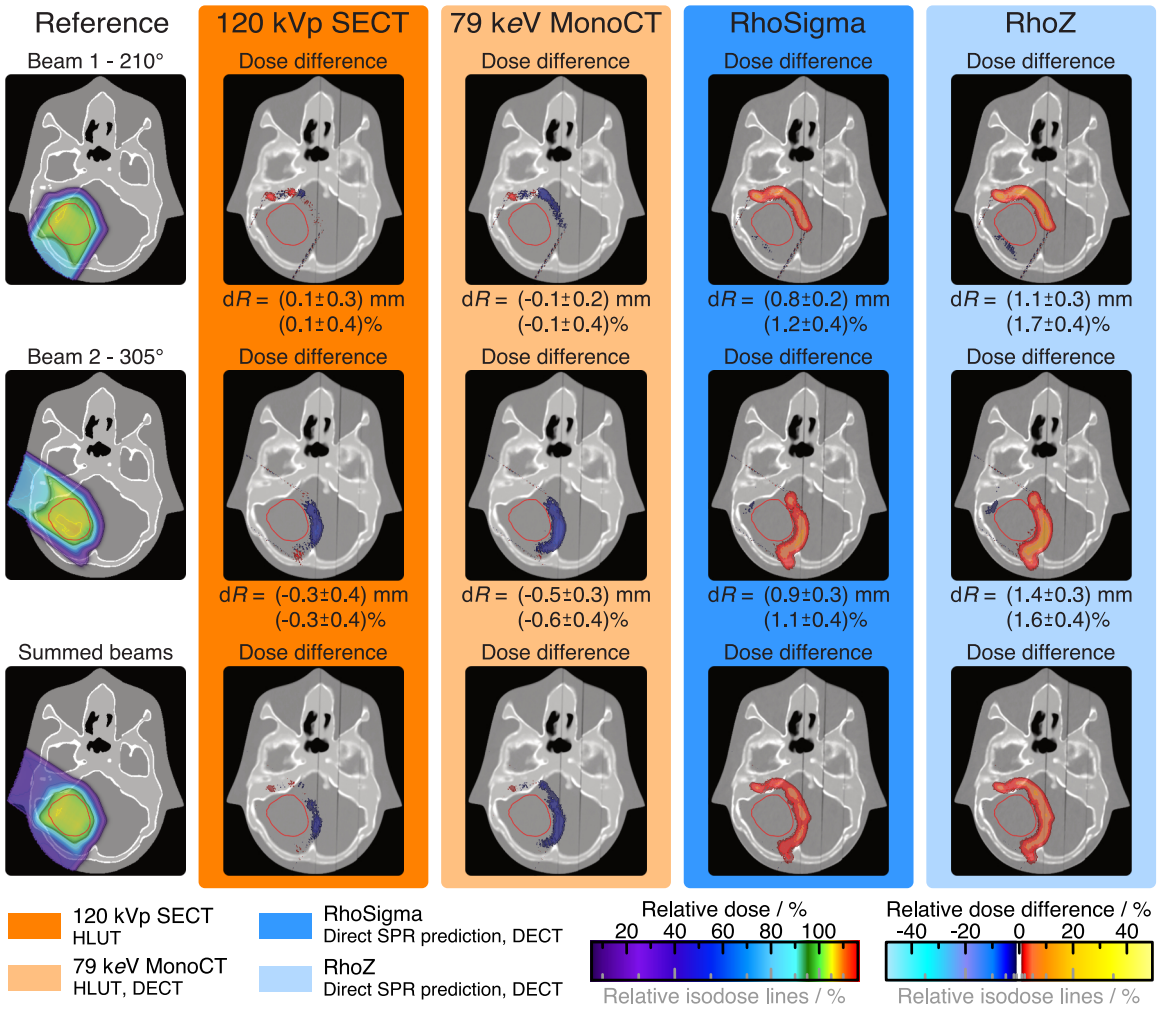

Figure 6.5: Dose difference and mean range deviation (dR $\pm$ standard deviation) for proton dose calculation based on CT-derived SPR datasets and the SPR reference of the anthropomorphic head phantom. Adapted from Wohlfahrt et al. (2018a).

6.1.3 Discussion of SPR and Range Accuracy

For non-small volumes, the DirectSPR methods yield a consistently better SPR prediction accuracy than the HLUT approaches. Comparing both DirectSPR approaches, RhoSigma was slightly more accurate than RhoZ. In general, the findings in regions not dominated by CT image smoothing are in agreement with earlier results in homogeneous tissue substitutes (Hünemohr et al., 2014; Hansen et al., 2015; Hudobivnik et al., 2016).
Moreover, a general influence of image reconstruction was found, namely the sharpness of reconstruction kernels and voxel discretisation, which leads to washout of material edges. The effect dominates in small-volume materials in proximity to high-density gradients, resulting in SPR under- or overestimation. This can be visualised by studying the SPR profile crossing different materials (Fig. 6.6). All SPR prediction methods are similarly affected by smoothing. In homogeneous slabs of the same small-volume phantom materials, the SPR prediction performed very well (mean absolute error $< 1\%$, excluding tooth enamel; Table D.2 of Supplement D). Hence, the smoothing effects are an additional, independent source of uncertainty. This is unexpected because CT vendors claim volumetric conservation of CT number at material edges in CT reconstruction (personal communication, Siemens Healthineers). In future studies, the deviations owing to non-sharp image reconstructions could be dedicatedly analysed (e.g. if it can be reduced by an increase of sharpness in image reconstruction – considering the trade-off between sharpness and noise).

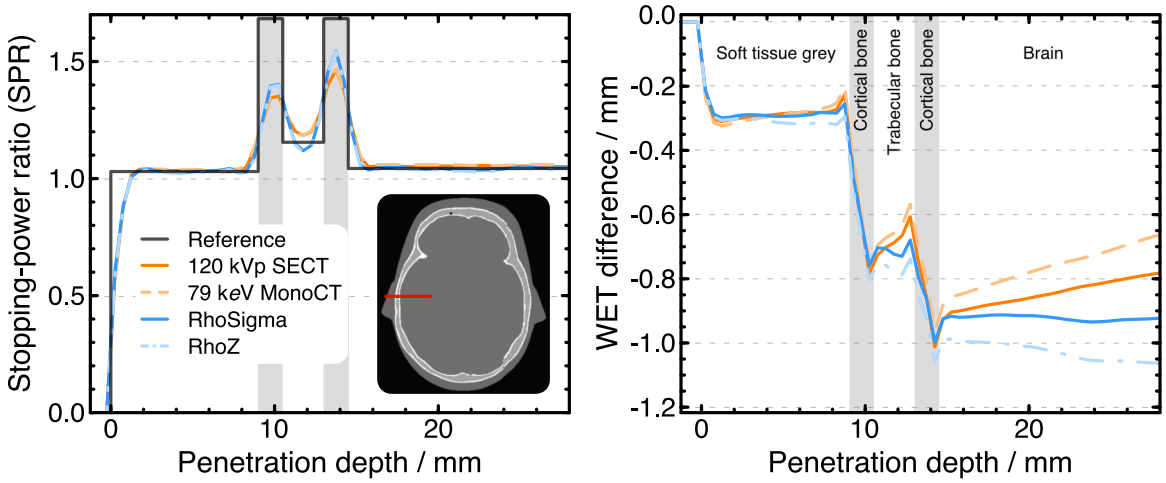

Figure 6.6: SPR distribution and deviation of water-equivalent thickness (WET) between CT-derived SPR datasets and the SPR reference for an exemplary beam direction within the anthropomorphic head phantom. Adapted from Wohlfahrt et al. (2018a).

Since not only voxelwise differences in SPR prediction but also the resulting dose distribution were evaluated within this study, it could be demonstrated that SPR deviations in different parts of the beam path can either add up or compensate each other (cf. cumulative WET in dependency of penetration depth; Fig. 6.6). Whereas smoothing affects all SPR algorithms similarly, especially in cortical bone, in other regions SPR deviations can have a quite variable influence. For the exemplary case in Fig. 6.6, hardly any compensation occurs for RhoSigma, because it accurately predicts the SPR of the three most frequent tissues. However, for the HLUT approaches, underestimation due to smoothing is partly compensated by an overestimation in trabecular bone and especially in brain. Although, on the first view, this might appear as a benefit of the HLUT approaches, in fact it demonstrates their non-robustness and case-dependency. Therefore, the two different causes of deviations in range prediction, namely (1) methodological limitations of SPR prediction and (2) effects from CT image smoothing, should be minimised independently. It is not an admissible option to hope for a compensation of the different effects.

There are a few limitations to be mentioned. First, the investigation is limited to the head-and-neck region, a treatment site of clinical importance for proton therapy. Owing to the complex effects in inhomogeneous targets, the extension of the evaluation to other body regions seems advisable.

Another limitation is the remaining delineation uncertainty of up to 1 mm. It was minimised by using a high-resolution CT scan for material-specific delineation. For the first three cases of the independent validation, the delineation uncertainty is mainly present in the definition of the external owing to voxel discretisation. The overall uncertainty increases with multiple transitions to low-density materials (air, sinus cavity), owing to material assignments depending on the image contrast adjusted by CT windowing, as well as with rounded shape. At the same time, this leads to considerably increased range mixing, deteriorating the depth-dose curve and hence the distal range at 80% of maximum dose used in the validation. This illustrates the difficulties and present limitations of independently verifying a ground truth for anthropomorphic geometries that can discriminate range differences in the lower and sub-millimeter scale. It should be stressed that these limitations are not CT-related but will affect any imaging-based validation approach that measures SPRs by their impact on range. However, in view of all difficulties in the validation procedure, the obtained results – median range differences smaller than ± 0.3 mm and more than 97% of all beam spots within ± 1 mm range difference – are rather convincing.

Moreover, the results for each SPR prediction method depend on the calibration procedure, that is the HLUT definition for 120 kVp SECT and 79 k*e*V MonoCT datasets or the definition of the calculation of stopping number from effective atomic number (RhoZ) or cross section (RhoSigma). In fact, there is an advantage for DirectSPR methods as the empirical influence on calibration is much smaller than for HLUT approaches (Wohlfahrt et al., 2017a). Currently, considerable variations in CT-number-to-SPR conversion between proton centres exist (e.g. due to different CT scan protocols and underlying HLUT definition). Besides, only two selected DECT approaches have been investigated in this study, although many more algorithms have been proposed. To facilitate investigations for others, the validated reference SPR map and CT datasets will be provided upon request.

6.2 Homogeneous Biological Tissue Samples

The accuracy of two SPR prediction methods (120 kVp SECT with HLUT and 80/Sn140 kVp DECT with RhoSigma) was experimentally assessed in homogeneous biological tissues. This study was performed and published by Möhler et al. (2018a) and is briefly summarised in the following.

To quantify the respective SPR accuracy and demonstrate potential differences between both approaches, a robust experimental setup for CT acquisition and relative ion range measurements with an overall SPR uncertainty below 0.1% was proposed. In total, 13 different porcine and bovine tissues (3 adipose tissues, 3 muscles, liver, kidney, brain, heart, blood, lung and bone) were analysed considering their relative incidence, homogeneity and availability. Finally, the deviation between measured reference SPR and CT-derived SPR of each tissue sample was determined.

For SECT, SPRs of most tissues (except brain and bone) significantly differ from the reference, resulting in a mean absolute error $\pm$ standard deviation of (1.27 $\pm$ 0.12)% and a mean signed error of (-0.84 $\pm$ 0.12)%. Especially the adipose tissues were underestimated by up to -2.7%.

SPRs derived from DECT scans are consistent with the reference values of all tissues except for bovine adipose showing a significant deviation of (0.19 $\pm$ 0.11)%. In total, a mean absolute error of (0.10 $\pm$ 0.15)% and a mean signed error of (-0.02 $\pm$ 0.15)% could be achieved.

Compared with SECT, DECT performs better for all tissue samples and significantly better for 10 out of 13 tissues (excluding brain, lung and bone). The intrinsic heterogeneity of lung and bone samples is associated with range degradation resulting in a considerable spread of the Bragg peak. Owing to the increased measurement uncertainty, it is not feasible to distinguish the performance of both methods for these two tissues. In summary, DECT allows for a highly accurate prediction of tissue-specific SPRs.

7 Clinical Translation and Validation of Dual-Energy Computed Tomography

For CT scan protocols optimised for radiotherapy, the accuracy of stopping-power prediction from clinical CT scans was assessed in an anthropomorphic head phantom and homogeneous biological tissues. In comparison with methods using an HLUT for CT-number-to-SPR conversion, DECT-based DirectSPR approaches showed a more robust and reliable overall performance resulting in an improved SPR accuracy. To conclude on the clinical applicability, safety and potential relevance of dual-energy CT for proton treatment planning, DECT scans of patients need to be considered, which are acquired within the routine clinical workflow. Since CT scans of patients are the basis of treatment planning, a change of CT scan protocols or even the shift from single-energy to dual-energy CT acquisition influence the entire radiotherapy chain from tumour delineation to treatment planning and finally dose application in patients.

Within this thesis, a stepwise procedure for a reliable clinical implementation of DECT in proton therapy was applied to continuously gather experience in daily clinical practice without interfering the current patient treatment. As a first step, it was analysed whether a DECT-derived MonoCT dataset, still using an HLUT for SPR prediction, yields a dose distribution comparable with the one derived from SECT (section 7.1), which is the current state-of-the-art imaging technique in radiotherapy. In a second step, differences in SPR, proton range and dose distribution between HLUT and DirectSPR approaches were quantified using patient DECT scans (sections 7.2-7.4). Based on the findings obtained in the systematic patient cohort analysis, the clinically applied HLUT could be refined to increase the accuracy of SPR prediction considering additional patient information derived from DECT (section 7.5). Finally, the clinical use of a patient-specific DirectSPR method might allow for a reduction of clinical safety margins and thus better sparing of healthy tissue.

All patient CT datasets were acquired at a single-source CT scanner Definition AS. The retrospective patient evaluations were approved by the local ethics committee (EK535122015).

7.1 Feasibility of Dual-Spiral Dual-Energy CT

Within this section, the clinical feasibility and safety of proton treatment planning based on DECT-derived MonoCT datasets is evaluated and discussed. The study results were published in Wohlfahrt et al. (2017b).

7.1.1 Evaluation Strategy

Clinical SECT and DECT scans (Table 5.1) of the head of the Whole Body Phantom PBU-60 (section 5.1.1) were acquired. A 79 k*e*V MonoCT dataset was generated from DECT using the image post-processing application syngo.MonoPlus. The SECT and 79 k*e*V MonoCT datasets were then evaluated concerning their influence on proton range calculation to verify consistent results and to ensure a safe application of treatment planning based on MonoCT datasets in a routine clinical workflow.

Proton treatment planning in double-scattering mode was performed with the TPS XiO using a $(1 \times 1 \times 1)$ mm^3 dose calculation grid. A proton beam was selected, which traverses a considerable amount of tissue heterogeneities in the phantom until reaching the distal edge of the target volume. The treatment plan was optimized on the 120 kVp SECT scan and recalculated on the 79 k*e*V MonoCT dataset.

Deviations in proton range prediction were analysed based on various line-dose profiles in beam direction extracted with the TPS RayStation 5.0. Absolute range differences ΔR were quantified using the distal range at 80% of the prescribed dose. Moreover, the overall dose distributions were compared using a 2D γ analysis with a passing criteria of 1% dose difference and 1 mm distance to agreement considering all axial CT slices receiving the prescribed dose.

Furthermore, to exclude possible differences between proton range prediction based on CT scans of a real human anatomy and a phantom consisting of tissue substitutes, the same analysis was performed for a single patient with sacral chordoma. For this patient, medically indicated SECT and DECT scans were acquired in direct succession. The two CT scans in dual-energy mode were acquired consecutively with a delay of approximately 10 to 15 seconds, which can differ depending on the investigated body region. The clinically applied passively scattered proton treatment plan with two beams from 150° and 210° was then evaluated.

7.1.2 Evaluation of Dose Calculation

To quantify differences in proton range prediction between a 120 kVp SECT and a DECT-derived 79 k*e*V MonoCT dataset, a treatment plan comparison was performed using the head of the Whole Body Phantom. In beam direction, 146 line-dose profiles with 1 mm spacing were analysed considering all axial CT slices receiving the prescribed dose. Comparing SECT- and MonoCT-based dose calculations, a mean absolute range difference ± standard deviation of (0.31 ± 0.13) mm was determined. The maximal absolute range difference was 0.59 mm. All proton range differences were thus smaller than the dose grid di-

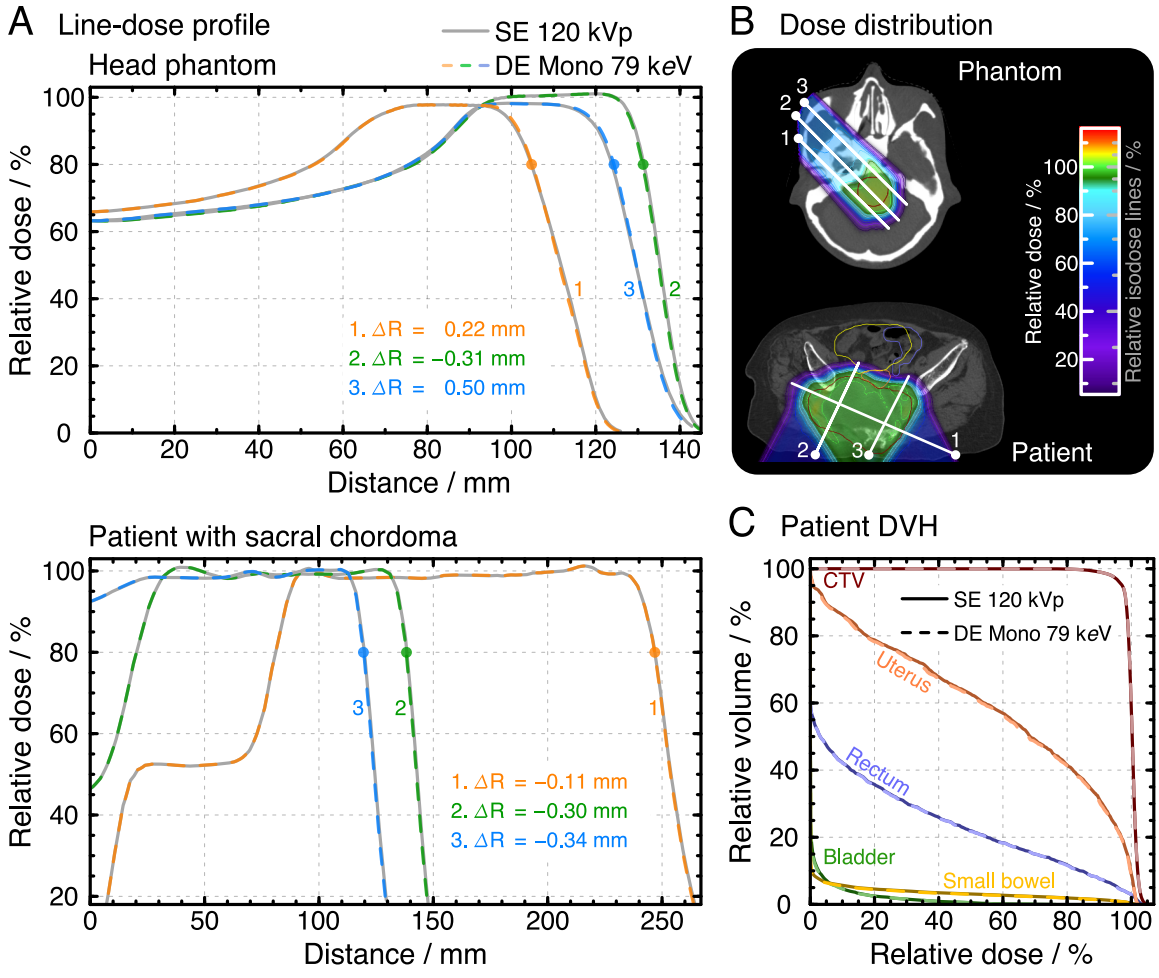

Figure 7.1: Representative (A) line-dose profiles and (B) dose distributions for a proton treatment plan of a head phantom with artificial tumour region and patient with sacral chordoma calculated on 120 kVp SECT scan and DECT-derived 79 k*e*V MonoCT dataset. Range deviations ΔR between both approaches were quantified using the distal range at 80% of prescribed dose. (C) Dose-volume histogram (DVH) of the patient treatment plan. Adapted from Wohlfahrt et al. (2017b).

mensions used for dose calculation. Three representative line-dose profiles and their range differences between 79 k*e*V MonoCT and 120 kVp SECT datasets are illustrated in Fig. 7.1. A 2D γ analysis (1%, 1 mm) of both dose distributions resulted in a mean and minimal γ passing rate of 99.92% and 99.60%, respectively. In summary, an excellent agreement between both proton dose distributions has been demonstrated within the limits of the chosen dose grid dimensions.
Furthermore, the agreement between SECT- and MonoCT-based dose calculations was also confirmed for a clinical patient treatment plan. Range deviations between both approaches were comparable to those determined in the head phantom and thus within dose grid dimensions (Fig. 7.1). Accordingly, the γ analysis revealed a mean and minimal γ passing rate greater than 99.99% and 99.98%, respectively. Consequently, no clinically relevant changes in the patient's dose-volume histogram (DVH) could be observed (Fig. 7.1 C).

7.1.3 Discussion of Clinical Feasibility

Since direct DECT-based SPR prediction algorithms (section 4.2) were still under development and could not be applied clinically at the time of this investigation, this study focused on the use of pseudo-monoenergetic CT datasets derived from DECT, still relying on a heuristic CT-number-to-SPR conversion. The clinical applicability and safety as well as slight benefits of this DECT application could be demonstrated for proton therapy.
In addition to the enhanced image quality of MonoCT datasets in comparison with 120 kVp SECT scans (section 5.2.2), the heuristic CT-number-to-SPR conversion is also slightly more precise using a 79 k*e*V MonoCT dataset (section 5.4.1). Further improvements relate to the CT number prediction of tabulated human tissues, which are commonly used for HLUT definition. For SECT, the CT numbers of tabulated human tissues are determined by a scanner-specific stoichiometric CT number prediction (section 4.1.2). However for MonoCT calculation, they can be obtained more simply using the respective tabulated monoenergetic X-ray attenuation of NIST (Berger et al., 1990) multiplied with the scanner-specific weighting-factor ratio $\hat{\alpha} = \alpha_{\text{syngo.MonoPlus}}\left(E_{\text{mono}}\right) / \alpha_{\text{MonoNIST}}\left(E_{\text{mono}}\right)$.
As demonstrated in a head phantom and especially in a clinical patient case, SECT- and MonoCT-based proton range predictions and dose distributions are consistent. It should be also emphasised that only one patient case could be included because both a SECT and DECT scan can only be justified in very rare cases according to the ALARA principle.

Therefore, a detailed and reliable range evaluation had to be performed on a phantom and then verified for an example patient case, which can be considered as sufficient to exclude possible relative differences of proton range predictions.

7.1.4 Routine Clinical Application of Dual-Energy CT

In consideration of all results achieved within this evaluation, proton and photon treatment planning based on DECT-derived 79 k*e*V MonoCT datasets were clinically implemented at OncoRay in 2015 and 2016, respectively, to reduce CT-related uncertainties caused by beam hardening and to make use of additional DECT options for delineating. Since dual-spiral DECT scans are acquired consecutively with the available single-source CT scanner, the obtained images are prone to patient motion (e.g. breathing, swallowing, or organ movements) occurring within the timespan of DECT acquisition. Consequently, treatment planning based on 79 k*e*V MonoCT datasets was initially implemented for tumour entities and body regions where motion can be neglected between both CT scans (e.g. brain and skull target sites – more than 50% of all patients at OncoRay).
On the basis of control CT scans, which are acquired in dual-energy mode for all tumour entities during the course of proton therapy, the impact of motion on dual-spiral DECT scans has been further analysed to widen the spectrum of tumour entities scanned in dual-energy mode for treatment planning. Patients with prostate cancer or a tumour located within the pelvic region revealed a clinically negligible influence of motion. Hence, the acquisition of clinical DECT scans for treatment planning was expanded at OncoRay and covers currently cerebral and pelvic tumour patients.

7.2 Range Prediction in Cerebral and Pelvic Tumour Patients

After the clinical implementation of DECT in radiotherapy, the resulting database of currently more than 1600 patients offers the opportunity to evaluate different CT-based range prediction methods in patients. To quantify range deviations caused by two CT-number-to-SPR conversions (clinical HLUT and RhoSigma as patient-specific DirectSPR approach) and to observe whether these are of clinical relevance, 100 treatment fields of 50 proton-therapy patients were analysed. The results were published in Wohlfahrt et al. (2017c) and are presented in the following.

7.2.1 Study Design

Differences between SPR prediction methods were assessed on various levels: voxelwise SPR distribution, proton range in beam direction as well as beam-specific and overall dose distribution.

DECT-Based SPR Prediction in Patients

For routine proton treatment planning of patients with several cancer types in the head and pelvic region, a dual-spiral DECT scan (80/140 kVp) with a $(1 \times 1 \times 2)\,\mathrm{mm}^3$ voxel spacing is acquired. Both CT datasets were reconstructed using an iterative reconstruction kernel with beam hardening correction concerning bone (Q34/5, SAFIRE) to decrease image noise (controlled by Siemens CARE Dose4D) and increase the patient-size dependent stability of CT numbers.
In addition to MonoCT datasets, voxelwise material parameters, namely electron density and photon attenuation cross section, were directly derived from DECT for the patient-specific DirectSPR approach RhoSigma (sections 4.2.3 and 5.4.2).

Patient Cohort and Treatment Planning

To evaluate the impact of SPR differences between the HLUT and RhoSigma approach on therapeutic dose distributions, 25 brain-tumour (ependymoma, germinoma, Ewing's sarcoma, astrocytoma and glioblastoma) and 25 prostate-cancer patients treated with protons at OncoRay were selected. Both cohorts were assembled to representatively cover the respective range of patient ages (brain: 2-73 years, prostate: 53-84 years). The brain-tumour cohort includes five children, ten women and ten men.
The passively scattered proton treatment plan of each patient consists of two to five treatment fields and was generated with the TPS XiO using a $(1 \times 1 \times 1)\,\mathrm{mm}^3$ dose calculation grid. All prostate-cancer patients were treated with two opposing beams from 90° and 270°. Within the brain-tumour patient cohort, the number of treatment fields, including beam and couch angle, varied depending on tumour position. The clinically applied proton treatment plan was recalculated on the SPR dataset derived from the RhoSigma approach and relative dose difference maps, normalised to the prescribed dose, between both SPR prediction methods were created.

Assessment of Proton Range Shifts

For the two treatment fields of each patient with the highest beam weights, depth-dose curves in beam direction were extracted in an orthogonal grid of 1 mm isotropic spacing using an in-house ray-tracing algorithm (Tschiche, 2016), which was implemented according to Siddon (1985). The origin of all depth-dose curves was defined by the external patient contour including immobilisation devices. Depth-dose curves inside each treatment field with a dose maximum larger than 95% of reference dose per beam were evaluated. The proton range in tissue ($R80_{\text{Tis}}$) was defined as distal range at 80% of reference dose. The range difference between line-dose profiles obtained with two different CT-number-to-SPR conversion methods corresponds to the range shift in tissue ($\Delta R80_{\text{Tis}} = R80_{\text{Tis, RhoSigma}} - R80_{\text{Tis, HLUT}}$). This shift $\Delta R80_{\text{Tis}}$ can then be translated into a water-equivalent proton range shift ($\Delta R80_{\text{WET}}$) according to

$$\Delta R80_{\text{WET}} = \sum_{n=1}^{N} \hat{S}_{\text{RhoSigma}}(n) \cdot \delta z(n) \tag{7.1}$$

with n as voxel number going from 1 to the total number of voxels N between $R80_{\text{Tis, HLUT}}$ and $R80_{\text{Tis, RhoSigma}}$ and $\delta z(n)$ as path length between two consecutive voxel boundaries. The quantity $\Delta R80_{\text{WET}}$ allows for a direct comparison with the range uncertainty applied for treatment planning, where water-equivalent quantities are used by default. Relative proton range shifts were derived by dividing $\Delta R80_{\text{WET}}$ by $R80_{\text{WET, RhoSigma}}$.
The intra-patient and inter-patient variability were defined as mean of the standard deviation and as standard deviation of the mean of patient-specific range shifts, respectively.
To determine whether both methods predict significantly different water-equivalent proton ranges, a one-sided t-test with a level of significance of 5% was applied.

Assessment of SPR Deviations

In addition to proton range shifts derived from dose distributions, the mean SPR deviation between both CT-based stopping-power prediction approaches ($\Delta\hat{S} = \hat{S}_{\text{HLUT}} - \hat{S}_{\text{RhoSigma}}$) was calculated including all CT voxels within the 20% isodose of at least one of the two dose distributions. Furthermore, the frequency distribution of voxelwise correlations of CT number and SPR derived from RhoSigma was determined, as exemplarily shown in Figs. 7.2 C and 7.3 C for a brain-tumour and a prostate-cancer patient case, respectively.

7.2.2 Results of Systematic Cohort Evaluation

First, an exemplary patient is presented for the brain-tumour and prostate-cancer cohorts to explicitly describe the different effects causing range deviations determined in the systematic patient cohort evaluation.

Exemplary Brain Case

Compared with the application of an HLUT, patient-specific DECT-based SPR predictions lead to clinical dose differences up to 26% relative to the prescribed dose at the distal fall-off (Fig. 7.2 A). The illustrated proton depth-dose curve reveals an absolute and relative proton range shift in tissue of 1.6 mm and 1.2%, respectively (Fig. 7.2 B). Since the proton beam traverses a considerable amount of water-filled ventricles and the HLUT is optimised to better fit soft tissues instead of water ($H = 0$ HU, $\hat{S} = 1$), the HLUT overestimates the SPR of water (zoomed inset of Fig. 7.2 C). To quantify its influence on proton range, ventricles were delineated, their SPR assigned to the one of water ($\hat{S} = 1$) and the proton dose distribution was recalculated. As a result, SPR deviations in ventricles add up to a range shift of 0.4 mm. The residual proton range shift of 1.2 mm is mainly induced by the systematic larger SPR for brain using the HLUT instead of RhoSigma (indicated by the red ellipse in Fig. 7.2 C). The clinical dose differences were not only present in a single treatment field but remained in the overall treatment (Fig. 7.2 D). Within both investigated treatment fields, a mean relative range shift and intra-patient variation ($\pm$ standard deviation) of (1.6 ± 0.7)% was determined.

Exemplary Prostate Case

Proton dose distributions derived from both SPR prediction methods differ considerably as exemplarily shown in Fig. 7.3 A. Here, dose differences of more than 50% relative to the prescribed dose were determined at the distal fall-off. For a representative depth-dose profile, this corresponds to a proton range shift of 5.1 mm in tissue (Fig. 7.3 B). Even in the target volume dose reductions of up to 1.5% occur, which cannot be compensated in the overall treatment by superimposing both fields (Fig. 7.3 D). The HLUT predicts systematically larger SPRs for muscle, bone marrow and trabecular bone (indicated by the red ellipse in Fig. 7.3 C).

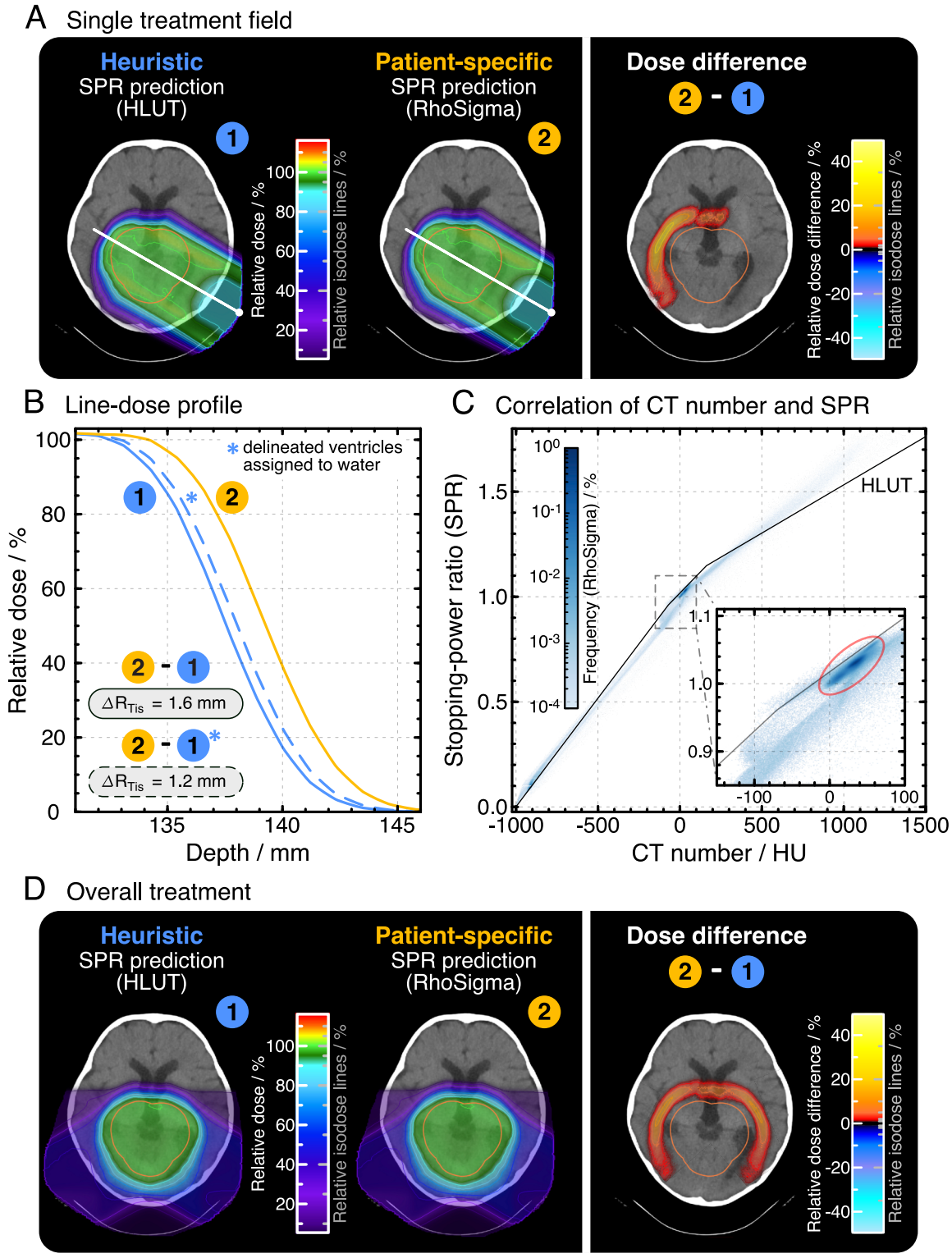

Figure 7.2: Proton treatment plan of a two-year-old patient with an ependymoma (#1) calculated using an HLUT (1) and a direct patient-specific SPR prediction approach (2) for CT-number-to-SPR conversion. The red ellipse indicates brain tissue. Adapted from Wohlfahrt et al. (2017c).

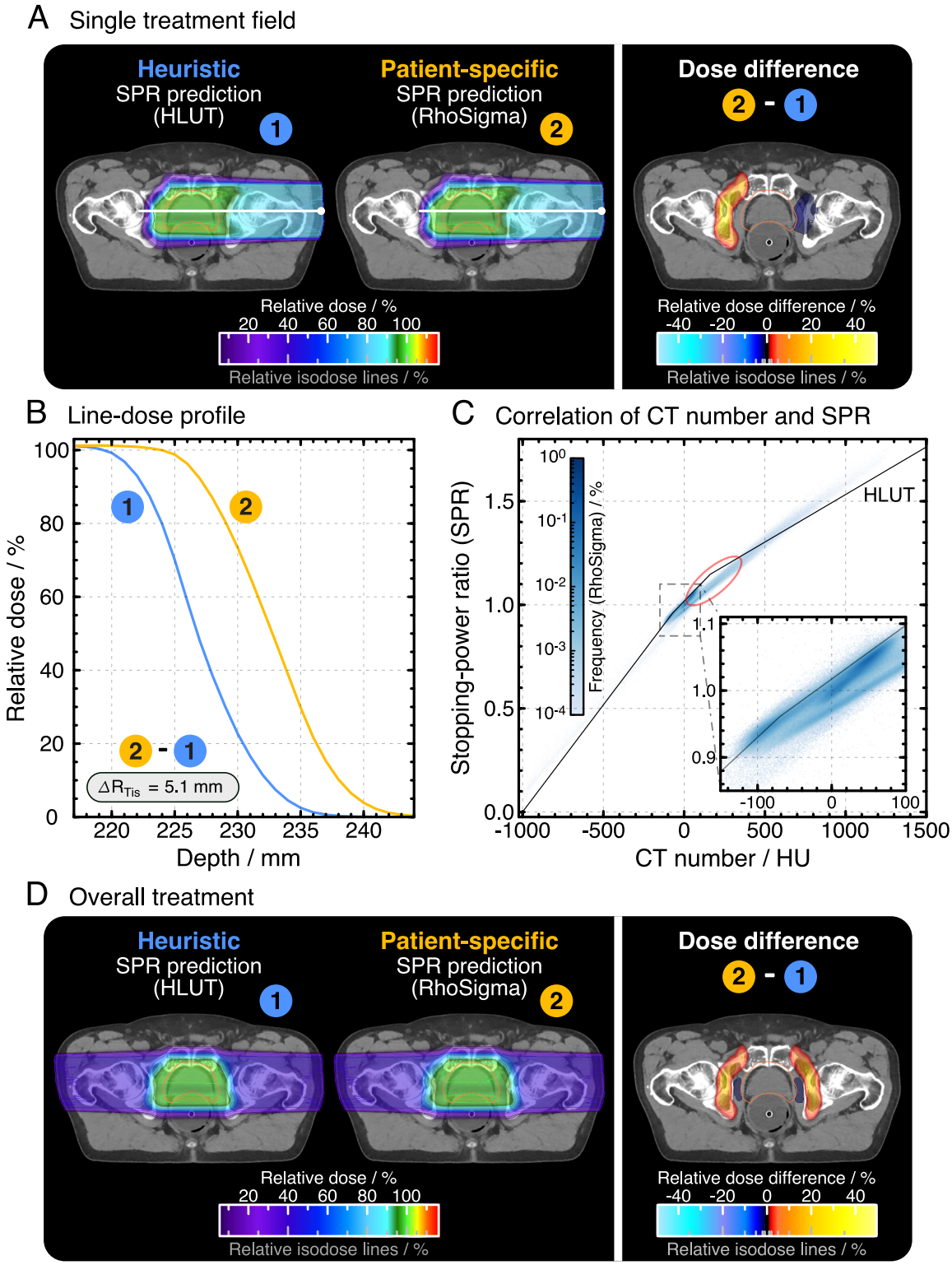

Figure 7.3: Proton treatment plan of a 73-year-old patient with prostate cancer (#3) calculated using an HLUT (1) and a direct patient-specific SPR prediction method (2) for CT-number-to-SPR conversion. The red ellipse indicates muscle and trabecular bone. Adapted from Wohlfahrt et al. (2017c).

Systematic Patient Cohort Evaluation

The results obtained from the presented individual patient cases are representative for the systematic evaluation of on average 5001 (min: 2682, max: 9450) proton depth-dose curves in beam direction for each treatment field. Regarding all evaluated depth-dose curves independent from the individual patient (Fig. 7.4), an overall median water-equivalent range shift $\pm$ standard deviation of (1.2 ± 1.0)% or $(1.1 \pm 0.9\,\text{mm})$ for brain-tumour and (1.7 ± 0.9)% or $(4.1 \pm 2.2\,\text{mm})$ for prostate-cancer patients were observed. The mean relative water-equivalent range shift of each patient (Fig. 7.5) is significantly larger than 1% for both cohorts ($p < 0.001$) and even significantly larger than 1.5% for patients with prostate cancer ($p < 0.001$).

As summarised in Table 7.1, about 34% and 66% of all depth-dose curves for the brain-tumour and prostate-cancer cohort, respectively, reveal water-equivalent range shifts larger than 1.5%. Mean SPR deviations within the irradiated volume agree well with range differences obtained from dose distributions (Fig. 7.5). Furthermore, for brain-tumour (prostate-cancer) patients, the intra-patient variation of relative water-equivalent range shifts with 0.91% (0.44%) is considerably larger than the inter-patient variability of 0.22% (0.24%). This is caused by differences in tissue type and relative amount of tissues traversed, i.e. soft tissues like fat, muscle or brain, low-density bone like trabecular bone and high-density bone as cortical bone. To illustrate the intra-patient variability of range shifts within a field,

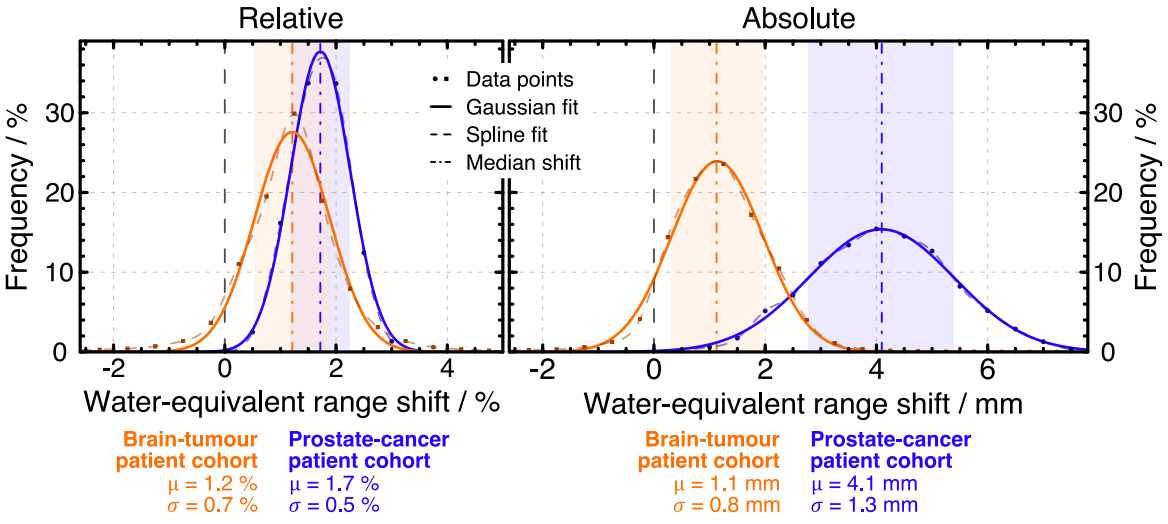

Figure 7.4: Distribution of relative and absolute water-equivalent range shifts for the investigated brain-tumour and prostate-cancer patient cohort. Adapted from Wohlfahrt et al. (2017c).

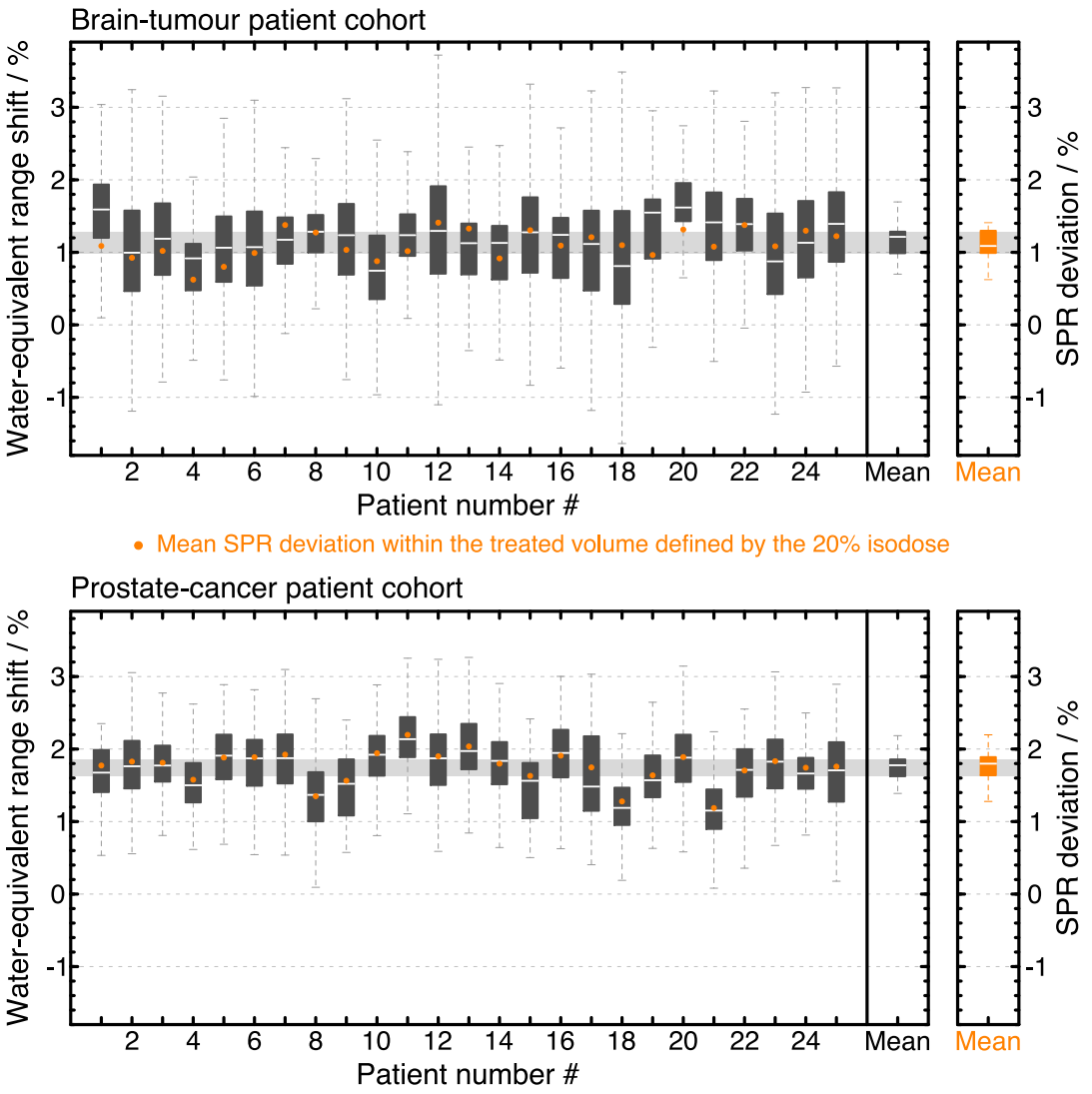

Figure 7.5: Distribution of intra-patient water-equivalent range shifts as well as inter-patient mean water-equivalent range shifts and mean SPR deviations. Box plots are defined as illustrated in Fig. 6.3. Adapted from Wohlfahrt et al. (2017c).

a range deviation map is shown in beam's eye view (BEV) for one patient of each cohort (Fig. 7.6).

In brain-tumour cases (Fig. 7.6 A), proton beams penetrate mainly soft tissue. Since the HLUT predicts systematically larger SPR for brain compared to RhoSigma, a shorter range is mostly calculated using the HLUT instead of RhoSigma. However, for parts of the beam mainly passing through cortical bone, the HLUT predicts systematically lower SPR resulting in larger proton ranges as predicted by RhoSigma (negative dose difference and range shifts). This is important for beams of short penetration depth, because directly after travers-

Table 7.1: Criterion-based classification of absolute water-equivalent range shifts between the clinical HLUT and the DirectSPR approach RhoSigma for CT-number-to-SPR conversion.

Patient cohort	Relative amount of absolute range shifts dR with					
	dR < 1.0%	dR > 1.0%	dR > 1.5%	dR > 2.0%	dR > 2.5%	dR > 3.0%
Brain	35.5%	64.5%	33.9%	14.5%	6.3%	3.0%
Prostate	8.8%	91.2%	66.0%	28.8%	5.2%	0.3%
	dR < 1 mm	dR > 1 mm	dR > 2 mm	dR > 3 mm	dR > 4 mm	dR > 5 mm
Brain	41.5%	58.5%	16.8%	2.0%	0.4%	0.1%
Prostate	0.4%	99.6%	95.0%	80.1%	53.1%	23.9%

ing the cranial bone, the WET difference caused by cortical bone cannot be fully compensated by the systematically larger SPR of brain.

Within treatment fields of prostate-cancer patients (Fig. 7.6 B), especially muscle, bone marrow and trabecular bone occur. Since the HLUT predicts larger SPRs for all these tissues compared to RhoSigma, a systematic shorter proton range is calculated. Traversing the femoral head causes the highest range shift (Figs. 7.6 B and 7.3 C), which is mostly induced by the high amount of trabecular bone in beam direction. This effect is only partly compensated by the small amount of cortical bone in the beam path, for which $\hat{S}_{\text{HLUT}} < \hat{S}_{\text{RhoSigma}}$.

Discussion of Range Deviations

The feasibility of patient-specific SPR prediction based on DECT scans could be demonstrated under clinical conditions using a commercial CT scanner, image post-processing software and TPS. The proton range deviations obtained in 100 clinical treatment fields of 50 proton-therapy patients with various brain-tumour entities and prostate cancer are in good agreement with range shifts observed in five head-trauma patients with hypothetical base of skull tumour (Hudobivnik et al., 2016). The magnitude of range deviation between both CT-number-to-SPR conversion methods is representative for tumour entities in the pelvic, abdominal as well as head-and-neck region and underlines the clinical relevance of accurate range prediction in particle therapy. However, to assess which of the two evaluated approaches is closer to reality, the respective SPR accuracy in patients needs to be directly verified or indirectly validated in close-to-clinical scenarios.

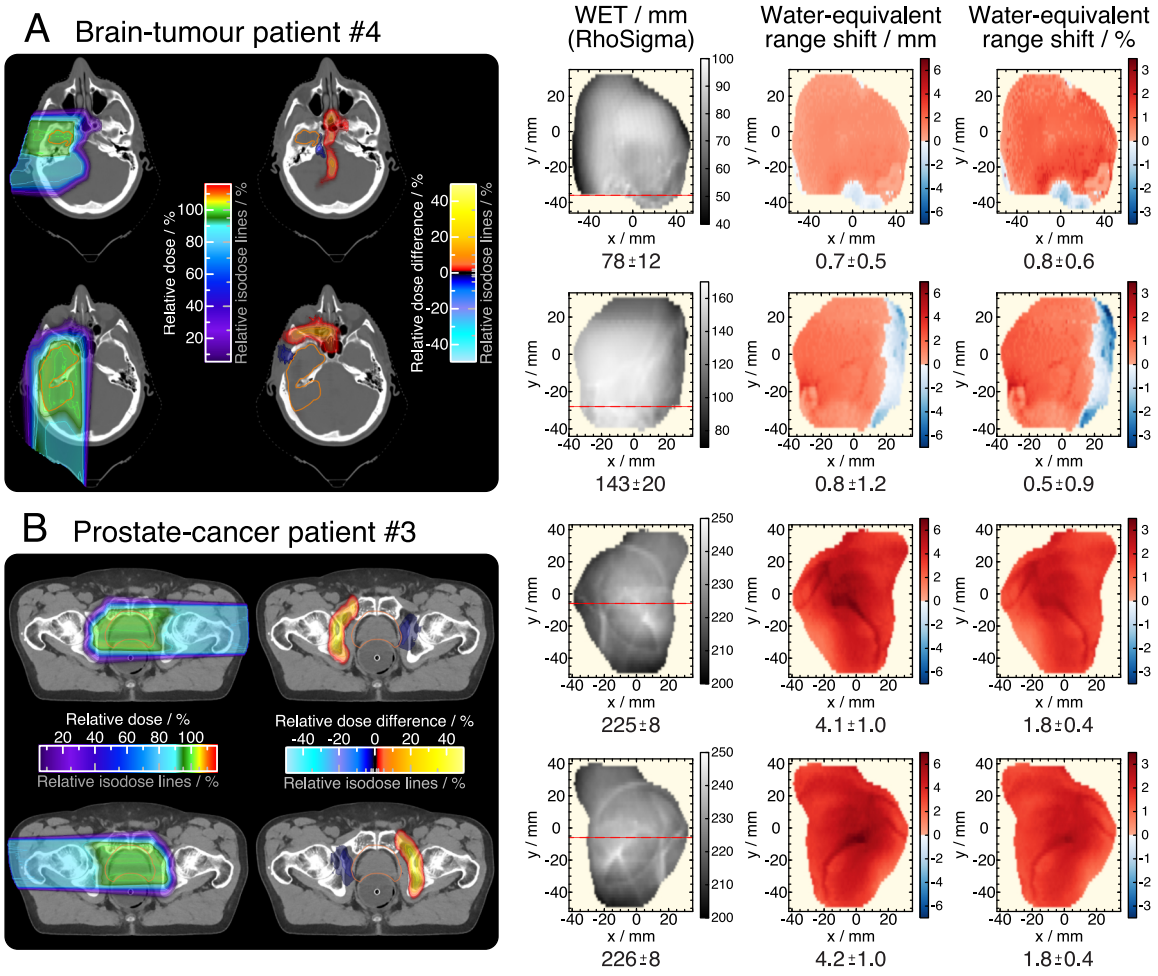

Figure 7.6: Assessment of water-equivalent thickness as well as absolute and relative range shifts in beam direction covering the whole treatment field. Mean values (± standard deviation) for each field are stated below the respective beam's eye view (BEV). The red dashed line illustrates the axial CT slice in BEV. Adapted from Wohlfahrt et al. (2017c).

Since both experimental studies performed within this thesis (chapter 6) demonstrated that CT-based SPR prediction using RhoSigma is more robust, reliable and accurate than an HLUT, it is justifiable to conclude that SPR prediction using RhoSigma is also more reliable and accurate for patients (Fig. 6.1). Consequently, the range differences obtained in patients indicate that DECT-based SPR prediction can improve particle range calculation and eventually lead to reduced range uncertainty margins. Further studies would be beneficial to finally assess the remaining uncertainties caused by image smoothing at high-density gradients (section 6.1.3) and to allow for an appropriate estimation of the CT-related range uncertainty in clinical practice.

Owing to the high SPR accuracy of RhoSigma, the mean SPR deviation within the irradiated volume of patients is certainly dominated by a systematic SPR overestimation of the HLUT for the major tissue types in beam direction (brain-tumour cohort: brain; prostate-cancer cohort: muscle, bone marrow and trabecular bone) as illustrated in Figs. 7.2 C and 7.3 C. These tissues mainly occur as large, almost homogeneous volumes without high-density gradients and are thus not influenced by smoothing during CT image reconstruction, which could hamper range prediction irrespective of the selected CT-number-to-SPR conversion (section 6.1.3). This effect of image smoothing, arising in small-volume tissues (cortical bone, air cavities), remains as uncertainty of absolute range prediction. However, since both methods are affected equally, the range shifts obtained within the investigated patients are virtually independent from this influence. Moreover, since the mean SPR deviations are comparable to mean relative range shifts derived from depth-dose curves (Fig. 7.5), the previously shown SPR accuracy of RhoSigma translates into mean range shifts.

Furthermore, the large intra-patient variation of range shifts illustrates the case dependency of a generic HLUT. Changes in the amount of different tissues traversed in beam direction can lead to large deviations in range prediction (Fig. 7.6). Therefore, a patient-specific DECT-based SPR prediction with high accuracy in each individual tissue type would be advisable. It is not admissible to hope for compensation of SPR over- and underestimation in different tissue types as this highly depends on the respective relative tissue amount along the beam path.

This study is subject to some restrictions. To assess range shifts directly related to the planned treatment, the clinically applied HLUT was used, which was defined following the clinical state-of-the-art procedure for CT calibration using tissue surrogates and tabulated human tissues (section 5.4.1). One could argue this HLUT is not optimised for the investigated patient cohorts and would thus contribute to an overestimation of range shifts. However, using only prior knowledge of currently available tabulated human tissues (Woodard and White, 1986), a sophisticated HLUT refinement is rather challenging if not impossible without including additional patient-specific information, e.g. derived from DECT. This illustrates a disadvantage of a generic HLUT, which cannot cover the overall tissue diversity and patient variability per definition and potentially leads to a systematic bias (Yang et al., 2010; Wohlfahrt et al., 2017a).

Furthermore, absolute proton ranges depend on the beam model and the dose calculation algorithm in the TPS. This influence can be neglected here, because only range shifts were

evaluated. The results are also transferable to pencil beam scanning, since the overall dose distribution of each treatment field was analysed.
A further limitation is the resolution of the CT scan and dose calculation grid. The overall influence on geometrical range calculation was reduced by linear interpolation of adjacent voxels to achieve a sub-voxel precision as commonly done in TPS.
This study is an important step toward clinical application of patient-specific DECT-based SPR prediction. However, a routine clinical use still requires an approved medical device provided by CT vendors, which is fully integrated in clinical workflow. Its calculated SPR dataset needs to be supported by all commercially available TPS.

7.3 Tissue Variability in Brain-Tumour Patients

Human tissues reveal large variations in elemental composition within one patient and between patients (Woodard and White, 1986). To quantify the respective tissue distribution and variability, appropriate imaging techniques need to be provided and adequately optimised to satisfy the requirements for each individual clinical purpose. The clinical application of dual-energy CT for proton treatment planning can inherently incorporate the intra- and inter-patient tissue variability in a patient-specific DirectSPR approach. This can contribute to reduce the restrictions associated with the generic HLUT used for CT-number-to-SPR conversion, which cannot adequately account for the tissue diversity in humans (Woodard and White, 1986; Yang et al., 2010).
Within this study, clinical DECT scans of a brain-tumour patient cohort were evaluated retrospectively to assess the influence of intra- and inter-patient tissue variability on CT-based stopping-power prediction in proton therapy. The presented results are currently in preparation for submission by Wohlfahrt et al. (2018b).

7.3.1 Study Design

In total, 102 brain-tumour patients (40 women, 40 men and 22 children younger than 20 years) treated with proton therapy at OncoRay were selected for this evaluation. This patient cohort was assembled to cover the wide range of brain-tumour entities (ependymoma, germinoma, craniopharyngioma, adenoma, sarcoma, glioma, meningioma, astrocytoma and glioblastoma) as well as patient ages (1-80 years).

DECT Acquisition of Brain-Tumour Patients

For each investigated brain-tumour patient, a dual-spiral 80/140 kVp DECT scan with a voxel spacing of $(1 \times 1 \times 2)\,\mathrm{mm}^3$ and a $\mathrm{CTDIvol}_{32\,\mathrm{cm}}$ of 20.8 mGy was acquired for proton treatment planning. The DECT image reconstruction was performed using the reconstruction kernel Q34/5 with SAFIRE of maximal strength to decrease the overall image noise level. For this scan setting, a noise level of 5 HU ($\pm$ two standard deviations) was obtained for both CT scans within an ROI in a homogeneous brain region of an anthropomorphic head phantom (Fig. 5.2). Due to the beam hardening correction concerning bone included in the reconstruction kernel, patient-size dependent CT number variations are clearly reduced within this brain-tumour patient cohort.

Extraction of Tissue Parameters

The clinical DECT scans were further processed using syngo.MonoPlus and syngo.RhoZ to calculate 79 k*e*V MonoCT, RED and EAN datasets. Afterwards, 3D RCS and SPR maps were derived from these three datasets. The SPR image dataset obtained by RhoSigma was saved in Digital Imaging and Communications in Medicine (DICOM) format. Here, the SPR in each CT voxel $\hat{S}_{\mathrm{CT}}$ is expressed in HU for a better comparability with X-ray CT scans (e.g. image contrast adjustment by CT windowing).

$$\hat{S}_{\mathrm{CT}} = (\hat{S} - 1) \cdot 1000 \tag{7.2}$$

For the applied implementation of RhoSigma and chosen CT scan settings, SPR datasets reveal an image noise level of 6 HU ($\pm$ two standard deviations) as determined in a homogeneous brain region of the anthropomorphic head phantom.
To consider only CT voxels within the patient, an external patient contour was automatically created based on the 80/140 kVp DECT scan using a threshold of -500 HU. Subsequently, this contour, covering the patient surface, was shrinked by 3 (5) voxels in x (y) direction to exclude remaining parts of immobilisation devices. In CT scan direction, the image datasets were limited to only include the head from chin to calvaria. Within this defined area, the frequency distribution of voxelwise correlations of two tissue parameters were determined, i.e. SPR and RED depending on CT number as well as EAN and RCS depending on RED as shown in Fig. 7.7.

The intra- and inter-patient variability was quantified based on the frequency distribution of (H, $\hat{S}$) correlations. The diversity of human soft tissues due to tissue mixtures and different tissue types was characterised by the intensity-weighted SPR spread Ω covering 95% of all CT voxels within the soft-tissue region (-125 HU $\leq H \leq$ 75 HU):

$$\Omega = \frac{1}{N_{\text{total}}} \sum_{H} N(H) \cdot \left[p_{97.5\%,\,\text{SPR}}(H) - p_{2.5\%,\,\text{SPR}}(H) \right] \tag{7.3}$$

with N_{total} as total number of voxels, $N(H)$ as number of voxels with respective CT number and $p_{x,\,\text{SPR}}$ as x^{th} SPR percentile.
Within the bony region (100 HU $\leq H \leq$ 1800 HU), the slope of an intensity-weighted linear regression serves as measure for variations in bones.

Compensation of Systematic Deviations in Stopping-Power Prediction

As demonstrated in the patient cohort analysis including brain-tumour and prostate-cancer patients (section 7.2), CT-based SPR prediction significantly differs between the application of an HLUT and a DECT-based DirectSPR approach. This resulted in a systematic global SPR and range deviation on average (Figs. 7.4 and 7.5).
To isolate the influence of tissue variability on SPR prediction, this systematic deviation needs to be separated by adapting the clinical HLUT. For this purpose, the median SPR of each CT number was obtained from the frequency distribution of (H, $\hat{S}$) correlations. Subsequently, the Hounsfield scale was divided in four regions corresponding to various tissue types: low-density (-950 HU $\leq H \leq$ -160 HU), adipose (-140 HU $\leq H \leq$ -40 HU), muscle and brain (-20 HU $\leq H \leq$ 40 HU) as well as bone tissue (100 HU $\leq H \leq$ 1800 HU). For each tissue region, the median SPR distribution was described by an intensity-weighted linear regression depending on the relative occurrence of the respective CT number within patients. The transitions between different regions were linearly connected.

Determination of Stopping-Power Deviations

The mean SPR deviation between both investigated CT-based SPR prediction approaches ($\Delta\hat{S} = \hat{S}_{\text{HLUT}} - \hat{S}_{\text{RhoSigma}}$) was calculated including all CT voxels within the patient's external contour. Tissue-dependent SPR differences were quantified using only CT voxels of the respective tissue type defined by the Hounsfield scale.

7.3.2 Assessment of Tissue Variability

The head region of the investigated patient cohort covers mainly soft and bone tissue with a mean fraction ± standard deviation of (78.6 ± 2.5)% and (18.9 ± 2.3)%, respectively. Only a small proportion of (2.5 ± 0.5)% are low-density tissues, which are often tissue mixtures between air cavities and various soft tissues or even bones.

Diversity Within Soft Tissues

As illustrated in Fig. 7.7, children and adults show a similar soft tissue distribution independent from the observed physical quantity (superposition of both colour bars appears

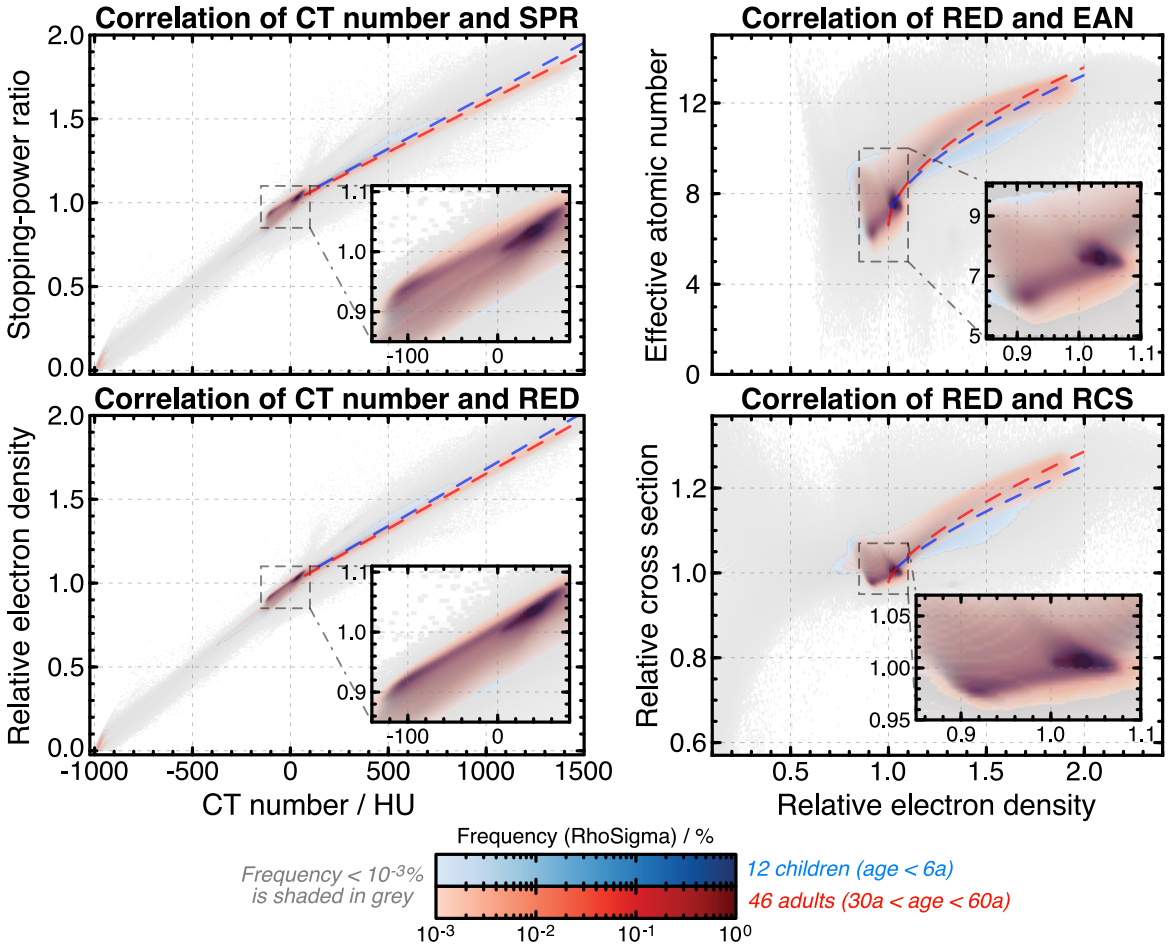

Figure 7.7: Frequency distribution of tissue parameters derived from dual-energy CT scans: relative electron density (RED), effective atomic number (EAN), relative photon attenuation cross section (RCS) and stopping-power ratio (SPR). Dashed lines illustrate the correlation within the bony region. The superposition of both colour bars appears purple. Adapted from Wohlfahrt et al. (2018b).

purple). The soft tissue region is dominated by brain ($H \approx 40$ HU, $\hat{\varrho}_e \approx 1.034$) and adipose tissue ($H \approx$ -100 HU, $\hat{\varrho}_e \approx 0.920$). Further tissue types, intra-tissue variations and tissue mixtures between brain and adipose tissue (indicated by a linear connection between the high-intensity areas of both tissue types) as well as between soft and low-density or bone tissues yield a broad SPR distribution. Considering the overall cohort of 102 brain-tumour patients, the soft tissue region shows a mean intra-patient SPR spread $\pm$ standard deviation of $\Omega = (5.6 \pm 0.7)\%$. This intra-patient SPR spread within the soft tissue region differs significantly between children and adults as demonstrated by a two-sample t-test with a level of significance of 5% (Fig. 7.8 A). Since the mean relative amount of adipose tissue in adults with $(16.5 \pm 4.0)\%$ is slightly higher compared to children with $(12.7 \pm 4.0)\%$, the increased soft tissue diversity in adults can potentially arise from the large intrinsic variability within adipose tissues (Woodard and White, 1986).

Variations Within Bone Tissues

The distribution of bone tissue differs between adults and children as indicated by a linear function for $\hat{S}(H)$ and $\hat{\varrho}_e(H)$ and power function for $Z_{\text{eff}}(\hat{\varrho}_e)$ and $\hat{\sigma}_e(\hat{\varrho}_e)$ in Fig. 7.7. Compared with adults, bones in children reveal a smaller effective atomic number for the same electron density, which is presumably associated with a smaller relative amount of calcium embedded in bones of children (Woodard and White, 1986; White et al., 1991). Since the calcium content in bones increases with age, the influence of the photoelectric effect on

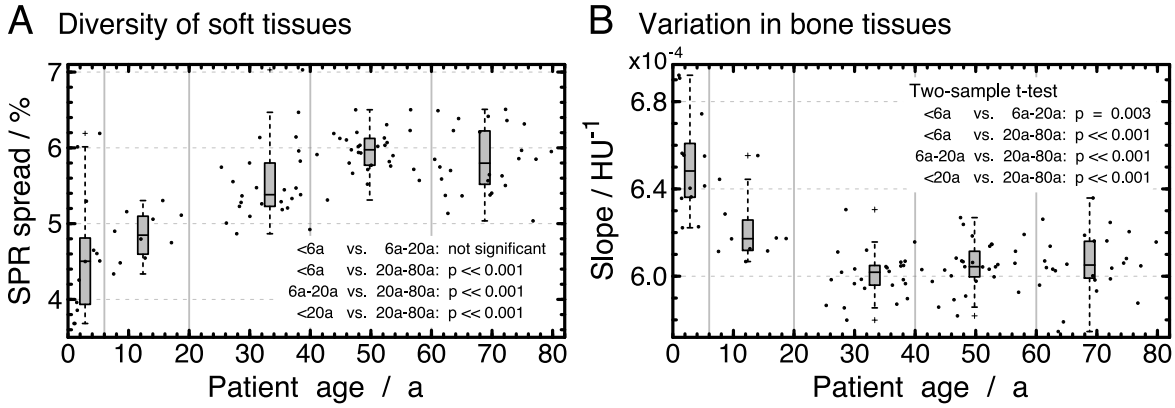

Figure 7.8: Age-related variation of the (A) SPR spread within the soft tissue region and (B) slope of the intensity-weighted linear regression within the bone region for (H, $\hat{S}$) correlations. Box plots are defined as illustrated in Fig. 6.3. A two-sample t-test was performed with a level of significance of 5%. Adapted from Wohlfahrt et al. (2018b).

CT number also increases. As shown in Fig. 7.8 B, this very likely leads to the age-related significant reduction of the slope in the bony region of the $\hat{S}(H)$ domain, which is relevant for proton treatment planning.

Tissue-Specific Stopping-Power Deviation

Since adults and children obviously differ in bone composition (Fig. 7.8 B), the clinically applied HLUT was adapted separately for each patient cohort based on the respective DECT information (Fig. 7.9). To assess whether this adaptation can compensate systematic deviations in stopping-power prediction between RhoSigma and clinically applied HLUT, SPR differences before (Fig. 7.10 A) and after adaptation (Fig. 7.10 B) were determined for adults and children, respectively.

The intra-patient SPR deviations of a representative child and adult are comparable to the SPR differences within the respective patient cohort (Fig. 7.10). SPR deviations of 10% (relative to the SPR of water, $\hat{S} = 1$) or even more can occur in the soft tissue or bone region including all (H, $\hat{S}$) correlations with a frequency larger than 10^{-3}% (Fig. 7.10, transition from grey-shaded to coloured frequency distribution).

For low-density and soft tissues, the clinically applied HLUT before adaptation predicts on average approximately 2% larger SPRs than RhoSigma (Fig. 7.11). The HLUT also calculates larger SPRs for low-density bones (100 HU $\leq H \leq$ 300 HU). However, smaller SPRs

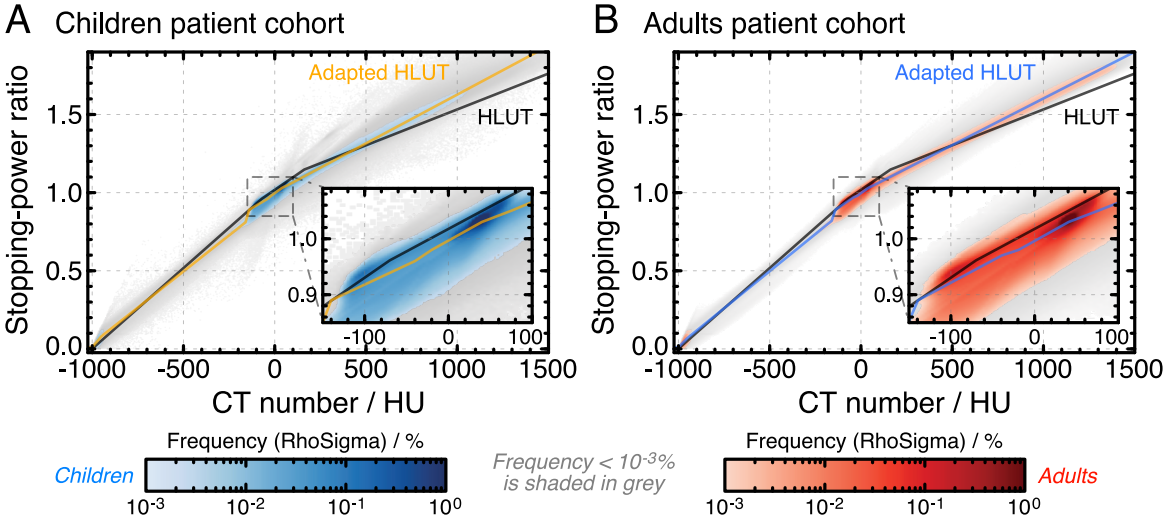

Figure 7.9: Frequency distribution of correlations between CT number and stopping-power ratio (SPR) for the (A) children and (B) adults patient cohort. Adapted from Wohlfahrt et al. (2018b).

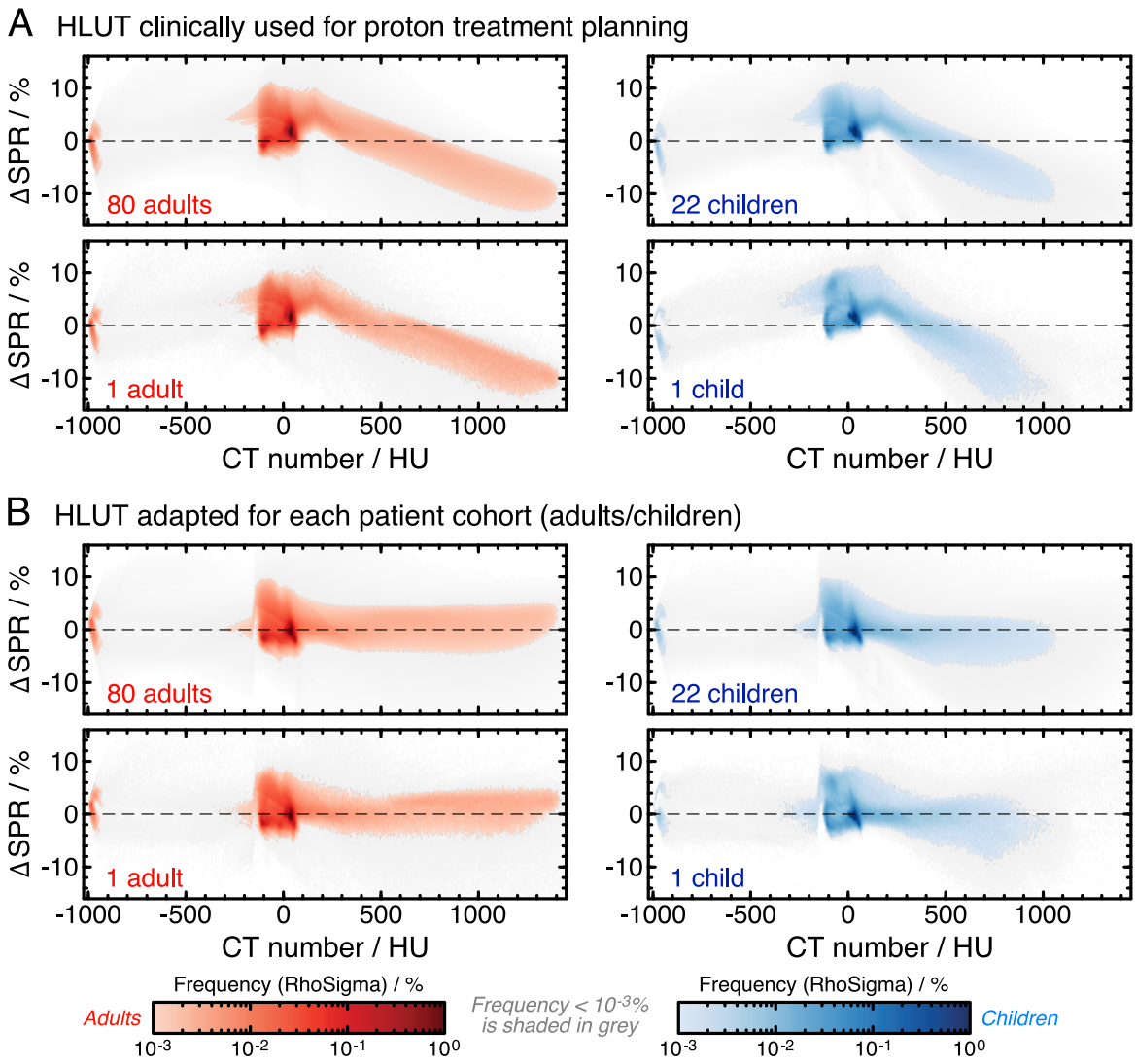

Figure 7.10: Difference in stopping-power ratio (SPR) between the DECT-based SPR prediction and (A) clinically applied or (B) cohort-specifically adapted Hounsfield look-up table (HLUT). For each cohort, a representative patient was selected in addition to illustrate the intra-patient variability. Adapted from Wohlfahrt et al. (2018b).

are obtained on average for all bones using the HLUT instead of RhoSigma. Consequently, SPR deviations in all tissue types can partly compensate, but still a global SPR deviation of 1.3% for children and 1.0% for adults remains. These SPR deviations are comparable with the results obtained in the systematic evaluation of proton range differences in a smaller patient cohort covering 25 brain-tumour patients (section 7.2).

The respective adapted HLUT can significantly reduce systematic tissue-specific and global SPR deviations (Fig. 7.11). However, the intra-patient SPR variation in soft tissues remains

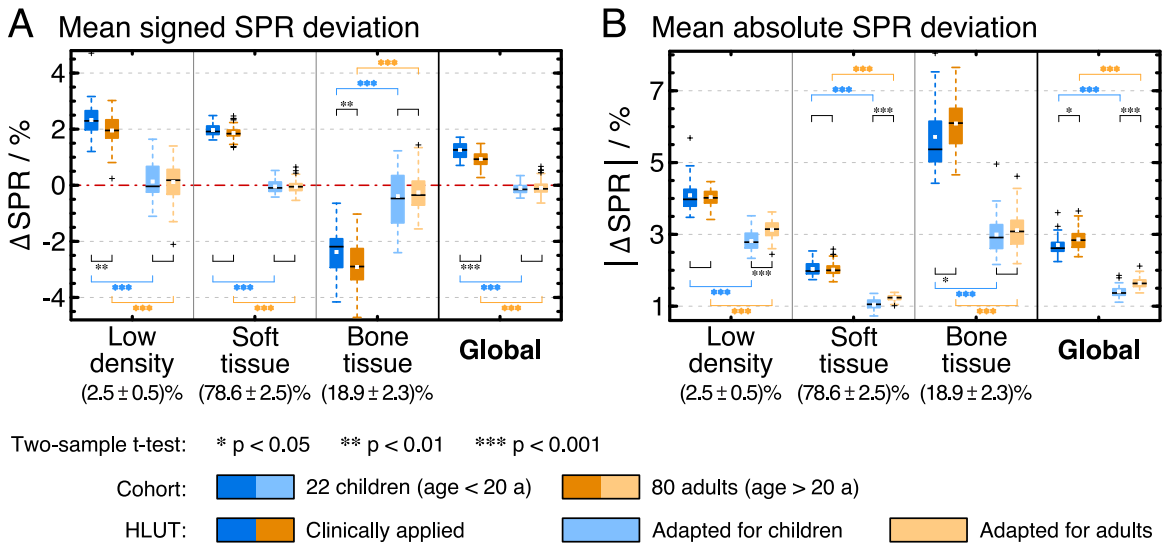

Figure 7.11: Global and tissue-specific (A) mean signed and (B) mean absolute deviations in stopping-power ratio (SPR) between DECT-based SPR prediction and clinically applied or adapted Hounsfield look-up table (HLUT). The relative amount of each tissue type ± standard deviation is quoted below the label. Box plots are defined as illustrated in Fig. 6.3. Adapted from Wohlfahrt et al. (2018b).

unchanged (Fig. 7.10 B). This translates into mean absolute SPR deviations of approximately 3% for low-density tissues and bones as well as 1% for soft tissues (Fig. 7.11). The large inter-patient variation of SPR deviations in bones (Fig. 7.11) illustrates the high variability in bone composition.

7.3.3 Discussion of Tissue Variability

The evaluation of DECT scans of 102 brain-tumour patients revealed a large intra-patient soft tissue diversity resulting in a broad SPR distribution with a mean intra-patient spread of $\Omega \approx 6\%$. Despite that an iterative reconstruction algorithm of maximal strength was applied on the patient DECT scans, the resulting SPR datasets had an image noise level ($\pm$ two standard deviations) of 6 HU in homogeneous areas, which is equivalent to a noise-induced SPR uncertainty of 0.6% (relative to the SPR of water). Consequently, the mean SPR spread of $\Omega = (5.6 \pm 0.7)\%$ in the soft tissue region does not only cover SPR variations arising from different tissue types, tissue mixtures and intra-tissue variability, but also includes noise-induced SPR variations. The influence of image noise on the SPR spread can be estimated with 1.2% (related to the SPR of water), which equals twice the image noise level. Assuming a Gaussian distribution for SPR variations due to tissue diversity as

well as image noise, the noise-induced effect can be quadratically subtracted from Ω resulting in a mean SPR spread of $\Omega = 5.5\%$. Even for a direct subtraction of the noise-induced deviation as a more conservative consideration, a large mean SPR spread of $\Omega = 4.4\%$ still remains for soft tissues. This intra-patient SPR spread is associated with a mean absolute SPR deviation of 1.2% in the soft tissue region.

Furthermore, differences in bone composition between adults and children were observed using RhoSigma as CT-number-to-SPR conversion. An HLUT adapted for adults would cause a SPR underestimation of approximately 5% for children younger than 6 years. Consequently, the age-related bone variation – especially in children – and the large soft tissue variability in general cannot be fully covered by a generic HLUT and lead to deviations by definition (Yang et al., 2010).

A subgroup-specific adaptation of the clinical HLUT can on average significantly reduce the systematic global and tissue-specific SPR deviations between both CT-number-to-SPR conversion methods. Since the intra- and inter-patient tissue variability cannot be considered by a generic HLUT, an accurate patient-specific SPR prediction using dual-energy CT, which correctly handles tissue mixtures, is advisable for treatment planning.

To further increase the validity of a DECT-based prediction of age-related changes in bone composition or to allow for a better age resolution, additional datasets of children could be evaluated. Further studies could also analyse whether DECT can contribute to quantify senile osteoporosis in patients. Moreover, the intra- and inter-patient tissue variability can be evaluated in other body regions, such as thorax and pelvis to detect potential differences in tissue composition and distribution.

7.4 Feasibility of 4D Dual-Spiral Dual-Energy CT

Dual-spiral dual-energy CT is prone to uncertainties due to patient motion during imaging (e.g. breathing, swallowing, heartbeat and gastro-intestinal peristalsis), leading to a different representation of the patient anatomy in the two subsequent 80 kVp and 140 kVp CT datasets. Therefore, only DECT scans of cerebral and pelvic tumour patients are currently acquired in the clinical routine at OncoRay for proton and photon treatment planning. In this study, the feasibility of dual-spiral time-resolved dual-energy CT (4D-DECT) for proton treatment planning within the thoracic region was analysed, i.e. in the presence of respira-

tory motion. For this purpose, the geometrical similarity of the two consecutively acquired 4D-DECT scans as well as the impact of DECT-derived CT datasets on tumour delineation and dose calculation were assessed. In addition, the clinical applicability of patient-specific DECT-based stopping-power prediction using RhoSigma was investigated. This study was published by Wohlfahrt et al. (2018c).

7.4.1 Design of Proof-of-Principle Study

Three consecutive patients with an advanced stage non-small-cell lung cancer (NSCLC) participating in the phase II clinical trial PRONTOX (Zschaeck et al., 2016) were selected for this feasibility study. The individual patient and tumour characteristics are summarised in Table E.1 of Supplement E.A.

CT Acquisition of Lung-Cancer Patients

For treatment planning, 120 kVp time-resolved single-energy CT (4D-SECT) scans with $(1 \times 1 \times 2)\,\mathrm{mm}^3$ voxel spacing were acquired. An iterative reconstruction kernel with beam hardening correction concerning bone (Q34/5, SAFIRE, CARE Dose4D) was applied.
The respiratory motion during CT acquisition was recorded using a pressure belt system (ANZAI, Anzai Medical Co., Ltd, Tokyo, Japan) positioned onto the patient's abdomen. Four CT datasets representing different breathing phases (maximum and slopes of inhalation as well as exhalation) were reconstructed using relative local amplitude-based binning of CT projections according to the patient‘s breathing pattern (Werner et al., 2017). For a rotation time of 500 ms, a temporal resolution of around 250 ms can be achieved for each respiratory phase per breathing period (Flohr et al., 2003). Furthermore, a time-averaged CT dataset was reconstructed using all CT projections.
Based on the 4D-SECT scan, the patient-specific internal gross tumour volume (iGTV) was defined by an experienced radiation oncologist. The CTV encompassed the iGTV and involved lymph nodes with 8 mm isotropic margin subsequently corrected for anatomical boundaries (Fig. E.1 A of Supplement E.A). The respective tumour motion was determined in cranio-caudal, left-right and anterior-posterior direction using the centre-of-mass of the GTV, which was delineated on each respiratory phase of the 4D-SECT scan (Table E.1 of Supplement E.A). Furthermore, the motion of the diaphragm was quantified based on the visible diaphragm line in exhalation and inhalation CT datasets.

To assess anatomical and breathing motion changes during the course of treatment, the patients underwent weekly control 4D-SECT scans according to the clinical protocol. For the three selected patients, a dual-spiral 4D-DECT scan instead of a 4D-SECT scan was acquired with similar total CT dose in between fractions 14-19 and 27-32, respectively. Each dual-spiral 4D-DECT scan comprises two 4D-SECT scans of 80 kVp and 140 kVp (Table E.2 of Supplement E.A), which were consecutively recorded within approximately 95 s each and a 10 s time delay in between for returning to the start position of the CT acquisition (Fig. 7.12). Image reconstruction was performed as for 4D-SECT scans using the same nominal relative amplitude-based binning.

Proton Treatment Planning

Passively scattered proton treatment plans with three fields were generated in the TPS XiO using the time-averaged planning SECT scan and the clinical HLUT (Fig. 5.9). Average dose to the CTV was aimed at 66 Gy(RBE) using an RBE of 1.1. For hardware preparation as well as range and modulation determination, the mean density derived from the GTV of each 4D-SECT breathing phase was assigned to the iGTV. Treatment uncertainty was included in aperture margins and compensator smearing of 10 mm as well as in a range uncertainty of $\pm(3.5\% + 2\,\text{mm})$. Dose calculations were performed without density assignment to the iGTV using a $(1 \times 1 \times 1)\,\text{mm}^3$ dose grid and a pencil-beam algorithm.
Additionally, worst-case-scenario treatment plans were generated using a single lateral proton beam covering an artificial target volume that encompassed parts of the diaphragm, the anatomical region where the largest motion occurred (Fig. E.1 B of Supplement E.A).

4D-DECT Image Post-Processing

The image post-processing application syngo.MonoPlus was used for dual-spiral 4D-DECT scans to generate MonoCT datasets of 58 k*e*V ($\alpha = 1$) and 79 k*e*V ($\alpha = 0$) comprising similar X-ray attenuation information as the initial 80 kVp and 140 kVp CT scans, respectively. During this internal processing, the two consecutively acquired 80 kVp and 140 kVp CT scans were aligned by DIR (Fig. 7.12). Due to the image post-processing, the 58 k*e*V and 79 k*e*V MonoCT datasets contained less image noise compared with the initial 80 kVp and 140 kVp CT scans (section 2.3.1). SPR datasets were calculated by RhoSigma using 3D image stacks of RED and RCS.

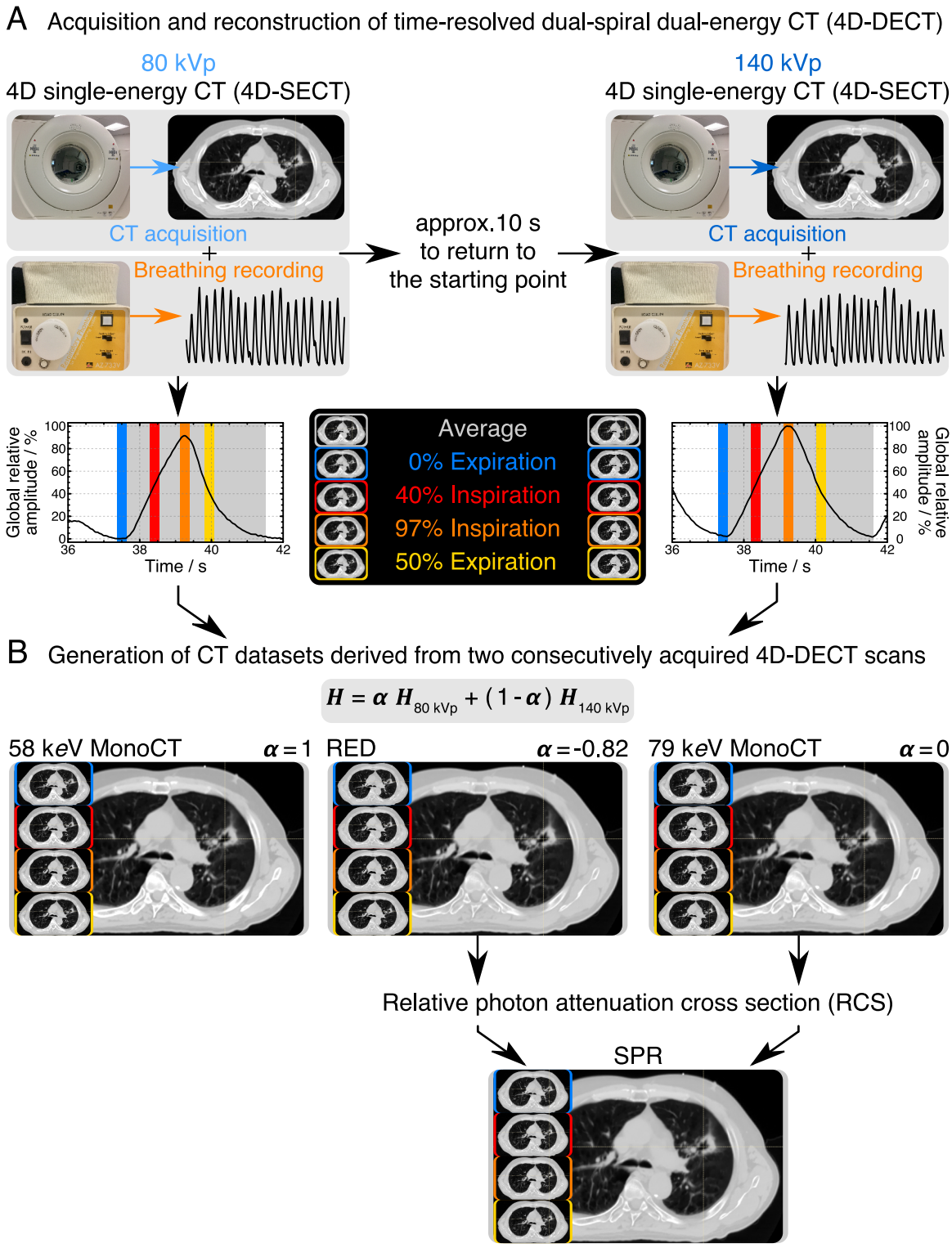

Figure 7.12: (A) Clinical acquisition of dual-spiral 4D-DECT and reconstruction of time-averaged 3D images and datasets considering only specific respiratory phases. (B) Investigated image datasets derived from 4D-DECT. Adapted from Wohlfahrt et al. (2018c).

Assessment of 4D-DECT Scan Similarity

For a quantitative comparison of CT datasets representing different X-ray attenuations, their CT numbers need to be equalised to account for differences in the attenuation behaviour. Based on the frequency distribution of correlations between CT numbers of a 58 k*e*V and 79 k*e*V MonoCT dataset of a rigid thorax phantom (Dynamic Thorax Phantom, Model 008A, CIRS, Norfolk, VA), which ensures a constant anatomy, a linear conversion was established (Figure E.2 of Supplement E.B). The geometrical similarity of dual-spiral 4D-DECT datasets before (80 kVp and 140 kVp) and after (58 k*e*V and 79 k*e*V) image post-processing including DIR was assessed visually and by normalised cross correlation (NCC)

$$\mathrm{NCC}_{\mathrm{ROI}} = 100\% \cdot \left(\frac{\sum H_i H_j}{\sum H_i^2 \sum H_j^2} \right)_{\mathrm{ROI}} \tag{7.4}$$

including CT numbers of both datasets, H_i and H_j, within regions of interest (ROIs), e.g. patient body, CTV, heart and total lung. NCC of 100% declares perfect agreement and 0% no conformity.

To estimate the sensitivity of NCC against geometrical deviation, a patient dataset was globally shifted between 1 mm to 10 mm in cranio-caudal, posterior-inferior and left-right direction and then compared with the non-shifted CT dataset (Table E.3 and Fig. E.3 of Supplement E.B).

Furthermore, the recorded breathing patterns during the subsequent acquisition of dual-spiral 4D-DECT scans were compared for each lung-cancer patient with regard to their variability in respiratory cycle time and the feasibility to identify visual differences in DECT-derived image datasets.

Evaluation of 79 k*e*V MonoCT Reliability

To assess the influence of anatomical changes in between the two consecutively acquired dual-spiral 4D-DECT scans and its handling during image post-processing on proton dose calculation, the clinical and worst-case-scenario proton treatment plans were recalculated on DECT-derived 79 k*e*V MonoCT datasets and their associated 140 kVp SECT scans as reference, respectively. Proton dose calculations were performed in the TPS RayStation 6.0 using the same clinical HLUT (Fig. 5.9), because both CT datasets represent a similar X-ray attenuation. For time-averaged CT datasets and four breathing phases differences in

dose distributions were quantified by voxelwise dose deviations and a global 2D γ analysis with a relative dose threshold of 5% as well as two evaluation criteria of $\gamma(1\,\text{mm}, 0.1\%)$ and $\gamma(1\,\text{mm}, 1\%)$. Furthermore, deviations in DVH parameters were evaluated for CTV and different OARs such as heart, oesophagus and total lung.

Application of RhoSigma Approach

Since a direct import of SPR datasets for dose calculation is not yet supported by the TPS RayStation 6.0, XiO was used to recalculate clinical treatment plans on 79 k*e*V MonoCT datasets applying the clinical HLUT and SPR datasets derived by RhoSigma. Deviations in dose distribution were evaluated as described above for time-averaged CT datasets and the breathing phases. To assess water-equivalent range shifts between the RhoSigma and HLUT approach (eq. 7.1), depth-dose curves in beam direction traversing the CTV with 1 mm spacing were analysed for each proton treatment field using an in-house implemented ray-tracing algorithm.
For the time-averaged CT datasets, the correlation of CT number and SPR obtained from RhoSigma were determined within the irradiated volume (20% isodose) and illustrated as frequency distribution.

Evaluation of Delineation Variability

Adjustments in CT acquisition and reconstruction parameters can change the image contrast of anatomical structures, which potentially has an impact on tumour detection and eventually the overall patient treatment. To evaluate this influence, an experienced radiation oncologist delineated the GTV of each patient on several time-averaged CT datasets. First, only the 79 k*e*V MonoCT dataset was used, which resembles a 140 kVp SECT scan and represents the clinical standard procedure. In a second step, the DECT-derived RED and RCS datasets were jointly provided as individual CT image stacks separating the main X-ray interaction processes (inelastic scattering and photoelectric effect). The GTV delineations were repeated once after one week to quantify the respective intra-observer variability. The conformity of the GTV contours was assessed by the Jaccard index, defined as the intersection between two segmentations divided by their union, and Hausdorff distance, defined as the 95^{th} quantile of minimal distances between two contours (finite set of points), for each patient (Jaccard, 1912; Taha and Hanbury, 2015).

7.4.2 Results

Only small anatomical differences were found between the two 80 kVp and 140 kVp dual-spiral 4D-DECT scans, which were mainly visible on the upper anterior thorax wall and were in accordance with the observable variability of the breathing amplitudes (Fig. E.4 of Supplement E.C). Changes in respiratory frequency were minor (Table E.4 of Supplement E.C) and were virtually adjusted in image reconstruction. For time-averaged CT datasets, the patient body, CTV and heart revealed a NCC $>$ 99.5% and the total lung a NCC $>$ 96% (Table 7.2), indicating mean shifts between each scan equivalent to global shifts of less than 0.5 mm (Fig. E.3 of Supplement E.B). CT datasets of individual breathing phases showed slightly less similarity and the respective NCC corresponded to shifts of approximately 1 mm to 2 mm. This confirms the general high resemblance of dual-spiral 4D-DECT scans. NCCs for all patients and ROIs are provided in Supplement E.D.

Patient movement had a larger impact than breathing: In one case (patient 2, 4D-DECT scan 1), the patient coughed at the end of the first 4D-DECT scan acquired with 80 kVp, which changed his overall body position, visible by an altered position of the vertebrae

Table 7.2: Conformity assessed by NCC for 80 kVp and 140 kVp CT scans before as well as the corresponding 58 k*e*V and 79 k*e*V MonoCT datasets after DIR. The time-averaged datasets and four respiratory phases of two dual-spiral 4D-DECT scans for each investigated lung-cancer patient were evaluated.

Mean normalised cross correlation (NCC) $\pm$ standard deviation* / %				
Before DIR	80 kVp and 140 kVp CT scans			
	Temporal average		Respiratory phases	
	Body	Lung	Body	Lung
Patient cohort**	99.64 ± 0.09	97.36 ± 0.57	98.90 ± 0.15	89.09 ± 3.05
Coughing patient	97.84	88.35	96.42 ± 0.08	72.47 ± 6.37
After DIR	58 k*e*V and 79 k*e*V MonoCT datasets			
	Temporal average		Respiratory phases	
	Body	Lung	Body	Lung
Patient cohort**	99.90 ± 0.02	99.84 ± 0.03	99.85 ± 0.04	99.61 ± 0.15
Coughing patient	99.80	99.80	99.59 ± 0.15	98.97 ± 0.70

* determined including all 4D-DECT datasets independent from the individual patient
** except for the first 4D-DECT dataset of patient 2 (coughing patient)

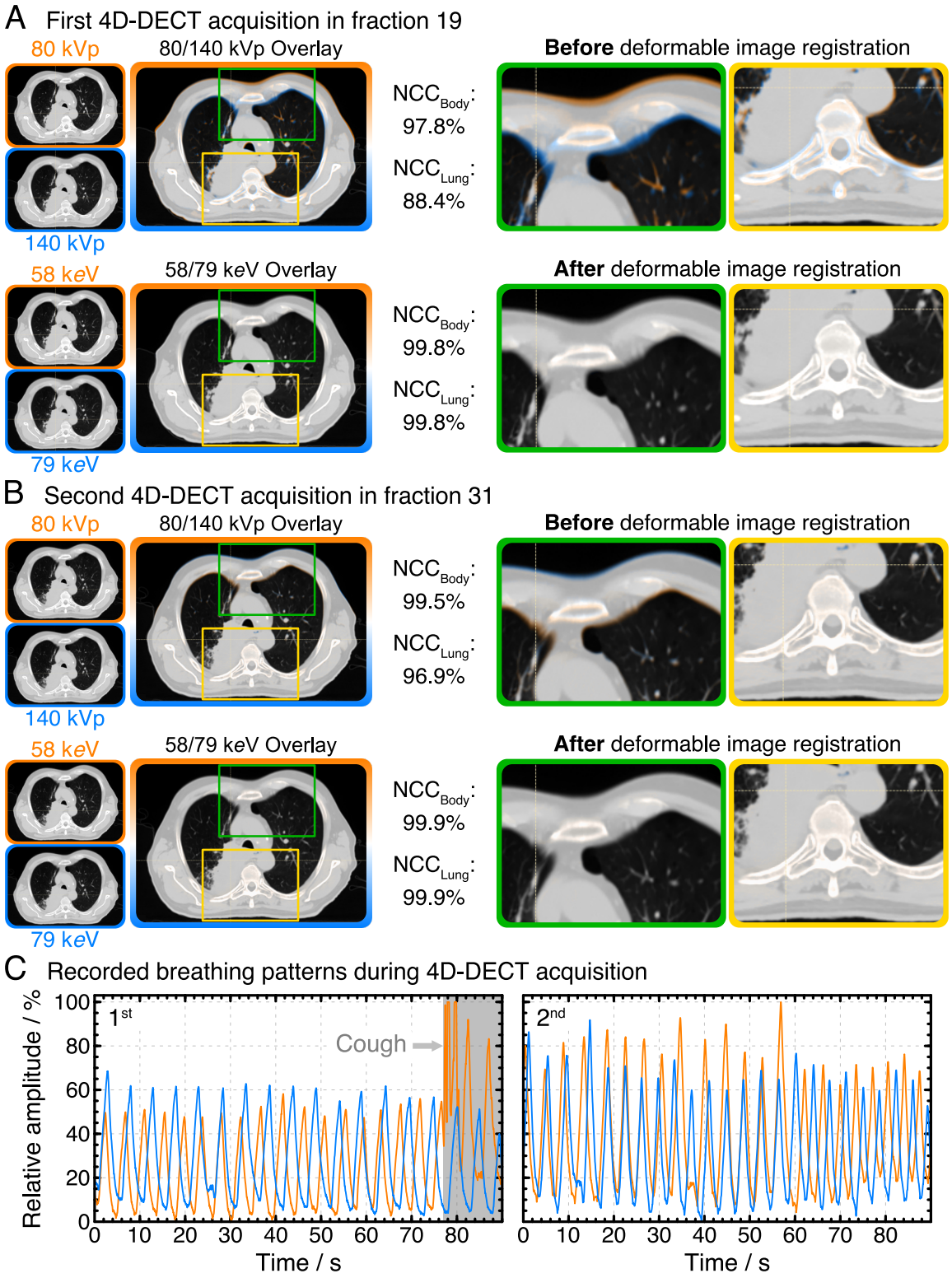

Figure 7.13: Exemplary axial CT slices of the time-averaged 80 kVp and 140 kVp CT scans before as well as the corresponding 58 k*e*V and 79 k*e*V MonoCT datasets after DIR for two 4D-DECT scans of patient 2 acquired in fraction 19 (A) and 31 (B). This patient coughed at the end of the 80 kVp CT scan during the first 4D-DECT acquisition as illustrated in the breathing pattern (C). Adapted from Wohlfahrt et al. (2018c).

(Fig. 7.13 A and C). The NCC dropped distinctly to 97.8% for body and 88.4% for total lung, similar to a global shift of approximately 1.3 mm between the time-averaged 80 kVp and 140 kVp CT datasets.
The differences caused by respiratory motion could almost be completely corrected by DIR, which was applied to the two 80 kVp and 140 kVp CT datasets prior to further image post-processing. This resulted in increased NCCs between 58 k*e*V and 79 k*e*V MonoCT datasets, indicating shifts of less than 0.2 mm, observable also in the coughing patient (Table 7.2, Fig. 7.13).
In contrast, movement of other organs or structures, e.g. the oesophagus or gas in the stomach, and irregularities in respiratory motion visible at the diaphragm could not be sufficiently corrected by DIR and led to remaining uncertainties in DECT-derived datasets. Since these volumes were quite small, they did not influence the NCC, but were well visible as artefacts in DECT-derived datasets, such as the SPR (Fig. 7.14).

Reliability of 79 k*e*V MonoCT for Dose Calculation

Dose distributions calculated on 140 kVp and DECT-derived 79 k*e*V MonoCT datasets were highly similar, leading to no differences in DVH parameters of OARs and CTV. Maximum dose differences for clinical treatment plans ranged between 0.2 Gy(RBE) and 0.6 Gy(RBE), resulting in $\gamma(1\,\text{mm}, 1\%) = 100\%$ for all time-averaged CT datasets and evaluated breathing phases. Even the tighter γ criterion revealed average and minimum γ passing rates of $\gamma_{\text{avg}}(1\,\text{mm}, 0.1\%) = 99.9\%$ and $\gamma_{\text{min}}(1\,\text{mm}, 0.1\%) = 99.2\%$.
Dose differences of up to 2.2 Gy(RBE) were obtained for worst-case scenarios, which still led to high γ passing rates of $\gamma_{\text{avg}}(1\,\text{mm}, 0.1\%) = 99.3\%$, $\gamma_{\text{min}}(1\,\text{mm}, 0.1\%) = 92.4\%$ and $\gamma_{\text{min}}(1\,\text{mm}, 1\%) = 98.0\%$. DVH parameters of OARs and CTV did not change.

Application of Patient-Specific Stopping-Power Prediction

The high conformity of the two 4D-DECT datasets after DIR in most cases allows for a reliable application of the patient-specific DirectSPR approach RhoSigma. In comparison to the state-of-the-art CT-number-to-SPR conversion using a generic HLUT, RhoSigma resulted in proton dose differences of up to 21.2 Gy(RBE). Overall and field-specific differences and their associated water-equivalent range shifts are illustrated in Fig. 7.15. The impact on DVH parameters depended on patient anatomy and beam direction. The volume of

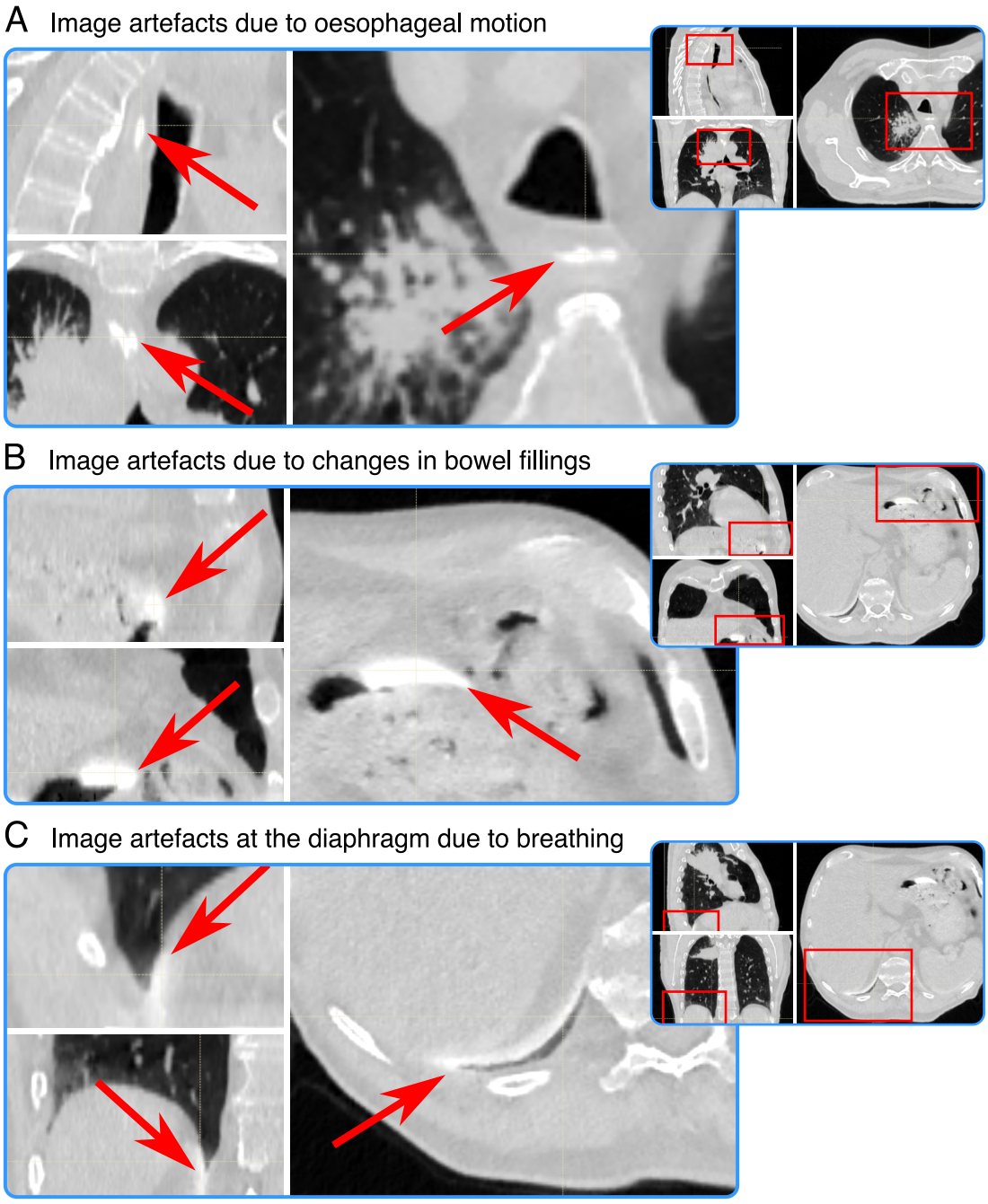

Figure 7.14: Image artefacts due to uncompensated motion in (A) oesophagus, (B) stomach and (C) diaphragm, visible as bright shining areas in the 50% exhale stopping-power datasets of patient 2. Adapted from Wohlfahrt et al. (2018c).

the contralateral lung receiving 5 Gy(RBE) increased by 4% for one patient with one beam exiting into this region (Fig. 7.15 B), while the other two patients showed smaller changes of 1.5% and 0%, respectively. Target coverage, defined by the dose applied to 98% of the

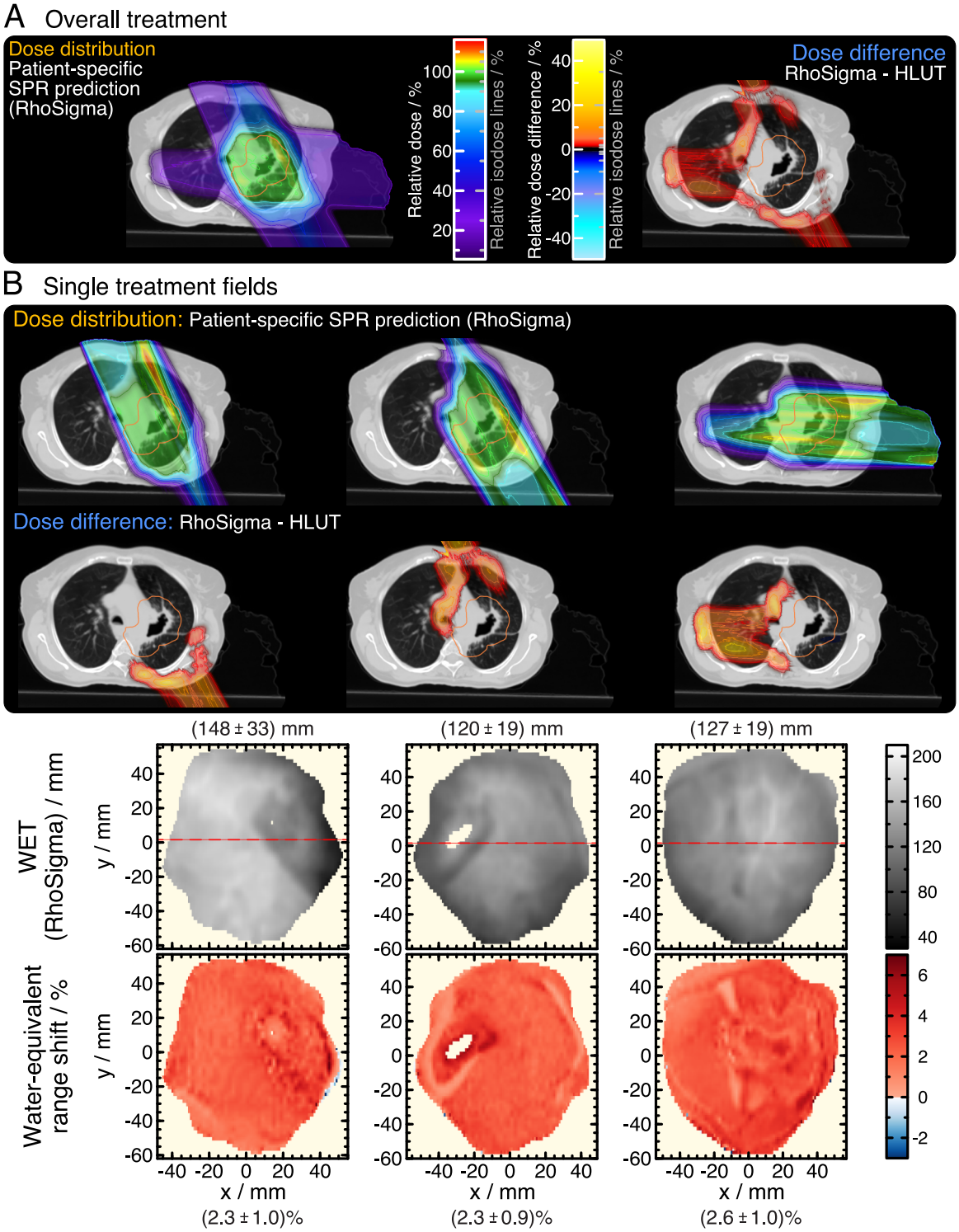

Figure 7.15: Dose distribution and difference between patient-specific SPR prediction RhoSigma and HLUT for (A) the overall treatment and (B) single treatment fields of patient 1. Assessment of WET and relative range shifts in beam direction for each treatment field. The (mean ± standard deviation) is stated for each BEV. The red dashed line indicates the axial CT slice in BEV. Adapted from Wohlfahrt et al. (2018c).

CTV, remained stable for all patients with reductions of only 0.1%. This demonstrates the robustness of the treatment planning approach against the CT-related uncertainty.

Considering all investigated depth-dose profiles obtained for all 4D-DECT datasets of each patient, a mean relative water-equivalent range shift $\pm$ standard deviation of (2.2 ± 1.2)% between the RhoSigma and HLUT approach was determined (Fig. 7.16 A). This relative shift is slightly higher compared with differences derived in cerebral and pelvic tumour patients (section 7.2). For the evaluated penetration depths, this relative shift corresponds to a mean absolute water-equivalent range shift of (2.9 ± 1.4) mm. This global bias occurred, because the HLUT predicts in particular larger SPR for different tissues such as muscles ($H \approx 40$ HU), trabecular bone ($100\,\text{HU} \leq H \leq 300\,\text{HU}$) and tissue mixtures with CT numbers ranging from -400 HU to 100 HU (Fig. 7.16 B). However, proton range shifts within a treatment field depended on the distribution of tissues traversed in beam direction and resulted in an intra-patient variability of 1.1%. This is clearly larger than the inter-patient variation of 0.1% (Fig. 7.16 A). Furthermore, range shifts were similar using the time-averaged CT dataset (2.3%) or one single breathing phase (2.2%) for dose calculation.

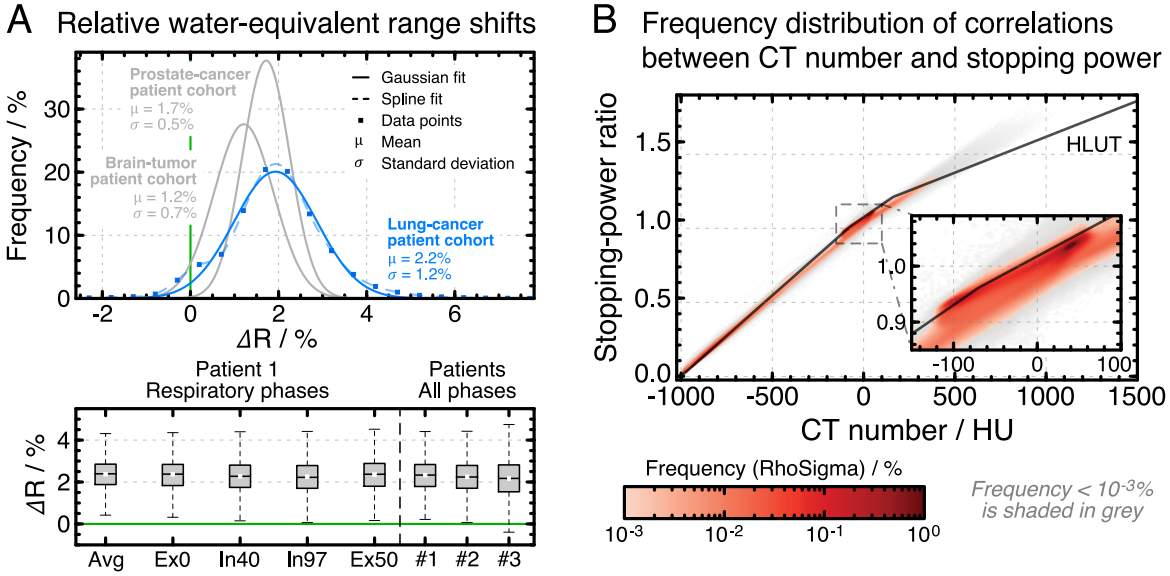

Figure 7.16: (A) Relative water-equivalent range shifts (ΔR) between RhoSigma and HLUT illustrated as frequency distribution including all depth-dose profiles and as box plot to quantify differences between respiratory phases of one representative patient and to assess the inter-patient variability considering all phases. For comparison, the ΔR distributions obtained in the brain-tumour and prostate-cancer patient cohort were additionally shown (section 7.2). Box plots are defined as illustrated in Fig. 6.3. (B) Frequency distribution of voxelwise correlations between CT number and SPR for the three evaluated NSCLC patients. Adapted from Wohlfahrt et al. (2018c).

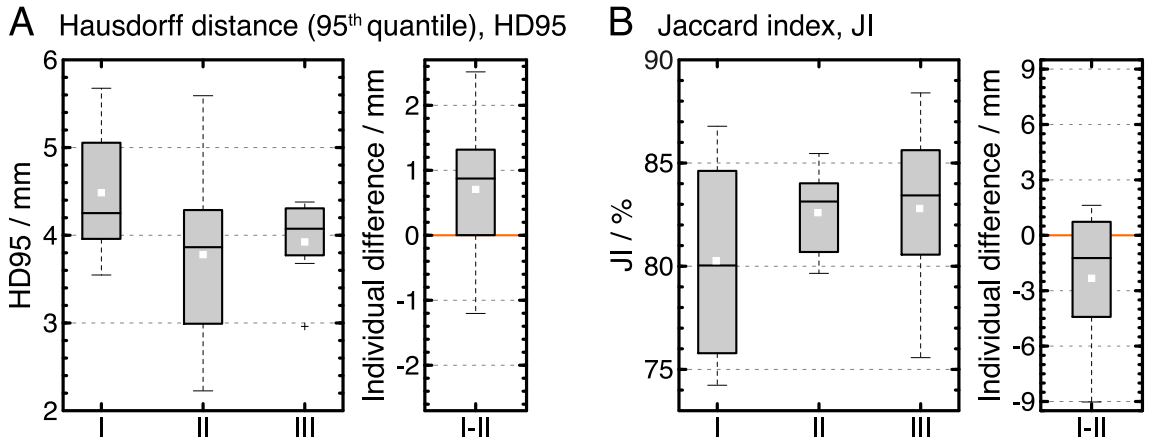

Figure 7.17: Intra-observer variability of GTV delineation using a 79 k*e*V MonoCT dataset (I) as well as a combination of a DECT-derived electron-density and 79 k*e*V cross-section dataset (II) assessed by Hausdorff distance (A) and Jaccard index (B). To quantify the delineation variability between both modalities (III), the fused GTV contours of both delineation sessions were applied. Box plots are defined as illustrated in Fig. 6.3. Adapted from Wohlfahrt et al. (2018c).

Assessment of Variability in Tumour Delineation

The intra-observer variability of GTV delineation (Supplement E.E) could be slightly reduced by jointly using DECT-derived RED and RCS datasets rather than only the 79 k*e*V MonoCT dataset (Fig. 7.17). This was indicated by an increased mean Jaccard index $\pm$ standard deviation of (82.6 ± 2.1)% compared to (80.3 ± 4.9)% and reduced mean Hausdorff distance of (3.8 ± 1.1) mm compared to (4.5 ± 0.8) mm.

The agreement between GTV contours (fusion of repeated delineations) obtained on 79 k*e*V MonoCT as well as combined RED and RCS datasets led to a mean Jaccard index of (82.8 ± 4.2)% and Hausdorff distance of (3.9 ± 0.5) mm. Since the intra-observer variability revealed comparable results, the precision of GTV delineation is almost independent from the provided datasets.

7.4.3 Discussion of Proof-of-Principle Study

This study demonstrated the clinical feasibility of dual-spiral 4D-DECT in terms of anatomical and dosimetrical consistency for treatment planning in the thoracic region based on a DECT-derived 79 k*e*V MonoCT dataset still using an HLUT. Furthermore, the large variety of image datasets for potentially improving tumour delineation as well as patient-specific DECT-based SPR prediction could be outlined.

Dual-spiral 4D-DECT assumes a high similarity in motion and anatomy between the two consecutively acquired 4D-DECT scans. Guckenberger et al. (2007) demonstrated that for the majority of patients, the position and motion patterns are stable within a 30 minute timeframe determined by multiple 4D-SECT scans. Malinowski et al. (2012) and Shah et al. (2012) showed that relevant changes in respiratory motion and tumour position become more probable with treatment time. In their lung-cancer patient cohort, the mean tumour position changed by more than 5 mm only in 2% of all cases within the first 20 minutes, but already in 13% considering a 30 minute timeframe (Malinowski et al., 2012). Since a dual-spiral 4D-DECT scan takes only a couple of minutes, it can be expected based on these investigations that relevant position and motion changes will usually occur after a longer time period as opposed to that required for dual-spiral 4D-DECT. For the patients investigated in the presented study, the differences between the two consecutively acquired 4D-DECT scans were found to be small. This allows for reliable image post-processing and eventually application of dual-spiral 4D-DECT for such a patient cohort. Thus the more accurate SPR prediction approach RhoSigma is feasible within the thoracic region.

The acquisition of 4D-DECT scans provides more detailed patient information of crucial importance for three aspects of proton therapy. First, patient-specific SPR predictions consider tissue heterogeneity and patient variability, which can lead to a more reliable dose calculation for lung-cancer patients. Since only range shifts were evaluated in this study, the impact of using a pencil-beam dose algorithm, which limits the precision of dose calculations in heterogeneous anatomical regions as thorax compared with a more sophisticated Monte Carlo approach (Grassberger et al., 2014), remains small and would not change the conclusions drawn here.

Second, multiple datasets of different image contrast can be derived from DECT, which might support a more reliable target delineation as potentially suggested by the slightly reduced intra-observer variability of GTV delineation in this NSCLC patient cohort. To determine the effect on delineation more adequately, further studies should include more patients, more physicians to assess the inter-observer variability and additional DECT-derived datasets to obtain optimal settings. As delineation of lung tumours is supposed to be more robust, owing to the large CT image contrast to surrounding tissues, such a study should also be extended to other tumour entities to analyse site-specific advantages.

Third, information on motion variability can be gained. Differences in breathing pattern over time are a general challenge in radiotherapy, where a 4D-SECT scan acquired days to

weeks before treatment is used as single baseline for therapy. The comparison of the two CT datasets of a dual-spiral 4D-DECT scan can contribute to identify patients with irregular and non-representative breathing patterns or to illustrate oesophageal motion and regions of severe gastro-intestinal peristalsis during CT acquisition. These patients might currently not be appropriate for reliable and accurate DECT-based SPR prediction. However, since SPR datasets visualise regions of severe motion, an additional image-based algorithm can be developed in the future to detect motion-induced changes and consider them in SPR prediction. Even if too large differences during dual-spiral 4D-DECT acquisition hamper the calculation of reliable DECT-based datasets, still important information on motion variability and reliability regarding iGTV delineation can be gathered. The two consecutively acquired 4D-DECT scans could also be included in robust optimisation techniques incorporating breathing variability in treatment planning (Li et al., 2015; Van Der Voort et al., 2016; Stützer et al., 2017b). Furthermore, this could also highlight patients who may require the application of a breathing suppression technique, a close intra-therapeutic monitoring to ensure short-term plan adaptations or even real-time imaging during treatment (Péguret et al., 2016).

As the quality of 4D-DECT depends on the respiration reproducibility between the two DECT scans, all patients within this clinical trial received detailed instructions and explanations about the upcoming procedure in order to calm down and relax. After final patient preparation, the radiation therapy technologist wait until the breathing pattern is regular and reproducible and then start CT acquisition. Clinical time pressure might oppose that aim resulting in unstable respiration cycles. In such cases, standard SECT-based dose calculation can always be performed without limitations using only the 140 kVp CT dataset. Thus, DECT scans of patients will provide additional information without being a disadvantage for the individual patient.

In this proof-of-principle study, only six dual-spiral 4D-DECT scans of three advanced stage NSCLC patients with small tumour motion were investigated. As most advanced stage NSCLC tumours do not move substantially (Li et al., 2014), the presented results will be valid for the majority of these patients. To assess whether the presented results can be translated to patients with more complex tumour geometries and movements, an additional study on 4D-DECT is currently being planned including more patients with larger tumour motion and other tumour locations within the lung, which may have a larger impact on proton dose calculation as shown for the diaphragm region.

7.5 DECT-Based Refinement of the Hounsfield Look-Up Table

As demonstrated in the previous sections, the acquisition of dual-spiral DECT scans for proton treatment planning is clinically feasible for patients with cerebral, pelvic or thoracic tumours. For each investigated patient cohort, systematic proton range deviations between two CT-number-to-SPR conversions – the state-of-the-art HLUT and patient-specific Direct-SPR approach RhoSigma – were determined ranging from 1.2% (brain) to 2.3% (lung) on average. A refinement of the HLUT using stopping-power information obtained from patient DECT scans, as introduced in section 7.3 for brain-tumour patients, can significantly reduce systematic SPR deviations between the two methods by considering the composition and distribution of tissues within patients instead of using tissue surrogates for CT scanner characterisation and HLUT specification (Wohlfahrt et al., 2017a).
In the following study, the brain-, prostate- and lung-cancer patient cohorts were analysed to determine whether the reduction of systematic SPR deviations achieved by an HLUT refinement directly translates into decreased proton range shifts, which eventually contributes to an improved dose calculation. Furthermore, it was assessed whether an individual optimisation of the HLUT for each patient cohort performs better than a single HLUT adaptation including all patient information independent from the treated tumour entity.

7.5.1 Optimisation of the Hounsfield Look-Up Table

The HLUT refinement introduced in section 7.3 was based on the distribution of human tissues in the external contour of brain-tumour patients. To perform an optimal adaptation for proton therapy, the respective tissue distribution within the irradiated volume of each patient including also immobilisation devices would be a more realistic selection of the regions to be considered in treatment planning. DECT scans of the 25 brain-tumour and 25 prostate-cancer patients presented in section 7.2 as well as the three lung-cancer patients analysed in section 7.4 were investigated to refine the clinical HLUT using DECT-derived patient information within the irradiated volume defined by the 20% isodose.

Specification of the Adapted Hounsfield Look-Up Table

Based on the frequency distribution of voxelwise correlations between CT numbers of a 79 k*e*V MonoCT dataset and SPRs derived from RhoSigma, the median SPR of each

CT number was determined. Subsequently, the Hounsfield scale was divided in four regions representing different tissue groups: low-density (-900 HU $\leq H \leq$ -150 HU), adipose (-120 HU $\leq H \leq$ -70 HU), muscle and brain (-20 HU $\leq H \leq$ 70 HU) as well as bone tissue (200 HU $\leq H \leq$ 1350 HU). For each group, the median SPR distribution was described by an intensity-weighted linear regression depending on the relative occurrence of the respective CT number. The transitions between different regions were linearly connected.
The HLUT was adapted separately for each patient cohort as well as collectively considering the frequency distributions of (H, $\hat{S}$) correlations equally weighted for all cohorts (Fig. 7.18). To assess the performance of each adapted HLUT compared with RhoSigma, SPR deviations and proton range shifts were quantified as described in section 7.2.

Assessment of Differences in Stopping-Power Ratio

In accordance with the results obtained for 102 brain-tumour patients (Fig. 7.11), an HLUT refinement based on DECT can substantially reduce systematic SPR deviations between RhoSigma and the clinically applied HLUT in the evaluated cerebral, pelvic and thoracic tumour patients (Fig 7.19). After the cohort-specific as well as global HLUT adaptation, the mean SPR deviation of each investigated patient cohort was within 0.2%. In comparison to a globally adapted HLUT considering all patients independent from their tumour entity, an

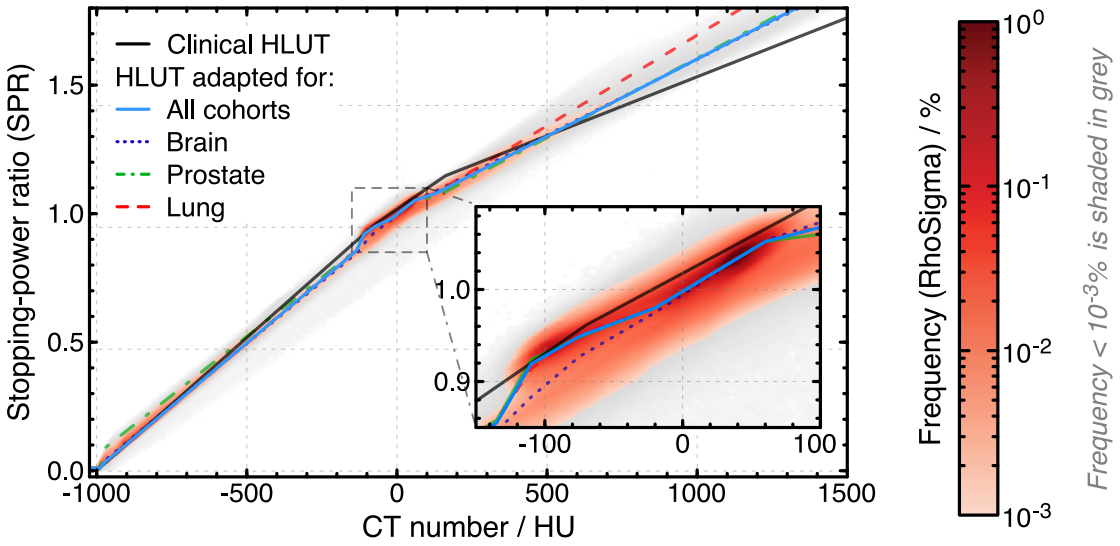

Figure 7.18: Frequency distribution of voxelwise correlations between CT number obtained from 79 keV MonoCT datasets and SPR derived by RhoSigma as well as the respective HLUTs before and after HLUT refinement based on DECT information.

HLUT separately refined for each cohort performed only slightly better and led to a further reduction of absolute SPR deviations of approximately 0.1% on average. With respect to other uncertainties in dose calculation, the small improvement of a cohort-specific HLUT refinement can be neglected. From a clinical point of view, the application of a single HLUT would also facilitate the clinical workflow and prevent possible errors caused by an incorrectly assigned HLUT. Hence, the globally adapted HLUT was used for dose calculation to evaluate the influence of an HLUT refinement on proton range.

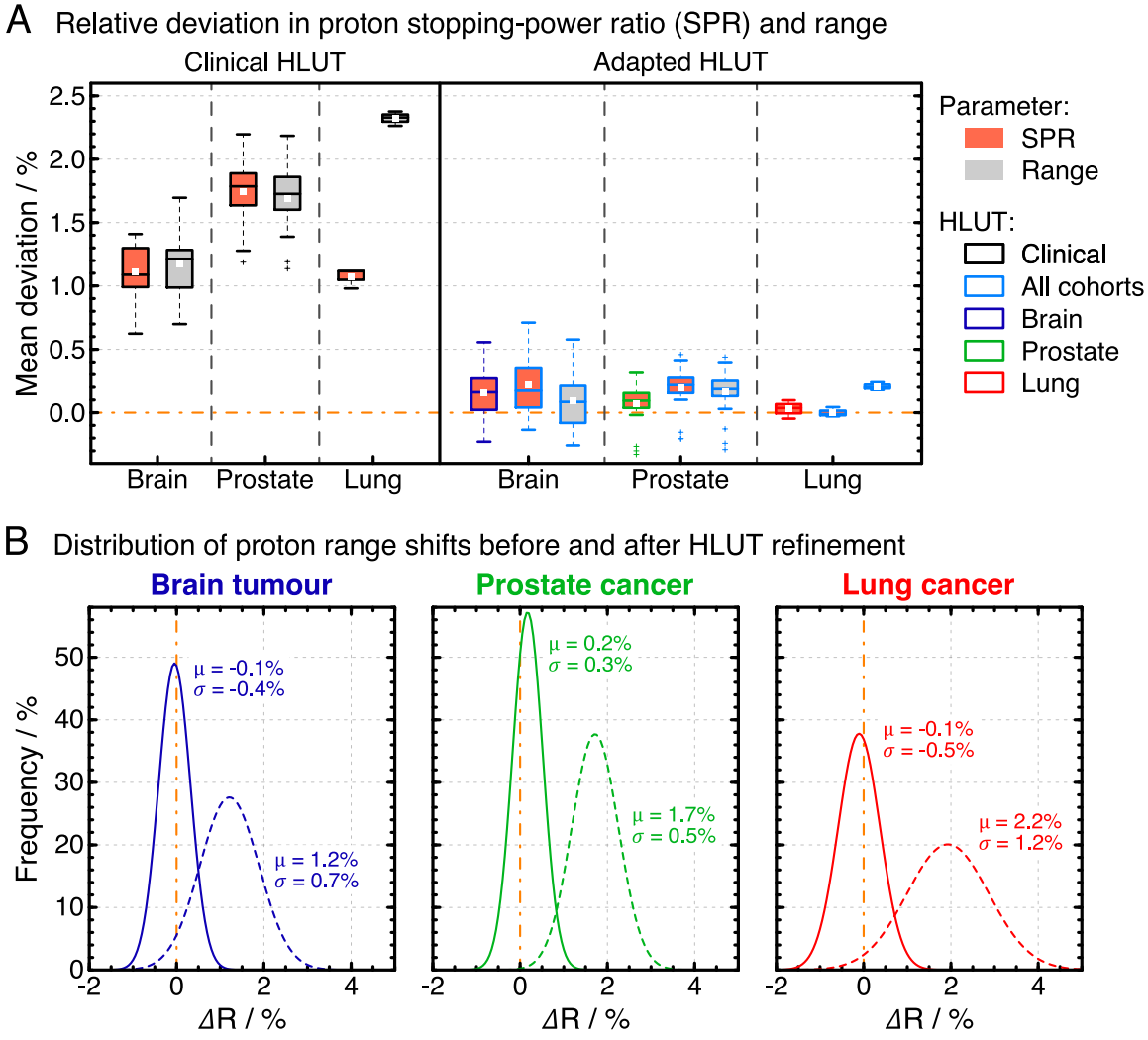

Figure 7.19: (A) Distribution of mean SPR deviations and water-equivalent range shifts between the DirectSPR approach RhoSigma and the clinically applied HLUT as well as the HLUT adapted separately for each patient cohort or collectively considering all cohorts. Box plots are defined as illustrated in Fig. 6.3. (B) Distribution of range shifts between RhoSigma and HLUT before (dashed line) and after (solid line) HLUT refinement. A Gaussian distribution was fitted to the data.

Assessment of Proton Range Shifts

The mean relative water-equivalent range shift ± standard deviation was reduced from (1.17 ± 0.22)% to (0.09 ± 0.20)% for cerebral, (1.69 ± 0.24)% to (0.16 ± 0.17)% for pelvic and (2.32 ± 0.05)% to (0.21 ± 0.02)% for thoracic tumour patients using the globally adapted HLUT (Fig. 7.19). This is consistent with the results obtained on the SPR level for brain-tumour and prostate-cancer patients.

However, the distributions of mean SPR deviations and water-equivalent range shifts differ considerably for the lung-cancer patient cohort (Fig. 7.19). This is certainly caused by the severe tissue inhomogeneities within the irradiated volume of lung-cancer patients, leading to an increase of multiple Coulomb scattering. Since proton scattering while traversing heterogeneous tissue regions is included in dose calculation, range shifts derived from dose distributions also cover its influence. However, on the SPR domain this effect cannot be considered.

The influence of a DECT-based HLUT refinement on dose distributions is exemplarily illustrated for a representative prostate-cancer patient in Fig. 7.20.

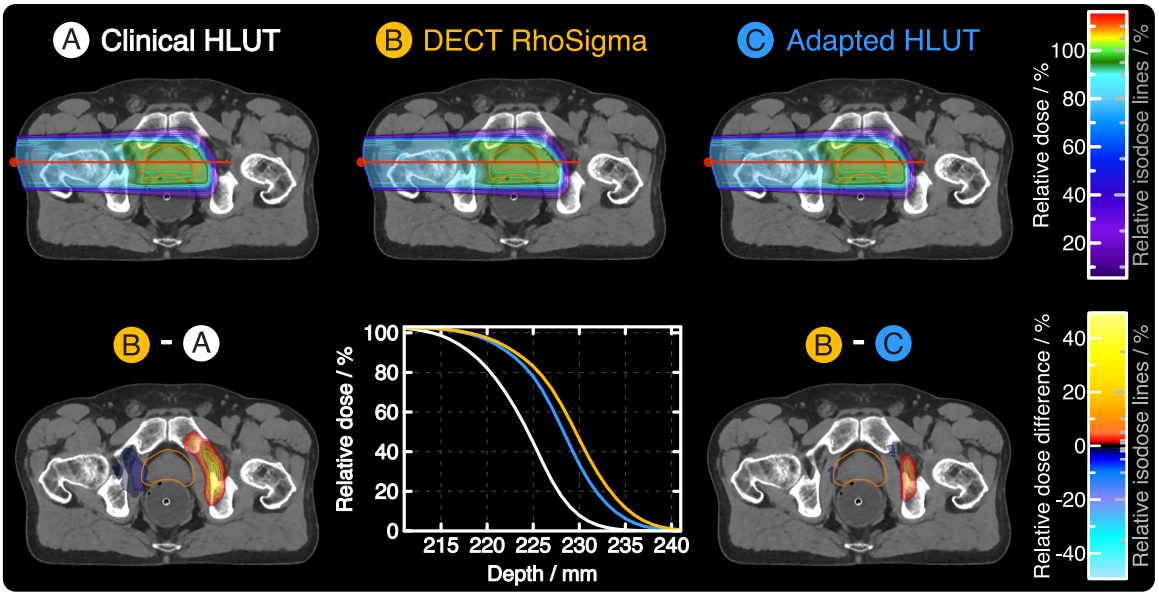

Figure 7.20: Single treatment field of a representative prostate-cancer patient calculated on (A) a 79 keV MonoCT dataset using the clinical HLUT, (B) patient-specific DECT-based SPR dataset obtained by RhoSigma and (C) a 79 keV MonoCT dataset using the DECT-based adapted HLUT including all patient cohorts. The dose-difference distribution between DECT-based and each HLUT-based treatment plan revealed clearly reduced dose deviations and range shifts using the adapted instead of the clinical HLUT. The red line indicates the evaluated beam path.

7.5.2 Discussion of the Clinical Relevance

The systematic bias in CT-based SPR and proton range prediction between a state-of-the-art HLUT and the patient-specific DirectSPR approach RhoSigma can be reduced by adapting the HLUT based on additional patient information derived from DECT. This can contribute to an increased SPR accuracy in proton therapy and could thus be used clinically until an approved medical device for patient-individualised scanner-specific DECT-based SPR prediction is available and fully integrated into routine treatment planning. A global HLUT adaptation including DECT information of patients with various tumour entities in different body regions led to SPR and range deviations of below 0.2% on average.

Still, the clinical use of an HLUT assumes an ideal compensation of SPR under- and overestimation for various tissues in beam direction. Beam paths differing from the mean tissue distribution will be further affected and case-dependent range deviations can occur. The application of a patient-specific DECT-based DirectSPR prediction would additionally account for the large intra- and inter-patient tissue variability in proton treatment planning (section 7.3).

Based on the presented investigations, the clinical HLUT was adapted at OncoRay in 2017 using patient-specific DECT information derived from the brain-tumour and prostate-cancer cohorts with 50 patients in total. The resulting HLUT is comparable to the global HLUT adapted for all patient cohorts. This HLUT refinement was a further step toward the routine clinical use of a patient-specific DECT-based stopping-power prediction.

8 Summary

Dual-energy CT (DECT) was already suggested in the 1970s as a promising imaging modality to reduce the CT-related range uncertainty in particle therapy (Goitein, 1977). However, it had not been introduced in radiotherapy until the work on this thesis has been started at the end of 2014 (van Elmpt et al., 2016). This thesis was dedicated to the translation of DECT into clinical application in particle therapy by assessing the accuracy and relevance of DECT for treatment planning in theoretical and experimental studies as well as retrospective patient cohort analyses. Major contributions were achieved in the:

- development of a DECT scan protocol appropriate for radiotherapy applications,
- experimental validation of SPR accuracy in ground-truth settings,
- assessment of the clinical relevance of DECT-based stopping-power prediction and its potential to incorporate the tissue variability of patients,
- clinical implementation of an HLUT that was refined using patient information gathered by DECT-based range prediction.

To gain an improved accuracy in radiotherapy with respect to DECT acquisition, a comprehensive characterisation of CT scanners and calibration of algorithms for electron-density as well as stopping-power prediction are indispensable. Quantitative CT scans with high spatial resolution, low image noise and high CT number constancy concerning variations in patient size are an integral component for reliable dose calculation. As demonstrated in this thesis, the influence of beam hardening on CT numbers is appropriately considered by a beam hardening correction for water and bone as included in a dedicated reconstruction kernel. Moreover, the application of an iterative reconstruction algorithm and image post-processing of DECT scans including a multi-band filtering lead to an efficient reduction of image noise.

The accuracy of stopping-power prediction based on DECT-derived voxelwise material parameters such as electron density and photon attenuation cross section was validated within this thesis. For this purpose, the geometrical heterogeneity and realistic human tis-

sue composition were uncoupled and investigated in two independent experimental studies. Due to the separation of both effects, an unprecedented measurement uncertainty of below 0.3% in SPR and 1 mm in proton range was achieved. For homogeneous biological tissue samples, the SPRs derived from DECT were within 0.2% accuracy and thus exceed the accuracy achieved by single-energy CT (SECT) with a mean absolute error of 1.3%. DECT also outperformed SECT on the SPR level in a ground-truth anthropomorphic head phantom as shown by a 10% to 15% higher γ passing rate. These validations confirmed the high accuracy of DECT-based SPR prediction and underlined the potential of DECT to reduce the CT-related uncertainty in proton treatment planning for patients. Despite the improved reliability of DECT compared with SECT on the SPR level, it was shown that image smoothing during image reconstruction and post-processing can still influence proton range computation in heterogeneous regions. This effect is independent from the applied SPR prediction approach and needs to be further assessed.

Within this thesis, a stepwise clinical implementation of dual-energy CT in proton therapy was introduced to ensure a safe application, allowing for a continuous improvement in a clinical setting. As a first step, the clinical applicability and safety of DECT-derived pseudo-monoenergetic CT (MonoCT) datasets, still relying on the same heuristic CT-number-to-SPR conversion (HLUT), were demonstrated for proton treatment planning. Furthermore, an enhanced image quality compared with 120 kVp SECT, the current standard CT imaging technique in radiation oncology, was determined without an increase in CT dose. Consequently, OncoRay – as the worldwide first proton therapy facility – has been performing proton treatment planning on DECT-derived 79 k*e*V MonoCT datasets since 2015. The continuously growing database of clinical DECT scans enabled a retrospective analysis for cerebral, pelvic and thoracic tumour patients. This study revealed clinically relevant proton range shifts between the application of a HLUT and a direct DECT-based SPR prediction, which were significantly larger than 1% on average and partly exceeded 2.5% of the total range. These large deviations in combination with the previously demonstrated superiority of DECT-based SPR prediction demanded for a refinement of the clinically applied proton range prediction. To minimise the systematic range deviations, an HLUT was specified according to the DECT-derived SPR distribution including information of brain-tumour and prostate-cancer patients. In July 2017, the resulting HLUT was clinically implemented at OncoRay. For the first time, treatment planning in proton therapy was thus clinically adapted based on the retrospectively applied direct DECT-based SPR prediction. This al-

ready leads to an improved range prediction in patients. However, the intra-patient soft tissue diversity and age-related variability in bone composition, resulting in a mean SPR variation of approximately 5% as determined within this thesis for brain-tumour patients, cannot be fully covered by a generic HLUT. The application of the patient-specific DECT-based SPR prediction would account for this tissue variability. Moreover, the development of a standardised scanner-specific calibration for electron-density and stopping-power prediction – e.g. directly included in the DECT image post-processing and provided by the CT vendor – would remove the necessity of cumbersome institute-specific calibration and validation. Furthermore, it would generate quantitative 3D images of tissue parameters fulfilling the high demands of radiotherapy applications, such as Monte Carlo dose calculation, and further techniques for quantitative image analysis such as radiomics (Aerts et al., 2014; Lambin et al., 2017).

Based on the results obtained in this thesis, it can be concluded that dual-energy CT is clinically applicable in radiotherapy and allows for an accurate, safe and reliable prediction of electron density and proton stopping power, which is required for treatment planning in photon and proton therapy, respectively. The improved accuracy and robustness of DECT-based SPR prediction might allow for a reduction of clinically applied margins accounting for the CT-related range uncertainty. This represents an important step to optimise the treatment delivery in proton therapy.

9 Zusammenfassung

Die Zwei-Spektren-Computertomographie (DECT) wurde bereits in den 1970er Jahren als eine vielversprechende Bildgebungsmethode angesehen, die zu einer Reduktion der CT-bedingten Reichweiteunsicherheit in der Partikeltherapie beitragen kann (Goitein, 1977). Trotzdessen wurde DECT bis zum Beginn dieser Arbeit im Jahr 2014 nicht in der Strahlentherapie eingesetzt (van Elmpt u. a., 2016). In der vorliegenden Arbeit wurde die klinische Anwendbarkeit von DECT in der Partikeltherapie untersucht. Hierbei wurde die Genauigkeit und Relevanz von DECT für die Bestrahlungsplanung in theoretischen und experimentellen Studien sowie retrospektiven Analysen von Patientenkohorten evaluiert. Im Rahmen dieser Arbeit wurden wesentliche Beiträge geleistet bei:

- der Entwicklung eines DECT-Scanprotokolls, welches für die Anwendungen in der Strahlentherapie geeignet ist,
- der experimentellen Validierung der Genauigkeit des relativen Bremsvermögens von Protonen (SPR) gegen eine absolute Referenz,
- der Bewertung der klinischen Relevanz von DECT-basierter SPR-Vorhersage und ihres Potentials zur Berücksichtigung der Gewebevariabilität von Patienten,
- der klinischen Implementierung einer heuristischen Konvertierung (HLUT), die auf Grundlage der Ergebnisse der DECT-basierten Reichweitevorhersage in Patienten neu definiert wurde.

Um eine Verbesserung der Genauigkeit in der Strahlentherapie mit Hilfe von DECT erreichen zu können, ist eine umfassende Charakterisierung des CT-Scanners und eine gründliche Kalibrierung der Algorithmen zur voxelweisen Bestimmung der Elektronendichte und des Bremsvermögens von Protonen unverzichtbar. Quantitative CT-Aufnahmen mit hoher Ortsauflösung, niedrigem Bildrauschen und hoher Stabilität von CT-Zahlen sind ein wichtiger Bestandteil für eine zuverlässige Dosisberechnung. In dieser Arbeit konnte gezeigt werden, dass der Einfluss von Strahlaufhärtung auf CT-Zahlen durch die Anwendung einer Strahlaufhärtungskorrektur bezüglich Wasser und Knochen, welche in dedizierten Rekon-

struktionskernen enthalten ist, angemessen berücksichtigt wird. Des Weiteren kann durch die Verwendung von iterativen Rekonstruktionsalgorithmen und Frequenzfiltern in der Bildnachbearbeitung von DECT-Aufnahmen das Bildrauschen effizient verringert werden.
In dieser Arbeit wurde außerdem die Genauigkeit der DECT-basierten SPR-Vorhersage auf Grundlage von voxelweisen Materialparametern wie der Elektronendichte und des Wechselwirkungsquerschnittes von Photonen validiert. Hierfür wurden zwei unabhängige Experimente durchgeführt, die zum Einen die Auswirkungen einer heterogenen Geometrie und zum Anderen den Einfluss von menschenähnlichen Geweben auf die SPR-Genauigkeit untersuchten. Durch die Separation der beiden Einflussgrößen konnte die Messunsicherheit in jedem Einzelexperiment auf unter 0.3% in SPR und 1 mm in der Protonenreichweite reduziert werden. Für homogene biologische Gewebeproben war die DECT-basierte SPR-Vorhersage stets innerhalb einer Genauigkeit von 0.2% and damit deutlich besser als die mittlere absolute Abweichung von 1.3%, die bei der Verwendung von nur einem CT-Scan (SECT) erreicht wurde. Auch im anthropomorphen Kopfphantom erzielte DECT bei der SPR-Vorhersage deutlich bessere Ergebnisse als SECT, was sich in einer 10% bis 15% höheren γ Erfolgsquote widerspiegelte. Diese experimentellen Validierungen bestätigen die hohe Genauigkeit einer DECT-basierten SPR-Vorhersage und unterstreichen das Potential von DECT, die CT-bedingte Unsicherheit in der Protonentherapie bei der Bestrahlungsplanung von Patienten zu reduzieren. Trotz der verbesserten Genauigkeit von DECT im Vergleich zu SECT auf SPR-Ebene konnte gezeigt werden, dass die Bildglättung während der Bildrekonstruktion und -nachbearbeitung dennoch die Berechnung der Protonenreichweite in heterogenen Bereichen beeinflussen kann. Dieser Effekt ist unabhängig von der verwendeten Vorhersagemethode und sollte in weiterführenden Studien näher untersucht werden.
Innerhalb dieser Arbeit wurde eine schrittweise klinische Einführung von DECT in die Protonentherapie vorgestellt, die eine sichere Anwendung zulässt und gleichzeitig eine stete Weiterentwicklung unter klinischen Bedingungen ermöglicht. Zunächst wurde die klinische Anwendbarkeit und Sicherheit von pseudo-monoenergetischen CT-Datensätzen (MonoCT) für die Bestrahlungsplanung in der Protonentherapie nachgewiesen. Diese MonoCT-Datensätze wurden mit Hilfe des DECT-Scans generiert und verwenden weiterhin eine heuristische Konversion von CT-Zahlen zu Protonenbremsvermögen (HLUT). Des Weiteren besitzen die MonoCT-Datensätze eine bessere Bildqualität im Vergleich zu 120 kVp SECT-Aufnahmen, die mit der gleichen Dosis aufgenommen wurden und das derzeitige Stan-

dardverfahren in der Strahlentherapie darstellen. Dementsprechend hat man sich am OncoRay im Jahr 2015 entschlossen, als erste Protonentherapie weltweit, die Bestrahlungsplanung auf 79 k*e*V MonoCT-Datensätzen durchzuführen. Die dadurch kontinuierlich wachsende Datenbank an klinischen DECT-Aufnahmen ermöglichte eine retrospektive Analyse von Krebspatienten mit Tumoren im Kopf, Becken oder Thorax. In dieser Studie konnten klinisch relevante Reichweiteverschiebungen zwischen der Anwendung einer HLUT und einer direkten DECT-basierten SPR-Vorhersage festgestellt werden. Diese waren signifikant größer als 1% im Mittel und teilweise sogar größer als 2.5% relativ zur Gesamtreichweite. Diese großen Abweichungen in Verbindung mit der bereits nachgewiesenen Genauigkeit der DECT-basierten SPR-Vorhersage erforderten eine Anpassung der klinisch verwendeten Reichweitevorhersage. Um die systematischen Reichweiteunterschiede zu minimieren, wurde eine HLUT auf Grundlage einer mit DECT generierten SPR-Verteilung von Kopftumor- und Prostatakrebspatienten erstellt. Im Juli 2017 wurde die resultierende HLUT schließlich am OncoRay klinisch eingeführt. Somit wurde erstmalig die Bestrahlungsplanung in der Protonentherapie auf Grundlage der retrospektiven Anwendung der DECT-basierten SPR-Vorhersage klinisch angepasst. Dies führte bereits zu einer besseren Reichweitevorhersage in Patienten. Jedoch kann die Vielfalt an Weichteilgeweben innerhalb eines Patienten sowie die altersbedingte Änderung der Knochenzusammensetzung von einer HLUT nicht vollständig abgedeckt werden, da diese jeweils zu einer mittleren SPR-Streuung von ungefähr 5% beitragen können, wie in Kopftumorpatienten im Rahmen dieser Arbeit festgestellt wurde. Die Anwendung einer patientenindividuellen DECT-basierten SPR-Vorhersage kann die Gewebevariabilität in der Berechnung berücksichtigen. Außerdem würde die Entwicklung einer standardisierten und scanner-spezifischen Kalibrierung zur genauen Vorhersage von Elektronendichte und Protonenbremsvermögen die Notwendigkeit einer umständlichen Kalibrierung und Validierung in jedem Institut aufheben. Ein solches Tool könnte direkt bei der Bildnachbearbeitung von DECT-Aufnahmen zum Einsatz kommen und von CT-Herstellern zur Verfügung gestellt werden. So könnten institutsübergreifend quantitative Bilddatensätze von Gewebeparametern generiert werden, die den hohen Anforderungen an Anwendungen in der Strahlentherapie, wie z.B. Monte Carlo basierte Dosisberechnung, und weiteren Bildanalysetechniken wie Radiomics gerecht werden (Aerts u. a., 2014; Lambin u. a., 2017).

Aus den Ergebnissen dieser Arbeit folgt, dass die Zwei-Spektren-Computertomographie klinisch in der Strahlentherapie anwendbar ist and eine genaue, sichere und verlässliche

Vorhersage von Elektronendichte und Protonenbremsvermögen liefert, die für die Bestrahlungsplanung in der Photonen- bzw. Protonentherapie notwendig sind. Die verbesserte Genauigkeit und Robustheit der DECT-basierten SPR-Vorhersage kann zukünftig eine Reduzierung des klinischen Sicherheitssaumes ermöglichen, der derzeit die CT-bezogene Reichweiteunsicherheit enthält. Dies ist ein wichtiger Schritt, um die Dosisapplikation in der Protonentherapie weiter zu optimieren.

Bibliography

Aerts HJWL, Velazquez ER, Leijenaar RTH, Parmar C, Grossmann P, Cavalho S, Bussink J, Monshouwer R, Haibe-Kains B, Rietveld D, Hoebers F, Rietbergen MM, Leemans CR, Dekker A, Quackenbush J, Gillies RJ, and Lambin P. 2014. Decoding Tumour Phenotype by Noninvasive Imaging Using a Quantitative Radiomics Approach. Nature Communications 5. DOI: 10.1038/ncomms5006. arXiv: arXiv:1011.1669v3.

Albrecht MH, Scholtz JE, Kraft J, Bauer RW, Kaup M, Dewes P, Bucher AM, Burck I, Wagenblast J, Lehnert T, Kerl JM, Vogl TJ, and Wichmann JL. 2015. Assessment of an Advanced Monoenergetic Reconstruction Technique in Dual-Energy Computed Tomography of Head and Neck Cancer. European Radiology 25:2493–2501. DOI: 10.1007/s00330-015-3627-1.

Almeida IP, Schyns LEJR, Öllers MC, van Elmpt W, Parodi K, Landry G, and Verhaegen F. 2017. Dual-Energy CT Quantitative Imaging: A Comparison Study Between Twin-Beam and Dual-Source CT Scanners. Medical Physics 44:171–179. DOI: 10.1002/mp.12000.

Apolle R, Rehm M, Bortfeld TR, Baumann M, and Troost EGC. 2017. The Clinical Target Volume in Lung, Head-and-Neck, and Esophageal Cancer: Lessons from Pathological Measurement and Recurrence Analysis. Clinical and Translational Radiation Oncology 3:1–8. DOI: 10.1016/j.ctro.2017.01.006.

Bär E, Lalonde A, Royle G, Lu HM, and Bouchard H. 2017. The Potential of Dual-Energy CT to Reduce Proton Beam Range Uncertainties. Medical Physics 44:2332–2344. DOI: 10.1002/mp.12215.

Baumann M, Krause M, Overgaard J, Debus J, Bentzen SM, Daartz J, Richter C, Zips D, and Bortfeld TR. 2016. Radiation Oncology in the Era of Precision Medicine. Nature Reviews Cancer 16:234–249. DOI: 10.1038/nrc.2016.18.

Berger MJ, Hubbell JH, Seltzer SM, Chang J, Coursey JS, Sukumar R, Zucker DS, and Olsen K. 1990. XCOM: Photon Cross Section Database (Online Version 1.5, 2010). NIST Standard Reference Database 8. URL: http://physics.nist.gov.xcom.

Bert C and Durante M. 2011. Motion in Radiotherapy: Particle Therapy. Physics in Medicine and Biology 56:R113–R144. DOI: 10.1088/0031-9155/56/16/R01.

Bethe H. 1930. Zur Theorie des Durchgangs schneller Korpuskularstrahlen durch Materie. Annalen der Physik 397:325–400. DOI: 10.1002/andp.19303970303.

Borras JM, Barton M, Grau C, Corral J, Verhoeven R, Lemmens V, van Eycken L, Henau K, Primic-Zakelj M, Strojan P, Trojanowski M, Dyzmann-Sroka A, Kubiak A, Gasparotto C, Defourny N, Malicki J, Dunscombe P, Coffey M, and Lievens Y. 2015. The Impact of Cancer Incidence and Stage on Optimal Utilization of Radiotherapy: Methodology of a Population Based Analysis by the ESTRO-HERO project. Radiotherapy and Oncology 116:45–50. DOI: 10.1016/j.radonc.2015.04.021.

Bortfeld T. 1997. An Analytical Approximation of the Bragg Curve for Therapeutic Proton Beams. Medical Physics 24:2024–2033. DOI: 10.1118/1.598116.

Bortfeld TR and Loeffler JS. 2017. Three Ways to Make Proton Therapy Affordable. Nature 549:451–453. DOI: 10.1038/549451a.

Bourque AE, Carrier JF, and Bouchard H. 2014. A Stoichiometric Calibration Method for Dual Energy Computed Tomography. Physics in Medicine and Biology 59:2059–2088. DOI: 10.1088/0031-9155/59/8/2059.

Bragg WH and Kleeman R. 1905. On the Alpha Particles of Radium, and Their Loss of Range in Passing Through Various Atoms and Molecules. Philosophical Magazine 10:318–340. DOI: 10.1080/14786440509463378.

Brooks RA. 1977. A Quantitative Theory of the Hounsfield Unit and its Application to Dual Energy Scanning. Journal of Computer Assisted Tomography 1:487–493. DOI: 10.1097/00004728-197710000-00016.

Chen GTY, Singh RP, Castro JR, Lyman JT, and Quivey JM. 1979. Treatment Planning for Heavy Ion Radiotherapy. International Journal of Radiation Oncology Biology Physics 5:1809–1819. DOI: 10.1016/0360-3016(79)90564-9.

Das IJ and Paganetti H (eds). 2015. Principles and Practice of Proton Beam Therapy. Medical Physics Publishing, Madinson, Winconsin, USA.

Enghardt W, Debus J, Haberer T, Hasch BG, Hinz R, Jäkel O, Krämer M, Lauckner K, Pawelke J, and Pönisch F. 1999. Positron Emission Tomography for Quality Assurance of Cancer Therapy with Light Ion Beams. Nuclear Physics A 654:1047c–1050c. DOI: 10.1016/S0375-9474(00)88597-8.

Enghardt W, Fromm WD, Geissel H, Heller H, Kraft G, Magel A, Manfrass P, Münzenberg G, Nickel F, Pawelke J, Schardt D, Scheidenberger C, and Sobiella M. 1992. The Spatial Distribution of Positron-Emitting Nuclei Generated by Relativistic Light Ion Beams in Organic Matter. Physics in Medicine and Biology 37:2127–2131. DOI: 10.1088/0031-9155/37/11/009.

Espina C, Herrero R, Sankaranarayanan R, Krug E, Wild CP, and Schüz J. 2018. Toward the World Code Against Cancer. Journal of Global Oncology:1–8. DOI: 10.1200/JGO.17.00145.

Farace P, Righetto R, and Meijers A. 2016. Pencil Beam Proton Radiography Using a Multilayer Ionization Chamber. Physics in Medicine and Biology 61:4078–4087. DOI: 10.1088/0031-9155/61/11/4078.

Fippel M and Soukup M. 2004. A Monte Carlo Dose Calculation Algorithm for Proton Therapy. Medical Physics 31:2263–2273. DOI: 10.1118/1.1769631.

Flohr T, Ohnesorge B, Bruder H, Stierstorfer K, Simon J, Suess C, and Schaller S. 2003. Image Reconstruction and Performance Evaluation for ECG-Gated Spiral Scanning with a 16-Slice CT System. Medical Physics 30:2650–2662. DOI: 10.1118/1.1593637.

Flohr TG, McCollough CH, Bruder H, Petersilka M, Gruber K, Süß C, Grasruck M, Stierstorfer K, Krauss B, Raupach R, Primak AN, Küttner A, Achenbach S, Becker C, Kopp A, and Ohnesorge BM. 2006. First Performance Evaluation of a Dual-Source CT (DSCT) System. European Radiology 16:256–268. DOI: 10.1007/s00330-005-2919-2.

Flohr TG, Stierstorfer K, Raupach R, Ulzheimer S, and Bruder H. 2004. Performance Evaluation of a 64-Slice CT System with Z-Flying Focal Spot. Fortschritte auf dem Gebiet der Röntgenstrahlen und der Bildgebenden Verfahren 176:1803–1810. DOI: 10.1055/s-2004-813717.

Flohr TG, Stierstorfer K, Ulzheimer S, Bruder H, Primak AN, and McCollough CH. 2005. Image Reconstruction and Image Quality Evaluation for a 64-Slice CT Scanner with Z-Flying Focal Spot. Medical Physics 32:2536–2547. DOI: 10.1118/1.1949787.

Forghani R, Levental M, Gupta R, Lam S, Dadfar N, and Curtin HD. 2015. Different Spectral Hounsfield Unit Curve and High-Energy Virtual Monochromatic Image Characteristics of Squamous Cell Carcinoma Compared with Nonossified Thyroid Cartilage. American Journal of Neuroradiology 36:1194–1200. DOI: 10.3174/ajnr.A4253.

Fredriksson A, Forsgren A, and Hårdemark B. 2011. Minimax Optimization for Handling Range and Setup Uncertainties in Proton Therapy. Medical Physics 38:1672–1684. DOI: 10.1118/1.3556559.

Fuchs T, Kachelrieß M, and Kalender WA. 2000. Direct Comparison of a Xenon and a Solid-State CT Detector System: Measurements Under Working Conditions. IEEE Transactions on Medical Imaging 19:941–948. DOI: 10.1109/42.887841.

Gensheimer MF, Yock TI, Liebsch NJ, Sharp GC, Paganetti H, Madan N, Grant PE, and Bortfeld TR. 2010. In Vivo Proton Beam Range Verification Using Spine MRI Changes. International Journal of Radiation Oncology Biology Physics 78:268–275. DOI: 10.1016/j.ijrobp.2009.11.060.

Gjesteby L, De Man B, Jin Y, Paganetti H, Verburg JM, Giantsoudi D, and Wang G. 2016. Metal Artifact Reduction in CT: Where Are We After Four Decades? IEEE Access 4:5826–5849. DOI: 10.1109/ACCESS.2016.2608621.

Goitein M. 1977. The measurement of tissue heterodensity to guide charged particle radiotherapy. International Journal of Radiation Oncology Biology Physics 3:27–33. DOI: 10.1016/0360-3016(77)90223-1.

Goitein M. 1985. Calculation of the Uncertainty in the Dose Delivered During Radiation Therapy. Medical Physics 12:608–612. DOI: 10.1118/1.595762.

Golnik C, Hueso-González F, Müller A, Dendooven P, Enghardt W, Fiedler F, Kormoll T, Römer K, Petzoldt J, Wagner A, and Pausch G. 2014. Range Assessment in Particle Therapy Based on Prompt γ-Ray Timing Measurements. Physics in Medicine and Biology 59:5399–422. DOI: 10.1088/0031-9155/59/18/5399.

Goodhead DT, Thacker J, and Cox R. 1993. Effects of Radiations of Different Qualities on Cells: Molecular Mechanisms of Damage and Repair. International Journal of Radiation Biology 63:543–556. DOI: 10.1080/09553009314450721.

Grant KL, Flohr TG, Krauss B, Sedlmair M, Thomas C, and Schmidt BT. 2014. Assessment of an Advanced Image-Based Technique to Calculate Virtual Monoenergetic Computed Tomographic Images from a Dual-Energy Examination to Improve Contrast-to-Noise Ratio in Examinations Using Iodinated Contrast Media. Investigative Radiology 49:586–592. DOI: 10.1097/RLI.0000000000000060.

Grant KL and Raupach R. 2012. SAFIRE: Sinogram Affirmed Iterative Reconstruction. SOMATOM Sessions - White Paper:1–8.

Grassberger C, Daartz J, Dowdell S, Ruggieri T, Sharp G, and Paganetti H. 2014. Quantification of Proton Dose Calculation Accuracy in the Lung. International Journal of Radiation Oncology Biology Physics 89:424–430. DOI: 10.1016/j.ijrobp.2014.02.023.

Guckenberger M, Wilbert J, Meyer J, Baier K, Richter A, and Flentje M. 2007. Is a Single Respiratory Correlated 4D-CT Study Sufficient for Evaluation of Breathing Motion? International Journal of Radiation Oncology Biology Physics 67:1352–1359. DOI: 10.1016/j.ijrobp.2006.11.025.

Han D, Siebers JV, and Williamson JF. 2016. A Linear, Separable Two-Parameter Model for Dual Energy CT Imaging of Proton Stopping Power Computation. Medical Physics 43:600–612. DOI: 10.1118/1.4939082.

Hansen DC, Seco J, Sørensen TS, Petersen JBB, Wildberger JE, Verhaegen F, and Landry G. 2015. A Simulation Study on Proton Computed Tomography (CT) Stopping Power Accuracy Using Dual Energy CT Scans as Benchmark. Acta Oncologica 54:1638–1642. DOI: 10.3109/0284186X.2015.1061212.

Heismann BJ, Leppert J, and Stierstorfer K. 2003. Density and Atomic Number Measurements with Spectral X-Ray Attenuation Method. Journal of Applied Physics 94:2073–2079. DOI: 10.1063/1.1586963.

Heismann BJ, Wirth S, Janssen S, and Spreiter Q. 2004. Technology and Image Results of a Spectral CT System. Medical Imaging 2004: Physics of Medical Imaging, Pts 1 and 2 5368:52–59. DOI: 10.1117/12530217.

Heitler W (ed). 1954. The Quantum Theory of Radiation: Third Edition. Oxford University Press, London, UK.

Herman GT. 1979. Correction for Beam Hardening in Computed Tomography. Physics in Medicine and Biology 24:81–106. DOI: 10.1118/1.594429.

Hinderling T, Rüegsegger P, Anliker M, and Dietschi C. 1979. Computed Tomography Reconstruction from Hollow Projections: An Application to In Vivo Evaluation of Artificial Hip Joints. 3:52–57.

Holley WR and Chatterjee A. 1996. Clusters of DNA Damage Induced by Ionizing Radiation: Formation of Short DNA Fragments. I. Theoretical Modeling. Radiation Research 145:188. DOI: 10.2307/3579174.

Hong L, Goitein M, Bucciolini M, Comiskey R, Gottschalk B, Rosenthal S, Serago C, and Urie MM. 1996. A Pencil Beam Algorithm for Proton Dose Calculations. Physics in Medicine and Biology 41:1305–1330. DOI: 10.1088/0031-9155/41/8/005.

Hounsfield GN. 1973. Computerized Transverse Axial Scanning (Tomography): Part 1. Description of System. The British Journal of Radiology 46:1016–1022. DOI: 10.1259/0007-1285-46-552-1016.

Hsieh J. 2015. Computed Tomography: Principles, Design, Artifacts, and Recent Advances. SPIE and John Wiley & Sons, Inc., Bellingham, Washington, USA.

Hsieh J, Nett B, Yu Z, Sauer K, Thibault JB, and Bouman CA. 2013. Recent Advances in CT Image Reconstruction. Current Radiology Reports 1:39–51. DOI: 10.1007/s40134-012-0003-7.

Hudobivnik N, Schwarz F, Johnson T, Agolli L, Dedes G, Tessonnier T, Verhaegen F, Thieke C, Belka C, Sommer WH, Parodi K, and Landry G. 2016. Comparison of Proton Therapy Treatment Planning for Head Tumors with a Pencil Beam Algorithm on Dual and Single Energy CT Images. Medical Physics 43:495–504. DOI: 10.1118/1.4939106.

Hünemohr N, Krauss B, Dinkel J, Gillmann C, Ackermann B, Jäkel O, and Greilich S. 2013. Ion Range Estimation by Using Dual Energy Computed Tomography. Zeitschrift für Medizinische Physik 23:300–313. DOI: 10.1016/j.zemedi.2013.03.001.

Hünemohr N, Krauss B, Tremmel C, Ackermann B, Jäkel O, and Greilich S. 2014. Experimental Verification of Ion Stopping Power Prediction from Dual Energy CT Data in Tissue Surrogates. Physics in Medicine and Biology 59:83–96. DOI: 10.1088/0031-9155/59/1/83.

Husarik DB, Gordic S, Desbiolles L, Krauss B, Leschka S, Wildermuth S, and Alkadhi H. 2015. Advanced Virtual Monoenergetic Computed Tomography of Hyperattenuating and Hypoattenuating Liver Lesions. Investigative Radiology 50:695–702. DOI: 10.1097/RLI.0000000000000171.

ICRU. 1993. Report 49: Stopping powers and ranges for protons and alpha particles. Tech. rep. International Commission on Radiation Units and Measurements, Bethesda, Maryland, USA.

Jaccard P. 1912. The Distribution of the Flora in the Alphine Zone. The New Phytologist XI:37–50. DOI: 10.1111/j.1469-8137.1912.tb05611.x.

Jackson DF and Hawkes DJ. 1981. X-ray Attenuation Coefficients of Elements and Mixtures. Physics Reports 70:169–233. DOI: 10.1016/0370-1573(81)90014-4.

Jäkel O, Jacob C, Schardt D, Karger CP, and Hartmann GH. 2001. Relation Between Carbon Ion Ranges and X-Ray CT Numbers. Medical Physics 28:701–703. DOI: 10.1118/1.1357455.

Jakobi A, Bandurska-Luque A, Stützer K, Haase R, Löck S, Wack LJ, Mönnich D, Thorwarth D, Perez D, Lühr A, Zips D, Krause M, Baumann M, Perrin R, and Richter C. 2015. Identification of Patient Benefit from Proton Therapy for Advanced Head and Neck Cancer Patients Based on Individual and Subgroup Normal Tissue Complication Probability Analysis. International Journal of Radiation Oncology Biology Physics 92:1165–1174. DOI: 10.1016/j.ijrobp.2015.04.031.

Johnson RP, Bashkirov V, DeWitt L, Giacometti V, Hurley RF, Piersimoni P, Plautz TE, Sadrozinski HFW, Schubert KE, Schulte RW, Schultze B, and Zatserklyaniy A. 2016. A Fast Experimental Scanner for Proton CT: Technical Performance and First Experience With Phantom Scans. IEEE Transactions on Nuclear Science 63:52–60. DOI: 10.1109/TNS.2015.2491918.

Kachelrieß M, Knaup M, and Kalender WA. 2004. Extended Parallel Backprojection for Standard Three-Dimensional and Phase-Correlated Four-Dimensional Axial and Spiral Cone-Beam CT with Arbitrary Pitch, Arbitrary Cone-Angle, and 100% Dose Usage. Medical Physics 31:1623–1641. DOI: 10.1118/1.1755569.

Kachelrieß M, Knaup M, Penßel C, and Kalender WA. 2006a. Flying Focal Spot (FFS) in Cone-Beam CT. IEEE Transactions on Nuclear Science 53:1238–1247. DOI: 10.1109/TNS.2006.874076.

Kachelrieß M and Krauss A. 2015. Iterative Metal Artifact Reduction (iMAR): Technical Principles and Clinical Results in Radiation Therapy. SOMATOM Sessions - White Paper:1–16.

Kachelrieß M, Sourbelle K, and Kalender WA. 2006b. Empirical Cupping Correction: A First-Order Raw Data Precorrection for Cone-Beam Computed Tomography. Medical Physics 33:1269–1274. DOI: 10.1118/1.2188076.

Kalender WA, Hebel R, and Ebersberger J. 1987. Reduction of CT Artifacts Caused by Metallic Implants. Radiology 164:576–577. DOI: 10.1148/radiology.164.2.3602406.

Kalender WA, Perman WH, Vetter JR, and Klotz E. 1986. Evaluation of a Prototype Dual-Energy Computed Tomographic Apparatus. I. Phantom Studies. Medical Physics 13:334–339. DOI: 10.1118/1.595958.

Karczewski KJ and Snyder MP. 2018. Integrative Omics for Health and Disease. Nature Reviews Genetics 19:299–310. DOI: 10.1038/nrg.2018.4.

Kaup M, Scholtz JE, Engler A, Albrecht MH, Bauer RW, Kerl JM, Beeres M, Lehnert T, Vogl TJ, and Wichmann JL. 2016. Dual-Energy Computed Tomography Virtual Monoenergetic Imaging of Lung Cancer: Assessment of Optimal Energy Levels. Journal of Computer Assisted Tomography 40:80–85. DOI: 10.1097/RCT.0000000000000319.

Kuchenbecker S, Faby S, Sawall S, Lell M, and Kachelrieß M. 2015. Dual Energy CT: How Well Can Pseudo-Monochromatic Imaging Reduce Metal Artifacts? Medical Physics 42:1023–1036. DOI: 10.1118/1.4905106.

Kyriakou Y, Meyer E, Prell D, and Kachelrieß M. 2010. Empirical Beam Hardening Correction (EBHC) for CT. Medical Physics 37:5179–5187. DOI: 10.1118/1.3477088.

Lambin P, Leijenaar RTH, Deist TM, Peerlings J, de Jong EEC, van Timmeren J, Sanduleanu S, Larue RTHM, Even AJG, Jochems A, van Wijk Y, Woodruff H, van Soest J, Lustberg T, Roelofs E, van Elmpt W, Dekker A, Mottaghy FM, Wildberger JE, and Walsh S. 2017. Radiomics: The Bridge Between Medical Imaging and Personalized Medicine. Nature Reviews Clinical Oncology 14:749–762. DOI: 10.1038/nrclinonc.2017.141.

Landry G, Seco J, Gaudreault M, and Verhaegen F. 2013. Deriving Effective Atomic Numbers from DECT Based on a Parameterization of the Ratio of High and Low Linear Attenuation Coefficients. Physics in Medicine and Biology 58:6851–66. DOI: 10.1088/0031-9155/58/19/6851.

Langendijk JA, Lambin P, De Ruysscher D, Widder J, Bos M, and Verheij M. 2013. Selection of Patients for Radiotherapy with Protons Aiming at Reduction of Side Effects: The Model-Based Approach. Radiotherapy and Oncology 107:267–273. DOI: 10.1016/j.radonc.2013.05.007.

Leng S, Zhou W, Yu Z, Halaweish AF, Krauss B, Schmidt BT, Yu L, Kappler S, and McCollough CH. 2017. Spectral Performance of a Whole-Body Research Photon Counting Detector CT: Quantitative Accuracy in Derived Image Sets. Physics in Medicine and Biology 62:7216–7232. DOI: 10.1088/1361-6560/aa8103.

Lestra T, Mulé S, Millet I, Carsin-Vu A, Taourel P, and Hoeffel C. 2016. Applications of Dual Energy Computed Tomography in Abdominal Imaging. Diagnostic and Interventional Imaging 97:593–603. DOI: 10.1016/j.diii.2015.11.018.

Li B, Lee HC, Duan X, Shen C, Zhou L, Jia X, and Yang M. 2017. Comprehensive Analysis of Proton Range Uncertainties Related to Stopping-Power-Ratio Estimation Using Dual-Energy CT Imaging. Physics in Medicine and Biology 62:7056–7074. DOI: 10.1088/1361-6560/aa7dc9.

Li H, Zhang X, Park P, Liu W, Chang J, Liao Z, Frank S, Li Y, Pönisch F, Mohan R, Gillin M, and Zhu R. 2015. Robust Optimization in Intensity-Modulated Proton Therapy to Account for Anatomy Changes in Lung Cancer Patients. Radiotherapy and Oncology 114:367–372. DOI: 10.1016/j.radonc.2015.01.017.

Li Y, Kardar L, Li X, Li H, Cao W, Chang JY, Liao L, Zhu RX, Sahoo N, Gillin M, Liao Z, Komaki R, Cox JD, Lim G, and Zhang X. 2014. On the Interplay Effects with Proton

Scanning Beams in Stage III Lung Cancer. Medical Physics 41:21721. DOI: 10.1118/1.4862076.

Lievens Y and Grau C. 2012. Health Economics in Radiation Oncology: Introducing the ESTRO HERO Project. Radiotherapy and Oncology 103:109–112. DOI: 10.1016/j.radonc.2011.12.026.

Lin XZ, Miao F, Li JY, Dong HP, Shen Y, and Chen KM. 2011. High-Definition CT Gemstone Spectral Imaging of the Brain. Journal of Computer Assisted Tomography 35:294–297. DOI: 10.1097/RCT.0b013e3182058d5c.

Lomax AJ. 1999. Intensity Modulation Methods for Proton Radiotherapy. Physics in Medicine and Biology 44:185–205. DOI: 10.1088/0031-9155/44/1/014.

Lomax AJ. 2008a. Intensity Modulated Proton Therapy and its Sensitivity to Treatment Uncertainties 1: The Potential Effects of Calculational Uncertainties. Physics in Medicine and Biology 53:1027–1042. DOI: 10.1088/0031-9155/53/4/014.

Lomax AJ. 2008b. Intensity Modulated Proton Therapy and its Sensitivity to Treatment Uncertainties 2: The Potential Effects of Inter-Fraction and Inter-Field Motions. Physics in Medicine and Biology 53:1043–1056. DOI: 10.1088/0031-9155/53/4/015.

Lomax AJ, Boehringer T, Coray A, Egger E, Goitein G, Grossmann M, Juelke P, Lin S, Pedroni E, Rohrer B, Roser W, Rossi B, Siegenthaler B, Stadelmann O, Stauble H, Vetter C, and Wisser L. 2001. Intensity Modulated Proton Therapy: A Clinical Example. Medical Physics 28:317–324. DOI: 10.1118/1.1350587.

Lomax AJ, Pedroni E, Rutz HP, and Goitein G. 2004. The Clinical Potential of Intensity Modulated Proton Therapy. Zeitschrift für Medizinische Physik 14:147–152. DOI: 10.1078/0939-3889-00217.

Low DA, Harms WB, Mutic S, and Purdy JA. 1998. A Technique for the Quantitative Evaluation of Dose Distributions. Medical Physics 25:656–61. DOI: 10.1118/1.598248.

Lowe M, Albertini F, Aitkenhead A, Lomax AJ, and MacKay RI. 2016. Incorporating the Effect of Fractionation in the Evaluation of Proton Plan Robustness to Setup Errors. Physics in Medicine and Biology 61:413–429. DOI: 10.1088/0031-9155/61/1/413.

Lühr A, Löck S, Jakobi A, Stützer K, Bandurska-Luque A, Vogelius IR, Enghardt W, Baumann M, and Krause M. 2017a. Modeling Tumor Control Probability for Spatially Inhomogeneous Risk of Failure Based on Clinical Outcome Data. Zeitschrift für Medizinische Physik 27:285–299. DOI: 10.1016/j.zemedi.2017.06.003.

Lühr A, von Neubeck C, Helmbrecht S, Baumann M, Enghardt W, and Krause M. 2017b. Modeling In Vivo Relative Biological Effectiveness in Particle Therapy for Clinically Relevant Endpoints. Acta Oncologica 56:1392–1398. DOI: 10.1080/0284186X.2017.1356468.

Malinowski K, McAvoy TJ, George R, Dietrich S, and D'Souza WD. 2012. Incidence of Changes in Respiration-Induced Tumor Motion and its Relationship with Respiratory Surrogates During Individual Treatment Fractions. International Journal of Radiation Oncology Biology Physics 82:1665–1673. DOI: 10.1016/j.ijrobp.2011.02.048.

Mangold S, Gatidis S, Luz O, König B, Schabel C, Bongers MN, Flohr TG, Claussen CD, and Thomas C. 2014. Single-Source Dual-Energy Computed Tomography: Use of Monoenergetic Extrapolation for a Reduction of Metal Artifacts. Investigative Radiology 49:788–793. DOI: 10.1097/RLI.0000000000000083.

Mayneord WV. 1937. The Significance of the Röntgen. Acta of the International Union Against Cancer 2:271–282.

Meinel FG, Canstein C, Schoepf UJ, Sedlmair M, Schmidt BT, Harris BS, Flohr TG, and Cecco CND. 2014. Image Quality and Radiation Dose of Low Tube Voltage 3rd Generation Dual-Source Coronary CT Angiography in Obese Patients: A Phantom Study. European Radiology 24:1643–1650. DOI: 10.1007/s00330-014-3194-x.

Meyer M, Haubenreisser H, Schoepf UJ, Vliegenthart R, Leidecker C, Allmendinger T, Lehmann R, Sudarski S, Borggrefe M, Schoenberg SO, and Henzler T. 2014. Closing in on the K Edge: Coronary CT Angiography at 100, 80, and 70 kV - Initial Comparison of a Second- Versus a Third-Generation Dual-Source CT System. Radiology 273:373–382. DOI: 10.1148/radiol.14140244.

Möhler C, Russ T, Wohlfahrt P, Elter A, Runz A, Richter C, and Greilich S. 2018a. Experimental Verification of Stopping-Power Prediction from Single- and Dual-Energy Com-

puted Tomography in Biological Tissues. Physics in Medicine and Biology 63:025001. DOI: 10.1088/1361-6560/aaa1c9. arXiv: 1708.07368.

Möhler C, Wohlfahrt P, Richter C, and Greilich S. 2016. Range Prediction for Tissue Mixtures Based on Dual-Energy CT. Physics in Medicine and Biology 61:N268–N275. DOI: 10.1088/0031-9155/61/11/N268.

Möhler C, Wohlfahrt P, Richter C, and Greilich S. 2017. Methodological Accuracy of Image-Based Electron Density Assessment Using Dual-Energy Computed Tomography. Medical Physics 44:2429–2437. DOI: 10.1002/mp.12265.

Möhler C, Wohlfahrt P, Richter C, and Greilich S. 2018b. On the Equivalence of Image-Based Dual-Energy CT Methods for the Determination of Electron Density and Effective Atomic Number in Radiotherapy. Physics and Imaging in Radiation Oncology 5:108–110. DOI: 10.1016/j.phro.2018.03.003.

Moscow JA, Fojo T, and Schilsky RL. 2017. The Evidence Framework for Precision Cancer Medicine. Nature Reviews Clinical Oncology 15:183–192. DOI: 10.1038/nrclinonc.2017.186.

Moyers MF, Miller DW, Bush DA, and Slater JD. 2001. Methodologies and Tools for Proton Beam Design for Lung Tumors. International Journal of Radiation Oncology Biology Physics 49:1429–1438. DOI: 10.1016/S0360-3016(00)01555-8.

Müller J, Neubert C, von Neubeck C, Baumann M, Krause M, Enghardt W, Bütof R, Dietrich A, and Lühr A. 2017. Proton Radiography for Inline Treatment Planning and Positioning Verification of Small Animals. Acta Oncologica 56:1399–1405. DOI: 10.1080/0284186X.2017.1352102.

Negwer FC. 2016. Evaluierung Iterativer Rekonstruktionsverfahren zur Optimierung der Bildqualität und Reduktion von Metallartefakten in der Computertomographie. TU Dresden, Bachelor thesis.

Newhauser WD and Zhang R. 2015. The Physics of Proton Therapy. Physics in Medicine and Biology 60:R155–R209. DOI: 10.1088/0031-9155/60/8/R155.

Nichols RC, Huh SN, Prado KL, Yi BY, Sharma NK, Ho MW, Hoppe BS, Mendenhall NP, Li Z, and Regine WF. 2012. Protons Offer Reduced Normal-Tissue Exposure for Patients

Receiving Postoperative Radiotherapy for Resected Pancreatic Head Cancer. International Journal of Radiation Oncology Biology Physics 83:158–163. DOI: 10.1016/j.ijrobp.2011.05.045.

Nischwitz SP, Bauer J, Welzel T, Rief H, Jäkel O, Haberer T, Frey K, Debus J, Parodi K, Combs SE, and Rieken S. 2015. Clinical Implementation and Range Evaluation of In Vivo PET Dosimetry for Particle Irradiation in Patients with Primary Glioma. Radiotherapy and Oncology 115:179–185. DOI: 10.1016/j.radonc.2015.03.022.

Ohnesorge BM, Flohr TG, and Klingenbeck-Regn K. 1999. Efficient Object Scatter Correction Algorithm for Third and Fourth Generation CT Scanners. European Radiology 9:563–569. DOI: 10.1007/s003300050710.

Paganetti H (ed). 2012a. Proton Therapy Physics. Taylor & Francis, Boca Raton, Florida, USA.

Paganetti H. 2012b. Range Uncertainties in Proton Therapy and the Role of Monte Carlo Simulations. Physics in Medicine and Biology 57:R99–R117. DOI: 10.1088/0031-9155/57/11/R99.

Paganetti H. 2014. Relative Biological Effectiveness (RBE) Values for Proton Beam Therapy. Variations as a Function of Biological Endpoint, Dose, and Linear Energy Transfer. Physics in Medicine and Biology 59:R419–R472. DOI: 10.1088/0031-9155/59/22/R419.

Paganetti H, Niemierko A, Ancukiewicz M, Gerweck LE, Goitein M, Loeffler JS, and Suit HD. 2002. Relative Biological Effectiveness (RBE) Values for Proton Beam Therapy. International Journal of Radiation Oncology Biology Physics 53:407–421. DOI: 10.1016/S0360-3016(02)02754-2.

Pausch G, Petzoldt J, Berthel M, Enghardt W, Fiedler F, Golnik C, Hueso-González F, Lentering R, Römer K, Ruhnau K, Stein J, Wolf A, and Kormoll T. 2016. Scintillator-Based High-Throughput Fast Timing Spectroscopy for Real-Time Range Verification in Particle Therapy. IEEE Transactions on Nuclear Science 63:664–672. DOI: 10.1109/TNS.2016.2527822.

Péguret N, Ozsahin M, Zeverino M, Belmondo B, Durham AD, Lovis A, Simons J, Long O, Duclos F, Prior J, Denys A, Beigelman C, Sozzi WJ, Grant K, Gautier-Dechaud V, Peters S, Vienne M, Moeckli R, and Bourhis J. 2016. Apnea-Like Suppression of Respiratory

Motion: First Evaluation in Radiotherapy. Radiotherapy and Oncology 118:220–226. DOI: 10.1016/j.radonc.2015.10.011.

Penfold SN, Rosenfeld AB, Schulte RW, and Schubert KE. 2009. A More Accurate Reconstruction System Matrix for Quantitative Proton Computed Tomography. Medical Physics 36:4511–4518. DOI: 10.1118/1.3218759.

Poludniowski G, Allinson NM, and Evans PM. 2015. Proton Radiography and Tomography with Application to Proton Therapy. The British Journal of Radiology 88:20150134. DOI: 10.1259/bjr.20150134.

Prall M, Durante M, Berger T, Przybyla B, Graeff C, Lang PM, LaTessa C, Shestov L, Simoniello P, Danly C, Mariam F, Merrill F, Nedrow P, Wilde C, and Varentsov D. 2016. High-Energy Proton Imaging for Biomedical Applications. Scientific Reports 6:27651. DOI: 10.1038/srep27651.

Radon J. 1917. Über die Bestimmung von Funktionen durch ihre Integralwerte längs gewisser Mannigfaltigkeiten. Berichte über die Verhandlungen der Königlich-Sächsischen Akademie der Wissenschaften zu Leipzig, Mathematisch-Physische Klasse 69:262–277.

Ramachandran GN and Lakshminarayanan AV. 1971. Three-Dimensional Reconstruction from Radiographs and Electron Micrographs: Application of Convolutions Instead of Fourier Transforms. Proceedings of the National Academy of Sciences 68:2236–2240. DOI: 10.1073/pnas.68.9.2236.

Ramirez-Giraldo JC, Grant KL, and Raupach R. 2016. ADMIRE: Advanced Modeled Iterative Reconstruction. SOMATOM Sessions - White Paper:1–16.

Richter C, Pausch G, Barczyk S, Priegnitz M, Keitz I, Thiele J, Smeets J, Vander Stappen F, Bombelli L, Fiorini C, Hotoiu L, Perali I, Prieels D, Enghardt W, and Baumann M. 2016. First Clinical Application of a Prompt Gamma Based In Vivo Proton Range Verification System. Radiotherapy and Oncology 118:232–237. DOI: 10.1016/j.radonc.2016.01.004.

Rutherford RA, Pullan BR, and Isherwood I. 1976. Measurement of Effective Atomic Number and Electron Density Using an EMI Scanner. Neuroradiology 11:15–21. DOI: 10.1007/BF00327253.

Rydberg B. 1996. Clusters of DNA Damage Induced by Ionizing Radiation: Formation of Short DNA Fragments. II. Experimental Detection. Radiation Research 145:200. DOI: 10.2307/3579175.

Saini J, Maes D, Egan A, Bowen SR, St James S, Janson M, Wong T, and Bloch C. 2017. Dosimetric Evaluation of a Commercial Proton Spot Scanning Monte-Carlo Dose Algorithm: Comparisons Against Measurements and Simulations. Physics in Medicine and Biology 62:7659–7681. DOI: 10.1088/1361-6560/aa82a5.

Saito M. 2012. Potential of Dual-Energy Subtraction for Converting CT Numbers to Electron Density Based on a Single Linear Relationship. Medical Physics 39:2021–2030. DOI: 10.1118/1.3694111.

Saito M and Sagara S. 2017a. A Simple Formulation for Deriving Effective Atomic Numbers via Electron Density Calibration from Dual-Energy CT Data in the Human Body. Medical Physics 44:2293–2303. DOI: 10.1002/mp.12176.

Saito M and Sagara S. 2017b. Simplified Derivation of Stopping Power Ratio in the Human Body from Dual-Energy CT Data. Medical Physics 44:4179–4187. DOI: 10.1002/mp.12386.

Schabel C, Bongers MN, Sedlmair M, Korn A, Grosse U, Mangold S, Claussen CD, and Thomas C. 2014. Assessment of the Hepatic Veins in Poor Contrast Conditions using Dual Energy CT: Evaluation of a Novel Monoenergetic Extrapolation Software Algorithm. Fortschritte auf dem Gebiet der Röntgenstrahlen und der Bildgebenden Verfahren 186:591–597. DOI: 10.1055/s-0034-1366423.

Schaffner B and Pedroni E. 1998. The precision of proton range calculations in proton radiotherapy treatment planning: experimental verification of the relation between CT-HU and proton stopping power. Physics in Medicine and Biology 43:1579–1592. DOI: 10.1088/0031-9155/43/6/016.

Schardt P, Deuringer J, Freudenberger J, Hell E, Knüpfer W, Mattern D, and Schild M. 2004. New X-Ray Tube Performance in Computed Tomography by Introducing the Rotating Envelope Tube Technology. Medical Physics 31:2699–2706. DOI: 10.1118/1.1783552.

Schneider U and Pedroni E. 1995. Proton Radiography as a Tool for Quality Control in Proton Therapy. Medical Physics 22:353–363. DOI: 10.1118/1.597470.

Schneider U, Pedroni E, and Lomax AJ. 1996. The Calibration of CT Hounsfield Units for Radiotherapy Treatment Planning. Physics in Medicine and Biology 41:111–124. DOI: 10.1088/0031-9155/41/1/009.

Schneider W, Bortfeld TR, and Schlegel W. 2000. Correlation Between CT Numbers and Tissue Parameters Needed for Monte Carlo Simulations of Clinical Dose Distributions. Physics in Medicine and Biology 45:459–478. URL: http://iopscience.iop.org/article/10.1088/0031-9155/45/2/314/meta.

Schuemann J, Dowdell S, Grassberger C, Min CH, and Paganetti H. 2014. Site-Specific Range Uncertainties Caused by Dose Calculation Algorithms for Proton Therapy. Physics in Medicine and Biology 59:4007–4031. DOI: 10.1088/0031-9155/59/15/4007.

Seltzer SM and Berger MJ. 1982. Evaluation of the collision stopping power of elements and compounds for electrons and positrons. The International Journal of Applied Radiation and Isotopes 33:1189–1218. DOI: 10.1016/0020-708X(82)90244-7.

Shah C, Grills IS, Kestin LL, McGrath S, Ye H, Martin SK, and Yan D. 2012. Intrafraction Variation of Mean Tumor Position During Image-Guided Hypofractionated Stereotactic Body Radiotherapy for Lung Cancer. International Journal of Radiation Oncology Biology Physics 82:1636–1641. DOI: 10.1016/j.ijrobp.2011.02.011.

Sharp GC, Fritscher KD, Pekar V, Peroni M, Shusharina N, Veeraraghavan H, and Yang J. 2014. Vision 20/20: Perspectives on Automated Image Segmentation for Radiotherapy. Medical Physics 41:50902. DOI: 10.1118/1.4871620.

Shepp LA and Logan BF. 1974. The Fourier Reconstruction of a Head Section. IEEE Transactions on Nuclear Science 21:21–43. DOI: 10.1109/TNS.1974.6499235.

Siddon RL. 1985. Fast Calculation of the Exact Radiological Path for a Three-Dimensional CT Array. Medical Physics 12:252–255. DOI: 10.1118/1.595715.

Smeets J, Roellinghoff F, Prieels D, Stichelbaut F, Benilov A, Busca P, Fiorini C, Peloso R, Basilavecchia M, Frizzi T, Dehaes JC, and Dubus A. 2012. Prompt Gamma Imaging with

a Slit Camera for Real-Time Range Control in Proton Therapy. Physics in Medicine and Biology 57:3371–3405. DOI: 10.1088/0031-9155/57/11/3371.

Soukup M, Fippel M, and Alber M. 2005. A Pencil Beam Algorithm for Intensity Modulated Proton Therapy Derived from Monte Carlo Simulations. Physics in Medicine and Biology 50:5089–5104. DOI: 10.1088/0031-9155/50/21/010.

Stewart BW and Wild CP. 2014. World Cancer Report 2014. Tech. rep. International Agency for Research on Cancer.

Stützer K, Jakobi A, Bandurska-Luque A, Barczyk S, Arnsmeyer C, Löck S, and Richter C. 2017a. Potential Proton and Photon Dose Degradation in Advanced Head and Neck Cancer Patients by Intratherapy Changes. Journal of Applied Clinical Medical Physics 18:104–113. DOI: 10.1002/acm2.12189.

Stützer K, Lin A, Kirk M, and Lin L. 2017b. Superiority in Robustness of Multifield Optimization Over Single-Field Optimization for Pencil-Beam Proton Therapy for Oropharynx Carcinoma: An Enhanced Robustness Analysis. International Journal of Radiation Oncology Biology Physics 99:738–749. DOI: 10.1016/j.ijrobp.2017.06.017.

Taasti VT, Høye EM, Hansen DC, Muren LP, Thygesen J, Skyt PS, Balling P, Bassler N, Grau C, Mierzwińska G, Rydygier M, Swakoń J, Olko P, and Petersen JBB. 2016a. Technical Note: Improving Proton Stopping Power Ratio Determination for a Deformable Silicone-Based 3D Dosimeter Using Dual Energy CT. Medical Physics 43:2780–2784. DOI: 10.1118/1.4948677.

Taasti VT, Petersen JBB, Muren LP, Thygesen J, and Hansen DC. 2016b. A Robust Empirical Parametrization of Proton Stopping Power Using Dual Energy CT. Medical Physics 43:5547–5560. DOI: 10.1118/1.4962934.

Taha AA and Hanbury A. 2015. Metrics for Evaluating 3D Medical Image Segmentation: Analysis, Selection, and Tool. BMC Medical Imaging 15:29. DOI: 10.1186/s12880-015-0068-x. arXiv: NIHMS150003.

Troost EGC, Thorwarth D, and Oyen WJG. 2015. Imaging-Based Treatment Adaptation in Radiation Oncology. Journal of Nuclear Medicine 56:1922–1929. DOI: 10.2967/jnumed.115.162529.

Tschiche M. 2016. Einstrahlrichtungsabhängige Berechnung und Visualisierung wasseräquivalenter Weglängen für den Einsatz in der Protonentherapie. TU Dresden, Master thesis.

Ulzheimer S and Freund J. 2011. Stellar Detector Performance in Computed Tomography. SOMATOM Sessions - White Paper 29:64–66.

Ulzheimer S and Kappler S. 2017. Photon-Counting Detectors in Clinical Computed Tomography. SOMATOM Sessions.

Unkelbach J, Chan TCY, and Bortfeld TR. 2007. Accounting for Range Uncertainties in the Optimization of Intensity Modulated Proton Therapy. Physics in Medicine and Biology 52:2755–2773. DOI: 10.1088/0031-9155/52/10/009.

Urie MM, Goitein M, Doppke K, Kutcher JG, LoSasso T, Mohan R, Munzenrider JE, Sontag M, and Wong JW. 1991. The Role of Uncertainty Analysis in Treatment Planning. International Journal of Radiation Oncology Biology Physics 21:91–107. DOI: 10.1016/0360-3016(91)90170-9.

Urie MM, Goitein M, Holley WR, and Chen GTY. 1986. Degradation of the Bragg Peak Due to Inhomogeneities. Physics in Medicine and Biology 31:1–15. DOI: 10.1088/0031-9155/31/1/001.

Van de Water TA, Bijl HP, Schilstra C, Pijls-Johannesma M, and Langendijk JA. 2011. The Potential Benefit of Radiotherapy with Protons in Head and Neck Cancer with Respect to Normal Tissue Sparing: A Systematic Review of Literature. The Oncologist 16:366–77. DOI: 10.1634/theoncologist.2010-0171.

Van Der Voort S, Van De Water S, Perkó Z, Heijmen B, Lathouwers D, and Hoogeman M. 2016. Robustness Recipes for Minimax Robust Optimization in Intensity Modulated Proton Therapy for Oropharyngeal Cancer Patients. International Journal of Radiation Oncology Biology Physics 95:163–170. DOI: 10.1016/j.ijrobp.2016.02.035.

Van Elmpt W, Landry G, Das M, and Verhaegen F. 2016. Dual Energy CT in Radiotherapy: Current Applications and Future Outlook. Radiotherapy and Oncology 119:137–144. DOI: 10.1016/j.radonc.2016.02.026.

Van Herk M. 2004. Errors and Margins in Radiotherapy. Seminars in Radiation Oncology 14:52–64. DOI: 10.1053/j.semradonc.2003.10.003. arXiv: 1510.03300.

Verburg JM and Seco J. 2014. Proton Range Verification Through Prompt Gamma-Ray Spectroscopy. Physics in Medicine and Biology 59:7089–7106. DOI: 10.1088/0031-9155/59/23/7089.

Verburg JM, Testa M, and Seco J. 2015. Range Verification of Passively Scattered Proton Beams Using Prompt Gamma-Ray Detection. Physics in Medicine and Biology 60:1019–1029. DOI: 10.1088/0031-9155/60/3/1019.

Werner R, Hofmann C, Mücke E, and Gauer T. 2017. Reduction of Breathing Irregularity-Related Motion Artifacts in Low-Pitch Spiral 4D CT by Optimized Projection Binning. Radiation Oncology 12:1–8. DOI: 10.1186/s13014-017-0835-7.

White DR, Widdowson EM, Woodard HQ, and Dickerson JWT. 1991. The Composition of Body Tissues. (II) Fetus to Young Adult. The British Journal of Radiology 64:149–159. DOI: 10.1259/0007-1285-64-758-149.

White DR, Woodard HQ, and Hammond SM. 1987. Average Soft-Tissue and Bone Models for Use in Radiation Dosimetry. British Journal of Radiology 60:907–913. DOI: 10.1259/0007-1285-60-717-907.

Wichmann JL, Nöske EM, Kraft J, Burck I, Wagenblast J, Eckardt A, Frellesen C, Kerl JM, Bauer RW, Bodelle B, Lehnert T, Vogl TJ, and Schulz B. 2014. Virtual Monoenergetic Dual-Energy Computed Tomography: Optimization of Kiloelectron Volt Settings in Head and Neck Cancer. Investigative Radiology 49:735–41. DOI: 10.1097/RLI.0000000000000077.

Wohlfahrt P. 2014. Einfluss der Computertomographie auf die Reichweiteberechnung von Protonen in der Protonenstrahltherapie. TU Dresden, Master thesis.

Wohlfahrt P, Möhler C, Greilich S, and Richter C. 2017a. Comment on: Dosimetric Comparison of Stopping-Power Calibration with Dual-Energy CT and Single-Energy CT in Proton Therapy Treatment Planning [Med. Phys. 43(6), 2845-2854 (2016)]. Medical Physics 44:5533–5536. DOI: 10.1002/mp.12418.

Wohlfahrt P, Möhler C, Hietschold V, Menkel S, Greilich S, Krause M, Baumann M, Enghardt W, and Richter C. 2017b. Clinical Implementation of Dual-Energy CT for Proton Treatment Planning on Pseudo-Monoenergetic CT Scans. International Journal of Radiation Oncology Biology Physics 97:427–434. DOI: 10.1016/j.ijrobp.2016.10.022.

Wohlfahrt P, Möhler C, Richter C, and Greilich S. 2018a. Evaluation of Stopping-Power Prediction by Dual- and Single-Energy Computed Tomography in an Anthropomorphic Ground-Truth Phantom. International Journal of Radiation Oncology Biology Physics 100:244–253. DOI: 10.1016/j.ijrobp.2017.09.025.

Wohlfahrt P, Möhler C, Stützer K, Greilich S, and Richter C. 2017c. Dual-Energy CT Based Proton Range Prediction in Head and Pelvic Tumor Patients. Radiotherapy and Oncology 125:526–533. DOI: 10.1016/j.radonc.2017.09.042.

Wohlfahrt P, Möhler C, Troost EGC, Greilich S, and Richter C. 2018b. Dual-Energy Computed Tomography to Assess Intra- and Inter-patient Tissue Variability in Proton Treatment Planning of Brain-Tumor Patients. Radiotherapy and Oncology in preparation.

Wohlfahrt P, Troost EGC, Hofmann C, Richter C, and Jakobi A. 2018c. Clinical Feasibility of Single-Source Dual-Spiral 4D Dual-Energy CT for Proton Treatment Planning Within the Thoracic Region. International Journal of Radiation Oncology Biology Physics. DOI: 10.1016/j.ijrobp.2018.06.044.

Woodard HQ and White DR. 1986. The Composition of Body Tissues. The British Journal of Radiology 59:1209–1219. DOI: 10.1259/0007-1285-59-708-1209.

Yang M, Virshup G, Clayton J, Zhu XR, Mohan R, and Dong L. 2010. Theoretical Variance Analysis of Single- and Dual-Energy Computed Tomography Methods for Calculating Proton Stopping Power Ratios of Biological Tissues. Physics in Medicine and Biology 55:1343–1362. DOI: 10.1088/0031-9155/55/5/006.

Yu Z, Leng S, Kappler S, Hahn K, Li Z, Halaweish AF, Henning A, and McCollough CH. 2016. Noise Performance of Low-Dose CT: Comparison Between an Energy Integrating Detector and a Photon Counting Detector Using a Whole-Body Research Photon Counting CT Scanner. Journal of Medical Imaging 3:043503. DOI: 10.1117/1.JMI.3.4.043503.

Yuan Y, Andronesi OC, Bortfeld TR, Richter C, Wolf R, Guimaraes AR, Hong TS, and Seco J. 2013. Feasibility Study of In Vivo MRI Based Dosimetric Verification of Proton End-of-Range for Liver Cancer Patients. Radiotherapy and Oncology 106:378–382. DOI: 10.1016/j.radonc.2013.01.016.

Zhu J and Penfold SN. 2016. Dosimetric Comparison of Stopping Power Calibration with Dual-Energy CT and Single-Energy CT in Proton Therapy Treatment Planning. Medical Physics 43:2845–2854. DOI: 10.1118/1.4948683.

Zschaeck S, Simon M, Löck S, Troost EGC, Stützer K, Wohlfahrt P, Appold S, Makocki S, Bütof R, Richter C, Baumann M, and Krause M. 2016. PRONTOX – Proton Therapy to Reduce Acute Normal Tissue Toxicity in Locally Advanced Non-Small-Cell Lung Carcinomas (NSCLC): Study Protocol for a Randomised Controlled Trial. Trials 17:543. DOI: 10.1186/s13063-016-1679-4.

Appendix

A Investigated Material Samples

Table A.1: Material-specific stopping-power ratio (SPR) for a proton energy of 150 M*e*V obtained by proton transmission measurements and calculations using the Bethe formula.

Material	Manufacturer	Calculated SPR	Measured SPR
Sinus cavity	CIRS	0.202	0.201 ± 0.002
Soft tissue grey	CIRS	1.032	1.030 ± 0.002
Spinal cord	CIRS	1.037	1.038 ± 0.002
Brain	CIRS	1.040	1.043 ± 0.002
Spinal disk	CIRS	1.073	1.073 ± 0.003
Trabecular bone	CIRS	1.152	1.155 ± 0.003
Tooth dentin	CIRS	1.500	1.501 ± 0.003
Cortical bone	CIRS	1.686	1.683 ± 0.003
Tooth enamel	CIRS	1.768	1.763 ± 0.003
Tooth enamel	CIRS	1.768	1.763 ± 0.003
Lung LN300	Gammex	0.293	0.273 ± 0.006
Lung LN450	Gammex	0.439	0.438 ± 0.006
Fat AP6	Gammex	0.916	0.940 ± 0.007
Solid Water	Gammex	0.994	0.996 ± 0.007
Muscle	Gammex	1.029	1.034 ± 0.007
Brain SR2	Gammex	1.067	1.062 ± 0.007
Bone 10% $CaCO_3$	Gammex	1.152	1.135 ± 0.007
Bone 30% $CaCO_3$	Gammex	1.275	1.261 ± 0.008
Bone 50% $CaCO_3$	Gammex	1.432	1.424 ± 0.008
Cortical bone SB3	Gammex	1.624	1.619 ± 0.009

B Spectral-Stoichiometric Prediction of X-Ray Attenuation

Within this thesis, the spectral-stoichiometric CT number prediction was introduced. This approach incorporates scanner-specific properties like the polychromatic X-ray spectrum $\Omega(E)$ (Fig. 2.2) and detector efficiency $\xi(E)$ (Heismann et al., 2003) to calculate material-specific CT numbers based on the elemental composition. Since the influence of beam-hardening on CT numbers can be considered in this method, especially the dependence on material size, a BHC algorithm with simplified assumptions was included.
Assuming a homogeneous object with projection-independent X-ray attenuation (cylindrical shape), a 3D image reconstruction using several X-ray projections is not required to determine its CT number. In this case, the X-ray attenuation coefficient μ arises directly from the measurable one-dimensional (1D) transmittance T after traversing the investigated material of thickness d.

$$T = e^{-\mu\, d} = \frac{\int_0^{E_{\text{max}}} \eta(E) \cdot \xi(E) \cdot \Omega(E) \cdot e^{-\int_0^d \mu(E,x)\,\mathrm{d}x}\,\mathrm{d}E}{\int_0^{E_{\text{max}}} \eta(E) \cdot \xi(E) \cdot \Omega(E)\,\mathrm{d}E} \tag{B.1}$$

The energy-dependent parameter $\eta(E)$ in eq. B.1 simulates the influence of beam hardening using a simplified ansatz:

$$\eta(E) = \left(\frac{E}{E_{\text{max}}}\right)^m \quad \text{with} \quad n \geq 0. \tag{B.2}$$

The spectral adjustment parameter η can be interpreted as suppression factor for low-energy photons. A rising grade of beam hardening corresponds to an increasing exponent m, which describes the attenuation of the scan setup surrounding the material of interest. Typical beam hardening conditions can be simulated by selecting a suitable m. The CT number of the investigated material is derived from eqs. 2.3 and B.1:

$$H(m) = a(m) \cdot \left[\frac{\ln T(m) - \ln T_{\text{water}}(m)}{\ln T_{\text{water}}(m) - \ln T_{\text{air}}(m)} \cdot 1000\right] + b(m) \tag{B.3}$$

with $a(m)$ and $b(m)$ as additional fit parameters to account for deviations from optimal CT scanner calibration (H_{water} = 0 HU and H_{air} = -1000 HU).

To mimic clinical BHC algorithms (section 2.2.3) and integrate their functionality in CT number prediction, a 1D water pre-correction and material-specific BHC are included as consecutive CT number adjustment. For this purpose, the size dependence of beam hardening is characterised to define a reference condition.

Size-Dependent Beam Hardening

The size-dependent X-ray attenuation $\mu\,(d)$ of a material with known elemental composition can be transferred to its expected attenuation $\tilde{\mu}$, corresponding to the initial X-ray spectrum, by a correction factor λ:

$$\tilde{\mu} = \mu\,(d_0) = \lambda\,(d)\ \mu\,(d) \quad \text{with} \quad d_0 = 100\,\mu\text{m}. \tag{B.4}$$

Since the initial X-ray spectrum remains almost unchanged after traversing a thin target ($d\ \rightarrow\ 0$), the expected attenuation $\tilde{\mu}$ is well approximated by eq. B.1 with $d = 100\,\mu$m for clinically applied X-ray spectra.

Water Pre-Correction

The size-dependent transmittance of water $T_{\text{w}}\,(d)$ and air $T_{\text{a}}\,(d)$ can be described as polynomial functions using eq. B.1. Based on $T_{\text{w}}\,(d)$, the transmittance of any material sample T_{s} can be transferred into a water-equivalent thickness $d_{\text{w}}(T_{\text{s}})$ assuming $T_{\text{s}} = T_{\text{w}}$. Consequently, the water-corrected CT number H_{wc} ensues from the size-dependent correction applied for water and air using eq. B.4.

$$H_{\text{wc}} = \frac{\lambda_{\text{w}}\,(d_{\text{w}})\ \mu\ -\ \lambda_{\text{w}}\,(d)\ \mu_{\text{w}}}{\lambda_{\text{w}}\,(d)\ \mu_{\text{w}}\ -\ \lambda_{\text{a}}\,(d)\ \mu_{\text{a}}}\ \cdot\ 1000 \tag{B.5}$$

Material-Specific BHC

For all materials with $H_{\text{wc}} > 0$, an additional material-specific BHC is applied, which relies on a database of different human tissues (BHC materials). This material database contains the water-corrected CT number $\tilde{H}_{\text{wc}}\,(T)$ of each BHC material as a function of transmittance derived from eq. B.1 and B.5. First, those two BHC materials (index $+$ and $-$) are identified, whose CT numbers differ least from the water-corrected CT number $H_{\text{wc}}\,(T_{\text{s}})$ of

the investigated material sample ($\tilde{H}^{+}_{\text{wc}} > H_{\text{wc}}\,,\ \tilde{H}^{-}_{\text{wc}} \leq H_{\text{wc}}$). Afterwards, the correction factors γ^{+} and γ^{-} are determined to transfer $\tilde{H}^{\pm}_{wc}\,(T_{\text{s}})$ into the expected CT numbers $\tilde{H}^{\pm}_{wc}\,(T_0)$ for the reference setting ($d = 100\,\mu\text{m}$):

$$\tilde{H}^{\pm}_{wc}\,(T_0) = \gamma^{\pm}\,\tilde{H}^{\pm}_{wc}\,(T_{\text{s}}) \quad \text{with} \quad T_0 = T\,(d = 100\,\mu\text{m})\,. \tag{B.6}$$

Finally, the material-corrected CT number H_{mc} of the investigated substance is calculated by multiplying $H_{\text{wc}}\,(T_{\text{s}})$ with a correction factor γ:

$$H_{\text{mc}} = \gamma^{p}\,H_{\text{wc}} = \left[\delta\,\gamma^{+} \,+\, (1-\delta)\,\gamma^{-}\right]^{p}\,H_{\text{wc}} \quad \text{with} \quad p = q + \frac{m}{10}. \tag{B.7}$$

The parameter δ equals the weighting factor of the linear interpolation between $\tilde{H}^{+}_{\text{wc}}$ and $\tilde{H}^{-}_{\text{wc}}$ resulting in H_{wc}. To regard different strength levels of BHC algorithms integrated in clinical reconstruction kernels (section 2.2.3), the purely empirical parameter p is introduced with $p = 1$ for an optimal BHC. The exponent p results from a kernel-specific BHC quality parameter q and the setup-specific parameter m (introduced in eq. B.2). The BHC quality parameter q is independent from the scan setup and describes a possible systematic under- ($p < 1$) or overestimation ($p > 1$) of beam hardening effects. To prevent the determination of a negative q based on the expectation $p \in [0, 2]$, m is divided by 10 to sum two parameters of comparable magnitude.

C Evaluation of Monoenergetic X-Ray Attenuation

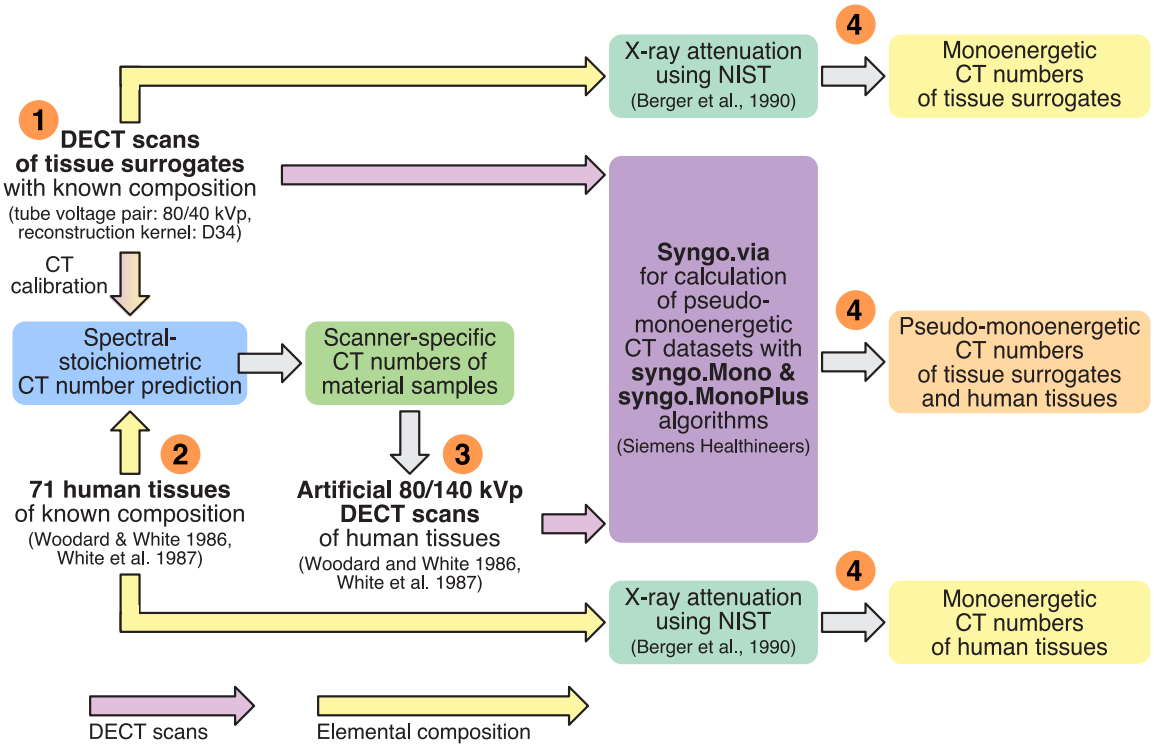

Figure C.1: Flow chart of the material-specific CT number prediction for calculating the energy-dependent weighting factor α of DECT-based MonoCT approaches. Predicted CT numbers were saved as pixel data in DICOM standard using measured CT scans in DICOM format as template. The numbers in orange circles denote the order of the respective calculation step.

Table C.1: Fit parameter of the energy-dependent MonoCT weighting factor α using the equation $\alpha = a \cdot \left(E_{\text{mono}}/\text{keV}\right)^{b} + c$.

Fit parameter	syngo.Mono	syngo.MonoPlus	MonoNIST
$a \cdot 10^3$	18.339 ± 1.883	17.441 ± 1.823	36.539 ± 3.251
b	-2.244 ± 0.026	-2.232 ± 0.026	-2.413 ± 0.023
c	-1.014 ± 0.011	-1.016 ± 0.011	-0.860 ± 0.010

D Experimental Verification of Stopping-Power Prediction

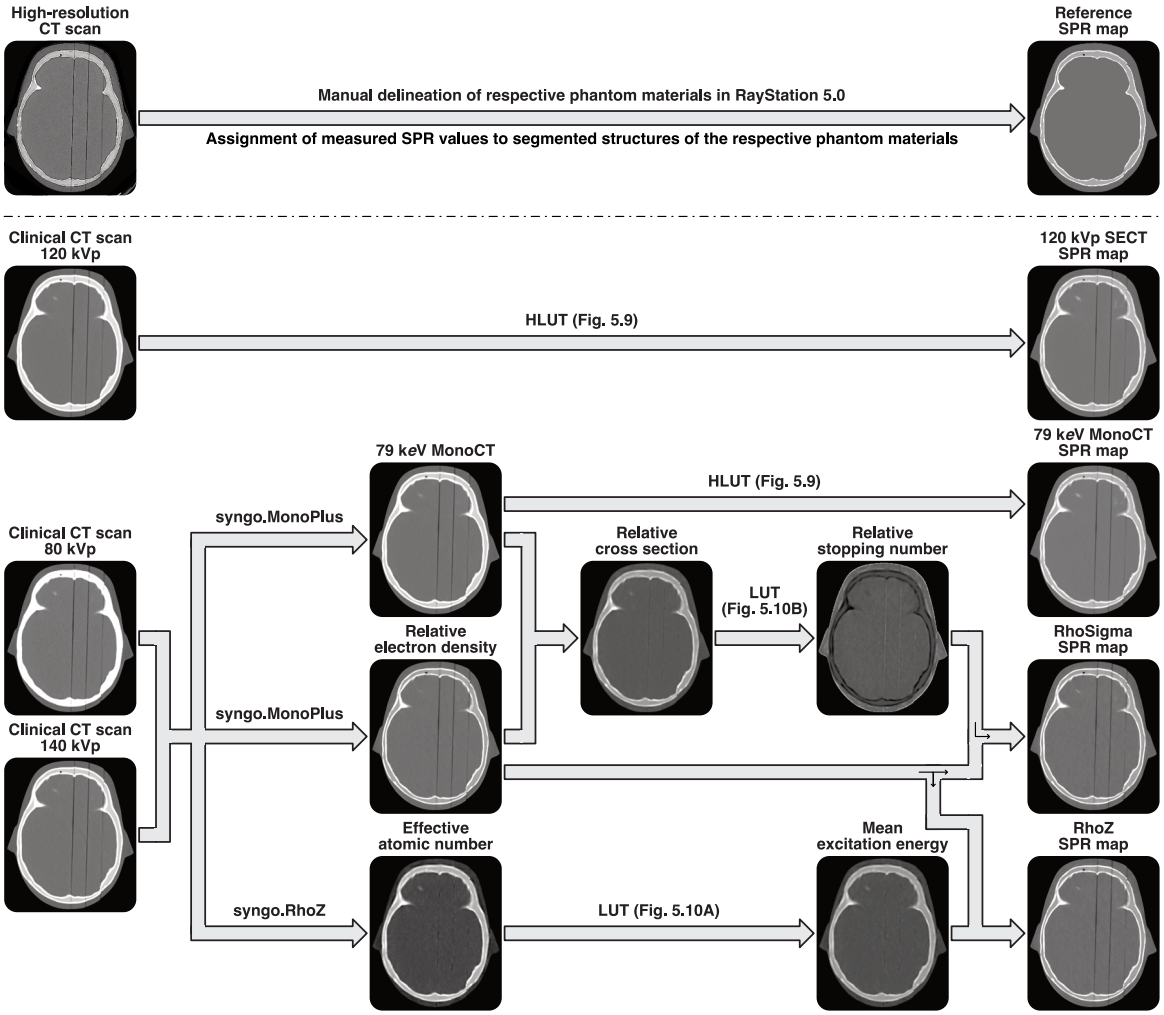

Figure D.1: Flow chart for CT-based generation of SPR maps for the four SPR prediction approaches investigated within this thesis and the reference dataset of the anthropomorphic head phantom.

Table D.1: Details for tissue surrogates used in Monte Carlo simulation of pencil beams with an energy of 150.91 M*e*V and a rectangular momentum spread of 5.455 M*e*V/c: I-values as given by FLUKA based on stoichiometry and as used to match the experimental SPRs; range (R_{80}) in water when passing through 10 mm of the respective material (statistical uncertainty given as standard error); stopping-power ratio and statistical uncertainty. The beam energy and momentum spread were adjusted to match the experimental depth-dose profile in water best. Differences in material thickness (simulation: 10 mm, measurement: 20 mm) result in minute relative changes of SPR, which are negligible compared to other uncertainties. The relatively large changes applied to denser bony tissue are likely to reflect the currently limited knowledge on the I-value of phosphorus, which is present in these surrogates.

Material	I / eV		Change in I / %	Range / mm	SPR
	stoichiom.	used			
Water	75.00	75.00	-	159.033 ± 0.008	1.000
Sinus cavity	69.57	73.32	5.1	167.034 ± 0.010	0.200 ± 0.001
Soft tissue grey	72.17	73.80	2.6	158.732 ± 0.007	1.030 ± 0.001
Spinal cord	72.76	72.45	–0.4	158.642 ± 0.011	1.039 ± 0.001
Brain	74.19	73.01	–1.6	158.598 ± 0.009	1.043 ± 0.001
Spinal disk	79.99	80.64	0.8	158.306 ± 0.011	1.073 ± 0.001
Trabecular bone	76.97	77.51	0.7	157.485 ± 0.008	1.155 ± 0.001
Tooth dentin	97.58	106.26	8.9	154.022 ± 0.012	1.501 ± 0.001
Cortical bone	106.73	120.07	12.5	152.183 ± 0.008	1.685 ± 0.001
Tooth enamel	114.46	133.07	16.3	151.393 ± 0.007	1.764 ± 0.001

Table D.2: Stopping-power ratio (SPR) of homogeneous material samples determined by different CT-based SPR prediction approaches. The material slabs of 20 mm nominal thickness were provided by the manufacturer and correspond to the materials built into the head phantom. The mean SPR ± standard deviation was evaluated in a ROI of the generated SPR datasets.

Material	SPR determined by			
	120 kVp SECT	79 k*e*V MonoCT	RhoSigma	RhoZ
Sinus cavity	0.209 ± 0.005	0.208 ± 0.006	0.204 ± 0.008	0.202 ± 0.006
Soft tissue grey	1.034 ± 0.004	1.039 ± 0.005	1.031 ± 0.009	1.026 ± 0.009
Spinal cord	1.040 ± 0.004	1.044 ± 0.004	1.030 ± 0.007	1.025 ± 0.008
Brain	1.046 ± 0.004	1.050 ± 0.004	1.037 ± 0.007	1.032 ± 0.008
Spinal disk	1.088 ± 0.004	1.096 ± 0.005	1.077 ± 0.008	1.070 ± 0.008
Trabecular bone	1.189 ± 0.003	1.189 ± 0.003	1.151 ± 0.008	1.143 ± 0.007
Tooth dentin	1.556 ± 0.004	1.554 ± 0.002	1.505 ± 0.011	1.496 ± 0.011
Cortical bone	1.663 ± 0.004	1.669 ± 0.004	1.707 ± 0.013	1.697 ± 0.012
Tooth enamel	1.969 ± 0.006	1.977 ± 0.006	1.920 ± 0.017	1.869 ± 0.018
Mean error*	1.1%	1.4%	0.1%	-0.5%
Mean abs. error*	1.8%	1.8%	0.8%	0.9%

* excluding tooth enamel

E Clinical Feasibility of 4D Dual-Energy CT

E.A Patient Information and CT Imaging Data

Table E.1: Patient and tumour characteristics. All lung-cancer patients participated in the PRONTOX trial (Zschaeck et al., 2016).

Characteristic	Patient 1	Patient 2	Patient 3
Gender	Female	Male	Male
Age / a	72	64	54
TNM - Stage	T4N2M0 - IIIB	T4N2M0 - IIIB	T2bN2M0 - IIIA
Target location	Left, upper lung central thorax	Right, upper lung central thorax	Left, upper lung middle left lung
GTV / ml (excluding lymph nodes)	187	200	30
CTV / ml (including lymph nodes)	387	395	190
Average breathing period / s	3.1	4.3	4.3
Diaphragm motion cranio-caudal / mm	13	15	23
GTV motion cranio-caudal / mm	0.2	0.0	0.6
GTV motion posterior-inferior / mm	0.3	0.0	1.9
GTV motion left-right / mm	0.1	0.0	0.8

Table E.2: Applied clinical control CT scan protocol during the course of treatment.

Scan parameter	Single-energy CT	Dual-energy CT	
Tube voltage / kV	120	80	140
Qual. Ref. mAs/rot	85	80	20
Slice collimation	16×1.2 mm		
Gantry rotation time / s	0.5		
Pitch	0.09		
Reconstruction algorithm	SAFIRE		
Reconstruction kernel	Q34/5		
Field of view	500		
Slice thickness / mm	2		

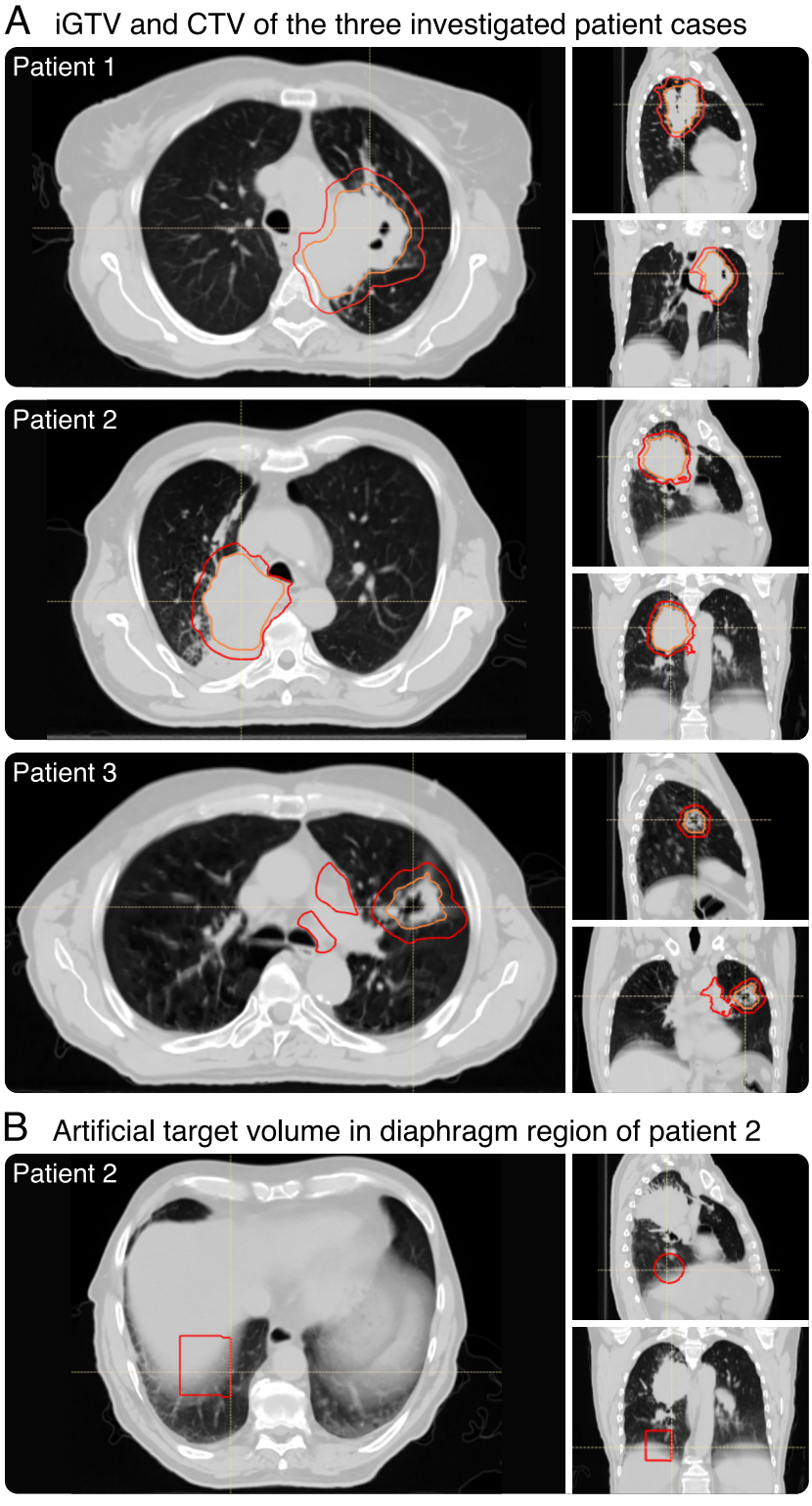

Figure E.1: Time-averaged CT dataset with (A) internal gross tumour volume (iGTV) in orange and clinical target volume (CTV) in red of each investigated patient as well as (B) artificial target volume in red of the worst-case treatment plan for patient 2. Adapted from Wohlfahrt et al. (2018c).

E.B Normalised Cross Correlation

To quantitatively compare CT datasets acquired with different X-ray spectra, CT numbers need to be converted to account for the different attenuation behaviour. A linear conversion was specified for a static thorax phantom using the frequency distribution of correlations between 58 k*e*V and 79 k*e*V CT numbers. The median 79 k*e*V CT number of each 58 k*e*V CT number was obtained. Subsequently, the Hounsfield scale on the x axis was divided in CT numbers smaller and larger than 0 HU. For both regions, the median CT number distribution was described by an intensity-weighted linear regression (Fig. E.2).

After equalising the CT numbers of two datasets, the conformity between both can be assessed by NCC. For a better interpretation of NCC, the NCC was correlated to global geometrical shifts of the patient. For this purpose, a patient CT dataset was shifted by 1 mm to 10 mm in cranio-caudal, posterior-inferior and left-right direction and compared with the non-shifted CT dataset. The conformity was again quantified by NCC. Consequently, the NCC sensitivity regarding geometrical deviation can be estimated (Table E.3, Fig. E.3).

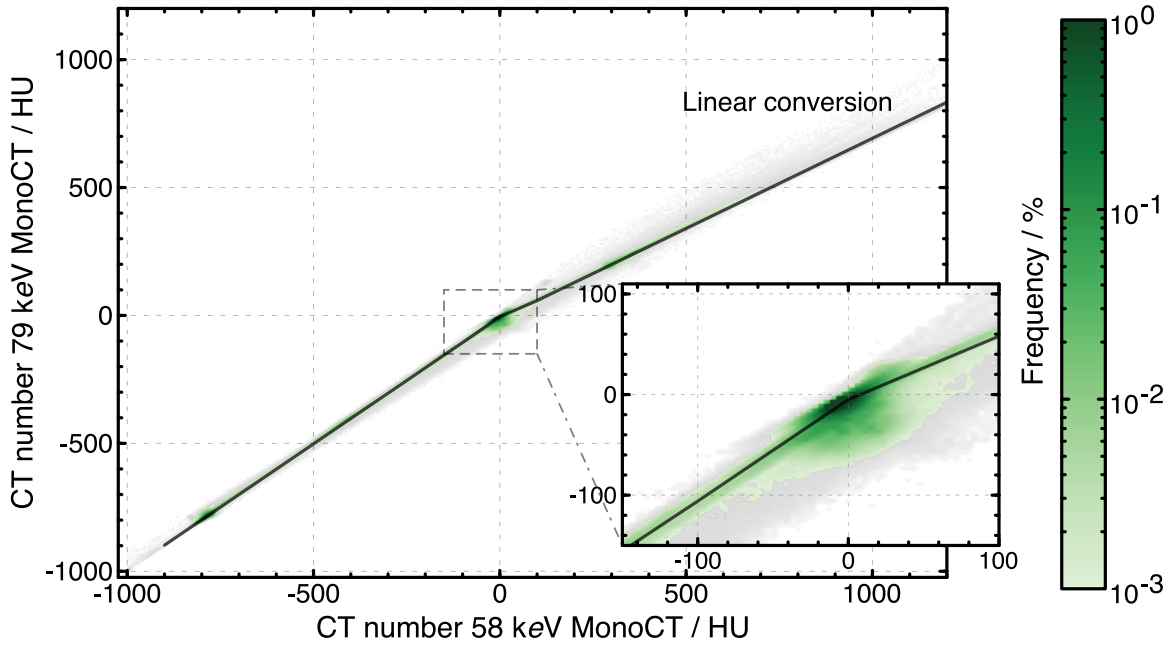

Figure E.2: Linear conversion of CT numbers for different MonoCT datasets. The 58 k*e*V and 79 k*e*V MonoCT datasets correspond to the 80 kVp and 140 kVp CT datasets after image post-processing including a deformable image registration, respectively. The respective time-averaged CT dataset reconstructed from a 4D-DECT scan of a static thorax phantom was used for this assessment. Adapted from Wohlfahrt et al. (2018c).

Table E.3: Normalised cross correlation (NCC) for a patient CT dataset globally shifted in cranio-caudal (CC), posterior-inferior (PI) or left-right (LR) direction. Without loss of generality, the 79 keV MonoCT dataset of maximal inspiration derived from the first 4D-DECT scan of patient 2 was used for this assessment.

Shift mm	Normalised cross correlation (NCC) / %											
	Body			CTV			Heart			Lung		
	CC	PI	LR	CC	PI	LR	CC	PI	LR	CC	PI	LR
1	99.4	99.4	99.2	98.9	99.0	98.8	99.9	99.9	99.9	92.4	92.8	90.5
2	98.8	98.2	97.7	97.8	97.1	96.7	99.9	99.9	99.8	84.7	79.1	74.3
3	97.9	97.0	96.1	95.9	95.1	94.7	99.8	99.8	99.6	74.8	66.6	61.7
4	96.9	95.7	94.8	93.9	93.4	93.0	99.7	99.8	99.3	64.9	56.7	53.3
6	95.1	93.3	92.3	90.1	90.4	90.1	99.5	99.6	98.6	53.5	44.0	43.7
8	93.5	90.9	89.8	86.6	87.9	87.4	99.3	99.3	97.7	46.9	36.9	38.5
10	92.2	88.5	87.5	83.4	85.8	84.9	98.9	98.9	96.7	42.7	32.5	35.5

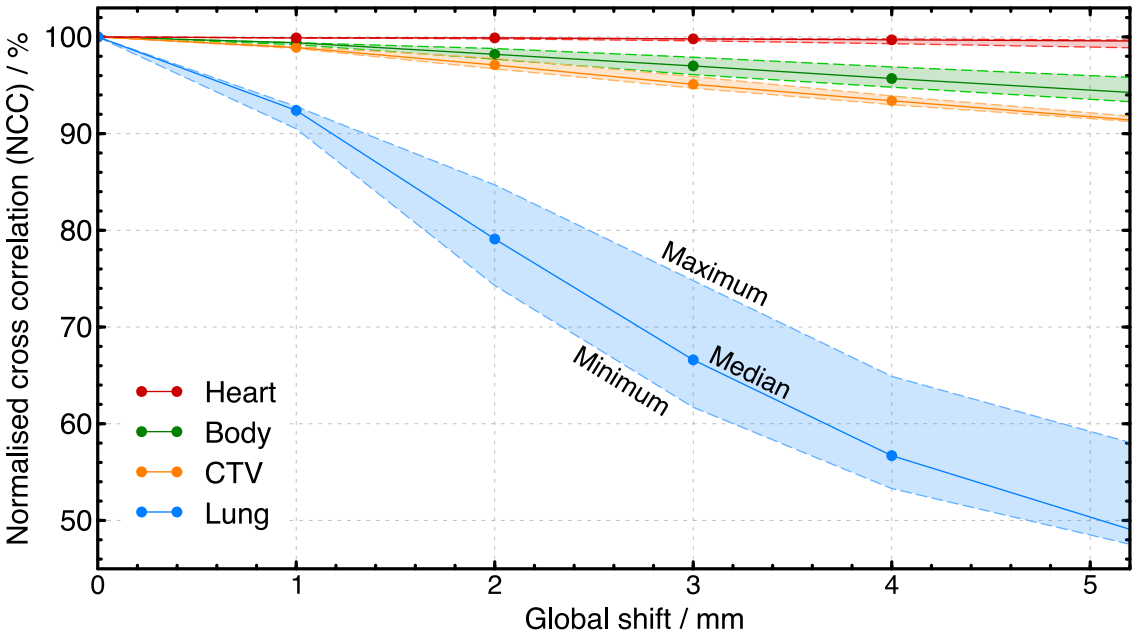

Figure E.3: Normalised cross correlation (NCC) for a patient CT dataset globally shifted in cranio-caudal, posterior-inferior or left-right direction. The illustrated values refer to Table E.3. Adapted from Wohlfahrt et al. (2018c).

E.C Patient Breathing Patterns During CT Acquisition

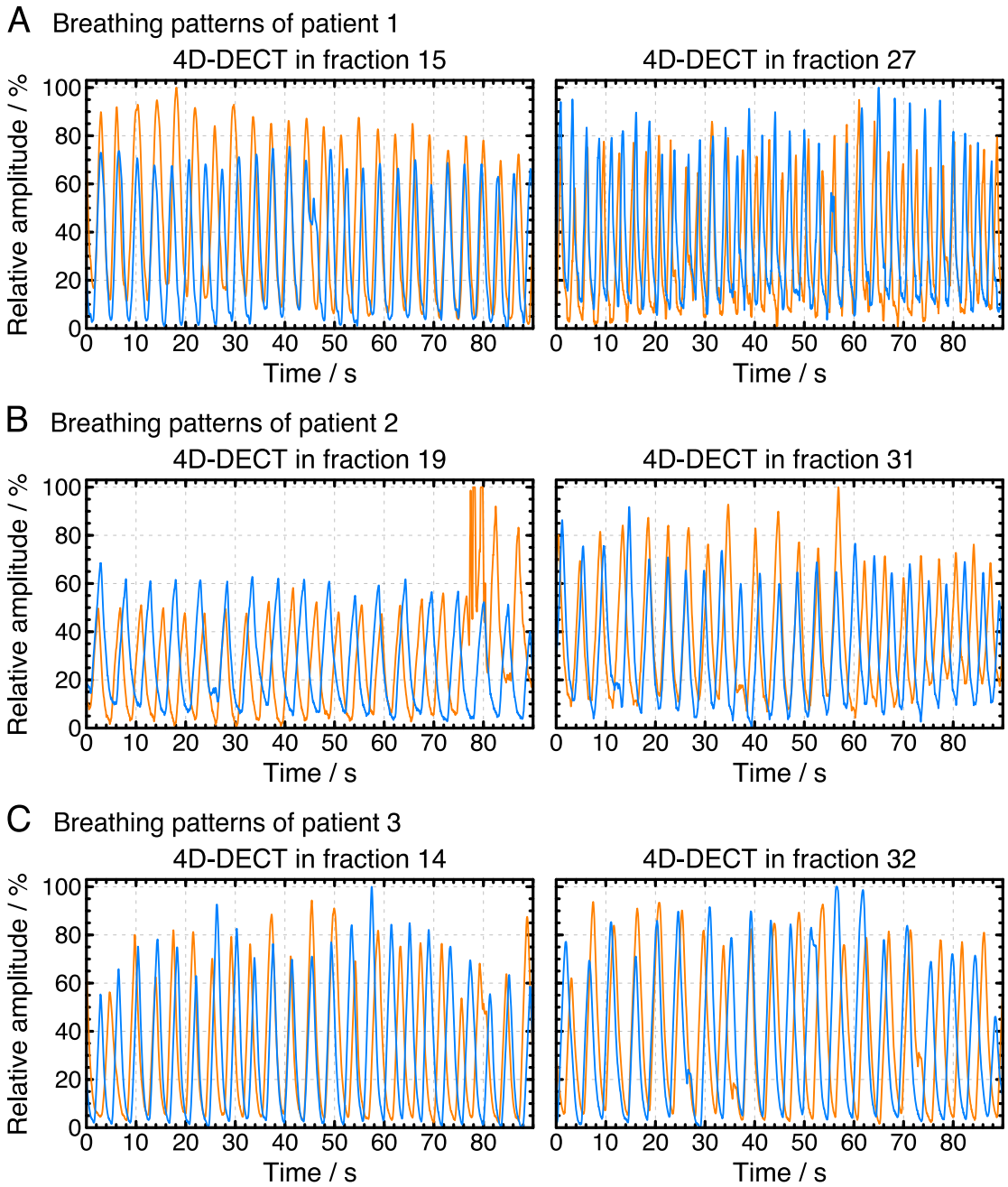

Figure E.4: Patient breathing patterns for dual-spiral time-resolved dual-energy CT (4D-DECT) scans consecutively acquired with 80 kVp (orange) and 140 kVp (blue). Adapted from Wohlfahrt et al. (2018c).

Table E.4: Average respiratory cycle time for each 80 kVp and 140 kVp 4D-DECT scan. Changes in average respiratory cycle time between the corresponding 80 kVp and 140 kVp 4D-DECT scans were within the respective standard deviation and thus relatively small.

Average respiratory cycle time $\pm$ standard deviation / s				
Patient	4D-DECT scan 1		4D-DECT scan 2	
	80 kVp	140 kVp	80 kVp	140 kVp
1	3.7 ± 0.2	3.5 ± 0.4	2.8 ± 0.3	2.7 ± 0.3
2	4.3 ± 0.5*	4.3 ± 0.3	4.1 ± 0.6	3.8 ± 0.4
3	4.2 ± 0.5	3.9 ± 0.2	4.3 ± 0.4	4.6 ± 0.7

* including only the breathing pattern before coughing

E.D Contour-Specific Assessment of Normalised Cross Correlation

NCC for all dual-spiral 4D-DECT datasets of each patient. NCCs are colour-coded corresponding to a global patient shift of $\geq$ 1 mm (green), $\geq$ 2 mm (yellow) and $>$ 2 mm (red). For a conservative estimation, the maximal NCC for each criterion was applied as reference.

Body	Normalised cross correlation (NCC) / %									
	80 kVp vs 140 kVp					58 keV vs 79 keV				
	Avg	Ex 0%	In 40%	In 97%	Ex 50%	Avg	Ex 0%	In 40%	In 97%	Ex 50%
Patient 1 DECT 1	99.5	99.0	99.0	98.9	99.0	99.9	99.9	99.9	99.9	99.9
Patient 1 DECT 2	99.6	99.0	99.1	99.1	99.1	99.9	99.9	99.9	99.9	99.9
Patient 2 DECT 1	97.8	96.3	96.4	96.5	96.5	99.8	99.6	99.3	99.7	99.7
Patient 2 DECT 2	99.5	98.7	98.7	98.6	98.7	99.9	99.8	99.8	99.8	99.8
Patient 3 DECT 1	99.7	99.0	99.0	98.8	99.0	99.9	99.8	99.8	99.8	99.8
Patient 3 DECT 2	99.7	98.9	98.9	98.9	98.8	99.9	99.8	99.8	99.8	99.8

CTV	Normalised cross correlation (NCC) / %									
	80 kVp vs 140 kVp					58 keV vs 79 keV				
	Avg	Ex 0%	In 40%	In 97%	Ex 50%	Avg	Ex 0%	In 40%	In 97%	Ex 50%
Patient 1 DECT 1	99.7	99.2	99.1	99.1	99.3	100	100	99.9	100	100
Patient 1 DECT 2	99.6	99.0	99.1	99.1	99.1	100	99.9	99.9	99.9	99.9
Patient 2 DECT 1	97.3	96.2	96.4	96.7	96.7	100	99.9	99.9	99.9	99.9
Patient 2 DECT 2	99.8	99.3	99.1	98.9	99.1	100	100	100	100	100
Patient 3 DECT 1	99.6	97.8	97.8	97.5	98.1	100	99.9	99.9	99.9	99.9
Patient 3 DECT 2	99.7	98.4	98.1	98.7	98.4	100	100	99.9	99.9	99.9

Heart	Normalised cross correlation (NCC) / %									
	80 kVp vs 140 kVp					58 keV vs 79 keV				
	Avg	Ex 0%	In 40%	In 97%	Ex 50%	Avg	Ex 0%	In 40%	In 97%	Ex 50%
Patient 1 DECT 1	100	99.8	99.9	99.8	99.8	100	100	100	100	100
Patient 1 DECT 2	100	99.9	99.8	99.8	99.9	100	100	100	100	100
Patient 2 DECT 1	100	99.5	99.6	99.5	99.5	100	99.9	99.9	99.9	99.9
Patient 2 DECT 2	100	99.5	99.6	99.5	99.5	100	99.9	99.9	99.9	99.8
Patient 3 DECT 1	100	99.6	99.6	99.6	99.6	100	99.9	99.9	99.9	99.9
Patient 3 DECT 2	100	99.6	99.7	99.4	99.6	100	99.9	99.9	99.9	99.9

Lung	Normalised cross correlation (NCC) / %									
	80 kVp vs 140 kVp					58 keV vs 79 keV				
	Avg	Ex 0%	In 40%	In 97%	Ex 50%	Avg	Ex 0%	In 40%	In 97%	Ex 50%
Patient 1 DECT 1	96.4	90.7	89.8	89.6	88.8	99.8	99.8	99.6	99.7	99.6
Patient 1 DECT 2	97.3	91.1	89.5	92.2	91.2	99.9	99.8	99.6	99.8	99.7
Patient 2 DECT 1	88.4	81.7	72.4	63.7	72.0	99.8	99.6	99.2	97.8	99.3
Patient 2 DECT 2	96.9	91.7	86.3	80.6	84.6	99.8	99.7	99.5	99.3	99.8
Patient 3 DECT 1	97.7	92.9	88.6	84.8	87.0	99.8	99.7	99.5	99.5	99.4
Patient 3 DECT 2	98.0	93.2	90.7	89.2	89.5	99.8	99.8	99.7	99.6	99.5

E.E Intra-Observer Variability of GTV Delineation

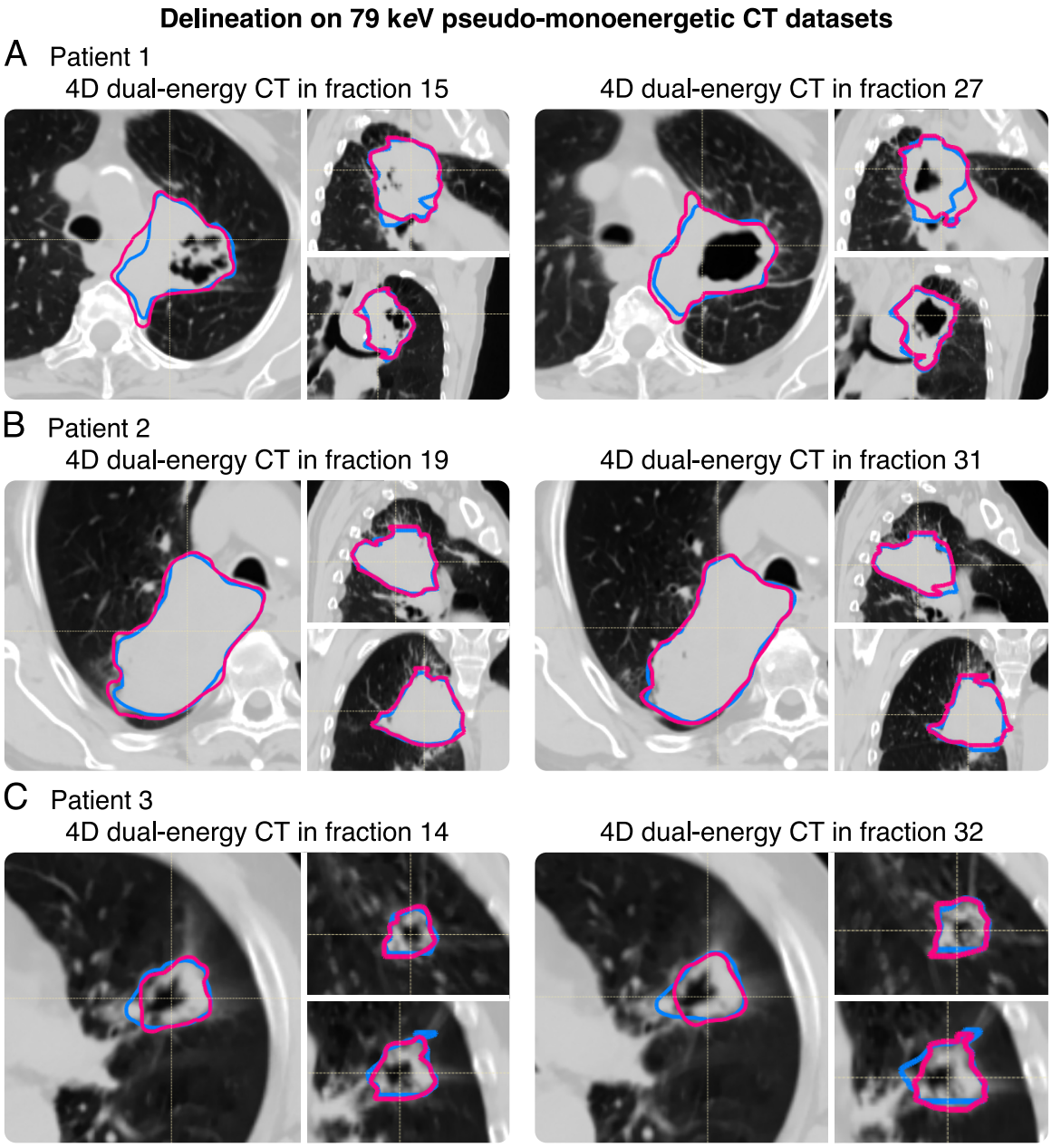

Figure E.5: GTV delineated by an experienced physician at day 1 (blue) and day 2 (magenta) on a time-averaged 79 k*e*V MonoCT dataset derived from dual-energy CT. Adapted from Wohlfahrt et al. (2018c).

The delineation on a combination of two datasets derived from dual-energy CT, which illustrate either the relative electron density (RED) or relative photon attenuation cross section (RCS), was performed in a multi-step procedure. First, the border of the tumour close to the

lung tissue was delineated on the RCS dataset using a lung CT window. Subsequently, this delineation was adapted on the RED dataset applying a lung CT window. Finally, the tumour border along the mediastinum was delineated on the RED dataset using a CT window for mediastinum.

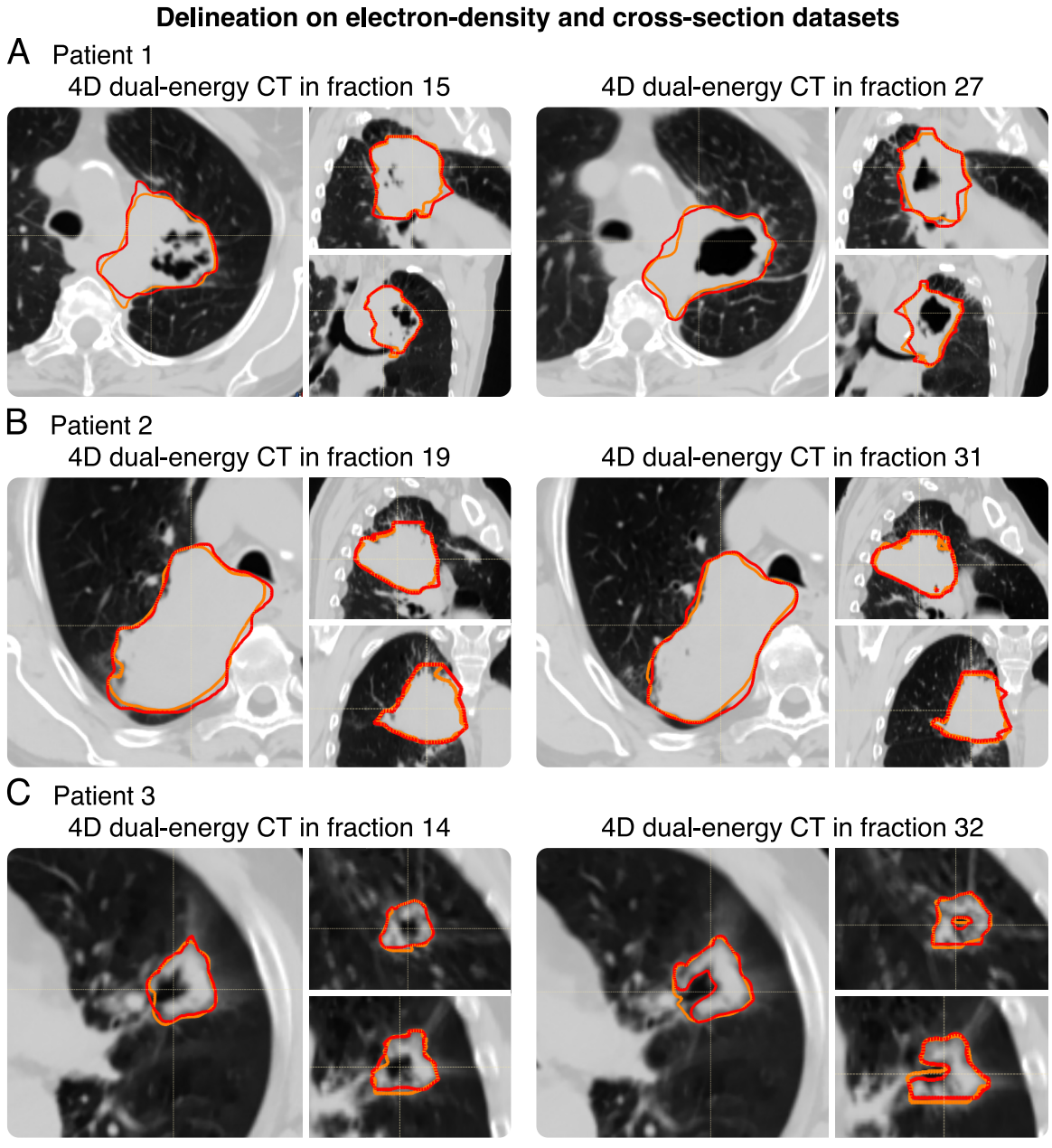

Figure E.6: GTV delineated by an experienced physician at day 1 (orange) and day 2 (red) on a combination of time-averaged electron-density and cross-section datasets derived from dual-energy CT. Adapted from Wohlfahrt et al. (2018c).

Acknowledgement

First of all, I would like to thank Prof. Dr. Wolfgang Enghardt for the opportunity to continue my work on CT-based proton range prediction within a PhD project at OncoRay in Dresden. I especially value his expert advices on theoretical and practical aspects of my thesis, his support and helpfulness as well as his always friendly ear. Furthermore, I thank him and Prof. Dr. Antony J. Lomax for the acceptance to review my PhD thesis.

I am deeply grateful to my supervisor Dr. Christian Richter for his never ending support, many hours of scientific discussions as well as helpful advices during internal and external review processes of publications, abstracts, presentations and posters. I especially liked the always open door of his office allowing for short-term discussions.

I would also like to thank my collaboration partners Dr. Christian Möhler and Dr. Steffen Greilich in Heidelberg for the outstanding teamwork, pleasant atmosphere in many meetings and open-minded discussions. Only due to this close cooperation, we could achieve all of our well-founded scientific results. I really enjoyed the last 3 years within the first joint project of the National Centre for Radiation Research in Oncology.

Furthermore I would like to thank all colleagues of the group "High precision radiotherapy" for the fruitful discussions and nice group excursions. Especially, I thank Dr. Annika Jakobi and Dr. Kristin Stützer for their support and helpful advices during the last years. I have learned a lot from their clinical and scientific experiences. A special thanks also to Stefan Leger for many hours of conversations in the morning with a cup of coffee, at lunch in the Caruso or in the evening with a half-and-half pizza. I will also acknowledge Nils Peters for many hours of proofreading my PhD thesis. I would also like to thank all bachelor and master students, who substantially contributed to this work on dual-energy CT, especially Felix Negwer, Carolin Arnsmeyer and Sebastian Munzert.

Moreover, I would like to acknowledge all clinical staff supporting the clinical implementation of dual-energy CT in our proton and photon therapy facility. A special thanks to Julia Thiele and her RTT team, which had to handle all the little workflow problems in the beginning. I would also like to thank Prof. Dr. Michael Baumann, Prof. Dr. Mechthild Krause and

Prof. Dr. Esther Troost for all the clinical contributions, confidence in our work and the spirit of translation. I am also grateful to all the medical physicists, especially Dr. Daniela Kunath and Dr. Stefan Menkel, who supported this project from the beginning.
I also thank our collaboration partners from Siemens Healthineers, especially Dr. Nora Hünemohr, Dr. Christian Hofmann and Gerald Reinig, for a very good and targeted cooperation.
I would like to thank all of my roommates at OncoRay, the active participants of OncoRow and of the ESTRO running team as well as all colleagues, who ensured the pleasant working atmosphere at OncoRay.
Finally, I would like to thank my family and all of my friends, who supported me during this time.

Erklärungen zur Eröffnung des Promotionsverfahrens

1. Hiermit versichere ich, dass ich die vorliegende Arbeit ohne unzulässige Hilfe Dritter und ohne Benutzung anderer als der angegebenen Hilfsmittel angefertigt habe; die aus fremden Quellen direkt oder indirekt übernommenen Gedanken sind als solche kenntlich gemacht.

2. Bei der Auswahl und Auswertung des Materials sowie bei der Herstellung des Manuskripts habe ich Unterstützungsleistungen von folgenden Personen erhalten:
   B.Sc. Felix Negwer,
   Dr. Steffen Greilich,
   Dr. Annika Jakobi,
   Dr. Christian Möhler,
   Dr. Christian Richter and
   Prof. Dr. Wolfgang Enghardt.

3. Weitere Personen waren an der geistigen Herstellung der vorliegenden Arbeit nicht beteiligt. Insbesondere habe ich nicht die Hilfe eines kommerziellen Promotionsberaters in Anspruch genommen. Dritte haben von mir weder unmittelbar noch mittelbar geldwerte Leistungen für Arbeiten erhalten, die im Zusammenhang mit dem Inhalt der vorgelegten Dissertation stehen.

4. Die Arbeit wurde bisher weder im Inland noch im Ausland in gleicher oder ähnlicher Form einer anderen Prüfungsbehörde vorgelegt.

5. Die Inhalte dieser Dissertation wurden in folgender Form veröffentlicht:

   - Möhler C, Wohlfahrt P, Richter C und Greilich S. 2016. Range Prediction for Tissue Mixtures Based on Dual-Energy CT. Physics in Medicine and Biology 61:N268–N275. DOI: 10.1088/0031-9155/61/11/N268

     This study was mainly carried out by C. Möhler at the German Cancer Research Centre (Heidelberg, Germany) in the framework of a joint project within the National Centre for Radiation Research in Oncology in Germany.

   - Wohlfahrt P, Möhler C, Hietschold V, Menkel S, Greilich S, Krause M, Baumann M, Enghardt W und Richter C. 2017. Clinical Implementation of Dual-Energy CT

for Proton Treatment Planning on Pseudo-Monoenergetic CT Scans. International Journal of Radiation Oncology Biology Physics 97:427–434. DOI: 10.1016/j.ijrobp.2016.10.022

This study was mainly carried out by P. Wohlfahrt at OncoRay (Dresden, Germany) in the framework of a joint project within the National Centre for Radiation Research in Oncology in Germany.

- Möhler C, Wohlfahrt P, Richter C und Greilich S. 2017. Methodological Accuracy of Image-Based Electron Density Assessment Using Dual-Energy Computed Tomography. Medical Physics 44:2429–2437. DOI: 10.1002/mp.12265

  This study was mainly carried out by C. Möhler at the German Cancer Research Centre (Heidelberg, Germany) in the framework of a joint project within the National Centre for Radiation Research in Oncology in Germany.

- Wohlfahrt P, Möhler C, Greilich S und Richter C. 2017. Comment on: Dosimetric Comparison of Stopping-Power Calibration with Dual-Energy CT and Single-Energy CT in Proton Therapy Treatment Planning [Med. Phys. 43(6), 2845-2854 (2016)]. Medical Physics 44:5533–5536. DOI: 10.1002/mp.12418

  This study was mainly carried out by P. Wohlfahrt at OncoRay (Dresden, Germany) in the framework of a joint project within the National Centre for Radiation Research in Oncology in Germany.

- Wohlfahrt P, Möhler C, Stützer K, Greilich S und Richter C. 2017. Dual-Energy CT Based Proton Range Prediction in Head and Pelvic Tumor Patients. Radiotherapy and Oncology 125:526–533. DOI: 10.1016/j.radonc.2017.09.042

  This study was mainly carried out by P. Wohlfahrt at OncoRay (Dresden, Germany) in the framework of a joint project within the National Centre for Radiation Research in Oncology in Germany.

- Wohlfahrt P, Möhler C, Richter C und Greilich S. 2018. Evaluation of Stopping-Power Prediction by Dual- and Single-Energy Computed Tomography in an Anthropomorphic Ground-Truth Phantom. International Journal of Radiation Oncology Biology Physics 100:244–253. DOI: 10.1016/j.ijrobp.2017.09.025

  This study was equally carried out by all authors.

- Möhler C, Russ T, Wohlfahrt P, Elter A, Runz A, Richter C und Greilich S. 2018. Experimental Verification of Stopping-Power Prediction from Single- and Dual-Energy Computed Tomography in Biological Tissues. Physics in Medicine and Biology 63:025001. DOI: 10.1088/1361-6560/aaa1c9. arXiv: 1708.07368

  This study was mainly carried out by C. Möhler at the German Cancer Research Centre (Heidelberg, Germany) in the framework of a joint project within the National Centre for Radiation Research in Oncology in Germany.

- Möhler C, Wohlfahrt P, Richter C und Greilich S. 2018. On the Equivalence of Image-Based Dual-Energy CT Methods for the Determination of Electron Density and Effective Atomic Number in Radiotherapy. Physics and Imaging in Radiation Oncology 5:108–110. DOI: 10.1016/j.phro.2018.03.003

  This study was mainly carried out by C. Möhler at the German Cancer Research Centre (Heidelberg, Germany) in the framework of a joint project within the National Centre for Radiation Research in Oncology in Germany.

- Wohlfahrt P, Troost EGC, Hofmann C, Richter C und Jakobi A. 2018. Clinical Feasibility of Single-Source Dual-Spiral 4D Dual-Energy CT for Proton Treatment Planning Within the Thoracic Region. International Journal of Radiation Oncology Biology Physics. DOI: 10.1016/j.ijrobp.2018.06.044

  This study was mainly carried out by P. Wohlfahrt at OncoRay (Dresden, Germany).

- Wohlfahrt P, Möhler C, Troost EGC, Greilich S und Richter C. 2018. Dual-Energy Computed Tomography to Assess Intra- and Inter-patient Tissue Variability in Proton Treatment Planning of Brain-Tumor Patients. Radiotherapy and Oncology in preparation

  This study was mainly carried out by P. Wohlfahrt at OncoRay (Dresden, Germany) in the framework of a joint project within the National Centre for Radiation Research in Oncology in Germany.

6. Ich bestätige, dass es keine zurückliegenden erfolglosen Promotionsverfahren gab.

7. Ich bestätige, dass ich die Promotionsordnung der Medizinischen Fakultät Carl Gustav Carus der Technischen Universität Dresden anerkenne.

8. Ich habe die Zitierrichtlinien für Dissertationen an der Medizinischen Fakultät der Technischen Universität Dresden zur Kenntnis genommen und befolgt.

Dresden, 2. Mai 2018 _____

Erklärung über die Einhaltung der gesetzlichen Bestimmungen

Hiermit bestätige ich die Einhaltung der folgenden aktuellen gesetzlichen Vorgaben im Rahmen meiner Dissertation

- ☐ das zustimmende Votum der Ethikkommission bei Klinischen Studien, epidemiologischen Untersuchungen mit Personenbezug oder Sachverhalten, die das Medizinproduktegesetz betreffen.
  EK535122015

- ☐ ~~die Einhaltung der Bestimmungen des Tierschutzgesetzes~~
  nicht zutreffend

- ☐ ~~die Einhaltung des Gentechnikgesetzes~~
  nicht zutreffend

- ☐ die Einhaltung von Datenschutzbestimmungen der Medizinischen Fakultät und des Universitätsklinikums Carl Gustav Carus.

Dresden, 2. Mai 2018 _____